Ultrasonic welding of PAEK thermoplastic composites

Margot Bonmatin

THÈSE

En vue de l'obtention du

DOCTORAT DE L'UNIVERSITÉ DE TOULOUSE

Délivré par :

Institut National Polytechnique de Toulouse (Toulouse INP)

Discipline ou spécialité :

Génie Mécanique, Mécanique des Matériaux

Présentée et soutenue par :

Mme MARGOT BONMATIN

le mardi 12 avril 2022

Titre :

Soudage par ultrasons de composites thermoplastiques à matrice PAEK

Ecole doctorale :

Mécanique, Energétique, Génie civil, Procédés (MEGeP)

Unité de recherche :

Laboratoire Institut Clément Ader (ICA)

Directeur(s) de Thèse :

M. THIERRY CUTARD

MME FRANCE CHABERT

Rapporteurs :

M. GILLES REGNIER, ENSAM - ARTS ET METIERS PARISTECH

MME IRENE FERNANDEZ VILLEGAS, UNIVERSITE DE DELFT

Membre(s) du jury :

M. FRÉDÉRIC RESTAGNO, UNIVERSITE PARIS-SACLAY, Président

M. GÉRARD BERNHART, ECOLE NLE SUP DES MINES ALBI CARMAUX, Invité(e)

MME FRANCE CHABERT, ECOLE NATIONALE D'INGENIEUR DE TARBES, Membre

M. STEVEN LE CORRE, POLYTECH NANTES, Membre

M. THIERRY CUTARD, ECOLE NLE SUP DES MINES ALBI CARMAUX, Membre

M. TOUFIK DJILALI, SOCIETE LAUAK INNOVATIVE SOLUTIONS, Invité(e)

Contents

Introduction **1**

1 State of the art about ultrasonic welding of thermoplastic composites **9**

1.1 Introduction 10

1.2 Joining of composite materials 10

1.2.1 Composite materials 10

1.2.2 Joining techniques of composites 14

1.2.3 Welding of thermoplastic composites 16

1.3 Ultrasonic welding 22

1.3.1 Static ultrasonic welding 24

1.3.2 Ultrasound propagation through materials 29

1.3.3 Dynamic ultrasonic welding 30

1.4 Temperature monitoring during joining process 32

1.4.1 Thermography 33

1.4.2 Thermocouple 34

1.4.3 The case of ultrasonic welding 34

1.5 Mechanical strength of joints 36

1.5.1 Experimental techniques 38

1.5.2 Failure mechanisms 40

1.6 Conclusion 42

2 Materials and experimental techniques **45**

2.1 Introduction . . . 46
2.2 Overview of the welded materials . . . 46
2.2.1 Thermoplastic polymer matrices . . . 46
2.2.2 APC-2 prepreg . . . 53
2.2.3 AE 250 prepreg . . . 54
2.3 Manufacturing of plates and specimens . . . 54
2.3.1 Vaccum bag process . . . 54
2.3.2 Plate characterization . . . 59
2.4 Ultrasonic welding device . . . 61
2.4.1 Welder modules . . . 61
2.4.2 Welding parameters . . . 64
2.4.3 Typical curves from the device output parameters . . . 65
2.5 Conclusion . . . 66

3 Rheological and crystallization behaviors of PAEK 69

3.1 Introduction . . . 70
3.2 Thermal properties of AE 250 and PEEK . . . 70
3.2.1 Thermal stability . . . 70
3.2.2 Effect of cooling rate on thermal transition . . . 72
3.3 Rheological characterization of AE 250 and PEEK . . . 77
3.3.1 Effect of time on complex viscosity . . . 77
3.3.2 Effect of temperature on complex viscosity . . . 79
3.4 Calculation of relaxation times . . . 84
3.4.1 Definition of η_0 . . . 84

3.4.2 Definition of J_e^0 . . . 85
3.4.3 Calculation of the molecular weight between entanglement . . . 88
3.4.4 Comparison to other PAEK . . . 89
3.5 Conclusion . . . 90

4 Thermal analysis of ultrasonic welding 93
4.1 Introduction . . . 94
4.2 Thermocouple insertion for welding specimens . . . 94
4.2.1 Thermocouple preparation . . . 94
4.2.2 Incorporation procedure . . . 95
4.2.3 Characterization of specimens with integrated thermocouple . . . 96
4.3 Applications to US welding . . . 97
4.3.1 Post-synchronization of temperature results with welding output parameters . . . 97
4.3.2 Temperature profiles during short impulsion time welding . . . 98
4.4 Temperature profile measurements during welding . . . 102
4.4.1 Analysis of a typical temperature curve . . . 102
4.4.2 Influence of welding parameters . . . 104
4.4.3 Influence of thermocouple on mechanical properties . . . 108
4.5 Thermal diffusion modeling from the interface . . . 109
4.5.1 Description of the finite element model . . . 110
4.5.2 Model results . . . 113
4.5.3 Influence of the number of PEI layers . . . 116
4.6 Conclusion . . . 119

5 Mechanical & morphological analyses of CF/PAEK welds **121**

5.1 Introduction . . . 122

5.2 Mechanical properties of CF/PEEK composite welds using a PEI energy director . . . 122

5.2.1 Single lap shear test . . . 122

5.2.2 Influence of welding parameters . . . 123

5.2.3 Influence of the number of PEI layers . . . 127

5.2.4 Influence of the ED nature . . . 130

5.2.5 Analysis of the sonotrode final displacement . . . 132

5.3 Characterization of the interphase & analysis of fracture mechanisms . . . 134

5.3.1 Interfacial fracture mechanisms . . . 134

5.3.2 Composition of PEI/PEEK interphase in the welded zone . . . 137

5.3.3 Properties of PEI/PEEK blends . . . 142

5.4 Ultrasonic welding of AE 250 composites . . . 152

5.5 Conclusion . . . 156

Conclusion & perspectives **157**

A Material datasheets **163**

B Raman spectroscopy **177**

C Characterization of PEEK/PEI blends **179**

Bibliography **183**

List of Figures

1.1 Chemical formulas of different PAEK polymers 12

1.2 Chemical formulas of isophthalic PEKK and terephthalic PEKK 13

1.3 Diagram of mechanical fastener 14

1.4 Diagram of adhesive bonding 16

1.5 Reptation of a macromolecular chain following the De Gennes' theory . . . 17

1.6 Intermolecular diffusion of chains at the interface 18

1.7 Diagram illustrating the different thermoplastic composite welding processes 19

1.8 Illustration of thermal welding processes 20

1.9 Illustration of electromagnetic welding processes 21

1.10 Illustration of friction welding processes 22

1.11 Number of publications and citations about US welding 23

1.12 Distribution of papers aboutUS welding 23

1.13 Diagram illustrating ultrasonic welding process 24

1.14 Common sonotrode shapes for ultrasonic welding 25

1.15 Input and output welding parameters 26

1.16 Power & displacement curves during welding 27

1.17 Interfacial fracture of CF/PEI welds 28

1.18 Triangular energy director during US welding 29

1.19 Sound frequency scale 30

1.20 Continuous US welding device prototype 31

1.21 Optical microscopies and single lap shear tests of 3 welding configurations . 31

1.22 Interfacial fracture after lap shear test 32
1.23 IR thermogram during transmission laser welding of PEKK 33
1.24 Temperature curves during welding of CF/PEEK specimens 35
1.25 Total dissipation model & temperature modelling 36
1.26 Crack propagation modes 37
1.27 Cross tensile test specimen configuration (a) and set up (b) 39
1.28 Diagram of single lap shear specimens configuration 40
1.29 Interfacial fracture micrographies of welded specimens 41

2.1 Chemical formula of PEEK 47
2.2 FTIR spectra of PEEK 450G and AE 250 48
2.3 Melting and glass transition temperatures of usual PAEK polymers 49
2.4 DSC curves of PEEK and AE 250 of slowly air-cooled samples 49
2.5 Thermal conductivities of PEEK and AE 250 50
2.6 Manufacturing process of films and flakes rheology samples 51
2.7 Temperature and pressure cycles to obtain the specimens for rheometry . . 51
2.8 Chemical formula of PEI 52
2.9 Unidirectional APC-2 tape from Solvay 53
2.10 Unidirectional AE 250 prepreg from Victrex 54
2.11 Cutting process of APC-2 (a) and AE 250 (b) prepregs 55
2.12 Stacking of APC-2 with a PEI layer 56
2.13 The different plate families 56
2.14 Diagram of the manufacturing process layout of the composite plates . . . 57
2.15 Photograph of manufacturing process after vaccum bagging 57

2.16 Thermal cycles undergone by APC-2 (a) and AE 250 (b) 58

2.17 Abrasive water-jet cutting of 300 x 300 mm^2 APC-2 plate 59

2.18 Surface roughness of a CF/PEEK specimen 60

2.19 Out-of-plane micrographs of plate P2, P3 and P5 60

2.20 Energy director thickness measurement at different locations of the plates . 61

2.21 Electrical Motion 20 (Rinco Ultrasonics) ultrasonic welding equipment . . 62

2.22 Clamping jaw of the welding specimens 63

2.23 Movement of the upper specimen due to the melting of the ED during welding 63

2.24 Input parameters of the welding device 64

2.25 Typical power, load and displacement curves during ultrasonic welding . . 66

3.1 TGA curves of PAEK AE 250 FM 71

3.2 TGA curves of PEEK in nitrogen and air atmospheres 71

3.3 DSC curves of FM, FL and FLc for heating rate of 20 $°C.min^{-1}$ 73

3.4 DSC curves of the cooling and 2nd heating stages 76

3.5 Influence of cooling rate on crystallinity and melting temperature 77

3.6 Effect of time on complex viscosity 78

3.7 Strain sweeps of the complex moduli of FMc for a frequency of 1 Hz . . . 80

3.8 G' and G'' for FLc (a) and FMc (b) 81

3.9 Master curves of G' and G'' for FLc and FMc with a reference temperature 82

3.10 Master curves of the complex viscosity for FLc & FMc 82

3.11 Arrhenius representation of the TTS shift factors of FLc (-□-) and FMc (-△-) 83

3.12 Cole-Cole representation of the complex viscosity of FMc 85

3.13 Complex moduli G' and G'' of FMc at 330 $°C$ 87

3.14 Relaxation times, τ_w (-□-) and τ_n (-△-), of FMc, FLc and PEEK 450G . . 87

3.15 Zero-shear viscosity with temperature for commercial PAEK 90

4.1 Layout of hand-made thermocouple from chromel and alumel wires 95

4.2 Thermocouple integration process inside the energy director 95

4.3 Micrographs of welding specimens after integration of thermocouples . . . 96

4.4 Layout of the profile temperature measurement set up 97

4.5 Synchronization of welding output data 98

4.6 Welding configuration for short impulsion time welding experiments 98

4.7 Temperature profiles for different impulsion time & welding load 99

4.8 Influence of the thermocouple location on the temperature measurement . 100

4.9 Micrographs of the welding interface before & after welding 101

4.10 Welding configuration for temperature profile measurements 103

4.11 Temperature and travel curves showing different steps 104

4.12 Temperature profiles & travel during USW for several welding loads 106

4.13 Effect of ultrasonic amplitude on temperature profiles and sonotrode travel 107

4.14 Influence of welding time on temperature profiles & travel during USW . . 108

4.15 Lap shear strength with and without thermocouple 109

4.16 Through-thickness model of the welding configuration 111

4.17 Mesh elements of the out-of-plane model 112

4.18 Experimental and numerical thermograms during welding process 114

4.19 Temperature profiles through the assembly for 3 PEI layers 115

4.20 Mesh elements of the out-of-plane model with one PEI layer 117

4.21 Temperature profiles through the assembly for one PEI layer 117

4.22 Temperature and cooling rate evolution through the interface 118

5.1 Single lap shear experiment layout 123

5.2 Lap shear strength for different values of welding load 124

5.3 Interfacial fracture of welded specimens in several welding conditions . . . 125

5.4 Lap shear strength for different values of amplitude 125

5.5 Lap shear strength for different values of welding time 126

5.6 Welding configurations using different numbers of PEI layers 128

5.7 Lap shear strength for different numbers of PEI layers 129

5.8 Interfacial fracture of welded specimens for all welding configurations . . . 130

5.9 LSS for different welding times and for PEI and PEEK energy director . . 131

5.10 Interfacial fracture of welds for welding times & PEEK energy director . . 132

5.11 Final sonotrode displacements for CF/PEEK welds 133

5.12 SEM micrographs of PEI-localized and PEEK-localized fractures 134

5.13 Cohesive failure within the CF/PEEK layer 135

5.14 Interfacial cohesive failure APC-2 plies through SEM and optical micrographs 136

5.15 SEM & optical micrograph of interfacial fracture 137

5.16 Out-of-plane cutting of welds for Raman spectroscopy 137

5.17 Raman spectra of PEEK, PEI and carbon fibers 138

5.18 Chemical bonds analyzed on Raman spectroscopy for PEEK and PEI . . . 138

5.19 Mapping of interphase zone using the band relative intensities ratio 139

5.20 Raman mapping of species distribution in the interphase zone 141

5.21 Mapping of interphase zone after welding using a multicurve regression . . 142

5.22 Glass transition temperature for different ratio of PEEK in PEI/PEEK blends 143

5.23 Loss factor from DMA for different ratio of PEEK in PEI/PEEK blend . . 144

5.24 DSC thermogram of PEI/PEEK blends for cooling rate of 20 $°K.min^{-1}$ . . 145

5.25 Normalized crystallinity of PEEK in PEI/PEEK blends 146

5.26 Storage (a) and loss (b) moduli of PEEK/PEI blends 147

5.27 Load-displacement curves of pure PEEK, pure PEI and different blend ratios 149

5.28 SEM micrograph of a PEEK-based fracture 149

5.29 Initial stiffness and maximum load of PEEK/PEI blends 150

5.30 Lap shear strength for different welding parameters of AE 250 specimens . 153

5.31 Interfacial fracture of AE 250 welds for different welding times 153

5.32 Lap shear strength in configuration B of PEEK and AE 250 composite welds 154

5.33 Final sonotrode displacements for AE 250 specimens in configuration B . . 155

C.1 Three-point-bending test from ASTM B5045-14 181

C.2 Load-displacement curves of pure PEEK, pure PEI and different blend ratios 182

List of Tables

1.1 Young's modulus of usual fibers 11

1.2 Common commercial grades of PEEK and PEKK 13

2.1 Summary of the materials available for this study. FMc are plates from films and FLc are plates from flakes. 54

3.1 Average thermal transitions and enthalpies for FM and FL and FLc 74

3.2 Activation energy for usual industrial PAEK 84

3.3 Cross-over values of the moduli for FLc and FMc 86

4.1 Thermal properties of APC-2 [Ageorges et al., 1998] 111

4.2 Thermal parameters of PEI [Don et al., 1990] 111

5.1 K_Q of pure PEEK, pure PEI and different blend ratios 151

C.1 Proportion of PEI and PEEK for each volume ratio 180

C.2 Initial stiffness and maximum load of pure PEEK, pure PEI and different blend ratios 181

Introduction

The increasing use of composites in industry opens the way towards new challenges and opportunities. Composite materials are made of long fibers embedded in an organic matrix. When these composites are made of carbon fibers, they allow to lighten structural parts and to obtain a high specific strength, given by the tensile strength divided by the density of the material. Complex geometries are manufactured by numerous and versatile processes. Their properties are adapted by using different raw materials or by changing the fiber content and orientation. These advantages are the reason for the widespread use of composite materials in the aerospace and other transportation industries. For over 40 years, the market was dominated by thermoset matrix composites. The last two decades have seen the emergence of thermoplastic matrix composites. These kinds of composites are a promising option to contribute to reduce the environmental impact: similar to any thermoplastic polymers, production wastes or end-of-life parts could be re-shaped into new parts. Moreover, they do not request to keep pre-impregnated semi-products under freezing conditions decreasing environmental costs. Also, thermoplastic composite parts are an opportunity to increase the competitiveness of companies: the manufacturing processes are faster than their thermoset counterparts, allowing reduction of production cycle times.

Nonetheless, a joining method must be found to bolster thermoplastic composites to a significant and sustainable place in the industry. Indeed, thermoplastic composites offer new assembling possibilities by fusion bonding. Mechanical fastening is the easiest way of joining composites parts, but it leads to corrosion around the bonding area and the weight is significantly increased. Adhesive bonding is also considered for assembling thermoplastic parts despite the difficulty to activate the surface, to increase the surface tension prior to adhesive spreading. The most suitable option appears to be fusion bonding, namely welding, since the drawbacks of other joining techniques are mainly prevented with this technique. Welding processes can be divided into three groups depending on how heat is generated at the interface: thermal welding, electromagnetic welding and friction welding. Induction and resistance welding belong to the electromagnetic group. The two are watched as promising way by the industry to assemble thermoplastic composites. Some companies have recently heavily invested in induction process to meet the joining strength required for aerospace parts. However, induction and resistance welding display long welding times of a few minutes and high energy consumption. They can also induce a material deconsolidation through the thickness which can have an influence on the consolidated composite material. Moreover, the materials must fulfil special properties, like electrical conductivity, to be

joined. Ultrasonic (US) welding, although not yet expanded for composites, appears as a better option, since no specific material property is requested and very short welding times of a few seconds are involved. No additional device is necessary to generate heat in the welding area in contrast to induction and resistance welding for which, susceptor and resistor are required, respectively.

Ultrasonic welding is a cost-effective friction welding process. Polymers with low melting temperature under 200 $°C$ such as polyethene or polypropylene are easily welded with this technique. High-frequency waves are created by a generator and transformed into mechanical waves by a piezoelectric convertor. Usually, the frequencies are between 20 kHz and 70 kHz. Those low-amplitude vibrations are amplified by a booster and sent to the metal part, called the sonotrode, in direct contact with the substrates. The sonotrode vibration is transmitted to the substrates, allowing melting of the interface. The geometry of the parts is essential as it directly impacts whether or not the energy will be concentrated at the welding interface. In the case of composite US welding, a polymer-based layer, called energy director, is generally placed at the interface to allow better heat generation in this location.

Although ultrasonic welding is widely chosen in automotive industry to assemble pure thermoplastics and short fiber reinforced thermoplastics, the process is barely used for long fiber thermoplastic composites. In academic research, only a few works have been released on the topic of ultrasonic welding of thermoplastic composites. The number of publications since 1990 is only about 150 articles. However, the constant increase of papers attests the rising interest for this process since 2016. The recent review by Bhudolia et al. [Bhudolia et al., 2020] highlights the strengths and weaknesses of US welding. Different thermoplastic matrices, such as polyetheretherketone, polyetherimide, polyamide, polypropylene and others have already been investigated. In addition, welding thermoplastic composites to thermoset composites and metals have been studied. A reasearch group at TU Delft demonstrated that the use of output parameters from the device such as power can be used to monitor the process and assess physical phenomena during welding [Villegas, 2015]. This team has contributed for a large proportion of articles published on this topic for the last decade.

Many parameters affect the ultrasonic welding quality, such as welding time, pressure, amplitude and type of energy director. Despite the recent works, the weld quality is not yet reliable and reproducible. In addition, each composite material needs a new parametric study, because the understanding of the effect of the parameters is not robust enough to be transposed from one material to another one. Another limitation comes from narrow

processing windows: the gap between no-adhesion and degradation is so tight that the transfer to industrial production lines is not reasonable at this step. To overcome this problem, a significant research effort must be devoted towards a deeper understanding of the effect of each parameter on the welding strength.

In France, the study of US welding process applied to thermoplastic composites started in 2007 with Levy's thesis [Levy, 2010]. He modeled polymer flowing and thermal transfer during welding to identify the most influential process parameters. However, no large experimental campaign has been carried out until now to compare the simulation results.

This project was launched, funded and driven by LAUAK Group (Tarbes, France), a company specialized in manufacturing of aerospace parts. Since 1975, LAUAK Group has been growing to reach 1560 collaborators in 2021. LAUAK is present worldwide with subsidiaries in Canada, India, Portugal and Mexico. The company activities focus on machining, welding and assembling of metallic and composite parts and subassemblies for major aerospace companies such as Airbus, Safran, Daher, Liebherr and Dassault Aviation. The group builds competitive solutions tailored to the needs of its customers in the aeronautics, space, defense, energy and transportation sectors. The company includes a research and innovation department which aims to promote new materials and technologies within the group. The desire to maintain an active position in the aerospace industry motivates many of the research and development programs developed by LAUAK. For this reason, the researchers of the innovation department of LAUAK have identified very early the opportunity brought by thermoplastic composites. They have experienced many processes for the manufacturing of thermoplastic composites parts with complex shapes and thick parts [Martineau, 2018]. Alongside part manufacturing, the assembling issue comes naturally. LAUAK has chosen to invest in ultrasonic welding to assemble composite parts. The materials of interest are mainly continuous carbon fibers with PEEK matrix. To date, the ultrasonic welding of carbon/PEEK (polyetheretherketone) composites refers to only 7 articles worldwide, including 3 since this project was launched. Based on this lack of knowledge, LAUAK has identified the need to strengthen through a PhD thesis funding.

This work was carried out in two laboratories: Materials and Composite Structures team of Institut Clément Ader (CNRS UMR 5312) at IMT Mines Albi, France and Mechanics, Materials and Processes department of Laboratoire Génie de Production (EA1905) at Ecole Nationale d'Ingénieurs de Tarbes (ENIT-INPT), France. Half of the three-year duration was spent in each laboratory.

The company Victrex, United Kingdom, was also involved in the project. Victrex has supplied a new carbon/PAEK (polyaryletherketone) tape and pure PAEK to be evaluated

regarding its ability to be welded by ultrasonic welding. This PhD thesis fits the previous works carried out on ultrasonic welding of composites, with new scopes to be taken up. Long carbon fiber/PEEK composites are chosen. PEEK is a high-performance polymer able to withstand severe environment thanks to high mechanical stiffness, thermal stability and resistance to most chemicals. The main goal is to get high strength welds while increasing the process reliability. To reach this goal, a deeper understanding of the physical phenomena taking place at the interface is yet necessary. The polymer flowing and fusion bonding mainly depend on heat distribution across the composite specimens. The process is usually controlled from the welder data: the physical changes of the polymer drive the sonotrode displacement and the measured pressure. This way, polymer melting, polymer solidification and degradation can be detected. To complete this crucial information, we have chosen to in-situ monitor the temperature cycle undergone by the assembly. The main difficulty comes from the closed contact: when the two parts are brought together, measuring temperature is very difficult. To date, no optimal method has been proposed to overcome this issue. Moreover, the influence of the welding parameters on the mechanical resistance of welds is not clearly elucidated in the case of carbon/PEEK composites.

This PhD thesis is in line with three scientific objectives defined at the beginning of the project, keeping in mind the will of the company:

- To characterize PEEK and new PAEK matrices with regards to their rheological properties with the aim of assessing the agreement of relaxation times with ultrasonic welding.
- To develop a non-intrusive temperature measurement method to determine the thermal cycle undergone by the assembly as close as possible to the interface.
- To perform a parametric study of carbon/PEEK and carbon/PAEK welding to select the welding conditions allowing the best mechanical properties of the welds.

This manuscript is divided into five chapters. **Chapter 1** is an introduction on ultrasonic welding of thermoplastic composites. It goes from a more global point of view about joining such materials to the particular case of US welding. The functionalities of the process and how it has been used so far in the literature are highlighted. Welding characterization methods, from temperature measurement to mechanical strength quantification, for polymer composites are investigated with the aim to list and examine what can be adapted to US welding.

Chapter 2 focuses on the different materials used in this thesis. The new matrix from

Victrex, called Victrex PAEK AE 250, and PEEK matrix composites are used. High-performance polymer films are used at the welding interface, such as PEI, PEEK and PAEK AE 250. Therefore, the manufacturing process of welding specimens is detailed. Furthermore, a presentation of the ultrasonic welding device purchased for the thesis is made, alongside all possible welding configurations and welding parameters.

Due to the novelty of AE 250, a thorough analysis is necessary to fully understand its thermal behavior during welding. Rheological and crystallization behaviors of AE 250 and PEEK are thus investigated in **Chapter 3**. The main objective of this chapter is to reach characteristic relaxation times and a sufficient understanding of the polymer melting behavior in order to be associated with physical phenomena occurring during the welding process.

Chapter 4 is a thermal analysis of ultrasonic welding of CF/PEEK specimens using a PEI film at the welding interface. The complicated temperature monitoring of the process is tackled by developing a relatively non-intrusive measurement method using thermocouple. It is placed inside the polymer-based layer at the interface to limit the impact of the thermocouple on heat generation. The influence of welding parameters on temperature profiles is investigated. Finally, a basic thermal diffusion modelling from the interface to the external surfaces of specimens is made. The aim is to evaluate heat dissipation through the composite specimens.

The results obtained in Chapter 4 were completed in **Chapter 5** through the study of mechanical properties and morphological observations after fracture. This chapter first focuses on CF/PEEK welds using a PEI or a PEEK film at the interface and CF/AE 250 welds using an AE 250 film. The influence of different parameters is explored, such as welding parameters, the number of polymer layers at the interface, and the nature of the polymer layer. The characterization of welds is studied through single-lap shear tests, scanning electron microscope, Raman spectroscopy and rheology.

Finally, a conclusion is given to summarize and it highlights the important findings of this work. Perspectives about future works are proposed to improve the knowledge of this process.

Dissemination

The content of this thesis is based on an extension of the contributions presented in the following publications and conferences:

Journal papers

- Bonmatin, M., Chabert, F., Bernhart, G., Djilali, T. (2021). Rheological and crystallization behaviors of low processing temperature poly(aryl ether ketone). Journal of Applied Polymer Science, 138(47).
- Bonmatin, M., Chabert, F., Bernhart, G., Djilali, T. (2022). Ultrasonic welding of CF/PEEK composites: influence of welding parameters on interfacial temperature profiles and mechanical properties. Composites Part A: Applied Science and Manufacturing.
  (submitted)

National and international conferences

- Bonmatin M., Bernhart, G., M., Chabert, F., Djilali, T. (2021). Soudage par ultrasons de composites poly(éther éther cétone) (PEEK)/fibres de carbone (CF) - Ultrasonic welding of poly(ether ether ketone) (PEEK)/carbon fiber (CF) specimens. *Journées Nationales sur les Composites*, France (virtual), June, 2021.
- Bonmatin M., Chabert, F., Bernhart, G., Cutard T., Djilali, T. (2021). Ultrasonic welding of PAEK composites. *SAMPE Europe Conference 21*, Switzerland, September, 2021.
- Bonmatin M., Chabert, F., Bernhart, G., Cutard T., Djilali, T. (2021). Ultrasonic welding of CF/PEEK composites: Influence of welding parameters on temperature profiles and on mechanical resistance of welds. 2^{nd} *International Conference on Advanced Joining Processes*, Portugal, October, 2021.
- Bonmatin M., Chabert, F., Bernhart, G., Cutard T., Djilali, T. (2021). Soudage par ultrasons de composites thermoplastiques - Ultrasonic welding of thermoplastic composites. *Journées techniques SAMPE France*, France, November, 2021.

- Bonmatin M., Chabert F., Bernhart, G., Cutard T., Carassus F., Djilali, T. (2022). Non-intrusive temperature measurement to predict the morphology of PEEK/PEI interphase in ultrasonic welding of thermoplastic composites, *The GEP-SLAP Conference*, Spain, May, 2022.

Awards

- 2^{nd} Prize of the SAMPE France *Materials & Process* Student Competition, France, June, 2021.
- Winner of the 36^{th} SAMPE Europe Students Seminar 2021, Switzerland, September, 2021.

Chapter 1

State of the art about ultrasonic welding of thermoplastic composites

Contents

1.1 Introduction 10

1.2 Joining of composite materials 10

1.2.1 Composites materials 10

1.2.2 Joining techniques of composites 14

1.2.3 Welding of thermoplastic composites 16

1.3 Ultrasonic welding 23

1.3.1 Static ultrasonic welding 24

1.3.2 Ultrasound propagation through materials 30

1.3.3 Dynamic ultrasonic welding 31

1.4 Temperature monitoring during joining process 33

1.4.1 Thermography 33

1.4.2 Thermocouple 34

1.4.3 The case of ultrasonic welding 34

1.5 Mechanical strength of joints 37

1.5.1 Experimental techniques 38

1.5.2 Failure mechanisms 40

1.6 Conclusion 42

1.1 Introduction

This chapter presents the fundamental concepts necessary to understand the physical phenomenon occuring during polymer welding. An overview of ultrasonic welding process on thermoplastic composites is presented. The different joining processes currently used in industry for thermoplastic composites are highlighted. The increasingly use of thermoplastic composites has led to the development of new joining techniques such as welding. Hence, a classification of the different welding processes is introduced in a following section. From an industrial point of view, resistance welding and induction welding are the most developed.

Ultrasonic (US) welding is a well-known process for thermoplastic polymers. It has the advantages to be faster than induction welding and resistance welding, as well as a lower energy consumption. However, its suitability for composites is still under investigation. A section of this chapter is dedicated to US welding, its principle and economic stakes. Moreover, a significant scientific challenge about US welding is linked to the interface temperature measurement during welding. A section is devoted to the temperature measurement methods that can be found in the literature concerning welding of polymers. Finally, a brief literature review concerns the different ways of quantifying the mechanical properties of a joint.

1.2 Joining of composite materials

The development of composite materials in industry has brought to light a new challenge: assembling several elements together. Numerous joining methods currently exist and are presented in the following section.

1.2.1 Composite materials

1.2.1.1 Definition

A composite material is commonly defined as a non-miscible mixture of at least two materials: the matrix and the reinforcement, the reinforcement being embedded in the matrix. The benefit of composites is to merge the properties of the two in order to obtain a material with synergetic properties. The matrix can be ceramic, metallic or polymeric materials.

The reinforcement can be either organic or inorganic nature. Various shape factors are chosen, from spherical nanoparticles to long fibers depending on the target properties. In the industry, composite structural parts are usually continuous long fiber polymer-based matrix composites.

In the aerospace industry, composite parts are mainly made of epoxy resin with carbon fibers. The latter bring high rigidity due to their outstanding mechanical properties, as seen in Table 1.1. The fiber orientation in the matrix determines the final mechanical properties of the composite. The raw material is commercially available in the form of fibers or fabrics impregnated by resin called prepregs. In the case of unidirectional prepregs, the orientation of long fibers is optimized according to the load undergone by the part, *i.e.* the fibers have to be preferentially oriented in the load direction. It is possible to produce parts with a quasi-isotropic behavior by choosing the following fiber orientations: 0°, ± 45° and 90°.

Materials	Young's modulus *(GPa)*
Carbon fiber	200 to 600
Aramid fiber	$\sim$ 100
Glass fiber	$\sim$ 80

Table 1.1: Young's modulus of usual fibers

The interface between the fibers and the matrix has to maximize the load transfer between the two constituents during a mechanical stress [Chatain, 2001]. The mechanical resistance of the whole composite strongly depends on the fiber/matrix interfacial adhesion. The interface must maximize the transfer of load stress upon mechanical solicitation from the matrix to the fibers, which support the mechanical load due to their high elastic modulus. For that, fibers are often coated with a polymer layer, called sizing, whose chemical composition is in affinity with both the fibers and the matrix.

1.2.1.2 Thermoplastic composites

For 15 years, thermoplastic matrix composites (TPC) are tending to replace thermoset matrix composites. However, only high performance (HP) thermoplastics can compete with thermosets in terms of properties. HP TPC are defined as thermostable, *i.e.* the temperature range and service life are significantly higher than those of conventional polymers. Thermoplastics are made of long macromolecular chains that can be organized, we talk about semi-crystalline polymers, or disorganized, called amorphous polymers. Typically,

HP amorphous polymers have glass transition temperature higher than 150 $°C$. These polymers are polyetherimide (PEI) or polysulfones (PSU) for example. HP semi-cristalline polymers have a melting temperature around 300 $°C$. The family of poly(aryl ether ketone) (PAEK) is one of them and dominates the industrial sectors.

1.2.1.3 PAEK matrix composites

Monomers of PAEK polymers are composed of aromatic rings linked by ether or ketone groups. The chemical formulas of different PAEK polymers, such as PEKK, PEEK or PEK, are shown in Fig. 1.1. The difference between these polymers can be seen in their mechanical properties and in particular because of their crystallinity, which differ from one to another [Dominguez, 2013, Ho et al., 1994, Bas et al., 1994]. They exhibit high chemical resistance but also low density, that allow them to save weight compared to metals. In addition, melting temperature also varies depending on the chemical structure of the PAEK. For example, PEKK has several configurations, isophthalic (I) and terephthalic (T) which correspond, respectively, to a meta and para position of the groups surrounding the benzene ring, as can be seen in Fig. 1.2. Depending on the T/I ratio, melting temperature and crystallinity of PEKK vary.

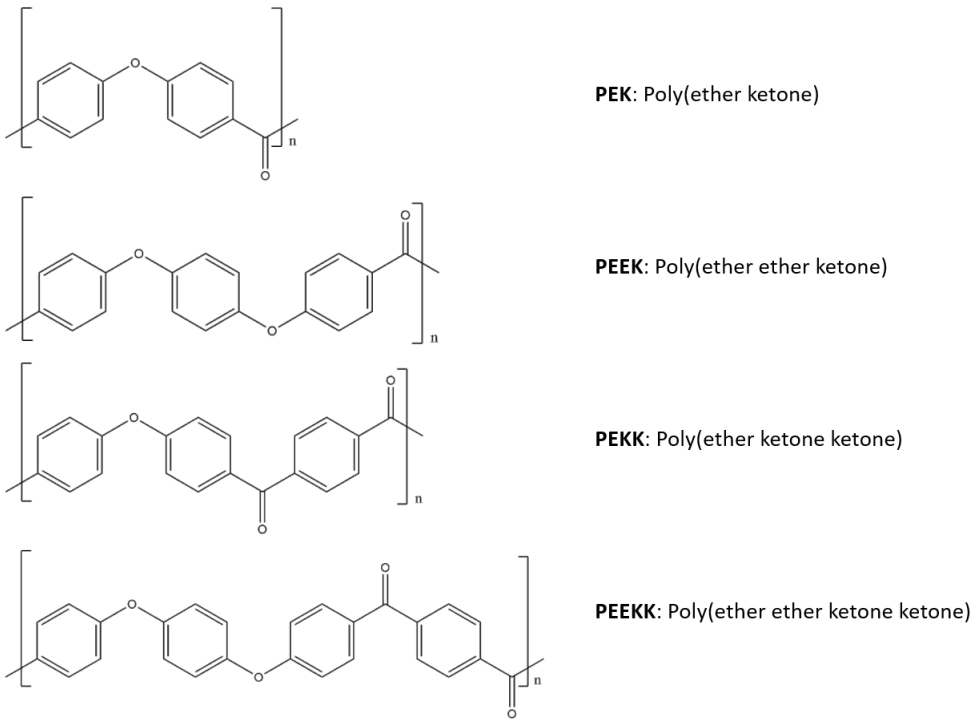

Figure 1.1: Chemical formulas of different PAEK polymers

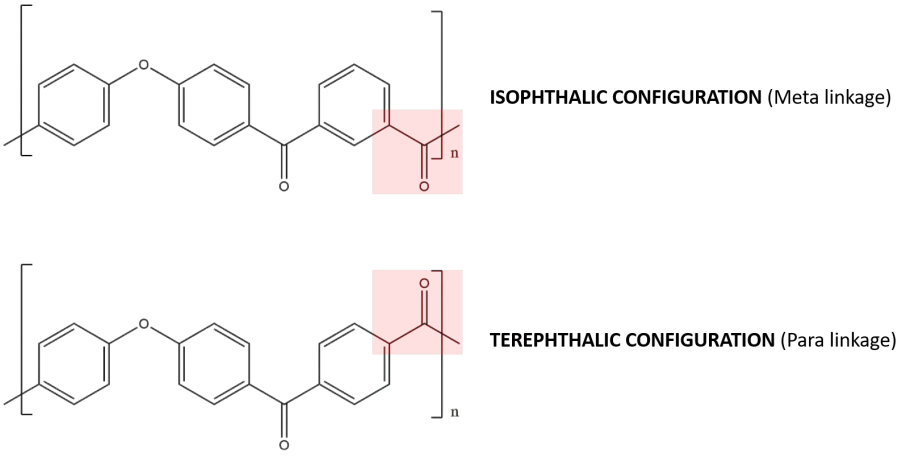

Figure 1.2: Chemical formulas of isophthalic PEKK and terephthalic PEKK

PEEK is still the most widely used PAEK in industry, followed by PEKK. Different commercial grades can be found from several manufacturers, as seen in Table 1.2. PEEK and PEKK are available in different shapes such as pellets, films, plates, fibers, filaments, powders, etc. Some compounders offer semi-finished products that include components with tailored properties, such as the use of Teflon to improve friction properties or the use of carbon fibers or glass fibers to enhance stiffness. For example, Cetex from Toray and APC-2 from Solvay are carbon-reinforced PEEK prepregs. Some PEKK grades have an advantage over PEEK since they can be processed at lower temperatures, thus facilitating the process. PEEK can be found in aeronautical, medical or oil and gas applications for example. Despite its outstanding properties, its high price limits the range of applications.

Material	Trade name	Manufacturer
PEEK	PEEK	VICTREX (GB)
	KETRON	MCAM (CH)
	SUSTAPEEK	ROCHLING (GE)
	KETASPIRE	SOLVAY (BE)
PEKK	KEPSTAN	ARKEMA (FR)

Table 1.2: Common commercial grades of PEEK and PEKK

1.2.2 Joining techniques of composites

Joining means connecting two parts together, permanently or not permanently [Cognard, 2003]. Joining of TPC can be divided into three classes:

- Mechanical fastener,
- Adhesive bonding,
- Welding.

This section presents only mechanical joining and adhesive bonding. Section 1.2.3. is entirely devoted to welding in the following.

1.2.2.1 Mechanical fastener

A mechanical fastener joint usually requires drilling of the composite. It is a practical and easy way of joining and repairing composite parts. Mechanical fasteners are often metallic ones, which can induce a significant increase in mass as well as negative effects on the durability of the joint: galvanic corrosion, stress concentrations, stresses due to thermal expansion. In spite of this, this technique makes it possible to obtain reliable and reversible joints. Their control is also simple and fast. Finally, it is not necessary to carry out surface treatment beforehand. A schematic of such joints is shown in Fig. 1.3.

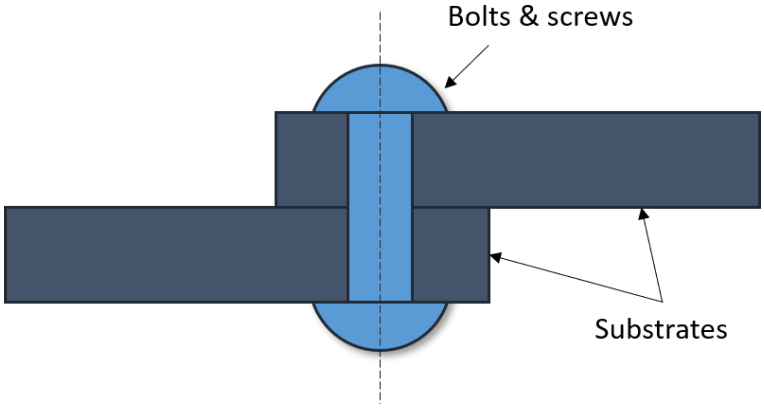

Figure 1.3: Diagram of mechanical fastener

Most of the studies available in the literature about the drilling of composites are related to thermoset-based composites. Concerning a thermoplastic matrix, the behavior

between the drill and the material differs from thermoset as thermoplastics are usually more ductile, and their physical structure and thermal behavior make them more suitable to plastic deformation during drilling [Xu et al., 2020]. The matrix is also frequently degraded at the screw wall [Zitoune et al., 2013]. Fibers are responsible for the excellent mechanical properties of the composite. Therefore, cutting them harms the integrity of the part, especially in the case of long fibers. Drilling a hole in the substrate can cause delamination of the input and output layers. In the case of thermoplastic composites, it has been shown that fiber pullout and fiber/matrix debonding can occur at the hole wall surfaces [Xu et al., 2020]. Considering these drawbacks, this technique does not seem to be the most suitable for joining thermoplastic composites.

1.2.2.2 Adhesive bonding

Adhesive bonding is another way of joining composite parts, as shown in Fig. 1.4. Epoxy based resins are the most frequently used adhesives. It is a rather long process and thus expensive since two steps are necessary: pretreatment and curing in autoclave. Also, the non-destructive testing techniques usually used in the industry are unable to evaluate an adhesive joint. However, the process allows a tight interface and excellent fatigue resistance while preventing corrosion [Cognard, 2003]. Adhesive bonding joints are also known to be lightweight compared to mechanical fastening.

Usually, a surface treatment is necessary to get a good quality bond. Otherwise, a failure mechanism is more likely to occur. Surface treatments are less complicated and more effective for thermoset than for thermoplastic composites, explaining why thermoset composites are more easily bonded by adhesive bonding than thermoplastic ones. It is well known that a simple light abrasion followed by solvent cleaning is sufficient for a good surface preparation considering thermoset composites. It is quite challenging to bond thermoplastic composites because it is necessary to have clean surfaces with controlled roughness to facilitate interface wetting. Light abrasion and solvent cleaning are not enough to ensure high strength joints. That is why studies have focused on plasma treatment, and it was proven to be the most efficient way of getting good quality bonds [Vinodhini et al., 2021, Novacek et al., 2017, Blackman et al., 1994], especially in the case of PEEK where surface tension is a big issue for adhesive bonding. In any case, surface treatment takes time and money, suggesting that adhesive bonding does not seem to fit the bonding of thermoplastic composite parts.

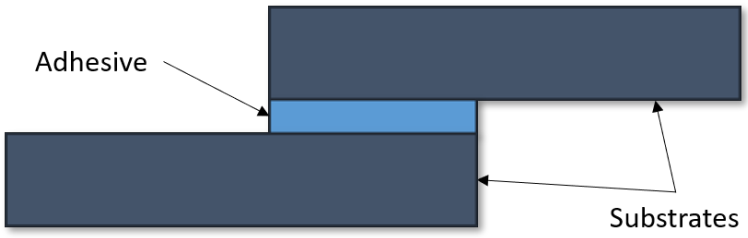

Figure 1.4: Diagram of adhesive bonding

1.2.3 Welding of thermoplastic composites

1.2.3.1 Definition

Polymer welding is a process known for several decades that involves bringing energy at the interface to assemble the parts. The energy is generally brought by heating, but a solvent can play the same role. The principle is to set the macromolecules in motion to diffuse through the interface, creating a bond. Considering this definition, not all polymers have the ability to be welded. Thermoplastics, unlike thermosets, have the ability to flow, giving them the ability to be welded. Weak physical bonds are existing between the chains of thermoplastics that can be broken when increasing the temperature. Thermosets cannot be welded because of their three-dimensional cross-linking network that does not allow chain diffusion, whatever the temperature. Therefore, welding is under intense development because it can potentially avoid the various problems mentioned in section 1.2.2.

Welding provides a one-part material that can transmit stress through the welding interface, unlike adhesive bonding, where a third body (an adhesive) is found between the two substrates. The main advantage of welding is that no external material is required for the process, except for ultrasonic welding which is presented in the following. The term *welding* refers to a large number of processes whose differences lie in how heat is generated at the interface. These processes cannot be used in all configurations and for all materials. Nevertheless, the physical mechanisms involved in the creation of the joint are similar regardless of the welding process used. Parameters involved are time, temperature and pressure whatever the process. Therefore, this section proposes a description of these mechanisms and a classification of the different welding processes for thermoplastic matrix composites.

1.2.3.2 Physical mechanisms during welding

The theory of reptation described by de Gennes [de Gennes, 1971] explains the movement of macromolecular chains of a polymer in the molten state. Topological constraints limits the movements of a chain due to the presence of the nearest neighboring chains. These defects define a theoretical "tube", called reptation tube, whose shape is similar to the shape of the macromolecule, as shown in Fig. 1.5. A chain can move along its tube by Brownian motions, *i.e.* back and forth along the tube. The macromolecule escapes gradually from its original reptation tube. From then on, de Gennes defined a time called reptation time, noted t_r, which corresponds to the time necessary for the molecule to leave its original tube entirely and create a new one. This time decreases when temperature increases.

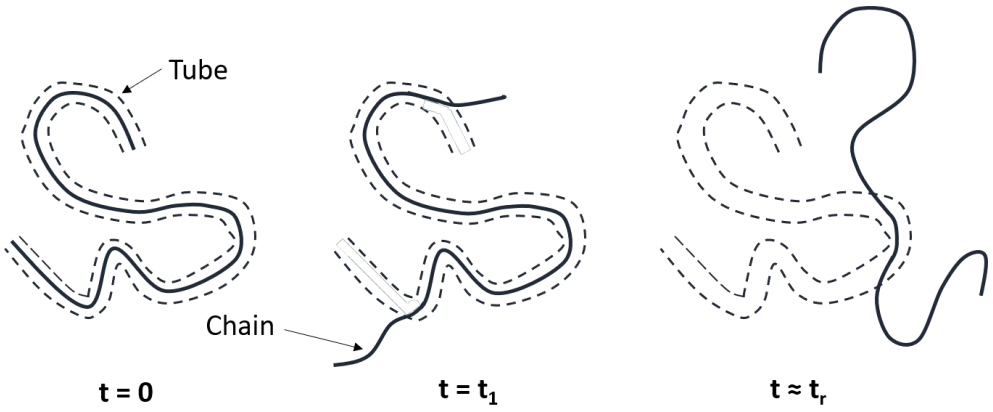

Figure 1.5: Reptation of a macromolecular chain following the De Gennes' theory (from [de Gennes, 1971])

When leaving their original tube, chains can diffuse from one layer to another one, this is called interdiffusion. Interdiffusion depends on several chain parameters, such as the chain length and rigidity or entanglement rate. Indeed, these parameters have consequences on properties such as viscosity, molecular weight or crystallinity. For semi-crystalline polymers, the presence of the crystalline phase prevents the mobility of the amorphous phase when below T_m and lead to only localized movements of chains [Lamèthe et al., 2005, Wool et al., 1989]. Unmelted crystallites are obstacles to the movement of chains of the amorphous phase. Therefore, it is necessary to reach melting temperature to see more global movements of the chains. Amorphous polymers exhibit higher chain mobility above T_g with more global movements of chains, promoting the formation of a bond. The higher the temperature, the faster interdiffusion is likely to occur [Awaja, 2016].

Moreover, a good quality bond requires intimate contact between the two surfaces to allow the chains to properly diffuse. Without it, chains cannot interlock and create a good quality joint. Surface roughness is therefore a critical parameter to homogeneously heat the interface. The pressure applied on top of the substrate is an important parameter in the welding process as it influences the intimate contact between the two parts. Indeed, when heating and melting, the polymer starts to flow which changes the surface roughness.

When these conditions are met (i.e intimate contact and sufficient temperature), ends of chains have gained enough freedom to diffuse across the interface and entangled. The healing process can start and the interface disappears and generates an interphase, as seen in Fig. 1.6. Considering semi-crystalline polymers, crystallization is an important phenomenon during cooling. It has been shown that crystallinity is generally higher at the interface because smaller chains diffuse and crystallize more rapidly [Martineau et al., 2019]. If crystallization is too fast, it can prevent the diffusion of longer chains. At first glance, this has a negative influence on the mechanical properties of an assembly. However, the same authors have shown that an interface with a high crystallinity increases its tensile strength. Therefore, to obtain good quality joints, it is necessary to find a compromise between crystallization and chain diffusion, the latter being essential for forming a strong bond.

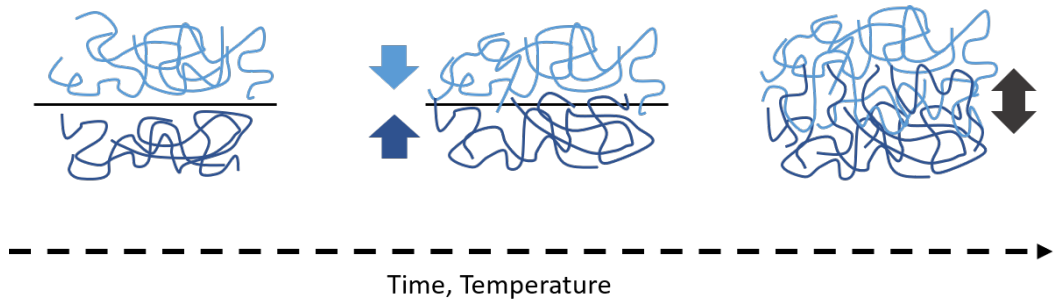

Figure 1.6: Intermolecular diffusion of chains at the interface

During welding, the material undergoes significant thermal variations. One of the main consequences is the modification of the mechanical properties of the composite due to changes in morphology and structure. Moreover, during heating, the material is submitted to physical changes related to temperature changes. Thermal degradation of the composite can occur and thus a loss of mechanical properties [Villegas, 2014]. Finally, melting can lead to the delamination of some layers of the composite and consequently a loss of mechanical properties. Parameters such as time, temperature and pressure have a significant influence on these physical changes.

When welding two different polymers, the compatibility between the two is necessary for the diffusion to occur, which ultimately means that they must be miscible. Looking at the second law of thermodynamics, it is challenging to blend different polymers since the entropy of the blend must be lower than the entropies of the polymers, and it is usually not the case. Indeed, entropy is already high since chains are disorganized, especially for amorphous polymer. Therefore, the first law of thermodynamics must be looked at: a blend is only possible if the blend energy is lower than the energy of the different polymers, meaning that the enthalpy of the blend must be low or negative. Also, the solubility parameters of the two polymers must be similar. For this reason, welding is often implemented between two parts made of identical polymers.

1.2.3.3 Description of the different welding processes

Polymer welding is a set of processes allowing joining of two thermoplastic parts. The difference between welding processes is how heat is generated at the interface. An external element can provide heat, or heat can be generated at the interface by the process itself. The process chosen depends on the material and the desired applications. Considering this, Yousefpour et al. [Yousefpour et al., 2004] classified these processes into three broad categories as shown in Fig. 1.7.

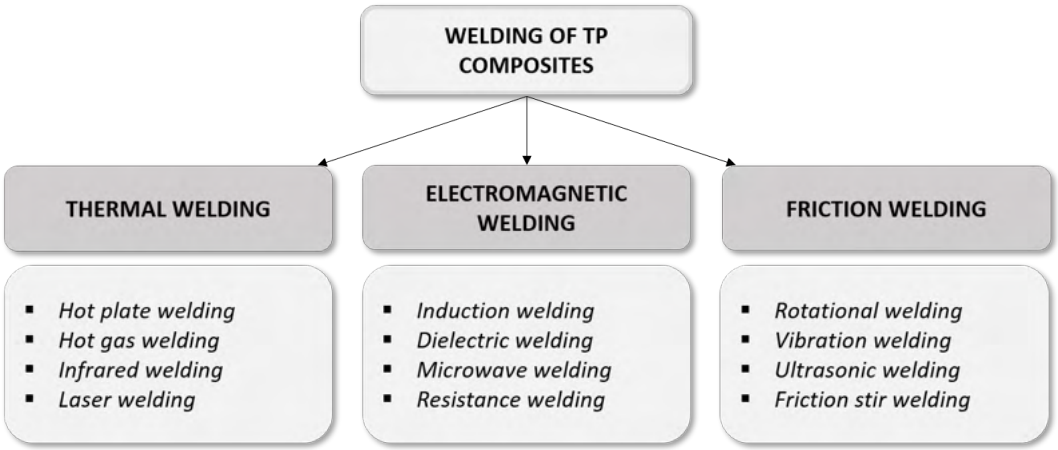

Figure 1.7: Diagram illustrating the different thermoplastic composite welding processes, from [Yousefpour et al., 2004]

Thermal welding The first category is thermal welding, which requires two steps. First, the two surfaces are heated separately using an external energy source (infrared, laser, hot plates, etc.) [Wise, 1999]. The parts are then brought into contact. A significant drawback

is the limited size of the parts since the entire surface must be heated in one step. A scheme of these processes is shown in Fig. 1.8. Only laser transmission welding requires the two parts to be in contact during heating of the interface [Wool et al., 1989, Costa et al., 2012, Taylor et al., 1989]. In this specific case, one of the two materials must be transparent to the laser wavelength [Villar et al., 2018].

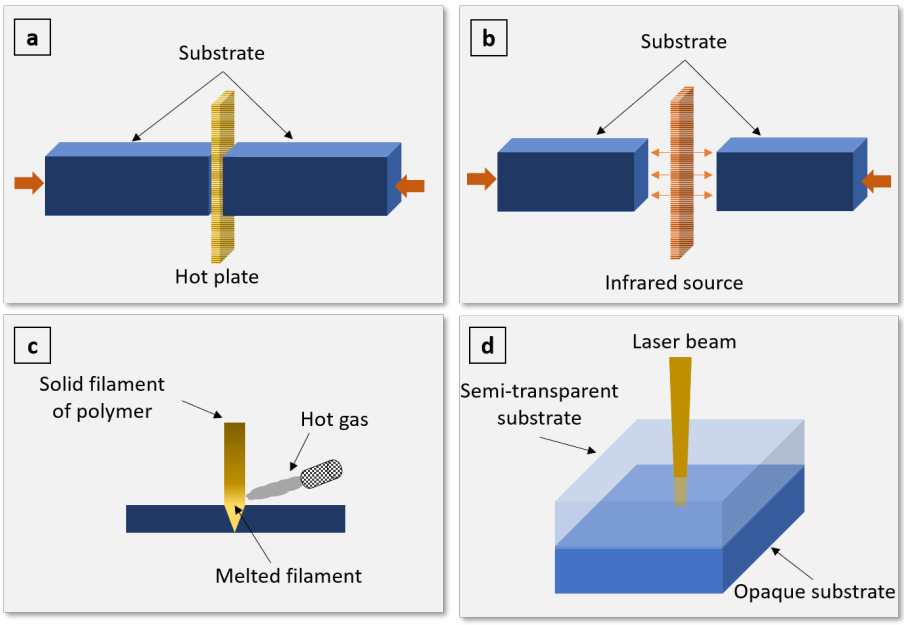

Figure 1.8: Illustration of thermal welding processes: hot plate welding (a), infrared welding (b), hot gas welding (c) and laser welding (d)

Electromagnetic welding Electromagnetic welding involves heating powders or metal inserts at the interface using a high-frequency electromagnetic field. Pressure is required to consolidate the joint. Induction welding, dielectric welding (or high-frequency welding), microwave welding and resistance welding are electromagnetic-based welding [Wise, 1999] (Fig. 1.9). High-frequency welding is a particular case of electromagnetic welding since it requires the use of a thermoplastic polymer film at the interface to avoid melting of the entire thickness of the part. The polymer must have a loss factor higher than the composite matrix to reach its flowing temperature before those of the composite. Otherwise, delamination of the composite layers could occur [Yousefpour et al., 2004]. This high-frequency process is more suitable for thin composites. Nevertheless, no indication of the maximal thickness is given by the authors.

Induction welding also presents some particularities. Two types of induction welding exist: with and without susceptors. The susceptor is a conductive metallic material that

absorb electromagnetic energy and convert it into thermal energy. It locates the energy at the interface but also reduces the mechanical properties and quality of the joint since it stays between the parts after welding. Induction welding with the use of a susceptor is currently prohibited in aerospace since it brings a third material at the welding interface [Bernhart and Erb, 2018]. In the case of direct induction welding (without susceptor), heat is generated by conduction through the reinforcing carbon fibers in the composite (such a process is not valid for other kind of fibers like glass or aramid). In some cases, it can lead to deconsolidation/reconsolidation phenomena, detrimental to the mechanical properties. Finally, with or without a susceptor, induction welding is a technique that heats more or less the entire thickness of the substrate, which can eventually degrade the composite matrix or cause delamination.

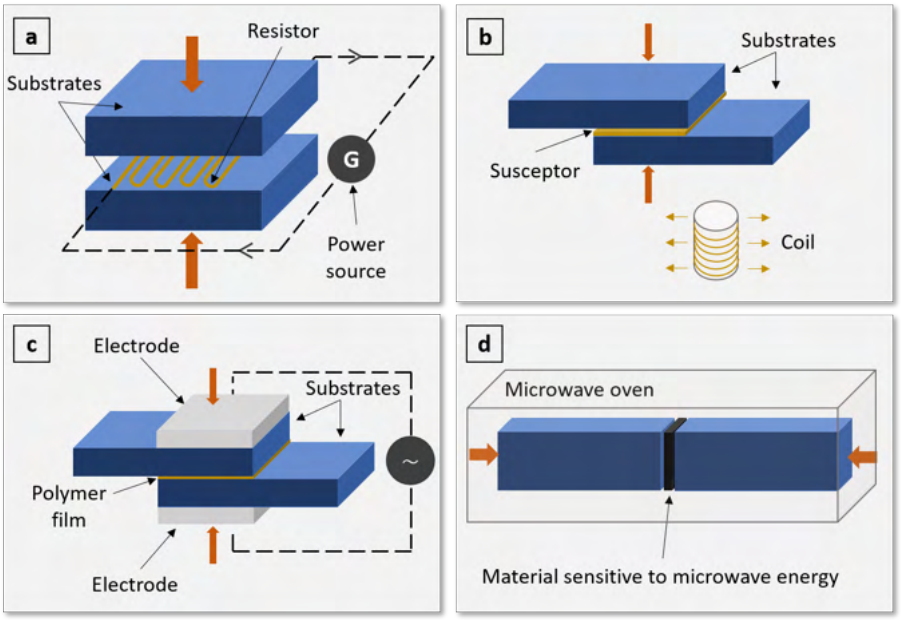

Figure 1.9: Illustration of electromagnetic welding processes: resistance welding (a), induction welding (b), dielectic welding (c) and microwave welding (d)

Friction welding The last category involves the friction of the interface due to the process itself. These processes are spin welding, vibration welding, ultrasonic welding and friction stir welding [Wise, 1999] (Fig. 1.10). After the friction step, the two parts need to remain in contact during cooling to consolidate. These techniques do not require any external energy input; only the interaction between the parts to be welded is important.

The ultrasonic welding process is quite different because a polymer material, called *energy director* (ED), must be placed at the welding interface [Liu et al., 2001]. The

energy director is not needed for other friction welding processes because in those cases, heat is already generated at the interface. In the case of ultrasonic welding, this energy director localizes the energy at the interface and thus heats preferentially in this location. Indeed, its rigidity being lower compared to the composite, it will dissipate more energy by viscous flow. Moreover, good quality welds can be obtained quickly at low cost. The process is easily implemented industrially and has short cycle times, around several hundred milliseconds. Its energy consumption is also lower than induction welding or resistance welding [Villegas et al., 2013]. These different advantages are the reasons why this process is scrutinized by the industry. However, US welding is barely used for composites at the moment. It is not reproducible yet because the influence of the welding parameters on the joint quality and the physical phenomena are not fully understood. This technique is detailed in part 1.3.

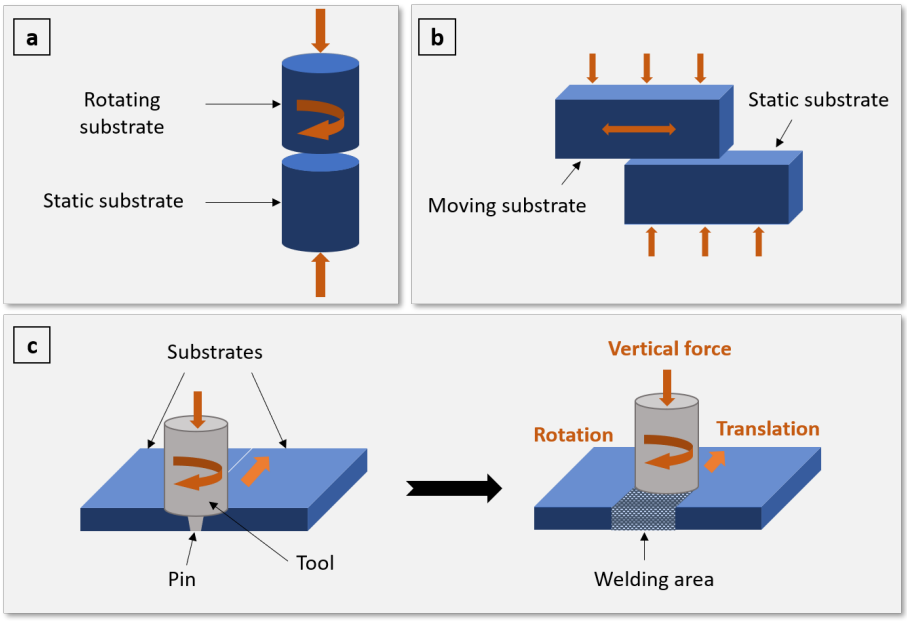

Figure 1.10: Illustration of friction welding processes: rotational welding (a), vibration welding (b) and friction stir welding (c)

1.3 Ultrasonic welding

Ultrasonic welding can be easily implemented in industry. It is already commonly used to weld unreinforced TP polymers, but very few studies are available for composite materials. Fig 1.11 shows the evolution of the number of publications and citations about ultrasonic welding of thermoplastic composites over the last 20 years. The emergence of interest has

appeared since 2010 and it has increased exponentially since then. However, few research groups are currently working on this topic. As can be seen in Fig. 1.12, one research group at the Delft University of Technology concentrates almost one-quarter of publications on this topic. Three others groups are showing interest with around ten papers each. 51 % of papers about this topic are made by universities that have published five times or less.

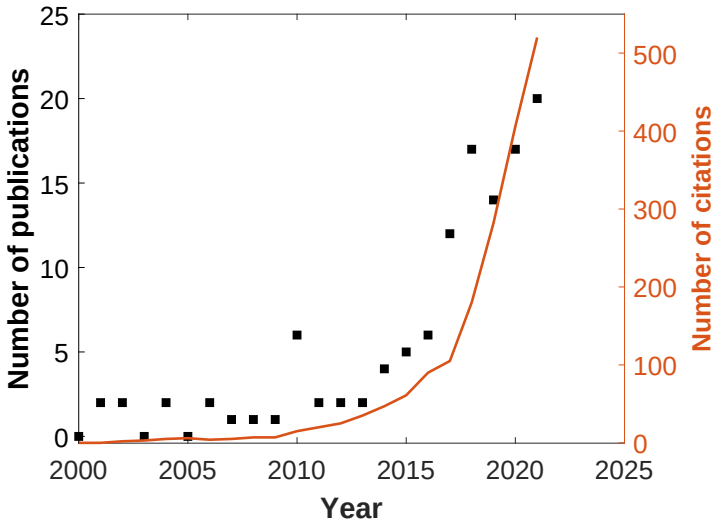

Figure 1.11: Number of publications and citations about ultrasonic welding of thermoplastic composites throughout the last 20 years

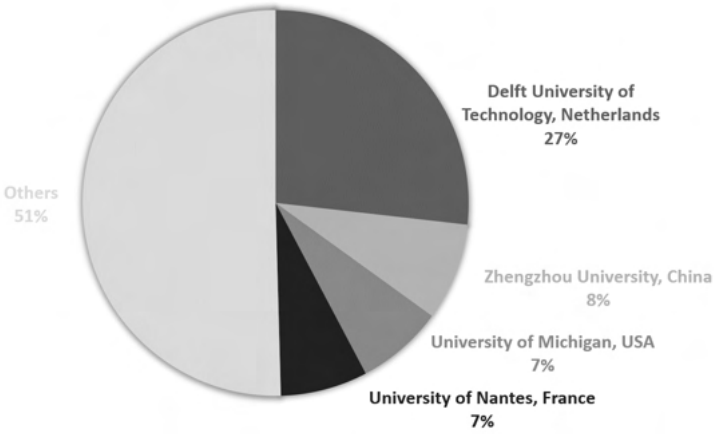

Figure 1.12: Distribution of papers about ultrasonic welding of thermoplastic composites among research groups

Ultrasonic welding is a process known for several decades considering thermoplastic polymers but much more recent for assembling composites. This section is dedicated to

the presentation of the ultrasonic welding process and studies conducted on TPC until now.

1.3.1 Static ultrasonic welding

Ultrasonic welding device is composed of four elements, as presented in Fig. 1.13:

- a frequency generator,
- a piezoelectric convertor,
- a booster,
- a sonotrode.

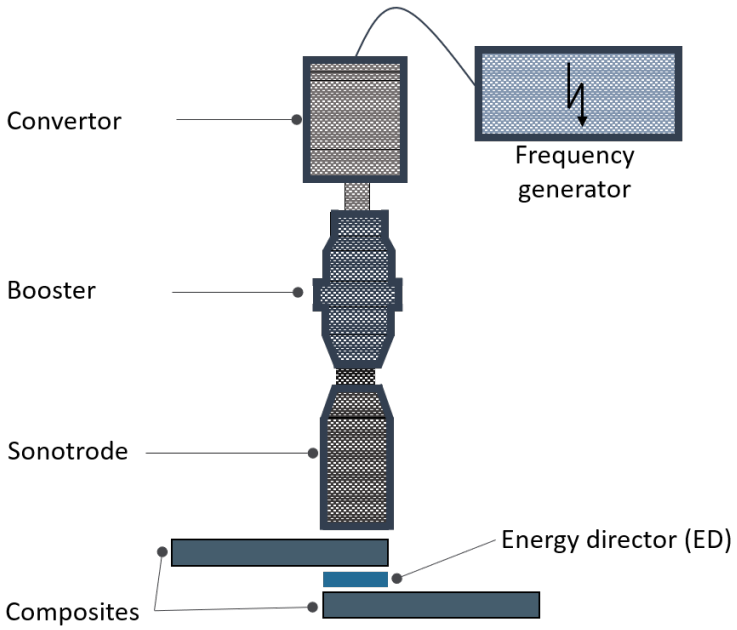

Figure 1.13: Diagram illustrating ultrasonic welding process

The frequency generator creates a high-frequency wave, usually between 20 kHz and 50 kHz, sent to the piezoelectric converter. The latter transforms this electrical energy into mechanical energy of low amplitude. The booster increases the amplitude of this mechanical wave, which is then transferred to the sonotrode. The sonotrode is a metal

part in contact with the upper substrate, and it vibrates and moves along the vertical axis. Thanks to the sonotrode, the upper composite substrate can vibrate. The lower substrate is fixed on the jig and does not move during welding. The upper specimen comes into contact with the lower one when the sonotrode applies pressure on both. Therefore, it creates an alternating contact and the interface heats by dissipation of mechanical energy. As presented before, it is necessary to use ED placed at the interface in addition to parts to be welded. The ED is usually made of the same material as the composite matrix. The stiffness of the polymer being lower than the composite one, it concentrates the friction phenomenon at the interface, where heat is preferentially generated. Heat is also generated in a more homogeneous way compared to no use of energy director. US welding without ED is more likely to thermally affect the entire thickness of the specimens, and it also reduces the joint mechanical strength [Tao et al., 2019].

The sonotrode is an acoustic part usually made of titanium, steel or aluminium based metals. It also maintains the pressure load during welding. Its shape depends on the needs of each welding operation, *i.e.* the part geometry, the jig dimension or eventually, the desired final amplification of vibration. Common shapes are presented in Fig. 1.14. The section of the sonotrode at the top is noted y while the one at the bottom is noted x. The ratio between y and x is the value of the amplitude increase. The area of the sonotrode in contact with the parts can have rectangular or circular shapes. Sonotrodes can be tooled to weld larger areas of specimens or to weld multiple parts at the same time, depending on the need.

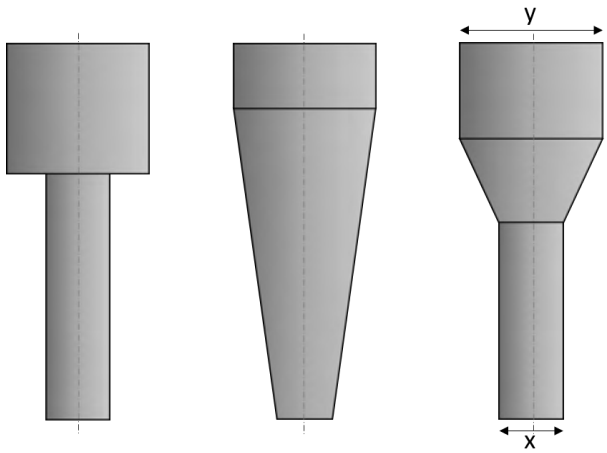

Figure 1.14: Common sonotrode shapes for ultrasonic welding

Ultrasonic welding involves a large number of parameters that influence the joint quality [Liu et al., 2001, Villegas, 2014, Palardy and Villegas, 2015, Wang et al., 2017b]. It

is possible to classify these parameters into two categories: input parameters and output parameters. *Input parameters* can be modified prior welding directly on the welder. *Output parameters* are the data provided by the device after welding. These parameters are shown in Fig. 1.15. Welding time is the duration of vibration of the sonotrode while pressing on the upper substrate at a pressure equivalent to the welding load. Welding energy is the energy required for welding. Vibration amplitude is the maximum value reached by the sinusoid corresponding to the ultrasonic wave. After the end of vibration, the sonotrode stays in contact with the upper specimen for a time called holding time, and at a pressure called holding pressure. Welding power and sonotrode displacement are the output data provided by the device, and their values are measured throughout the welding process. To better understand the process, it is worth pointing out that a shutdown condition is chosen prior welding. It can either be a time, an energy or a displacement of the sonotrode, explaining why these three parameters are on the same level in Fig. 1.15. The choice of the shutdown parameter, and its value, depends only on the operator.

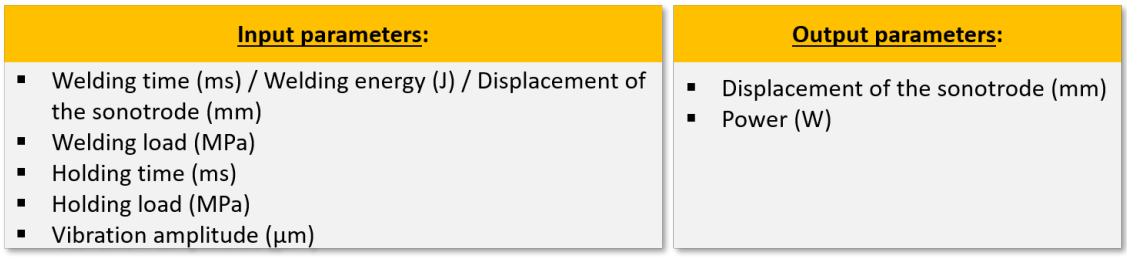

Figure 1.15: Input and output welding parameters

Benatar et al. [Benatar and Gutowski, 1989] and Villegas et al. [Villegas, 2015] have used output data provided by the welder to perform in-situ control of the process. The device has electronics and sensors that measure the sonotrode displacement and the power during the welding process. The different steps observed on these curves are correlated to the physical phenomena at the interface. The Fig. 1.16 shows an example of the power/displacement curves versus time [Villegas, 2015]. Five stages are identified in the case of semi-cristalline thermoplastic material and ED:

Stage 1 Heating of the energy director at the interface occurs due to friction phenomena. The quasi-linear increase in power comes from these two phenomena. The sonotrode does not move because the different materials involved in this step are still rigid and have not undergone any change of state.

Stage 2 The ED continues to heat up. When the temperature reaches the glass transition temperature T_g, a viscoelastic heating phenomenon is added to the friction. It begins to flow due to the nucleation and growth of hot spots at various locations in the overlap area of the weld. The local melting of the energy director causes a decrease in power and a displacement of the sonotrode. This displacement is slight since some parts of the ED are still solid. Also, a positive variation of sonotrode displacement on the curve means that the sonotrode is going down, *i.e.* towards the joint.

Stage 3 Viscous flow of the entire energy director is occurring, resulting in wetting of the interface. Power and displacement curves increase linearly. Moreover, the displacement is more important in this stage compared to stage 2, meaning that more polymer is flowing.

Stage 4 In this step, the ED is still flowing while the polymer matrix undergoes local melting when heat is transferred from the interface to the substrates. Local melting of the substrate is seen as a decrease of power, while flowing of the ED is an increase in power. As a result, the power curve is balanced and becomes constant.

Stage 5 Almost no ED is left at the welding interface which causes the squeeze flow of the polymer matrix and moving of carbon fibers of the first plies.

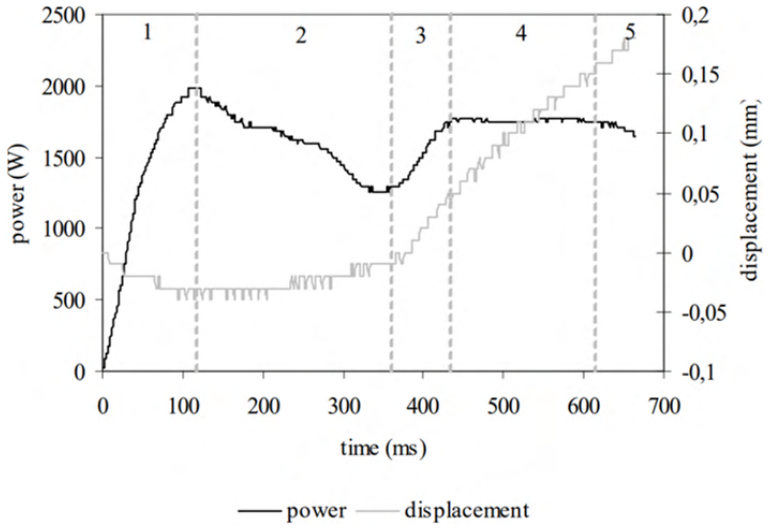

Figure 1.16: Power & displacement curves during welding [Villegas, 2015]

Several authors showed that welding parameters can have a huge impact on the quality of a joint, and especially on mechanical properties. From Liu et al. [Liu et al., 2001] study,

vibration amplitude is the process parameter that has the biggest impact on the mechanical strength, followed by welding time. An example of interfacial fractures at different vibration amplitudes is presented in Fig. 1.17. It can be seen that the highest value of amplitude (Fig. 1.17 (a)) leads to matrix and fibers flow at the edge and matrix degradation with brown color while Fig. 1.17 (b) do not exhibit those phenomena. Several authors [Tao et al., 2019, Villegas, 2015, Zhi et al., , Gao et al., 2018] have also explained that an optimization of the process can be done using welding time. Too short vibration times lead to a gap between the ED and the specimens. Long vibration times lead to voids, cracks, and heat-affected zones that degrade the polymer matrix. The welding energy has also been investigated [Goto et al., 2019, Wang et al., 2017b, Villegas, 2014, Wang et al., 2017a]. The authors described that increasing the welding energy can increase the mechanical properties of the joint until a limitation is reached, which is usually a degradation of the matrix. Finally, it has been explained that welding load and vibration amplitude have an influence on cooling rate, which implies an influence on the ED crystallinity at the interface [Koutras et al., 2019]. Overall, optimum parameters have been found in the literature. However, the real issue of ultrasonic welding is that optimum parameters only apply to one material and its configuration, *i.e.* thickness or geometry of the energy director for example.

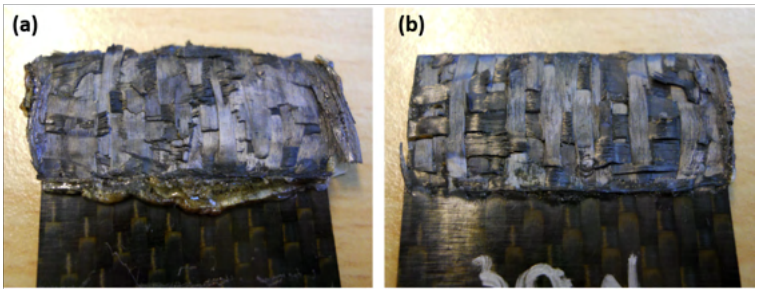

Figure 1.17: Interfacial fracture of CF/PEI welds at 300 N load and 86.2 μm amplitude (a) and 300 N load and 51.8 μm amplitude (b) [Villegas, 2014]

Moreover, the geometry of the ED has also an effect on the quality of the joint since surface roughness plays an important role in heat generation. In early studies of TPC ultrasonic welding, ED had a triangular shape, as shown in Fig. 1.18 [Liu et al., 2001, Fernandez Villegas and Palardy, 2017, Villegas and Bersee, 2010]. Triangular EDs are usually made by thermocompression when the prepreg are consolidated. The triangular shape is machined directly in the mold. Polymer powder is inserted into these channels, and the composite prepregs are deposited on top [Villegas and Bersee, 2010]. However, triangular shapes are quite inconvenient on an industrial level. For this reason, Villegas et al. [Villegas et al., 2015] highlighted that using an energy director in the form of a film, which is simpler to implement, offers lap shear strength values similar to triangular-shaped

ED, around $30 - 35\ MPa$. From then on, most studies in the literature used EDs in film form. For the Delft University research groups, the ED thickness is generally 0.25 mm [Villegas, 2015, Villegas, 2014, Palardy and Villegas, 2015, Fernandez Villegas and Palardy, 2016]. They studied the impact of using a thick (0.25 mm) and a thin (0.06 mm) ED and proved that the use of 0.25 mm is more appropriate for static US welding [Palardy and Villegas, 2015].

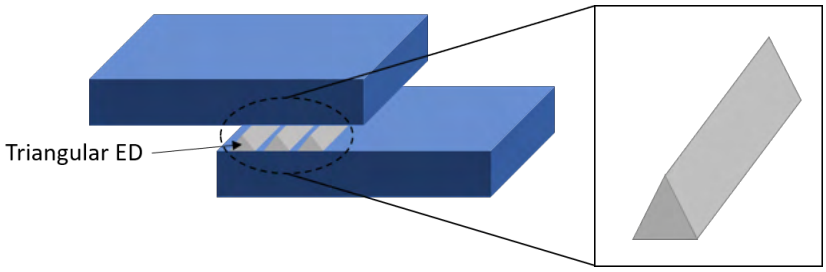

Figure 1.18: Triangular energy director during US welding

In the literature, several studies on high performance thermoplastic composites can be found. Delft University of Technology (DUT) research group has worked on CF/PEI and CF/PPS fabric reinforced composites. University of Nantes research group has mainly worked on modeling heating phenomena during welding with several collaborations with DUT. Zhenghzhou University research group has worked on short carbon fibers reinforced polyamide 6, University of Michigan research group has worked on short carbon fibers reinforced polyamide 66. Others research groups have worked on a lot of different materials, ranging from glass fiber reinforced polyethylene to CF/PEEK.

1.3.2 Ultrasound propagation through materials

A sound frequency scale is presented in Fig. 1.19. Ultrasounds are high frequency sounds inaudible for the humain ear, above 20 kHz. They can be longitudinal compressional waves that travel through fluids and solids. Unlike sound, ultrasound is more easily attenuated during its propagation. For example, in the air, a 30 kHz wave is attenuated by about 30 dB when propagated over 10 meters, whereas a 4 kHz wave is attenuated by 0.7 dB over the same distance [Chatillon, 2006]. An ultrasonic wave is characterized by the following parameters: frequency, wavelength, propagation speed and power. Also, a distinction is possible between low power ultrasound (less than 1 Watt) and high power ultrasound (higher than 10 Watt) [Pétrier et al., 2008]. The first ones do not modify the navigated area, while the second one can generate physical or chemical modifications.

Regarding ultrasonic welding, it is possible to distinguish two categories: near-field and far-field welding. The difference is the length between the edge of the sonotrode and the welding interface, the limit between them being 6 mm. In near-field welding, ultrasonic vibration waves have no impact on the material because vibration amplitude at the edge of the sonotrode is almost the same as at the energy director. In the case of far-field welding, wave propagation through the material is significant. Far-field ultrasonic welding is a term that has been used when people started to get interest in US welding [Roopa et al., 2008, Chuah et al., 2000, Benatar and Cheng, 1989]. However, this term has not being used for several years since most studies are made in near-field configuration. This is due to the fact that higher energy is required to weld in far-field configuration [Rashli et al., 2013].

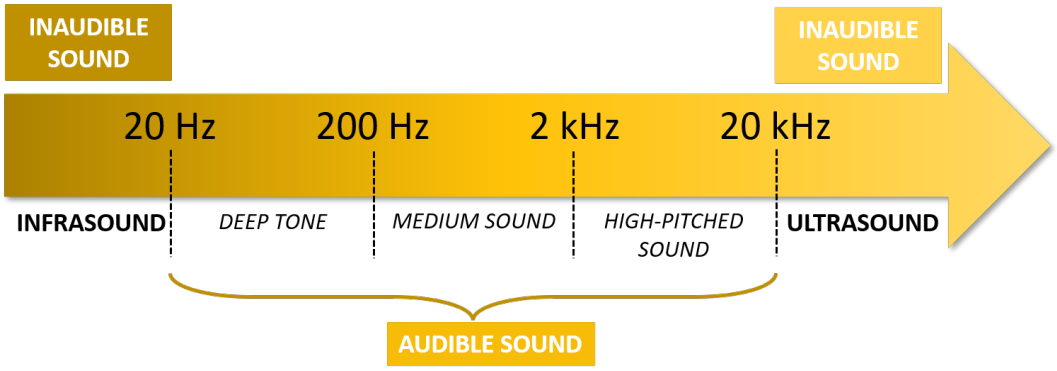

Figure 1.19: Sound frequency scale

1.3.3 Dynamic ultrasonic welding

To this date, dynamic US welding has been studied at the laboratory scale. The final objective is to apply this process continuously, *i.e.* welding parts whose length is greater than the size of the sonotrode. The process must be able to fit the size of the part but also to weld several places in a single pass. Parts requiring sealing needs to be continuous welded to avoid leaks. Very few studies are available on continuous TPC ultrasonic welding, and research is still needed to develop this process before being transfered in the industry.

The main disadvantage of using continuous US welding is related to the flow of the melted ED. Indeed, only the surface under the sonotrode is melted during vibration. The rest of the film is still solid, preventing the flow of the molten part of the ED. In order to solve this problem, Van Burden [Van Beurden, 2015] has developed a prototype of continuous welding equipment based on the static one, shown in Fig. 1.20. The principle

is to make several passes of the sonotrode to decrease the thickness of the interface. Fig. 1.21 (a) shows final interfacial thickness of regular welds (static ultrasonic welding), first pass welds and second pass welds (continuous US welding). Final thickness is similar between regular and second pass welds whereas the one of first pass welds is higher. The single lap shear strength (LSS) values in Fig. 1.21 (b) of both regular and second pass welds are around 20 MPa, which leads to the conclusion that welds are of similar quality. However, the mechanical strength of first pass weld is lower.

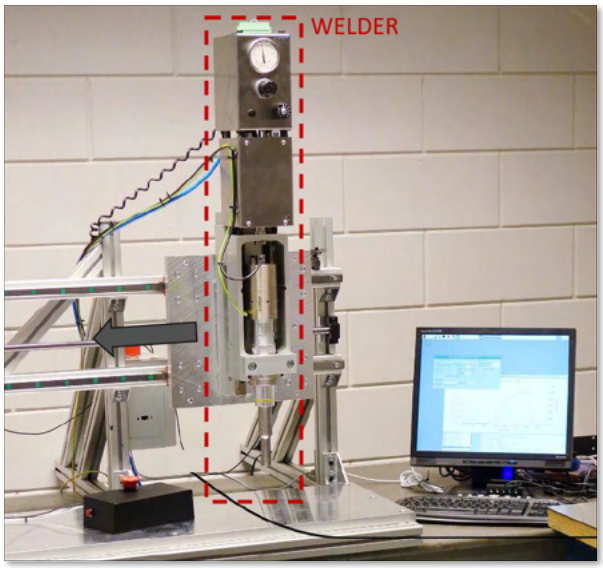

Figure 1.20: Continuous US welding device prototype [Van Beurden, 2015]

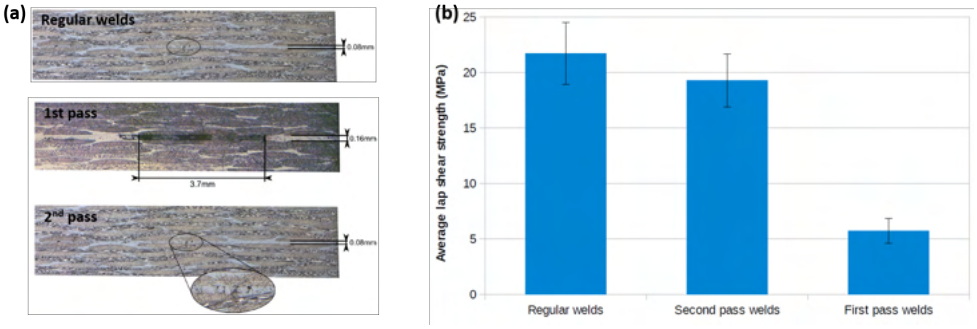

Figure 1.21: Optical microscopy of cross section of 3 welding configurations (standard US welding, one-pass welding and two-passes welding) (a) Single lap shear test results for each configuration on CF/PPS specimens (b) [Van Beurden, 2015]

Senders et al. have brought a second option to this issue [Senders, 2016]. It consists of using a ED whose thickness is small enough to consider that no flow is occurring during the sonotrode pass. They used the same equipment as Van Burden [Van Beurden, 2015]. The

authors have shown that a film thickness of 80 μm implies a sonotrode displacement of only 0.01 mm during welding of CF/PPS. Nevertheless, the LSS values are lower than a standard static weld with a 0.25 mm thick film. Indeed, 29 MPa are measured for continuous welding (ED thickness = 0.08 m) against 37 MPa for standard static welding (ED thickness = 0.25 mm) in the same welding conditions. The authors explained that no pressure is applied after the sonotrode has passed, preventing a good interface consolidation. An additional study was performed by Jongbloed et al. [Jongbloed et al., 2018] where the aim is to replace the film with a 200 μm thick mesh of the same polymer, as seen in Fig. 1.22. The objective is to equalize heat distribution by reducing void areas between the substrates and the ED. By doing this, the LSS value is increased from 20 MPa (film) to 34 MPa (mesh).

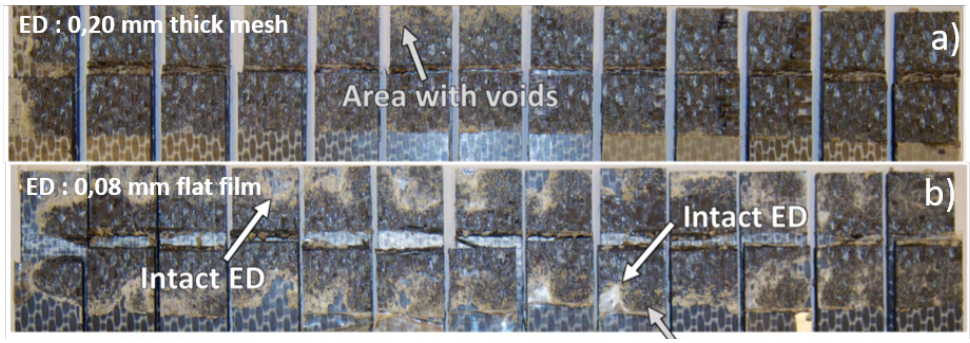

Figure 1.22: Interfacial fracture after lap shear test with mesh ED (a) and film ED (b) [Jongbloed et al., 2018]

These few studies show the long way to go for the development of the process. Many points are still to be examined in order to make continuous ultrasonic welding a reality. At the moment, only one team worldwide has published scientific papers on continuous welding of thermoplastic matrix composites: Delft University of Technology. In any case, continuous welding cannot be developed without a complete understanding of static ultrasonic welding of composites, which is far from being the case yet.

1.4 Temperature monitoring during joining process

Temperature monitoring is a crucial step considering welding since the interface is a closed contact, there is no direct access to measure the temperature. Knowing thermal conditions throughout the experiment is a way of evaluating and controlling the process. Therefore, welding parameters could be chosen in order to get a specific temperature. Indeed, if you

combined the rheological parameters of the polymer to the temperature measurement, it would possible to identify a range of parameters in which the polymer would diffuse and create an extremely good bond at the interface. Thermal history is necessary to make sure enough energy is brought at the interface to favor macromolecular diffusion and prevent overheating resulting in thermal degradation. It can also help reducing welding time by keeping the suitable temperature no longer than necessary. Usual means to access the interfacial temperature such as thermocouples and infrared thermography are presented in the following section.

1.4.1 Thermography

Infrared thermography is a non-intrusive analysis and monitoring method that relies on assessing thermal profiles of objects, generally with the use of a thermal camera. It is also a non-destructive and non-instrusive technique. The temperature measured by the infrared device is dependent on the material emissivity. The emissivity coincides with the capacity of a material or a surface to absorb and re-emit heat by radiation. An IR camera measures data send to a processing software to obtain a thermal mapping. This technique has already been used for laser welding [Villar et al., 2018, Speka et al., 2008], resistance welding [Brown and Bangs, 1986, Lee et al., 2011] and conduction welding [Mitschang et al., 2002].

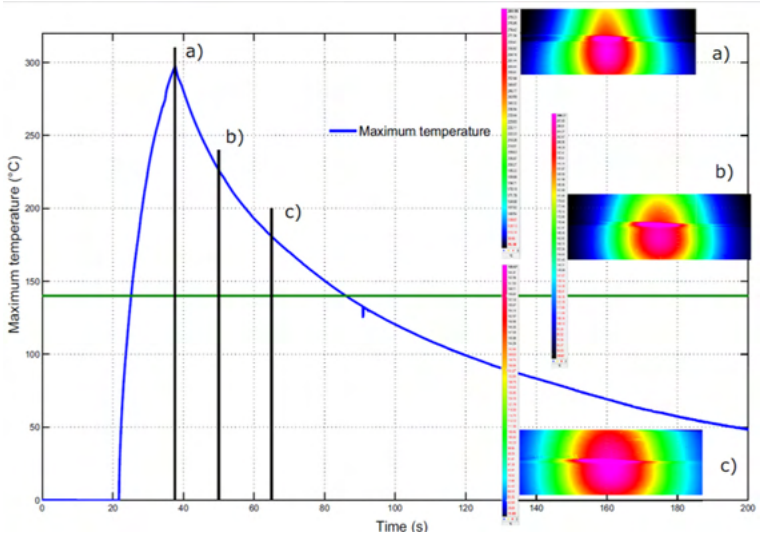

Figure 1.23: IR thermogram during transmission laser welding of PEKK [Villar et al., 2018]

An example is shown in Fig. 1.23. From the curves, heating and cooling rates can be

calculated as well as maximum reached temperature. However, determining the emissivity of polymers is quite difficult and imprecise, especially for PAEK polymers for which few optical data are available in the literature. That is why this technique does not seem to fit ultrasonic welding. It also requires access to the welding interface during the process.

1.4.2 Thermocouple

Different types of thermocouple (TC) exist, matching several applications. Thermocouples are made with a combination of two metal wires. One must be a positive conductor while the other one needs to be a negative conductor. The most common combination are K, T and J-type thermocouples. In the case of polymer or composite welding, K-type TC with small diameters (under 0.3 mm) are usually used to limit their impact on the process. TC are placed at the welding interface between the two specimens [Dubé et al., 2007, Howie et al., 1993].

1.4.3 The case of ultrasonic welding

Measuring temperature at the welding interface is a big challenge considering ultrasonic welding. The closed contact between the two specimens makes it hard to know what is happening at the interface during welding, explaining why limited studies can be found in the literature about temperature monitoring. Also, if the temperature is tricky to monitor, it makes it impossible to control the process. However, the temperature cycle has a considerable impact on the mechanical properties of polymers. First of all, degradation or delamination of composite layers can occur if too high temperatures are reached. Besides, the cooling rate has a significant impact on the crystallinity and thus on the mechanical strength of the weld.

Some authors have used K-type thermocouples placed at the welding interface [Tao et al., 2019, Gao et al., 2018, Koutras et al., 2019]. Tao et al. [Tao et al., 2019] used 0.125 mm diameter thermocouples to assess temperature data during welding of CF/PEEK specimens with and without PEEK ED. The curves with ED are presented in Fig. 1.24. Thermocouples were placed between the two specimens prior welding. It appears that the use of an ED decreases the maximal reached temperature (416 $°C$ with ED versus 443 $°C$ without ED), probably because heat is absorbed by the ED melting. The presence of the ED also increases the heating rate, which is due to viscoelastic heating of the polymer, as explained by the authors.

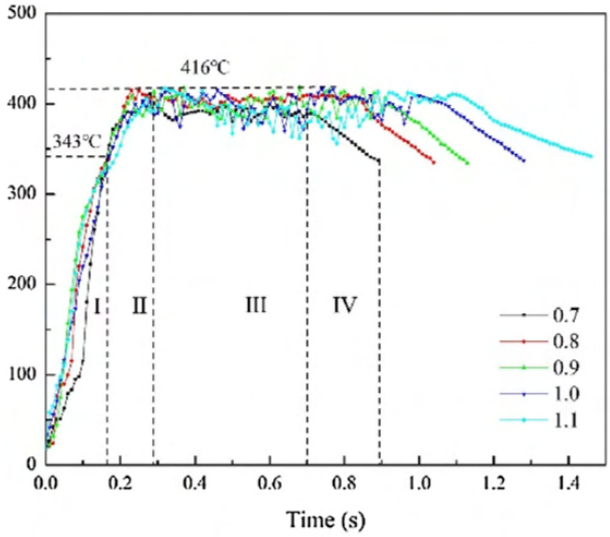

Figure 1.24: Temperature curves during welding of CF/PEEK specimens using a flat PEEK ED at different welding times (0.7 s, 0.8 s, 0.9 s, 1 s and 1.1 s) [Tao et al., 2019]

Even though they obtain results, *i.e.* smooth curves, it is important to note that any object placed at the welding interface will alter heat generation. TC are a good way of measuring the temperature since low-diameter TC can make measurements even in short cycle times. However, this technique is still too invasive to measure the real temperature. It always affects heat generation and especially in the area around the TC. The roughness is critical since any asperity can become an energy director and modify heat generation. In such cases, the output temperature values do not match the actual process temperature, and the mechanical properties are altered. Koutras et al. [Koutras et al., 2019] embedded K-type thermocouple of 0.1 mm diameter inside the ED prior welding. They manufactured by thermocompression their 0.32 mm thick ED with 4 layers of PPS film and placed the thermocouple at the middle. Their methodology is less invasive than the one of Tao et al. [Tao et al., 2019]. Nonetheless, they could only measure one temperature value every 100 ms, making temperature curves imprecise due to the rapidity of the process. Gao et al. [Gao et al., 2018] made small holes of 1 mm diameter inside the upper specimen, one at 0.2 mm from the top and another one at 0.2 mm from the bottom (*i.e.* 0.2 mm from the welding interface). They secured them with epoxy compound put inside these holes. As for the previously mentioned paper by Koutras et al., the measurement frequency seems to be relatively small, with around four measured temperature values per second (the sampling frequency is not indicated). However, they proved that heat is generated firstly at the interface. Then, heat dissipation occurs through the entire thickness since the temperature is higher during the vibration phase at the welding interface than at the

top of the specimen. They also assessed that temperature starts decreasing as soon as the vibration stops.

That is why Levy et al. [Levy et al., 2014] got interested in creating a numerical model to simulate physical phenomena. They completed a finite element model on ultrasonic welding of CF/poly(ether imide) (PEI) using flat PEI ED. The authors demonstrated friction phenomenon is predominant at first but replaced by viscoelastic dissipation when temperature increases and adhesion begins, as seen in Fig. 1.25 (a). Indeed, the total simulated dissipation is made of two components, friction dissipation and visco-elastic dissipation. The simulation seems to correlate well with experimental power from the device. They also obtained with their model that heat is firstly generated at the edge of the contact area between the two specimens. Fig. 1.25 (b) shows the temperature along the area of the welding interface, from the center to the edge, at different characteristic times. The temperature is way higher at the edges than at the center. Overall, all these studies highlight that temperature profile is hard to obtain during ultrasonic welding, but the use of thermocouple seems to be the best solution.

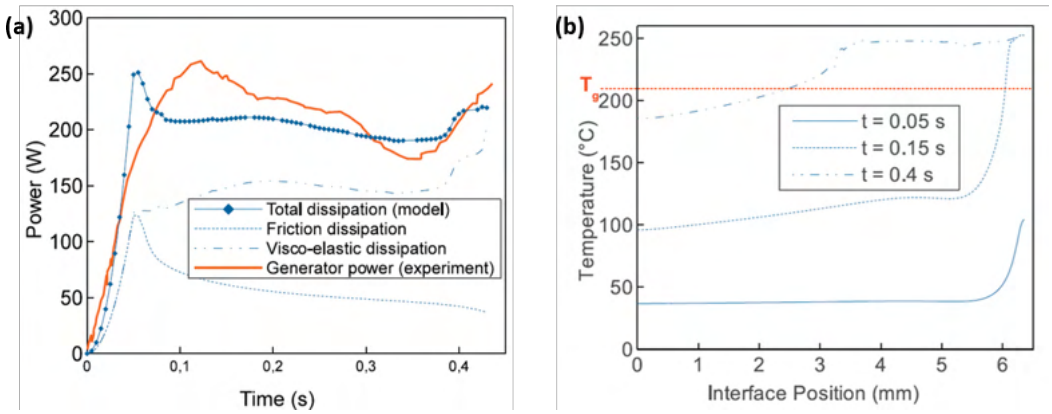

Figure 1.25: Total dissipation model and power from the device of CF/PEI at a vibration amplitude of 86.2 μm and a welding load of 500 N (a) and temperature modelling along the interface at different times during welding (b) [Levy et al., 2014]

1.5 Mechanical strength of joints

Characterizing the interfacial resistance of composite assemblies is challenging. The following section aims to review the main different tests existing and to understand the interest and complementarity of these various experiments.

In aerospace, analysis of crack propagation is essential when designing structural parts. Indeed, the bond between layers is never perfect. Defects are always present, even infinitely small ones. Undetectable microcracks and microporosities are present composite. This phenomenon involves the notion of damage tolerance, *i.e.* an undetectable crack must not become critical before it can be detected [Bouvet, 2019]. For that, models are set up in order to be able to apprehend these cracks as well as possible. There are three crack propagation modes, presented in Fig. 1.26:

- Mode I : Opening mode,
- Mode II : In-plane shearing mode,
- Mode III : Tearing (out-of-plane) mode.

The physical quantity related to fracture mechanisms is called energy release rate, G. G is related to the toughness of the composite, *i.e.* the energy released by the crack to propagate on a surface δS. The objective of each mode is to evaluate the critical strain energy release rate for the considered stress. G_{Ic} is the capacity of the material to resist the advancement of cracks in opening mode. When G is lower than G_{Ic}, cracks do not propagate. On the other hand, if this value exceeds G_{Ic}, cracks propagate in a stable ($G = G_{Ic}$) or unstable ($G > G_{Ic}$) way.

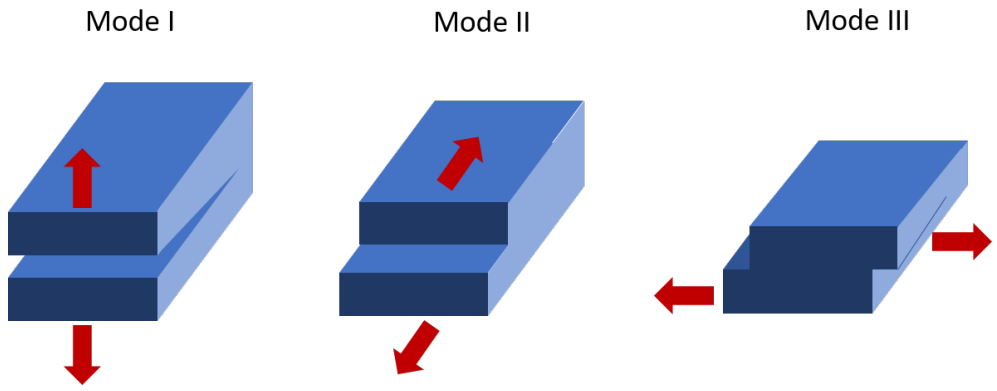

Figure 1.26: Crack propagation modes

In order to determine G_{Ic}, it is sufficient to perform a crack propagation test and to measure the energy dissipated by this operation.

1.5.1 Experimental techniques

1.5.1.1 Double cantilever beam (DCB)

In the case of mode I, this is called a DCB test, which consists in pulling in two opposite directions the edges of the same side. Usually, the crack is initiated with a polymer film. Toughness is calculated from the following relationship:

$$\Delta W_{ext} = \Delta E_{el} + \Delta E_c + \Delta E_d + G.\Delta S$$

where ΔW_{ext} is the work of external forces, ΔE_{el} is the elastic energy variation, ΔE_c the kinetic energy variation, ΔE_d the dissipated energy variation and ΔS the surface variation. This equation is simplified and gives the following result:

$$G_I = \frac{3.F.u}{2.b.a}$$

where F est the load, u is the vertical displacement between the two specimens, b is the specimen thickness and a is the crack length. The determination of G_{Ic} requires propagation of the crack over a significant distance (typically 100 to 150 mm). This technique is therefore not suitable for static welds, for which the welded area is small compared to the surface specimens. Moreover, it is difficult to prepare the specimens, but also difficult to monitore the crack and to estimate the crack length over the test. Avenet [Avenet, 2018] used DCB tests to characterize CF/PEKK assemblies made by induction welding on an experimental set up. They found out that the crack propagation seems unstable but the value of G_{Ic} at the beginning of the crack is a good way of evaluating the adhesion of the assembly.

1.5.1.2 Cross tensile test

In addition to DCB, a new cross tensile test method (*Cross Tensile Test*, CTT) was developed by Goto et al. [Goto et al., 2019] in order to evaluate the tensile behavior to match more with the industrial challenges. The specimens are welded to form a cross, as shown in Fig. 1.27 (a). A schematic of the tensile setup is shown in Fig. 1.27 (b). The authors defined the *Cross Tensile Strength 1*, CTS1, and *Cross Tensile Strength 2*, CTS2, as, respectively, the maximum stress supported by the joint divided by the overlap area and the maximum stress supported by the joint divided by the welding area. Basicaly, it means that CTS1 evaluate the 'welding efficiency' while CTS2 evaluate the 'welding quality'. To

the best of our knowledge, there are the only ones to have used this method.

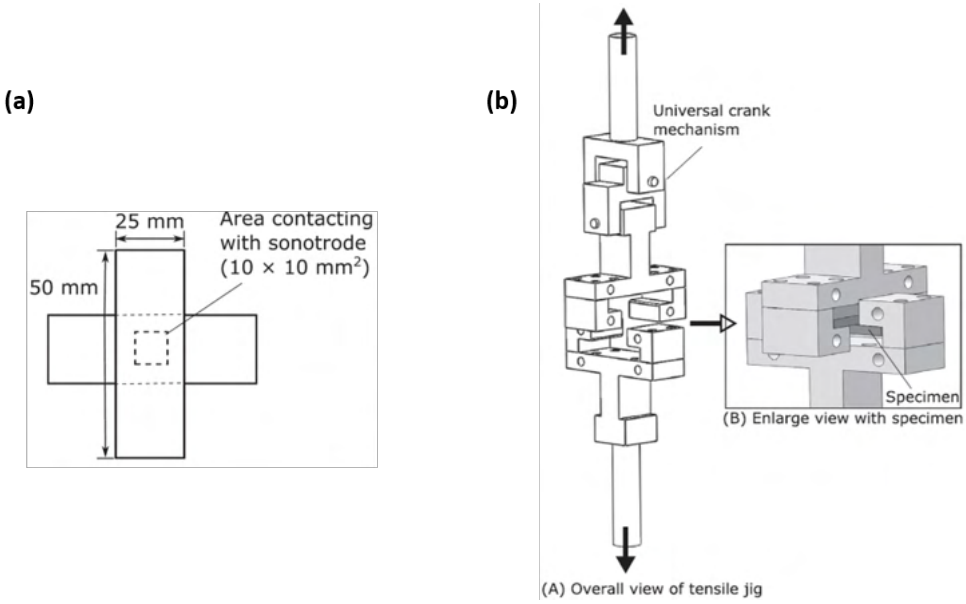

Figure 1.27: Cross tensile test specimen configuration (a) and set up (b)

The authors welded woven and cross-ply CF/PA6 with and without a flat ED. They were able to evaluate the influence of the welding energy on the tensile behavior. The maximal cross tensile strength they obtained was around 6 MPa for CTS2 of both cross-ply and woven laminate joints welded with an ED. These values of cross tensile test are quite low compared to the results they assessed when evaluating the shear behavior of their joints (maximal value around 40 MPa).

1.5.1.3 Single lap shear

Single lap shear is the easiest joint characterization in the case of welding. A setup schematic is shown in Fig. 1.28. Longitudinal loading is applied to each extremity of the specimens, which increases over time until the joint fails. The mechanical quantity calculated is called LSS for *Single Lap Shear*, and it is the ratio between the maximum load and the overlap area between the two specimens. This technique is used by most research groups working on welding of thermoplastic composites. Also, Villegas et al. [Villegas and Bersee, 2010] defined another value called LSS2, which is the ratio between the maximum load and the actual welding area. According to the authors, LSS gives an idea about joint efficiency, whereas LSS2 is more about joint quality. We choose this method to characterize the interfacial strength of US welded composites because no specific specimen

preparation is required, LSS is easily calculated, and it is easy to handle. Finally, there is the possibility to compare with other results in the literature.

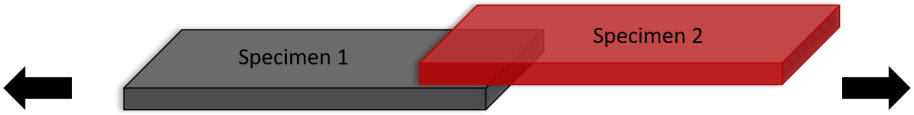

Figure 1.28: Diagram of single lap shear specimens configuration

Villegas et al. [Villegas, 2014] found LSS values of 39 MPa for CF/PEI specimens with a PEI energy director and 35 MPa for CF/PPS specimens with a PPS energy director [Fernandez Villegas and Palardy, 2017]. Tao et al. [Tao et al., 2019] worked on US welding of CF/PEEK associated with a PEEK energy director and determined a LSS at 28 MPa. Regarding other bonding processes, it was found by Li et al. [Li et al., 2021] a 46 MPa value of LSS for CF/PEEK resistance welded joints and a 49 MPa value by Smiley et al. [Smiley et al., 1991] using Thermabond process on CF/PEEK specimens with a PEI interlayer.

1.5.2 Failure mechanisms

Characterization of an assembly is done through mechanical tests and interfacial fracture analyses. In the case of composites, fracture mechanics are often used to study damage modes taking place at the interface. Some means and methods of characterization are found quite regularly in the literature to evaluate an assembly made by welding. In order to evaluate the quality of the weld, it is necessary to study the rupture between the layers after mechanical tests. A fracture can be caused by crack propagation, for example, and delamination of folds. Four fracture mechanisms can be observed:

- Cohesive failure in the ED (failure in the thickness of the energy director),
- Cohesive failure in the composite,
- Adhesive failure (between the ED and the composite),
- A mixture of the 3 previous ones.

It has been shown that interfacial fracture of welded joints depends on welding parameters. Fracture is usually analyzed by visual inspection of the welded joint after mechanical

testing. *Scanning Electron Microscopy* (SEM) is also often used to have a deeper understanding. When heat generation is not enough, unmelted areas of the ED have been observed, as seen in Fig. 1.29 (a). This means that the friction phenomenon was not sufficient to melt the entire overlap area. That is why, in these cases, mechanical values are typically low. Other cases have shown composite tearing (Fig. 1.29 (b)) associated with broken fibers (1.29 (c)). When interfacial tearing is happening, fibers from one layer imprint themselves on another layer or on the energy director, as seen in Fig. 1.29 (d). Finally, when welding parameters are critical, resin flakes and voids appear (Fig. 1.29 (e)), leading to the degradation of the matrix. It is common to notice a change of color of the matrix, correlated with the degradation of the polymer.

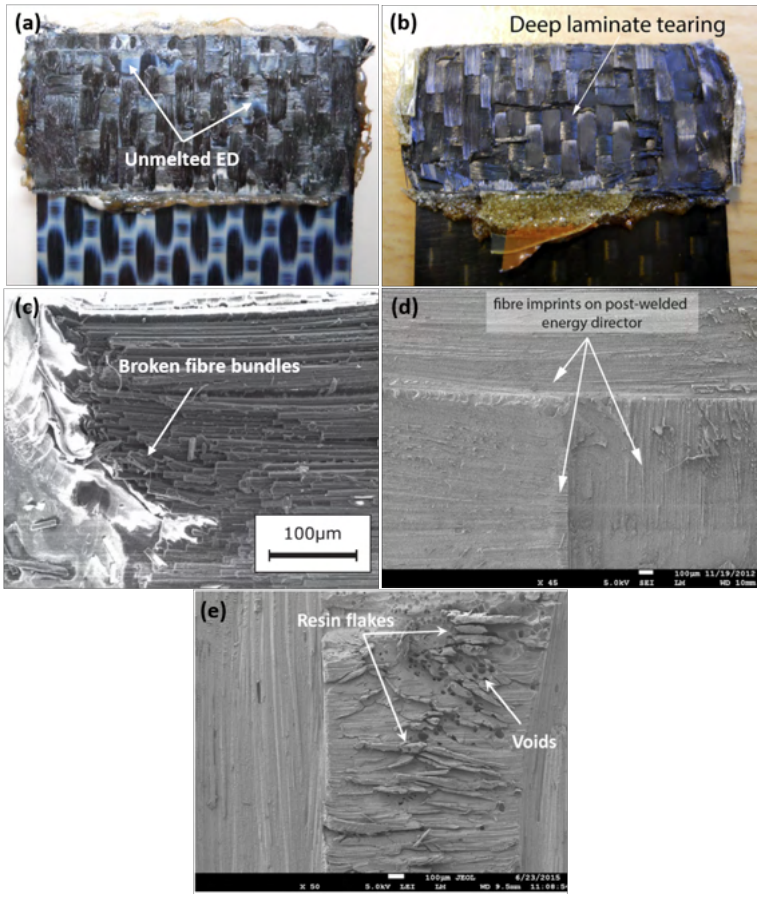

Figure 1.29: Interfacial fracture micrographies of welded specimens with different fracture mechanisms: unmelted areas [Fernandez Villegas and Palardy, 2017] (a), composite tearing [Villegas, 2014] (b), broken fibers [Goto et al., 2019] (c), fiber imprints [Villegas, 2014] (d) and resin flakes and voids [Palardy and Fernandez Villegas, 2017] (e)

The fracture mechanism also depends on the initial geometry of the substrate. Indeed, whether the composite is woven or unidirectional fabric, the behavior seems to be different.

In unidirectional composite welding, fibers seem to be easily pushed out the longitudinal edges of the specimens [Fernandez Villegas and Vizcaino Rubio, 2015]. On the other hand, woven composites seem to be crushed while no fiber bundles flow on the edges, like presented in Fig. 1.29 (d).

1.6 Conclusion

This chapter has brought to light some significant issues about ultrasonic welding of thermoplastic composites. First, we highlighted the different ways of joining thermoplastic composites, from more general and known methods to new welding processes. Temperature monitoring during joining processes has been explained, followed by the methods used to measure the mechanical strength of joints.

It appears from this state of the art that a variety of joining processes have been explored for thermoplastic composites, and no optimal solution has been found yet. Typical methods such as drilling and adhesive bonding are quite ineffective for this type of materials since they bring either a negative effect on mechanical properties or a significant time consumption due to the difficulty of adapting to composite. Welding seems to be a promising process to overcome these issues.

Usual welding processes in the industry are resistance and induction weldings. They are both energy consuming with relatively long welding times (it can go to a few minutes). Ultrasonic welding is a new process considering thermoplastic composites since most papers on this subject are only 15 years old maximum. It is industrially applied to polymers, but the influence of fibers on the process is not fully understood as well as the impact of the welding parameters.

It has been shown that the process can be monitored using output data from the welding device, such as displacement of the sonotrode and power. The obtained curves give information about the physical changes occurring during welding. Authors have measured mechanical shear strengths (LSS) of about 40 MPa at best, which shows the excellent potential of this welding technique. However, the lack of study on this subject does not allow a complete understanding of the process. Indeed, once they are determined, optimal parameters can be applied to only one material. Besides, the biggest challenge is to continuously weld more prominent parts, meaning that a movement of either the apparatus or the specimens is required. Only experimental setup in laboratories can be found in the literature so far, which shows the long way to go.

Moreover, temperature measurement is another issue since the closed contact between the specimen hinders the access to the interface. Infrared thermography and thermocouples are the most widely used technologies. In the case of ultrasonic welding, the use of thermocouples placed at the interface is the most common. However, TC can alter heat generation since any object placed between the parts acts as an energy director.

Finally, joint quality is typically evaluated through single lap shear tests. Failure mechanisms have shown that both cohesive and adhesive failures can occur, depending on welding parameters. When heat generation is insufficient, unmelted areas of the ED are observed, whereas matrix and fiber degradation is seen when too much heat is generated at the interface.

Chapter 2

Materials and experimental techniques

Contents

2.1 Introduction 46

2.2 Overview of the welded materials 46

2.2.1 Thermoplastic polymer matrices 46

2.2.2 APC-2 prepreg 53

2.2.3 AE 250 prepreg 54

2.3 Manufacturing of plates and specimens 54

2.3.1 Vaccum bag process 55

2.3.2 Plate characterization 59

2.4 Ultrasonic welding device 61

2.4.1 Welder modules 61

2.4.2 Welding parameters 64

2.4.3 Typical curves from the device output parameters 65

2.5 Conclusion 66

2.1 Introduction

This chapter presents the different materials and techniques used during this study. A first section is devoted to the polymers and composites used for welding. After that, the protocol set up for the realization of the welding specimens is exposed in a second section. The last section is intended to introduce the ultrasonic welding apparatus used for the welding experiment.

2.2 Overview of the welded materials

The materials used in this study are amorphous and semi-crystalline high-performance thermoplastic polymers and composites with long carbon fibers. This section lists those materials as well as their usual properties.

2.2.1 Thermoplastic polymer matrices

Several grades of poly(aryl ether ketones) (PAEK) are used as well as polyetherimide.

2.2.1.1 Poly(ether ether ketone)

Poly(ether ether ketone) (PEEK) is a semi-crystalline polymer. Its chemical structure is presented in Fig. 2.1. Among the PAEK family, PEEK poly(ether ether ketone) is by far the most used in the industry to find applications in automotive, aerospace and healthcare sectors [Kemmish and Hay, 1985, Cebe et al., 1987, Lu et al., 1996, Ma et al., 1992]. Indeed, PEEK exhibits high elastic modulus below its glass transition at 150 $°C$ and it can be used up to its melting temperature at 330 $°C$. In comparison to other semi-crystalline polymers, it also displays great chemical resistance to most solvents and severe conditions, and its biocompatibility makes it suitable to be used in biomedical applications [Monich et al., 2016].

Its association with carbon fibers has made PEEK-based composites essential in the thermoplastic composite industry. PEEK was first developed by ICI in the late 70's but since the early 80's, PEEK from Victrex company has accounted for the majority of the world demand. PEEK is synthesized by a nucleophilic substitution from hydroquinone,

fluorinated aromatic compound and dry potassium carbonate reagents. It is obtained by a polycondensation process in a polar aprotic solvent such as diphenyl sulfone (DPS) [Attwood et al., 1981]. Due to high production cost, PEEK is one of the most expensive thermoplastic materials. The synthesis is performed at high temperature (between 200 $°C$ and 400 $°C$) requiring high power energy.

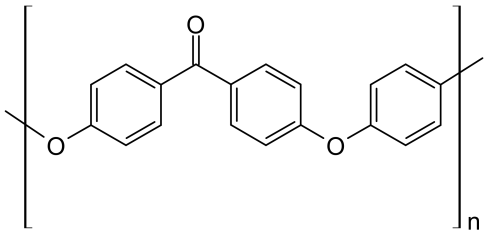

Figure 2.1: Chemical formula of PEEK

During this PhD, Victrex APTIV™ PEEK was supplied by GoodFellow as films of 0.125 mm thickness. Films are used in the following as energy directors for welding. The APTIV™ 2000 film grade, from which this material is derived, is the only commercial grade to offer PEEK in an amorphous structural state. The supplier does not disclose the molecular weight of the product, but different elements can be used to approximate its value. On the one hand, it is more accessible from a practical point of view to amorphize a semi-crystalline polymer with a high molecular weight because of slower crystallization kinetics. On the other hand, for the former generation of this grade of amorphous PEEK film, then named Stabar K200 and supplied by ICI (Imperial Chemical Industries), the average molecular weight was estimated by Bas to be 38 000 $g.mol^{-1}$ [Bas, 1994]. Therefore, it can be assumed that APTIV™ 2000 films are close to the PEEK 450G grade in terms of molecular weight.

Moreover, PEEK 450G from Victrex is used for thermal and rheological characterizations. The rheology samples are manufactured by compression molding. To do so, the pellets are dried in an oven for 3 hours at 150 $°C$. Then, they are put into a 149 mm x 76 mm x 2 mm steel mold and kept inside the mold with steel sheets located on each side of the mold. The compression press is pre-heated at 200 $°C$ and heated at 360°C at 10 $°C.min^{-1}$. When the target temperature is reached, a load of 50 kN is applied for 5 minutes. The cooling rate is 4 $°C.min^{-1}$ until reaching 200 $°C$, still under pressure. Finally, the plate is removed from the mold and cooled at ambient temperature.

2.2.1.2 PAEK AE 250

Lately, Victrex has elaborated a new PAEK named Victrex PAEK AE 250. It is an innovative material that promises a lower melting temperature (around 300 $°C$) while maintaining a glass transition and mechanical properties similar to PEEK. Some information is available in a patent about its chemical composition [Glynn et al., 2017]. Nevertheless, Fig. 2.2 shows that the FTIR spectrum of AE 250 is almost identical to PEEK 450G, which suggests that the chemical composition of AE 250 is similar to PEEK. Current PAEK have high glass transition temperature associated with high melting temperature. For instance, PEK, PEKK and PEKEKK exhibit higher T_g than PEEK but also higher T_m. There is a relationship between T_g and T_m for all PAEK, as their transitions are plotted in Fig. 2.3 according to the ether/ketone ratio. Increasing T_g means extending the thermal stability and therefore the operating temperature range, since these types of polymers are often used below T_g to benefit their high mechanical strength. The polymer manufacturers target to increase T_g. But until now, increasing T_g of PAEK was paired with increasing T_m.

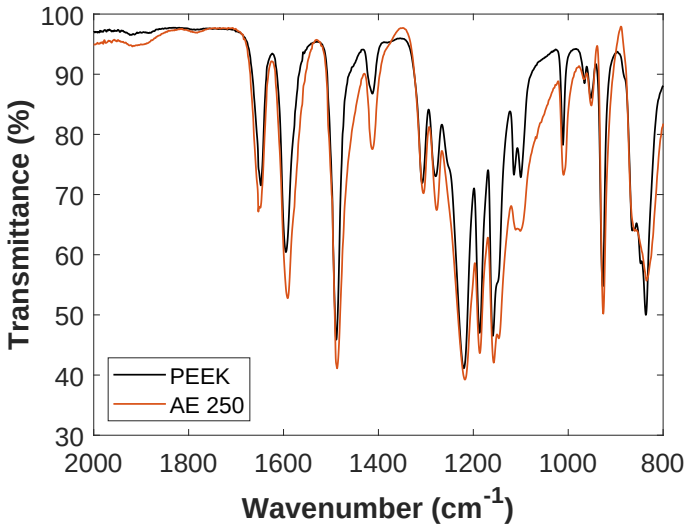

Figure 2.2: FTIR spectra of PEEK 450G and AE 250

Yet, high melting temperature brings specific hardships and challenges to be faced: the processing temperature is above T_m whatever the techniques: injection molding, extrusion or additive manufacturing. The high processing temperature of PEEK (350 $°C$ to 430 $°C$) associated with high viscosity restricts the machines available to process this polymer.

So, a new grade of PAEK combining high T_g and low T_m will facilitate the manufacturing

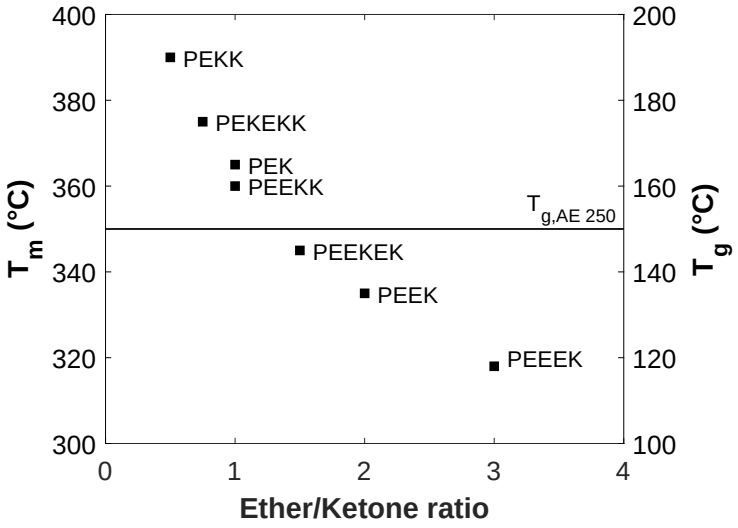

Figure 2.3: Melting and glass transition temperatures of usual PAEK polymers as a function of the ether/ketone ratio, from [Friedrich et al., 1995]

process. PAEK AE 250 fits this requirement with $T_g = 150\ °C$ and $T_m = 300\ °C$. The relationship between T_g and T_m is not valid anymore for this new grade. PAEK AE 250 does not follow usual behavior of PAEK polymers. It cannot be put into the graph since its melting temperature is around 300 $°C$ while its glass transition temperature remains around 150 $°C$. This new generation polymer is attractive because it can be processed at a temperature lower than usual PAEK.

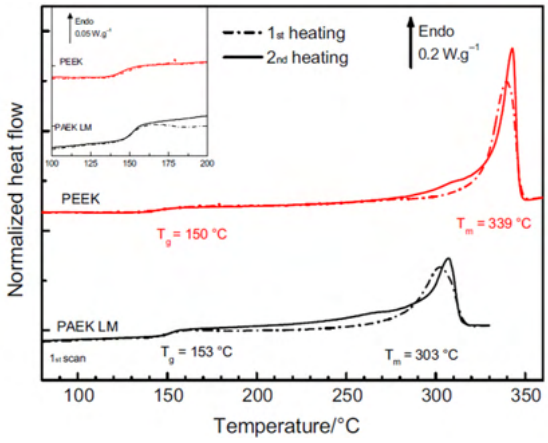

Figure 2.4: DSC curves of PEEK and AE 250 of slowly air-cooled samples [Audoit et al., 2018]

Nevertheless, few information is available about its chemical composition and properties due to its novelty. To date, the only study about the properties of PAEK AE 250 is by Audoit et al. [Audoit et al., 2018], who used differential scanning analysis (DSC), thermal conductivity measurements, dynamical mechanical analysis (DMA) and dynamic dielectric analysis to characterize it. It was confirmed that this PAEK has a melting temperature about 40 $°C$ lower than PEEK while maintaining a glass transition in the same temperature range, at 150 $°C$, as seen in Fig. 2.4. The authors also show that this polymer has a degree of crystallinity lower than PEEK. They explained that crystallization is faster for AE 250 and that configurational defects are present in its structure. Moreover, it was pointed out that the difference between melting (T_m) and crystallization (T_c) temperatures was higher for PAEK AE 250, which led to an easier processability of PAEK AE 250. Finally, thermal, mechanical and dielectrical properties of PAEK and PEEK are close to each other.

Thermal conductivities, λ, of both PEEK and AE 250 are plotted in Fig. 2.5 as a function of temperature. We note that λ increases with temperature, especially below reaching T_g. Around and above T_g, physical changes occur in the polymer, changing the thermal conductivity evolution with temperature. Overall, thermal conductivity seems similar for both materials.

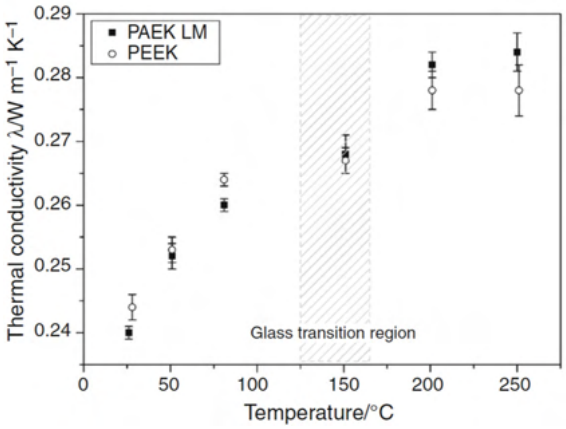

Figure 2.5: Thermal conductivities of PEEK and AE 250 at several temperatures measured by guarded hot plate [Audoit et al., 2018]

For this study, AE 250 was supplied by Victrex as 60 μm thick films (FM) and flakes (FL). They are both used for thermal and rheological characterization in Chapter 3. The manufacturing process of both films and flakes to obtain the specimens for rheometry is shown in Fig. 2.6. In each case, two steps are necessary.

For films, plates are made by thermocompression. The temperature and pressure cycles

are presented in Fig. 2.7. The films are heated at 350 $°C$ for 3 minutes while a load of 135 kN is applied only when the temperature has reached 350 $°C$ and stays on until the end of the slow cooling. 25 mm diameter disk-shaped samples are then water-jet cut.

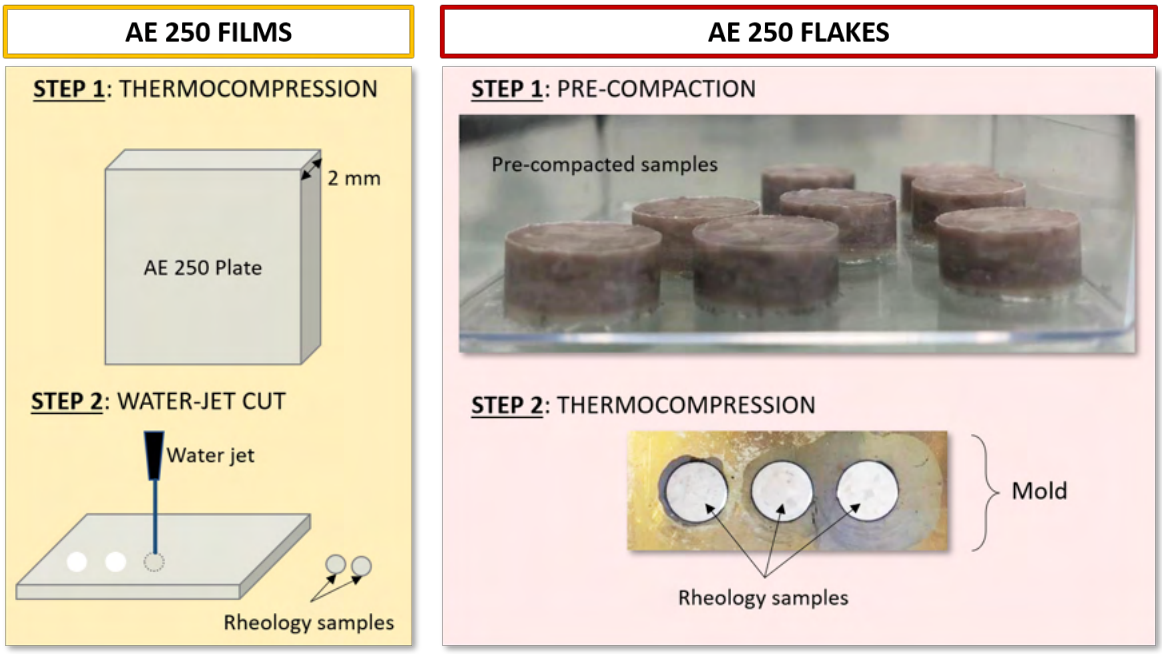

Figure 2.6: Manufacturing process of films and flakes rheology samples

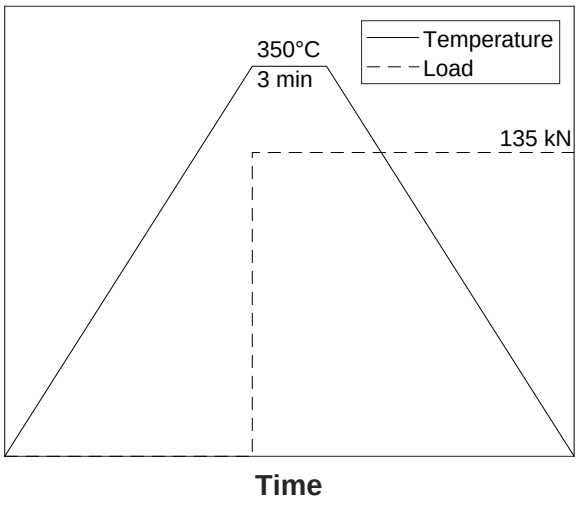

Figure 2.7: Temperature and pressure cycles to obtain the specimens for rheometry

In the case of flakes, a pre-compaction is necessary to hold them together. 25 mm diameter circular-shaped molds are used for thermocompression. The temperature and pressure cycles are the same as films. The specimens from films and flakes are called respectively, FMc and FLc.

Films are also used as energy directors for welding. The manufacturing process of welding specimens is presented in the next section of this chapter. All samples (FM, FL, FMc and FLc) were dried at 150 $°C$ in an oven for 4 hours before being used in any experimental procedures.

2.2.1.3 Poly(ether imide)

Polyetherimide (PEI), under the tradename Ultem by Sabic, is an amorphous polymer that has a glass transition temperature of 217 $°C$. It was first synthesized by General Electric Plastics in 1982, its chemical formula is in Fig. 2.8.

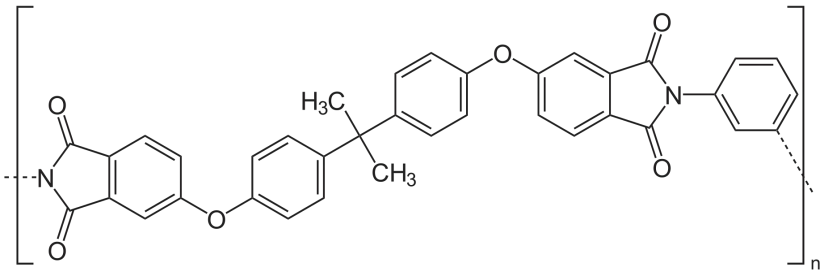

Figure 2.8: Chemical formula of PEI

For this study, PEI sheets were provided by GoodFellow in the following dimensions: 610 mm x 610 mm x 0.25 mm. PEI films are used as energy directors when welding CF/PEEK. PEI was chosen for two reasons. First, the US welding of dissimilar material (between the ED and the composite) has not been studied so far. The aim of using an amorphous polymer as ED is to weld CF/PEEK without reaching the melting temperature of PEEK. It is uncommon for polymers to be miscible one to each other. However, all PAEK are miscible one to each other. Also, PEI is the only polymer to be miscible with PEEK [Dominguez, 2013]. Ultem 1000 pellets supplied by Polymix are also used for PEEK/PEI blends in Chapter 5.

2.2.2 APC-2 prepreg

Unidirectional (UD) APC-2 (PEEK) prepreg was supplied by Solvay as a tape of 30 cm width, as seen in Fig. 2.9. The APC-2 datasheet is available in Appendix A. The thermal transitions of APC-2 are similar to PEEK: $T_g = 143\ °C$ and $T_m = 343\ °C$. A study has indicated that the PEEK matrix is an intermediary between PEEK 150G and PEEK 450G but closer to PEEK 450G [Nicodeau, 2005]. The prepreg resin content is 34 wt. %. The fibers are long carbon fibers developed by Hexcel under the name AS4 12,000 (12) filament count tows. From Hexcel data sheet in Appendix A, AS4 fibers have high tensile strength of 4447 MPa and an elastic modulus of 231 GPa. The area density M_s is 145 $g.m^{-2}$. The thickness of one ply, called e, is linked to M_s with the following equation:

$$e = \frac{M_s}{\rho_f V_f\%} \tag{2.1}$$

where ρ_f is the fiber density ($\rho_f = 1.79\ kg.m^{-3}$) and $V_f\%$ is the volume percentage of fibers. The latter is quantified with the following equation:

$$V_f\% = \frac{M_f\%}{M_f\% + \frac{\rho_f}{\rho_m}(1 - M_f\%)} \tag{2.2}$$

The manufacturers usually give the weight percentage of matrix, $M_m\% = 100 - M_f\%$. In the case of APC-2 prepreg, $M_m\% = 34$. ρ_m is the matrix density and is equal to 1.32 $kg.m^{-3}$. Therefore, the theoretical thickness of a ply after consolidation is equal to 140 μm.

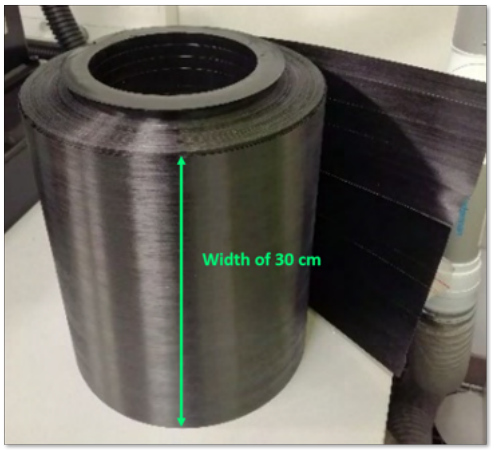

Figure 2.9: Unidirectional APC-2 tape from Solvay

2.2.3 AE 250 prepreg

As APC-2, unidirectional AE 250 tape was supplied by Victrex. Fig. 2.10 presents the tape of 5.3 cm width. Visually, it is hard to distinguish AE 250 tape and APC-2 tape. The same type of carbon fibers is used, AS4. The area density M_s is 143 $g.m^{-2}$. The polymer content is 34 wt. % while the volume percentage of fibers is 58 vol. %, from datasheet supplier in Appendix A. Finally, Table 2.1 summurize the available materials in this study.

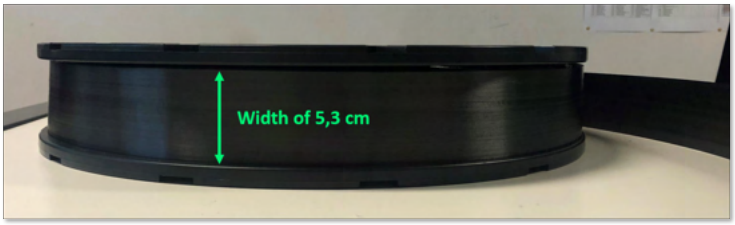

Figure 2.10: Unidirectional AE 250 prepreg from Victrex

	Film	*FMc*	*Pellets*	*Flakes*	*FLc*	*Prepreg*
PEI	√		√			
PEEK	√		√			√
AE 250	√	√		√	√	√

Table 2.1: Summary of the materials available for this study. FMc are plates from films and FLc are plates from flakes.

2.3 Manufacturing of plates and specimens

Welding specimens are made from the materials presented above. A protocol was developed during this thesis to make around 2-mm thick composite plates, detailed in the following section.

2.3.1 Vaccum bag process

2.3.1.1 Cutting of pregs and layout

Two categories of composite plates are made, one with APC-2 prepregs and a second one with AE 250 prepregs. In the case of APC-2, the prepregs are cut using 300 mm x 300

mm size dies and a hydraulic press applying pressure, as shown in Fig. 2.11 (a). A stack of 16 plies is made to obtain a mirror symmetry $[0,90]_{4,s}$ and a thickness around 2 mm.

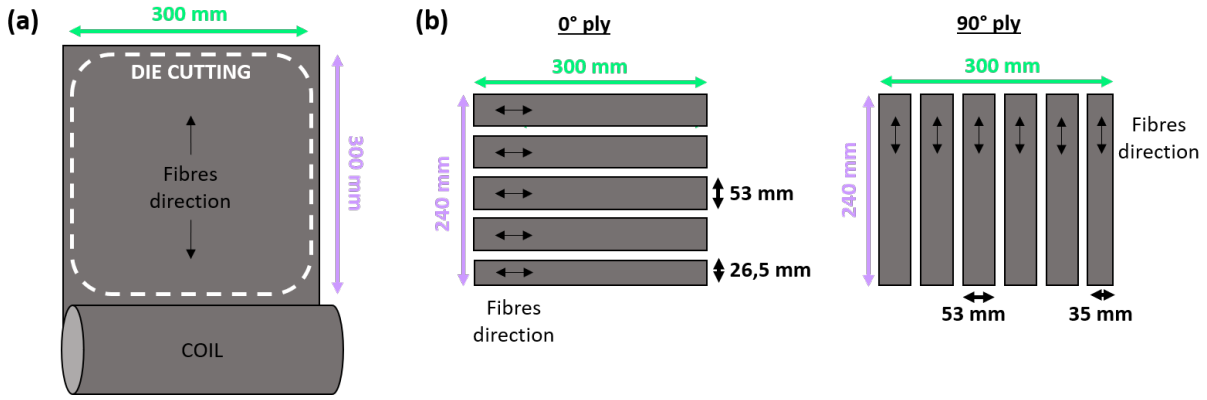

Figure 2.11: Cutting process of APC-2 (a) and AE 250 (b) prepregs

For AE 250 prepregs, using the 300 mm x 300 mm die is not possible because the tape is only 5.3 cm wide. Dimensions of 300 mm x 240 mm are chosen to minimize material loss while cutting the specimens. In order to obtain a thickness of approximatively 2 mm, 14 plies following stacking of $[0,90,0,90,0,90,0]_s$ is used. To create a 300 mm x 240 mm ply of preg, several strips of preg are aligned next to each other. They are manually cut and manually welded at the edges to hold them together. In the case of a 0° ply, 4 strips of 53 mm and 1 of 26.5 mm are necessary while 5 strips of 53 mm and 1 of 35 mm are required for a 90° ply. The cutting dimensions are shown in Fig. 2.11 (b).

2.3.1.2 Plate families

Two types of energy directors were considered for APC-2: PEI and PEEK. The thickness of the polymer layer is initially approximately 250 μm. After measurement of the thickness, it is found that the PEI thickness is 250 ± 20 μm. The energy director can be integrated at the specimen surface during manufacturing of welding specimens, or it can be free and placed at the interface right before welding. In the case of this thesis, it is chosen to integrate the film into the welding specimens, *i.e.* added to the stacking right before the vacuum bag process. Overall, three types of APC-2 plates were made: an APC-2 plate, an APC-2 plate with a PEI film and an APC-2 plate with a PEEK film. Fig. 2.12 shows the stacking of an APC-2 plate (a) and an APC-2 plate with a PEI layer.

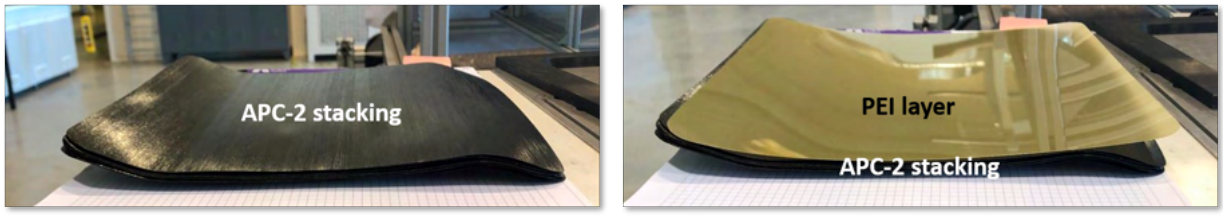

Figure 2.12: Stacking of APC-2 with a PEI layer

To sum up, 5 different plate families are made as shown in Fig. 2.13:

- APC-2 plate (P1),
- APC-2 plate with a PEI layer (P2),
- APC-2 plate with a PEEK layer (P3),
- CF/AE 250 plate (P4),
- CF/AE 250 plate with a AE 250 layer (P5).

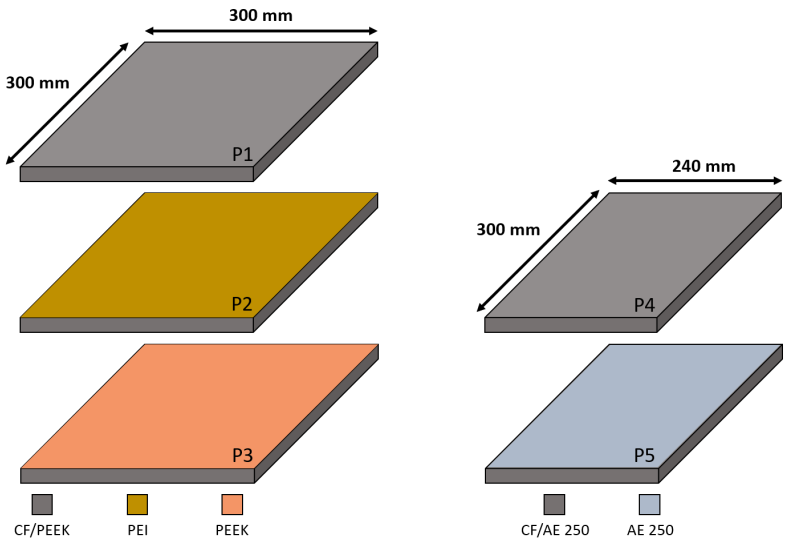

Figure 2.13: The different plate families: CF/PEEK (P1), CF/PEEK + PEI (P2), CF/PEEK + PEEK (P3), CF/AE 250 (P4), CF/AE 250 + AE 250 (P5)

2.3.1.3 Sheet manufacturing process presentation

The first step in plate manufacturing is the realization of composite plates of dimensions 300 x 300 x 2 mm^3. These plates are made in an oven using a vacuum bag process, Fig. 2.14 and 2.15. The stack of prepregs is placed between two low expansion coefficient metallic plates covered with a polyimide film. The latter ensures that a reproducible surface quality is obtained, *i.e.* a "smooth" surface. A glass fiber drainer is also used to contain the flow of the melted matrix. The metal grid provides a better vacuum level between the metallic horn and the rest of the layout. Finally, a polyimide film is used to cover the whole layout, and the sealing is ensured by a high-temperature tight seal. After starting the vacuum pump, the layout is put in the oven and it undergoes a selected temperature cycle.

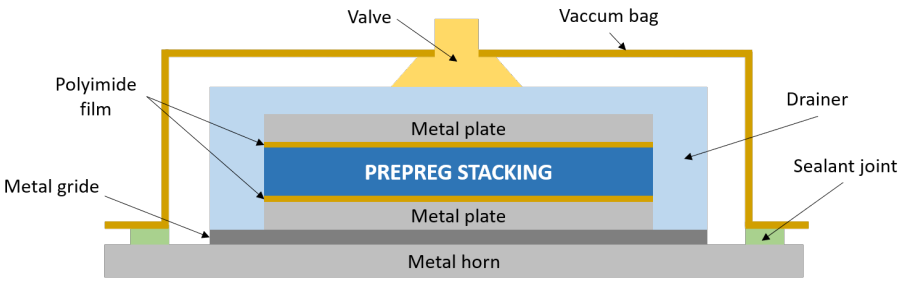

Figure 2.14: Diagram of the manufacturing process layout of the composite plates

Figure 2.15: Photograph of manufacturing process after vaccum bagging

2.3.1.4 Manufacturing thermal cycles

Two thermal cycles are used, one for APC-2 and another for AE 250 (the two cycles are presented in Fig. 2.16). They both consist of a temperature step at 100 $°C$ for 1 hour, which allows a first temperature homogeneization of the whole manufacturing stack. A second temperature step at 400 $°C$ for PEEK and 360 $°C$ for AE 250 are maintained during 30 minutes. Heating rates are set to 4 $°C.min^{-1}$. The maximal temperature is around 50 $°C$ above the melting temperature of each material. It is assumed that no matrix degradation occurs during those 30 minutes. Thermal cycles were chosen in accordance with recommended supplier process cycles.

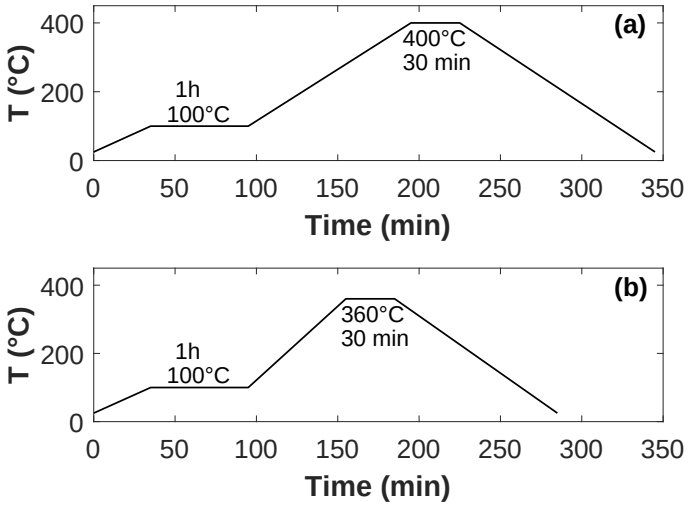

Figure 2.16: Thermal cycles undergone by APC-2 (a) and AE 250 (b)

Then, the cooling step is quite slow, about 3 $°C.min^{-1}$, and it is the same for both materials. It allows the matrix to fully crystallize. These are relatively long processes since they last between 5 and 6 hours.

2.3.1.5 Welding specimens cutting

Specimens of 100 mm x 25 mm are cut out of the plates by abrasive water jet, according to the scheme in Fig. 2.17. The specimens are cut following the fibers direction of the upper and lower plies. The cutting process has a precision of $\pm$ 0.2 mm. It requires a CAD (*Computer Aided Design*) modeling of the plate and the specimen dimensions. It is

also very fast since 18 specimens can be cut within 8 min in a 300 x 300 mm^2 plate.

Figure 2.17: Abrasive water-jet cutting of 300 x 300 mm^2 APC-2 plate

2.3.2 Plate characterization

The control of the plates is performed to determine the consolidation quality, including ply and polymer layer thicknesses and also the surface roughness. Samples are prepared for polishing and microscopic observation. The surface roughness is shown in Fig. 2.18 for a P1 (CF/PEEK) plate. The arithmetical mean height Sa, which expresses the difference in height of point compared to the arithmetical mean of the surface, is 0.646 μm. It is used to evaluate surface roughness, a low value indicating a smooth surface. In this case, the value is not really high but the impact of the carbon fibers during consolidation is visible through lines along the x and y axis. The polymer has flowed between the fibers, creating thoses waves.

Out-of-plane micrographs are presented in Fig. 2.19 for the three plates containing a polymer-rich layer (P2, P3 and P5). The samples are taken at the center of the plate and the PEI, PEEK and AE 250 layers are measured at 5 locations using ImageJ. The thickness ranges from 230 μm to 273 μm for PEI, probably due to the scattered initial thickness of the PEI film and the waves due to fibers. Moreover, some fibers are visible in the PEI-rich layer, which means they have moved during the consolidation and it is likely that PEI have diffused in the first APC-2 ply. The same trend is observed for PEEK and AE 250 layers, where both polymer thicknesses are scattered over a range of 30 to 50 μm. This difference in the thickness is important for setting the parameters of the welder and it will be explained in the following Section 2.4. Also, the ply thickness is closed to the theoretical

value for all ma p = 6μm, meaning that the consolidation process is successful.

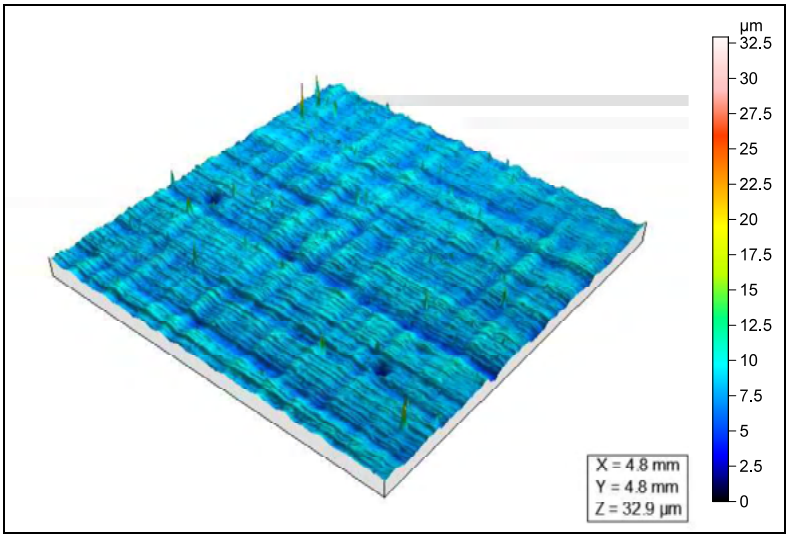

Figure 2.18: Surface roughness of a CF/PEEK specimen

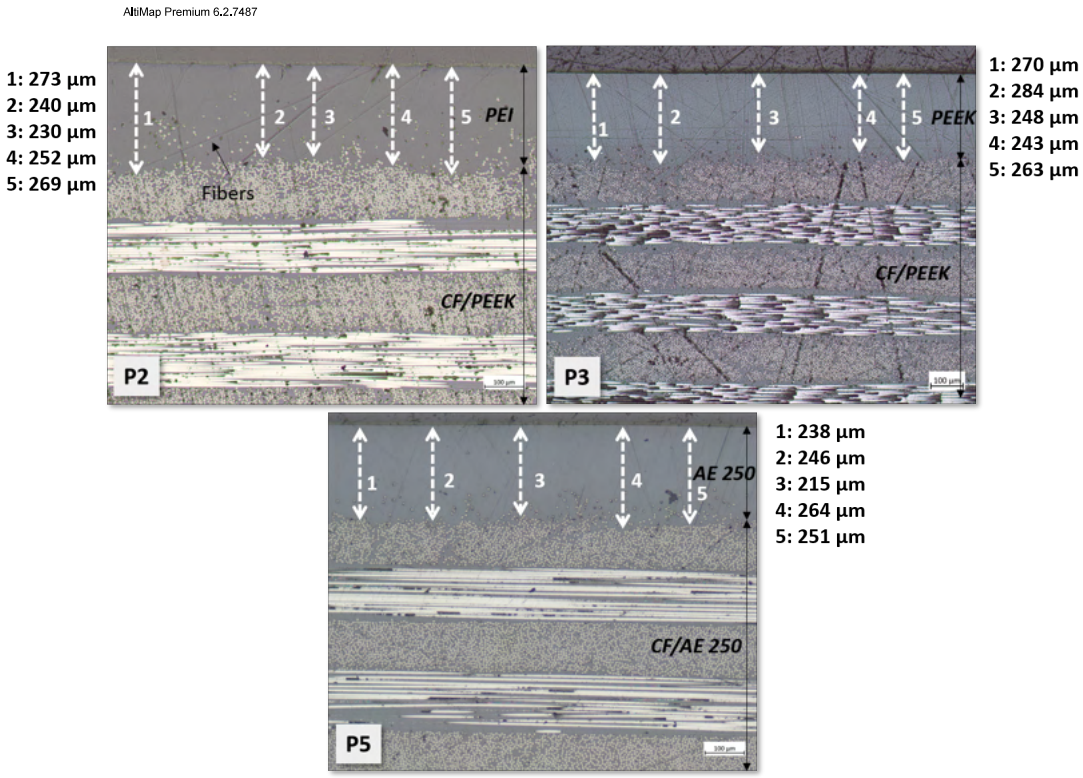

Figure 2.19: Out-of-plane micrographs of plate P2, P3 and P5

Besides, from Fig. 2.20, the ED thickness is not homogeneous all along the plate. The polymer flows upon squeezing or accumulates at the edges due to the applied vacuum. Therefore, lower or higher values of polymer thickness are observed, in the zones marked in color in Fig. 2.20. The material tends to flow following fibers direction (violet zone) while it can stay trapped in the perpendicular direction (green zone). Therefore, the four specimens at the edges of the plate (marked with a black cross) will not be used for welding. Welding experiments were made with the specimens located at the center of the plate. The welding area of such specimens is indicated by red rectangles in Fig. 2.20.

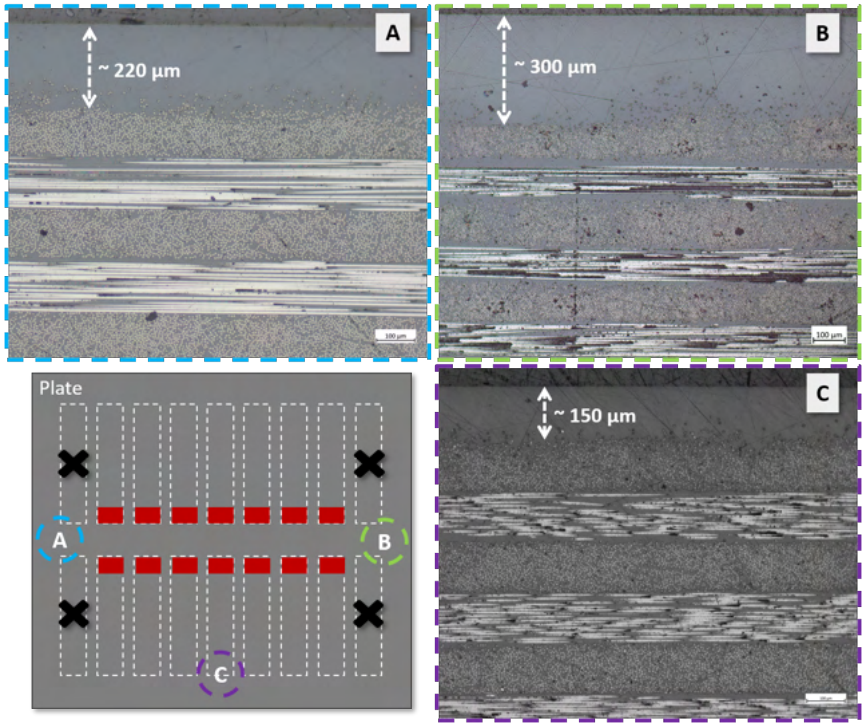

Figure 2.20: Energy director thickness measurement at different locations of the plates

2.4 Ultrasonic welding device

2.4.1 Welder modules

The welder used for this study is an Electrical Motion 20 from the supplier Rinco Ultrasonics. The device is fully electrical controlled with a maximum applicable load of 3000 N. Its installation requires only an electrical outlet. It is made of the following modules:

- A frequency generator,
- A converter,
- An amplifier,
- A titanium sonotrode,
- A clamping jaw.

The device is shown in Fig. 2.21 with the different modules. The generator creates an electrical wave with an operating frequency of 20 kHz. The converter transforms this electric energy into mechanical energy. The amplifier, or booster, increases the amplitude of the mechanical vibration. The titanium-based sonotrode vibrates along the z-axis and comes into contact with the specimens to be welded. Finally, a clamping jaw holds the specimens. A column allows the sonotrode to be moved vertically with a maximum stroke of 100 mm. A lubrification operation of the column is required by the device every time the device is switched on. Every command is operated from the touch-screen monitor.

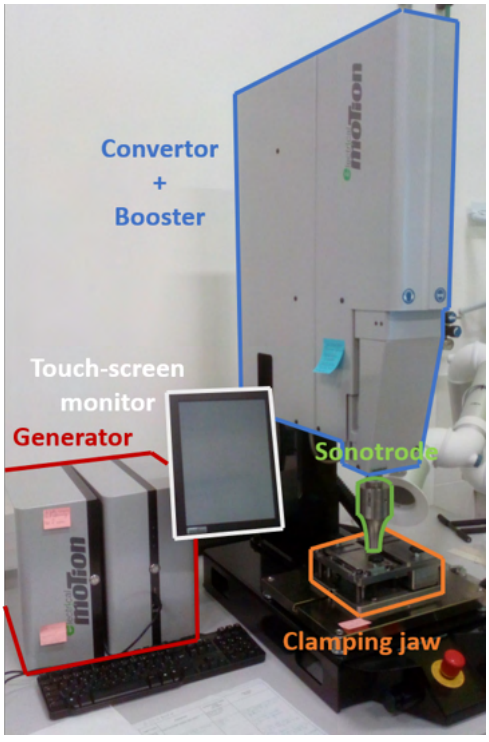

Figure 2.21: Electrical Motion 20 (Rinco Ultrasonics) ultrasonic welding equipment

The clamping jaw designed by Lauak Group is shown in Fig. 2.22. It was designed and manufactured in order to get single lap shear welded joints. The lower specimen is set up first and cannot move during welding. The upper specimen is then set up. The strings allow the upper specimen to go down when the energy director starts melting. They also make sure that the upper and lower specimens are always parallel. Indeed, without this descent, the specimens would no longer be parallel to each other, as seen in Fig. 2.23. It could induce residual stresses, impacting negatively the mechanical properties. A torque wrench is used to tighten the tooling nuts to 0.8 Nm and ensure assembly's better repeatability.

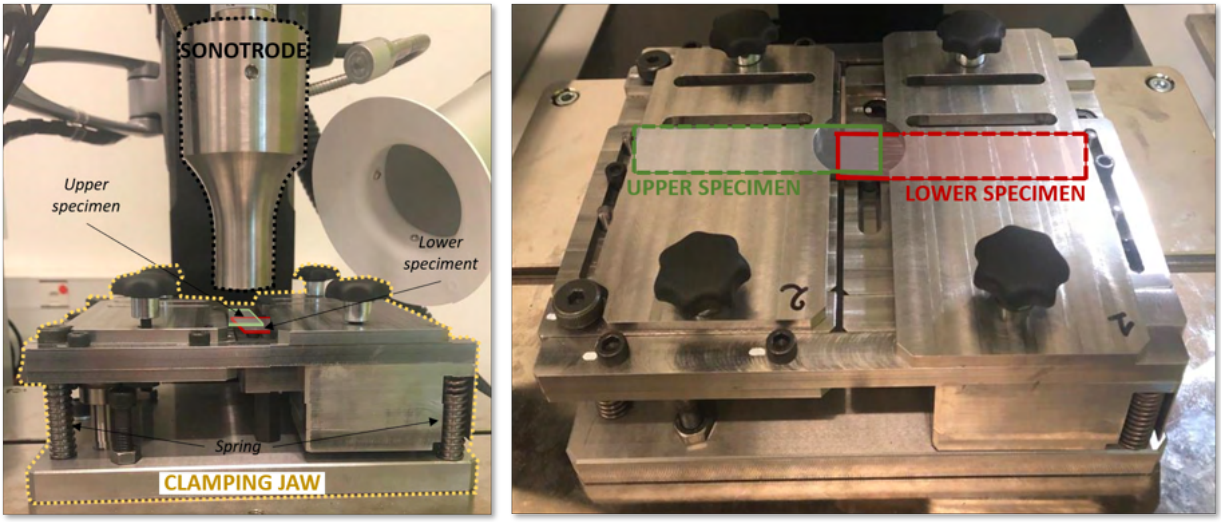

Figure 2.22: Clamping jaw of the welding specimens

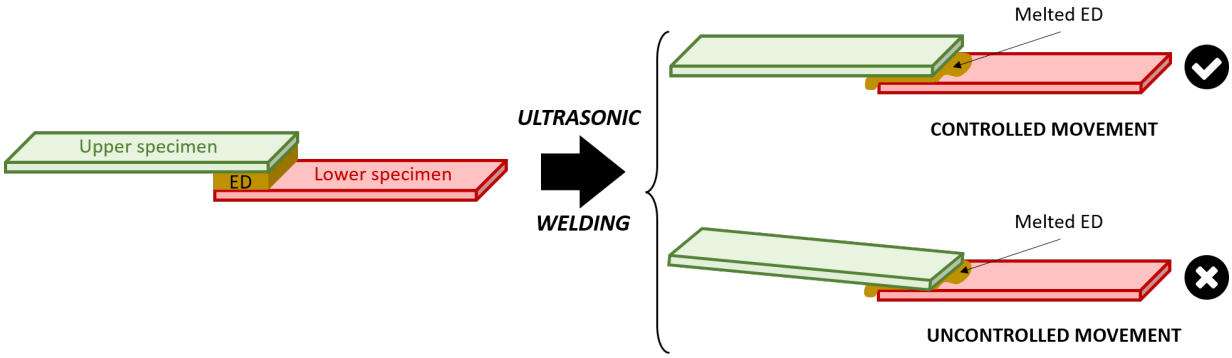

Figure 2.23: Movement of the upper specimen due to the melting of the ED during welding

2.4.2 Welding parameters

A parameter menu is available on the touch-screen monitor to define welding parameter conditions. Three steps need to be defined, as presented in Fig. 2.24. The first step indicates when the ultrasonic signal will be triggered. The second step is related to the welding conditions, *i.e.* the vibration shutdown condition is defined prior welding. Finally, a cooling stage is programmed after the end of the vibrations in step 3.

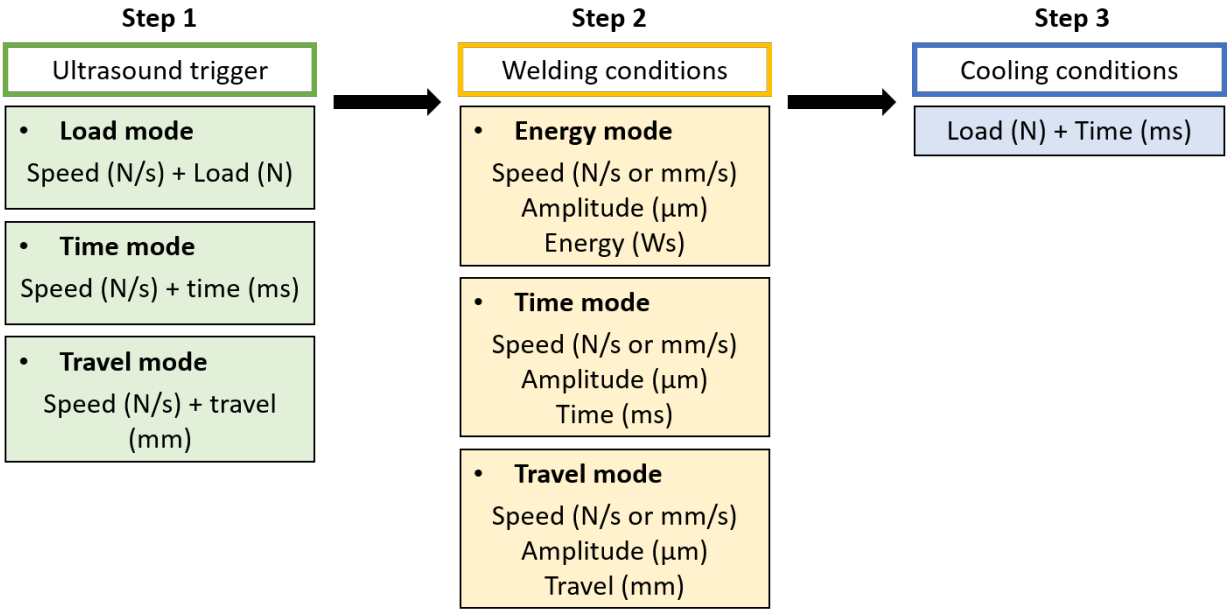

Figure 2.24: Input parameters of the welding device

Considering step 1, three triggering modes are available: load, time and travel modes. As a reminder, the travel measured by the device is the vertical displacement of the sonotrode during welding. The sonotrode goes up or down to match polymer swelling or flow, and to maintain a constant welding load all along welding time. The displacement can be absolute (*i.e.* the sonotrode position along the 100 mm height column) or differential (*i.e.* the difference between the sonotrode position at the beginning of the test and the sonotrode position at a given moment). A displacement speed of the column is also defined at 100 $N.s^{-1}$ to establish a contact between the sonotrode and the upper specimen. The ultrasounds start when the trigger value (load, time or displacement) is reached. In the case of this study, the load mode is chosen for this step.

For step 2, energy, time or travel define the duration of the vibrations. It means that when the input energy, time or displacement value is reached, the sonotrode stops vi-

brating. Also, a descent rate and amplitude values of the sonotrode have to be defined. For this thesis, all welds are made with no vertical movement of the column during this step, the speed load is set to zero. Most studies about ultrasonic welding of TC composites have used a displacement-controlled mode to set the end of the vibration phase [Fernandez Villegas and Palardy, 2017, Villegas, 2014, Palardy and Fernandez Villegas, 2017, Fernandez Villegas and Vizcaino Rubio, 2015]. Due to the scattered thicknesses of the energy director, it has been decided that this mode is not the best suited for our study. Therefore, a time-controlled mode is selected.

Finally, a holding load and a holding time have to be defined in the cooling step, step 3. The holding load is equal to the welding load and applied for 2500 ms.

In the following of this dissertation, the **welding load**, the **vibration amplitude** and the **welding time** are investigated. To sum up, the welding load is defined in step 1, and the vibration amplitude and the welding time are both defined in step 2.

2.4.3 Typical curves from the device output parameters

During ultrasonic welding, output data are registered by the welder control system all along each welding experiment, such as welding load, electrical power and sonotrode displacement. Welding load is a test set up parameter but its measurement allows a control of this value during welding. As seen in Benatar's and Villegas's works [Villegas, 2015, Benatar and Gutowski, 1989] (detailed in Chapter 1, Section 1.3.1), power and travel (*i.e.* displacement of the sonotrode) data are used to understand the physical structure evolution of the material during the experiment and five stages can be defined.

While maintaining a constant load of 500 N during the duration of the ultrasonic impulsion, it can be seen in Fig. 2.25 that the sonotrode moves slightly upward during stage 1 until reaching a maximum after 300 ms. This can be associated with the heating mechanism of thermoplastics (TP), that prone to expand when reaching melting or softening in the case of amorphous TP. It can also be noticed that the power curve exhibits a step rise during this heating phase of the polymer until reaching a peak at the same time as travel direction changes. According to Villegas [Villegas, 2015], the decrease of both travel and power curves in stage 2 is associated with the local melting of the energy director and in our case, with the beginning of local softening of the PEI.

A second power rise is noticed in stage 3, which is related to the squeeze flow of PEI. Right after this second peak, the welding load curve shows that it is difficult to maintain

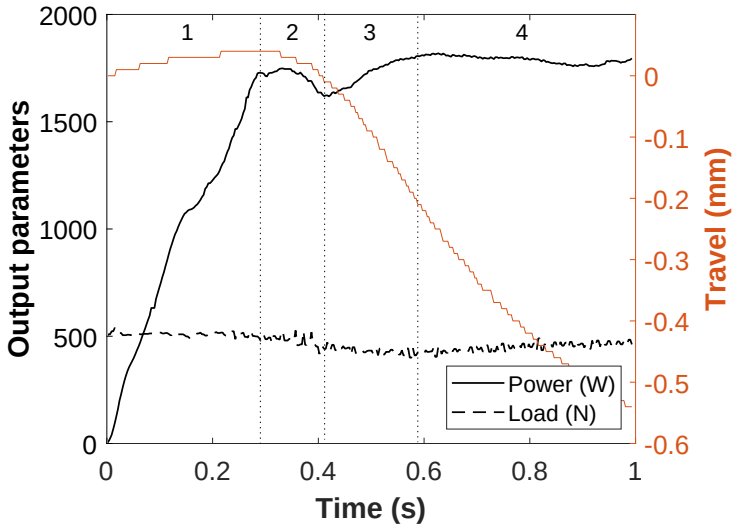

Figure 2.25: Typical power, load and displacement curves during ultrasonic welding of CF/PEEK + PEI specimens for a amplitude of 32 μm, a welding load of 500 N and a welding time of 1000 ms

its value at 500 N. We assume that high squeeze flow happens at the interface, forcing the sonotrode to go down to keep the 500 N welding load value. After reaching this second peak, the power curve reaches a plateau in stage 4, indicating that squeeze flow of PEI occurs and that PEEK starts melting. Villegas et al. [Villegas, 2015] explained this plateau by a competition between the squeeze flow of the energy director and the local melting of the resin.

2.5 Conclusion

This chapter aims to define the different material preparation in order to get welding specimens. The first section presents PEEK and AE 250 polymers and pregs. A second section focuses on the manufacturing of welding specimens, from preg to plates and their characterization. It has been shown that the polymer-rich layer thickness is not homogeneous along with the welding substrates.

The ultrasonic welding device is presented as well as the different modules and welding parameters. Welding time, welding load and vibration amplitude are the three welding parameters investigated in the following chapters. Finally, output data from the welder,

such as displacement of the sonotrode and the dissipated power, can be used to determine physical changes during welding.

Chapter 3

Rheological and crystallization behaviors of PAEK

Contents

3.1 Introduction 70

3.2 Thermal properties of AE 250 and PEEK 70

3.2.1 Thermal stability 70

3.2.2 Effect of cooling rate on thermal transition 72

3.3 Rheological characterization of AE 250 and PEEK 77

3.3.1 Effect of time on complex viscosity 77

3.3.2 Effect of temperature on complex viscosity 78

3.4 Calculation of relaxation times 84

3.4.1 Definition of η_0 84

3.4.2 Definition of J_e^0 85

3.4.3 Calculation of the molecular weigth between entanglement 88

3.4.4 Comparison to other PAEK 89

3.5 Conclusion 90

3.1 Introduction

This chapter focuses on the evaluation of thermal and rheological behaviors of PAEK AE 250 and PEEK matrices. After checking the thermal stability of the polymers in their melted state, the study focuses on the crystallization kinetics to compare AE 250 to well-known PEEK 450G. Then, relaxation times and morphological parameters are obtained from rheological characterization. The results are compared with other usual PAEK such as PEEK and PEKK from data available in the literature. The aim is to predict the diffusion time and the crystallization during welding. Some of these results have been published in Journal of Applied Polymer Science [Bonmatin et al., 2021].

3.2 Thermal properties of AE 250 and PEEK

3.2.1 Thermal stability

Poly(aryl ether ketone)s are sensitive to thermo-oxydative environments. Indeed, the environmental condition affects the material response, especially in the melting state [Avenet, 2018]. Moreover, Day et al. [Day et al., 1990b, Day et al., 1990a] has shown the leading decomposition mechanism of PEEK starts with the molecular chain scission of the ether bonds. It is followed by the hydrogen abstraction of the neighbouring polymeric chains which leads to stable phenolic end groups. The reaction ends with the cleavage of the latter. It implicates the creation of chemical species which are able to form phenol, the major product from pyrolyse reaction. The degradation of PAEK initially induces viscosity increase followed by a weight loss. Thus, it is necessary to evaluate the thermal stability considering the weight loss in a range of temperatures that will be used for processing AE 250 and PEEK. Fig. 3.1 presents the results for AE 250. As a reminder, FM stands for films.

The evolution of dried FM under high temperature conditions is evaluated through isothermal experiments on a TGA 2 Mettler Toledo device. Samples are between 5 and 15 mg. Fig. 3.1 (a) shows the weight variation of FM for two isothermal conditions: 320 °C and 350 $°C$ under inert and oxidizing atmospheres for 2 hours at 50 $mL.min^{-1}$. From the four curves, it is established that the atmosphere has a very little influence on the weight loss of AE 250 after 2 hours. At 320 $°C$, the weight loss is considered insignificant. At 350 $°C$, there is a slight difference (lower than 0.2 %) of the weight loss between air and

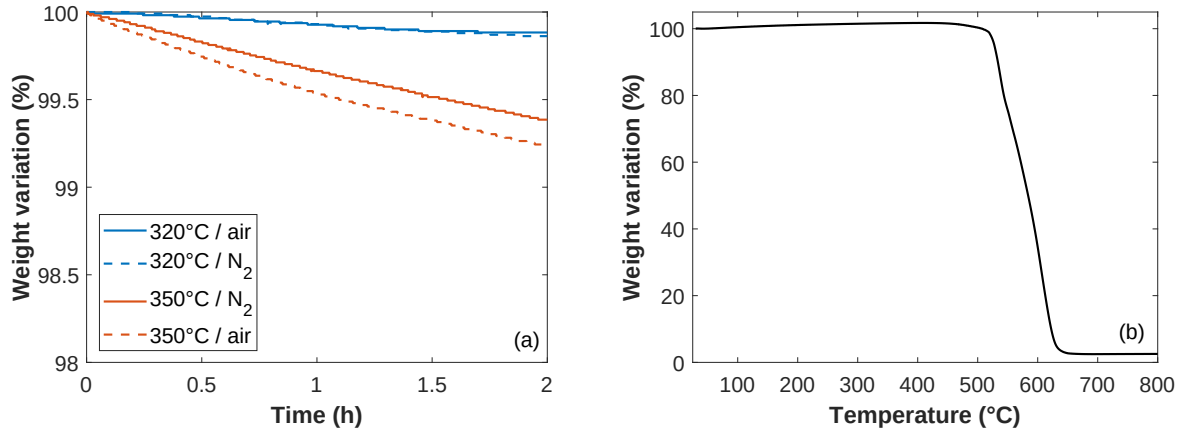

Figure 3.1: TGA curves of PAEK AE 250 FM at two isothermal conditions (320 °C and 350 °C) under inert (N_2) and oxidizing (air) atmospheres (a) & TGA curve of FM from 30 °C to 800 °C at 2 °$C.min^{-1}$ in an inert atmosphere (b)

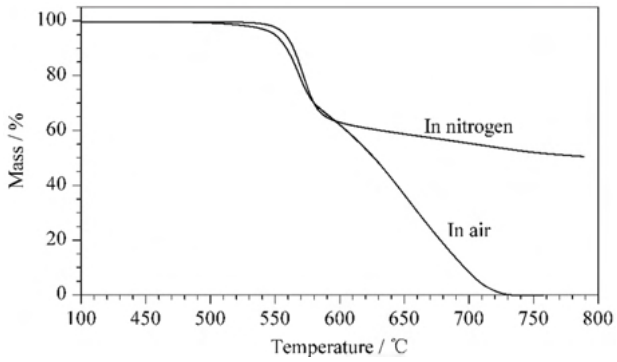

Figure 3.2: TGA curves of PEEK in nitrogen and air atmospheres [Shabaev et al., 2018]

nitrogen atmosphere testing. As expected, the degradation kinetics is faster under oxygen, due to the combination of oxydative reaction to thermal effect. Furthermore, for each test, the weight loss is at most 0.6 %. It is usually admit that of weight loss degradation starts for a weight loss above 5 %. Therefore, it is considered that there is no weight loss degradation, no matter the atmospheric conditions. Nevertheless, the absence of structural change is not excluded, as other techniques could reveal a degradation occuring by cross-linking and molecular re-organization without weight loss, such as rheometry for example [Mylläri et al., 2015, White et al., 2013]. To go further, Fig. 3.1 (b) presents the weight variation for a dynamical test between 30 °C and 800 °C at 2 °$C.min^{-1}$. It indicates that the degradation, considered when the weight loss is 5 %, starts at 573 °C for this test condition. Shabaev et al. [Shabaev et al., 2018] demonstrated that the degradation

of PEEK starts at around 550 $°C$, whether under air or inert atmosphere. The stability of AE 250 is thus similar to PEEK since the degradation phenomenon starts around the same temperature. PEEK TGA degradation curves are shown in Fig. 3.2. It can be seen that PEEK does not lose its entire mass after degradation, which is different from AE 250. Finally, the stability shown in Fig. 3.1 validates the use of AE 250 for further experiments at temperatures between 300 $°C$ and 400 $°C$ for a few minutes.

3.2.2 Effect of cooling rate on thermal transition

Crystallinity and thermal transitions have a strong impact on the mechanical properties of a polymer. As an illustration, the elastic modulus of amorphous PEEK at room temperature is 2 GPa whereas those of PEEK that reached its maximum crystallinity (around 40 %) is 3 GPa with a change in maximum strain at break [Martineau et al., 2016]. PEEK is known for its high melting temperature of 343 $°C$ which requires specific equipments for processing it and, therefore, a significant amount of energy input. This is why this new PAEK polymer is of great interest, it could facilitate the processing due to its lower melting temperature. Whereas PEEK has been intensively studied since the 80s, AE 250 requires a wide characterization to know and understand its behavior. In this section, the thermal behavior of FM, FL and FLc were studied via DSC analysis. As a reminder, FM and FL are the dried PAEK used as received whereas FLc undergone hot press cycles which could affect the polymer structure and thus its properties.

The effect of cooling rate on thermal transitions and enthalpy are determined using a Perkin Elmer Differential Scanning Calorimeter 8000. After heating at 360 °C to cancel the thermomechanical history, cooling rates at 2, 5, 10, 20, 50, 100 $°C.min^{-1}$ are applied under a nitrogen flow rate of 20 $mL.min^{-1}$ until reaching the glass transition temperature. The aim is to compare the structure of FM, FL, and FLc without taking into account their processing conditions. Finally, a second heating at 20 $°C.min^{-1}$ is undertaken from 80 to 360 $°C$ to measure thermal transitions. Each test is repeated at least 3 times. Crystallinity, χ_c, is determined using the following equation:

$$\chi_c = \frac{\Delta H_m - \Delta H_c}{\Delta H_\infty} \tag{3.1}$$

where ΔH_m and ΔH_c are the melting and cold crystallization enthalpies. ΔH_∞ is the theoretical enthalpy if the polymer was completely crystalline. The value is not available for AE 250. Therefore, the value of PEEK $\Delta H_\infty = 130\ J.g^{-1}$ was used. This adds uncertainty in the determination of χ_c but other authors have chosen this value as well

[Audoit et al., 2018], identically for PEKK whose ΔH_∞ is undetermined until now [Choupin et al., 2019].

Fig. 3.3 shows the first heating of the DSC analysis for the three shapes of samples. For each shape, the experiment was conducted at least 4 times. FM displays a glass transition at 157 $°C$, a cold crystallization temperature at 220 $°C$ and a melting temperature at 300 $°C$ with smooth results. The cold crystallization is probably due to the fast cooling during the film-making process, which led to an amorphous polymer. On the contrary, the curve of FL presents some discrepancies, especially with the presence of small peaks all over the temperature range. As a result of the wide range of sizes and shapes in the same batch of flakes, the contact area of the sample within the pan can change during the DSC measurements, specially when the polymer melts. Even before melting, the flakes can move when heated, affecting the data and altering the straightness of the curve. FLc first heating curve shows nonetheless less discrepancy than FL which implies that the compaction has a positive effect on DSC thermograms. The curves are more accurate and exhibit less undesired variations.

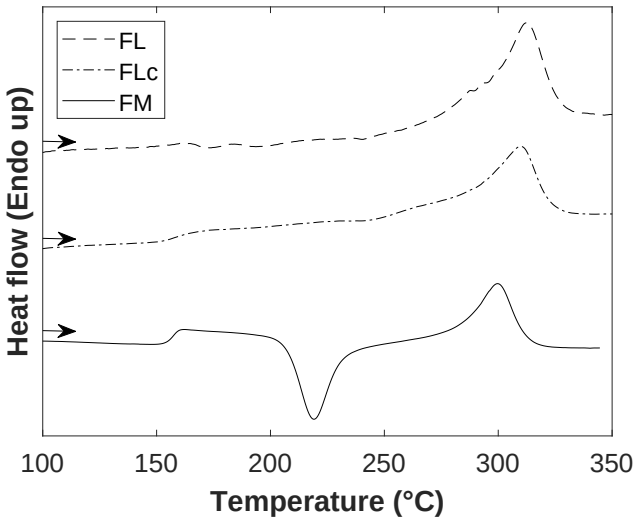

Figure 3.3: DSC curves of FM, FL and FLc for heating rate of 20 $°C.min^{-1}$

Despite the irregulary of the curves, the average of the melting temperature, glass transition temperature and enthalpies were calculated and presented in Table 3.1. Melting temperatures of FM, FL and FLc are lower than PEEK which aims to improve the processability of AE 250 compared to PEEK. The melting and crystallization temperatures correspond to the maximum of the peaks. The melting temperature of flakes (FL and FLc) is higher compared to those of films of about 10 $°C$. This difference could be

explained by the incorporation of small amount of additives in the formulation, the latter hinder or facilitate the crystallization by changing the free volume within the polymeric chains. Another hypothesis is the difference in molecular weights, polydispersity and chemical structure. The flakes do not show a cold crystallization, due to their processing: they have been slowly cooled down to allow the polymer to crystallize at most. Still in the case of flakes, the glass transition is not visible and, therefore, it is not reported in the Table. It can also be seen from the Table 3.1 that FL has a higher crystallinity, at 25 %, than compressed flakes at 19 %. An assumption is that the samples were cooled too fast during the elaboration of our samples by compression molding. Another hypothesis is linked to the structural evolution of AE 250 during the compression step. As explained in Section 3.2.1, a viscosity increase occurs before degradation. It stems from chain expansion comparable to cross-linking. The longer chains are less prone to crystallization. Finally, FM, FL and FLc feature a melting temperature significantly lower than PEEK 450G, about 40 $°C$, while keeping a glass transition in the same range. These results have a positive influence on the processing of PAEK AE 250 since it can be formed at lower temperatures.

	T_g $(°C)$ $\pm$ 2	T_{cc} $(°C)$ $\pm$ 2	T_m $(°C)$ $\pm$ 2	ΔH_{cc} $(J.g^{-1})$ $\pm$ 0.1	ΔH_f $(J.g^{-1})$ $\pm$ 0.1	χ_c $(\%)$ $\pm$ 0.2
FM	157	220	300	-22.7	22.0	0.6
FL	-	-	312	-	32.7	25.1
FLc	155	-	308	-	24.8	19.1
PEEK 450G	143	-	343	-	-	-

Table 3.1: Average thermal transitions and enthalpies for FM and FL and FLc

Fig. 3.4 (a) shows the cooling curves of FM. As expected, the crystallization is shifted towards lower temperatures when the cooling rate increases. As seen in Fig. 3.4 (c) and 3.4 (e), the same trend is noticeable for FL and FLc. This delay stems from both the inertia necessary for the chains to crystallize and the low thermal conductivity of the polymers, about 0.3 $W.m^{-1}.K^{-1}$ [Chen et al., 2016]. Moreover, the crystallization depends on the cooling rate, explaining why the area under the peak seems smaller when the cooling rate decreases. However, the cooling speed is taken into account for the calculation of the enthalpy. Crystallization and melting DSC peaks are associated with a population of crystallites with their own thickness [Velisaris and Seferis, 1986]. Fig. 3.4 (a) reveals crystallization peaks corresponding to large lamellae since it was shown by Doumeng et al. that the lamellae thickness of PEEK is 4.21 nm [Doumeng et al., 2022].

The second heatings of the same samples are presented in Fig. 3.4 (b) for FM, Fig.

3.4 (d) for FL and 3.4 (f) for FLc. From this data, the enthalpies and melting temperatures were calculated to evaluate the influence of cooling rate. Indeed, the DSC device is not calibrated on cooling, so the crystallization enthalpy is not reliable. The enthalpy must be evaluated from heating only, that is why a following heating run was carried out right after. For PEEK, an annealing or slow crystallization is necessary in order to allow the entire crystalline phase to crystallize [Ko and Woo, 1996]. It can be seen that a second crystalline peak appears at low cooling rate (from 20 $°C.min^{-1}$ to 2 $°C.min^{-1}$). The origin of this double-melting behavior is controversial and has been explained with different interpretations [Jiang et al., 2019]. An explaination could be the apparition of a second crystalline phase, as suggested by Ko et al. [Ko and Woo, 1996], implying that the morphology of AE 250 must be similar to those of PEEK. The primary cristallization of PEEK is really fast, around few seconds whereas the secondary crystallization is slower, corresponding to secondary lamellae growing between the primary lamellae. This is why this second crystalline peak becomes more intense at slow cooling rate.

Finally, melting enthalpies from the second heating were assessed and the crystallinities are presented in Fig. 3.5 (a). As expected for all samples, the highest crystallinity is obtained at low cooling speed. A low cooling rate allows a longer time for the macromolecular chains to self-organize into an ordered phase. The crystallinity of PEEK for a cooling rate of 30 $°C.min^{-1}$ is 33 %, which is higher than AE 250 at any cooling rate. A slight decrease of the crystallinity from 2 $°C.min^{-1}$ to 50 $°C.min^{-1}$ is also noticed. After 50 $°C.min^{-1}$, the crystallinity tends to stabilize to a threshold. The DSC device used in this study has a limited cooling rate of 100 $°C.min^{-1}$, this explains why there is no higher cooling rate analyzed. If higher cooling rates were investigated, it can be assumed that the polymer could reach an amorphous state as seen for FM, which is amorphous. However, this threshold is not observed for FL and FLc because of the large scattering of the results. This phenomenon is associated with the structure of flakes. They probably contain additives which can alter the crystallization and contribute to the scattered results. However, the maximum crystallinity obtained is around 30 %. Due to fast crystallization, mastering the crystallization rate of PEEK is a hard task. When processing PEEK from the glassy state, it has been demonstrated that there are two levels of crystallization for PEEK 450G, identified as amorphous, or low level, and a fully crystallized level [Doumeng et al., 2021]. At the first level, refered as low one, the rate is around 15 %. The second level of crystallinity is around 35% from glassy state. Intermediate crystallization rates are difficult to get because of fast crystallization. Thus, mastering the properties of PEEK products is challenging. A slower crystallization such as in PAEK AE 250 is thereby of great interest. The crystallization can be more easily controlled and the polymer can be

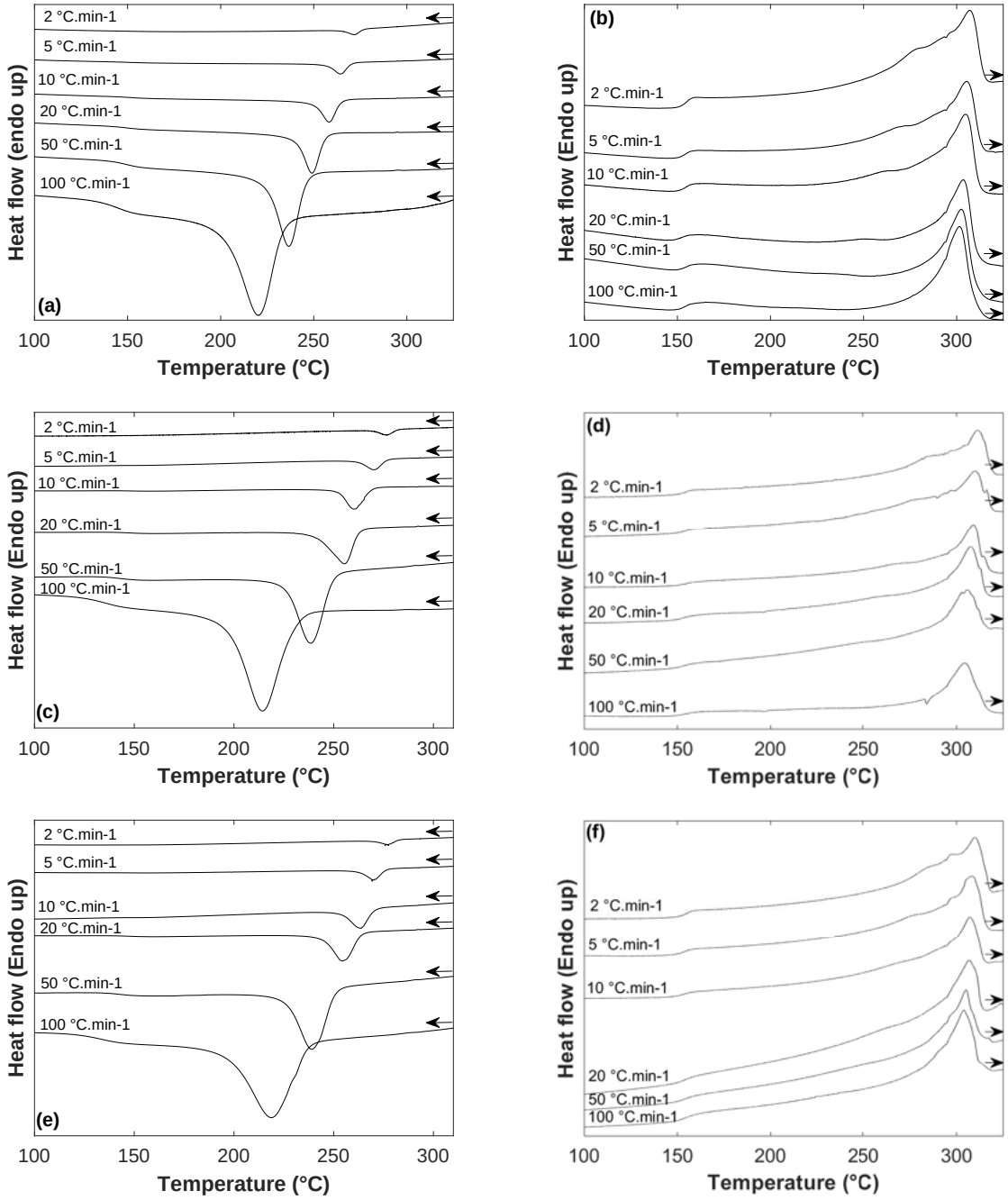

Figure 3.4: DSC curves of the cooling stage of FM (a), FL (c) and FLc (e) & the 2^{nd} heating of FM (b), FL (d) and FLc (f)

turned amorphous, such as FM, and thus transparent which is useful for some applications such as laser welding. Moreover, Martineau et al. [Martineau et al., 2019] studied

the autohesion, also called self-bonding, of PEEK and brought to light the competition between the diffusion of the macromolecular chains and the crystallization growth during cooling. To create a strong bond between two surfaces, the chains need to diffuse at the interface and later crystallize. However, if the crystallization process is too fast, it hinders the diffusion mechanism.

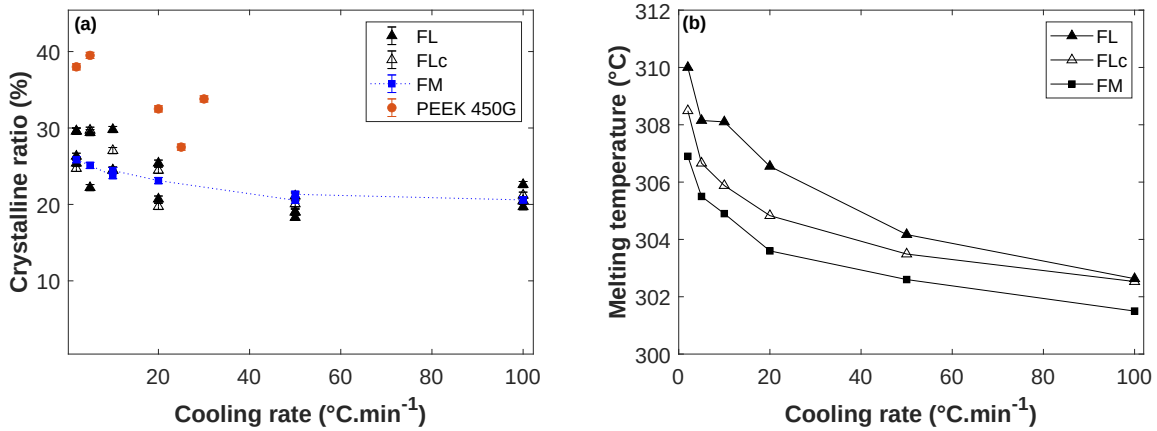

Figure 3.5: Influence of cooling rate on crystallinity (a) and melting temperature (b) with an absolute incertainty of measurement of 2 $°C$ for the melting temperature

The second heating curves also point out the impact of cooling rate on melting temperature, as shown in Fig. 3.5 (b). Only the melting point of the primary crystallization is taken into consideration for the Fig. 3.5.b. T_m decreases with the increase of the cooling rate for the three shapes. FM have the lowest melting temperatures in the entire range range of cooling rate and the highest ones are for FL as already outlined in the first heating curves.

3.3 Rheological characterization of AE 250 and PEEK

3.3.1 Effect of time on complex viscosity

Rheological behavior was investigated using a HAAKE MARS Rheometer by Thermofisher. The experiments are carried out using a 25 mm diameter parallel-plate configuration with a 2 mm gap, under argon atmosphere. Time sweeps have been performed to check the thermal stability of the polymer along the experiment. Despite a slight degradation revealed

by TGA in the previous section, time sweeps give an insight on the structural evolution of macromolecules. The curves are provided in Fig. 3.6 (a) and (b).

Rosa et al. [Rosa et al., 2016] plotted the storage modulus, G', as a function of time, in Fig. 3.6 (a) because it is sensitive to structural changes due to high temperatures and environmental conditions. They observed that at 370 $°C$, PEEK modulus is increasing after less than 4 minutes if under air atmosphere. However, under nitrogen atmosphere, PEEK modulus stays stable for at least 15 minutes at 370 $°C$, which is sufficient for frequency sweeps in the following of this chapter. In the case of AE 250 in Fig. 3.6 (b), the complex viscosity is evaluated. The complex viscosity η^* is given by the following equation, with ω the angular frequency:

$$|\eta^*| = \frac{\sqrt{G'^2 + G''^2}}{\omega} \tag{3.2}$$

where G' and G'' are respectively the conservtive and the loss moduli. η^* of FMc slowly increases with time. At 330 $°C$, it goes from 1600 to 1750 $Pa.s$, an increase of 9 %. At 390 $°C$, η^* goes from 750 to 900 $Pa.s$, an increase of 20 %. Time sweeps confirm that structural changes occur during the experiments, but it is assume that these changes are small enough to not influence nor this analysis neither conclusive remarks. Indeed, the values in the terminal regime are not considered for calculation of the relaxation times in the next sections: G' and G'' are extrapolated from the curves at higher frequencies, meaning the 10 first minutes of the frequency sweeps.

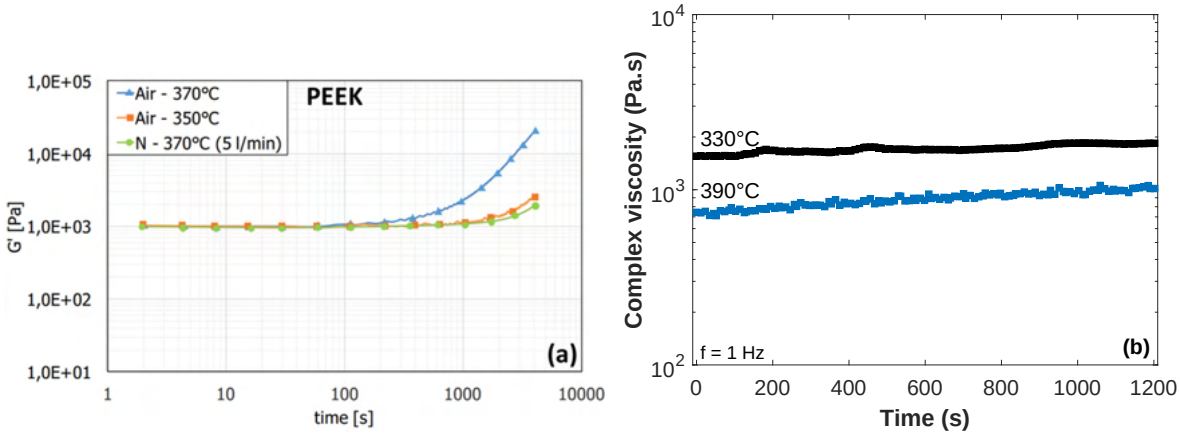

Figure 3.6: Storage modulus of PEEK for a 0.5 % strain and 1 $rad.s^{-1}$ at 350 $°C$ and 370 $°C$ [Rosa et al., 2016] (a) and complex viscosity of FMc for a 0.1 % strain and 1 Hz at 330 $°C$ and 390 $°C$ (b)

3.3.2 Effect of temperature on complex viscosity

The rheological tests were performed in isothermal conditions, at temperatures chosen right after the end of the melting peak of AE 250, while preventing its degradation at highest temperatures. All commercial PAEK are linear polymers as they are polymerized from bifunctional monomers. PAEK AE 250 is a linear polymer as described in the patent from Victrex (GB 2543362) [Glynn et al., 2017]: '*A polymer material, such as polyaryletherketone (PAEK) having a repeat unit of formula (I) $-O-R1-O-R3-$ and a repeat unit of formula (II) $-O-R2-O-R3-$ wherein R1 and R2 are different*'. The patent lists all the possible monomers, they are all bifunctional ones. Moreover, the chemical reaction is explained as '*polycondensation of two different di-hydroxy-containing compounds with one or more dihalogenated compounds*'. And these dihalogenated compounds are described as fluorine atoms, in the patent. It means that the condensation is a nucleophilic substitution, with the fluor attracting the labile H of the other monomer. The same reaction is carried out to synthetize PEEK from different monomers. This chemical reaction does lead to linear polymers.

Thus, to prevent the structural evolution, a new disk-shape sample was step up on the plate of the rheometer for each experiment. For the same reason, the frequency sweeps start at 628 s^{-1} for which the points are recorded fast, up to the low frequencies. Each sample ungergoes a fast temperature rise until reaching the targeted temperature (330 $°C$, 350 $°C$, 370 $°C$ or 390 $°C$). First, strain sweeps define the linear viscoelastic regime and characterize the strain dependent viscoelastic properties of the samples. The results are shown in Fig. 3.7. G' and G'' are respectively the conservative and loss moduli. The modulus G'' is always higher than G' in the studied domain, which indicates a liquid-like behavior as expected for molten polymers. G' and G'' exhibit a pronounced non-linear region at high strain amplitudes and tend towards a plateau at low strain amplitudes.

Then, dynamic frequency sweeps from 628 s^{-1} to 6.28 s^{-1} were carried out in order to quantify the conservative and loss moduli, G' and G'', from which the complex viscosity η^* is calculated. Conservative and loss viscosity, real and imaginary components of the complex viscosity, respectively η' and η'', depend on complex moduli and angular frequency according to:

$$\eta' = \frac{G''}{\omega} \tag{3.3}$$

$$\eta'' = \frac{G'}{\omega} \tag{3.4}$$

The experiments are conducted as a function of the frequency f, which depends on the

angular frequency of a factor 2π, $w = 2\pi f$. A dynamic test at ω is equivalent to a transient experiment for a duration $t = 1/\omega$ according to the Cox-Merck principle [Cox and Merz, 1958]. Thus, the relaxation times will be given as the inverse of the ω values.

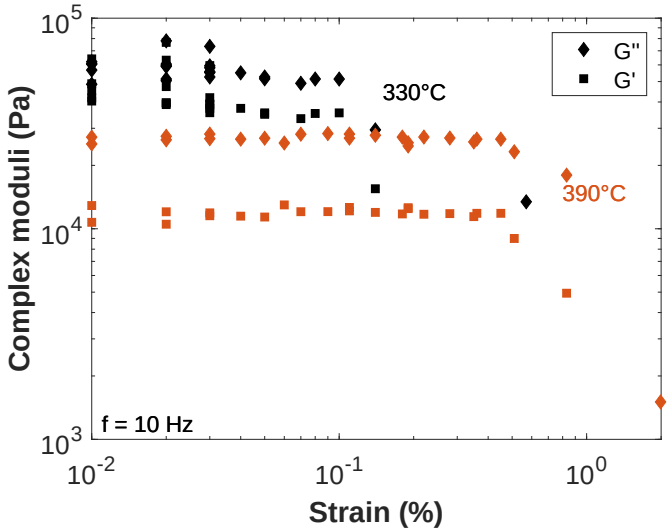

Figure 3.7: Strain sweep of the complex viscosity of FMc for a frequency of 1 Hz at 330 $°C$ and 390 $°C$

G' and G'' for each temperature are presented in Fig. 3.8. Both moduli present a temperature dependency since they regularly decrease with an increase of temperature. According to the Rouse model, the moduli follow the rule of $G' = G\omega^2\tau^2$ and $G'' = G\omega\tau$. So, the slopes of $log\ G'$ and $log\ G''$ are supposed to be of, respectively, 2 and 1 in the terminal region at low shear rate. As seen in Fig. 3.8, the Rouse model fails as predicting the behavior in the terminal regime. Indeed, the angular frequency dependency is $\omega^{1.04}$ and $\omega^{0.92}$ respectively for G' and G'' for FLc and $\omega^{1.11}$ and $\omega^{0.89}$ for FMc. Some data are available in the literature for PEEK grades only. For instance, a dependency of $\omega^{1.81}$ and $\omega^{0.99}$ is found by Bangarusampath et al. [Bangarusampath et al., 2009] for a Victrex PEEK 151. In Garcia-Leiner'work [Garcia-Leiner et al., 2017], the slopes are 1.54 and 0.91 for G' and G'' respectively for a PEEK Ketaspire KT-820NT and 1 and 0.75 for G' and G'' respectively for PEEK Victrex 450G. This deviation from the theoretical behavior is attributed to the evolution of the macromolecular structure during the experiment. Seo et al. [Seo et al., 2020] displays the expected shapes of G' and G'' curves for PEEK 450G by using Time Temperature Superposition (TTS) on data obtained at higher frequencies, for which the acquisition time at 350 °C is shorter enough to prevent structural changes.

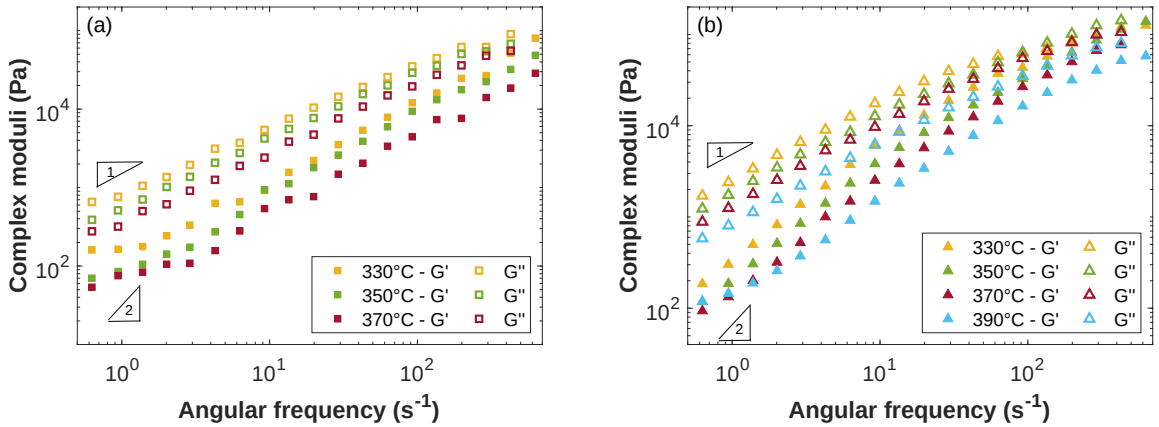

Figure 3.8: G' and G'' for FLc (a) and FMc (b)

PAEK AE 250 has initially a linear structure evolving towards a partially cross-linked system. Indeed, all PAEK are sensitive to thermo-oxidative degradation due to their chemical structure. From the previous studies of Day [Day et al., 1990b, Day et al., 1988] on the degradation mechanisms of PEEK, it is known that when PEEK is kept above 340°C in oxidative conditions, chain cleavage occurs adjacent to the carbonyl functional groups and subsequent hydrogen abstraction from the aromatic ring then leads to crosslinking between adjacent aryl rings. This recombination causes a color change, a dramatic increase of its shear viscosity and a reduction in the crystallizability of the material. The decomposition of this PAEK AE 250 has not been studied yet, but it could follow the same degradation mechanism, as its chemical structure is close to those of PEEK. The main concern is the cross-linking kinetics. From the time sweeps performed, it is clear that the cross-linking starts as soon as the polymer is exposed to temperature above its melting temperature.

Time Temperature Superposition (TTS) was applied on previous data and shift factors, a_T, were identified from G' and G'' moduli, for each temperature by horizontally shifting their curves. Between 6.28 s^{-1} and 62.8 s^{-1}, the time-temperature superposition gives good results, which confirms that this polymer follows more or less the expected behavior for melted polymers. However, below 6.28 s^{-1}, it becomes harder to match the different curves, especially for FLc. When comparing both master curves obtained for FL and FM in Fig. 3.9, the cross-over point is shifted towards low frequencies for FM, this indicates that the molecular weight for FM would be higher than those of FL [Wang et al., 1993].

Master curves of the complex viscosities of FMc and FLc are displayed in Fig. 3.10. They were calculated in both cases at a reference temperature of 330 $°C$. The curves exhibit a pseudo-Newtonian plateau in the range 0.628 s^{-1} to 62.8 s^{-1} and a shear-thinning region

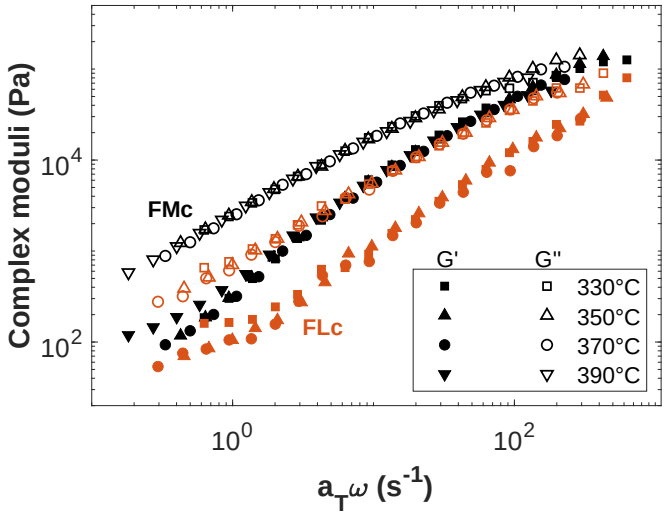

Figure 3.9: Master curves of G' and G'' for FLc and FMc with the reference temperature at 330 $°C$

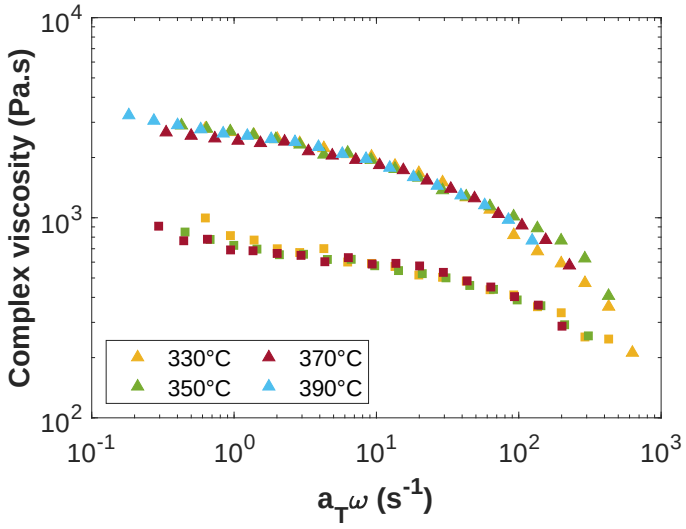

Figure 3.10: Master curves of the complex viscosity for FLc (-□-) and FMc (-△-) with the reference temperature of 330 $°C$

above 6.28 s^{-1}, following the well-known flow curve for melted polymers. The complex viscosity at the plateau is called the zero-shear viscosity, η_0. The zero-shear viscosity strongly depends on molecular weight: above a critical mass noted Mc, the zero-shear viscosity depends linearly on molecular weight whereas above Mc, it is supposed to rise

with $M^{3.4}$ [Berry and Fox, 1968]. Again, the complex viscosity for FM is higher than those for FL. It corroborates the idea that the molecular weight is higher for FM compared to FL. In both cases, the complex viscosity slightly rises at the lowest angular frequencies. The behavior at low frequencies is not classical since a plateau would be extend up to the zero-shear viscosity. Again, this is attributed to the evolution of the structure upon cross-linking of chains during degradation [Day et al., 1990b] as it was shown by Bakrani et al. [Shahriar et al., 2017] in viscosity curves for PEEK 450G. This phenomenon could explain the divergence in the shifting at low frequencies and the fact that no weight loss was observed by TGA analysis, *i.e.* a structural degradation without weight loss and possibly other phenomenons that are yet to be understood.

Shift factors of TTS are plotted in Fig. 3.11 for FLc and FMc. The data agree with the Arrhenius law as following :

$$ln(a_T) = A - \frac{E_a}{RT} \tag{3.5}$$

where E_a is the activation energy, R is the gas constant and T the temperature. The activation energies for FLc and FMc are, respectively, 61 $kJ.mol^{-1}$ and 66 $kJ.mol^{-1}$. The values of E_a are considered as identical regarding the uncertainty. The data found by other researchers are reported in Table 3.2. The activation energy of AE 250 is higher than E_a for PEEK 151G and lower than E_a for PEEK 450G and PEKK 6003 and PEKK 7003. This implies that AE 250 requires less energy to flow in the melted state than PEEK 450G and PEKK 6003 and PEKK 7003.

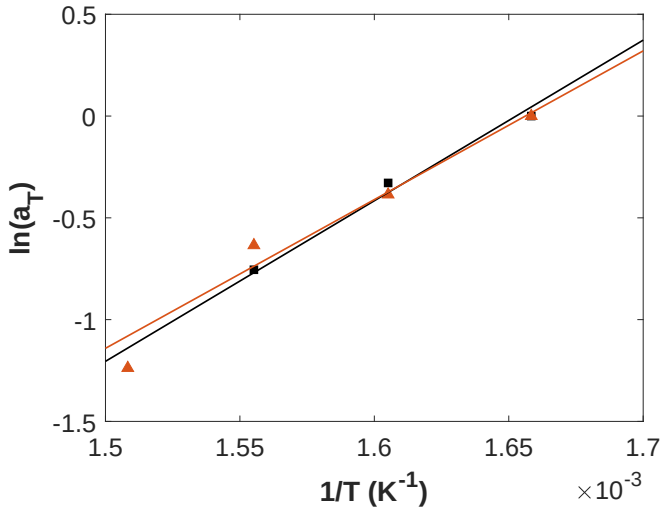

Figure 3.11: Arrhenius representation of the TTS shift factors of FLc (-□-) and FMc (-△-)

Materials	E_a $(kJ.mol^{-1})$
PEEK 151G [Bessard, 2012]	35
PAEK AE 250 - (FLc)	61
PAEK AE 250 - (FMc)	66
PEEK 450G [Lamethe, 2004]	90
PEKK 6003 [Coulson et al., 2018]	136
PEKK 7003 [Coulson et al., 2018]	156

Table 3.2: Activation energy for usual industrial PAEK

3.4 Calculation of relaxation times

To go further, the relaxation times are calculated from the frequency sweeps. Two average relaxation times are determined: τ_w is the mean relaxation time in the terminal region and τ_n is the mean relaxation time at the cross-over point. These relaxation times are assigned as the reptation time, the time required by a polymeric chain to escape from its tube in the theory of de Gennes [de Gennes, 1979]. These times are useful for any polymer processing when diffusion of chains is required such as welding, compression molding or additive manufacturing. Indeed, the chains need to diffuse across an interface to reach the next polymeric part or the next layer, resulting in the creation of a bond.

3.4.1 Definition of η_0

The relaxation time τ_w depends on the zero-shear viscosity, η_0, and the steady-state compliance, J_e^0, as follows:

$$\tau_w = J_e^0 \eta_0 \tag{3.6}$$

As explained above, the determination of the zero-shear viscosity is tricky due to the evolution of the structure during the experiments at low frequencies. To circumvent this drawback, it is convenient to use the Cole-Cole representation [Takahashi, 1954].

Fig. 3.12 features the Cole-Cole plot, depicting the loss viscosity, η', as a function of the storage viscosity, η'' for FMc. The experimental data are supposed to follow a semi-circle equation, and η_0 is the value when the semi-circle is crossing the x-axis in accordance with the equation given below:

$$\eta_0 = \sqrt{r^2 - y_c^2} + x_c \tag{3.7}$$

where x_c and y_c are the coordinates of the circle and r is the radius. The model is plotted as a continuous line in Fig. 3.12 and seems to be consistent with experimental data for each temperature. Experimental data at higher conservative viscosities show a deviation from the model, which can be explained by the evolution of the structure for the longest experiments. In our case, an assumption is that cross-linking occurs upon degradation.

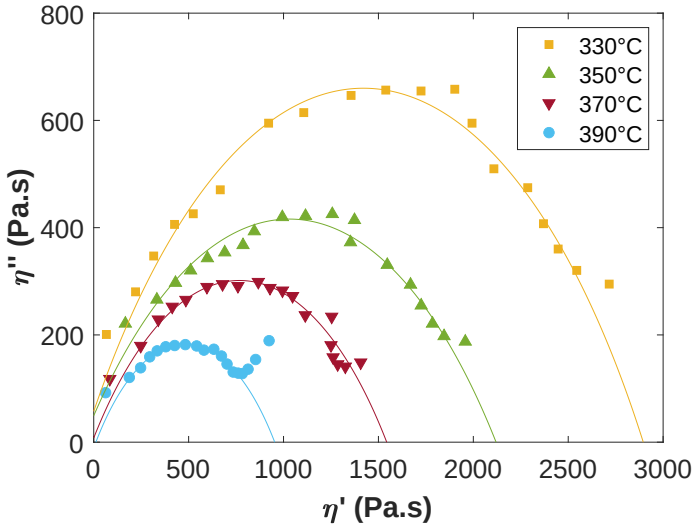

Figure 3.12: Cole-Cole representation of the complex viscosity of FMc : $\eta' = f(\eta'')$ for 330, 350, 370 and 390 $°C$

3.4.2 Definition of J_e^0

The steady-state compliance J_e^0 corresponds to the residual elasticity of the macromolecule due to the existence of an equilibrium conformation in coil chain under given temperature conditions. For melted polymers, J_e^0 is obtained from the intercept of the lines with slopes 1 and 2 of the moduli G'' and G' respectively, at low frequencies. Since they do not reach this behavior, an extrapolation is made and the intercept of the tangents of the extrapolated curves is considered. G' and G'' at low frequency gives a value of modulus G^* that follows the equation:

$$G^* = \frac{1}{J_e^0} \tag{3.8}$$

The value of the steady-state compliance, J_e^0, was identified for each temperature condition. Then, the mean relaxation time τ_w is calculated with the equation (3.6). τ_w is

associated with the motion of the longest chains. The mean relaxation time τ_n is associated to the motion of the shortest chains. It corresponds to the inverse of the frequency obtained at the cross-over point, meaning when $G' = G''$. For instance, the cross-over at 350 $°C$ is at a frequency of 20 Hz so τ_n is 0.05 s. The uncertainty of measurement of τ_w, called $\Delta\tau_w$, is calculated from the following equation:

$$\frac{\Delta\tau_w}{\tau_w} = \sqrt{(\frac{\Delta\eta_0}{\eta_0})^2 + (\frac{\Delta J_e^0}{J_e^0})^2} \tag{3.9}$$

$\Delta\eta_0$ is estimated at 200 $Pa.s$. ΔJ_e^0 is established using this equation:

$$\frac{\Delta J_e^0}{J_e^0} = \frac{\Delta G^*}{G^*} \tag{3.10}$$

ΔG^* is estimated at 1000 Pa. The uncertainty is thus calculated using the values of the modulus. Finally, the relative uncertainty of measurement of τ_n is identified as equal to 10 %.

The values of τ_n are presented in Table 3.3 with their corresponding modulus. The two methods of calculation are displayed in Fig. 3.13. The uncertainty of measurement is higher for τ_w due to the extrapolation.

	FLc		**FMc**	
Temperature ($°C$)	$G' = G''$ (Pa)	τ_n (ms)	$G' = G''$ (Pa)	τ_n (ms) (ms)
330	65000	2	84000	5
350	46000	1	125000	2.7
370	28600	0.7	75000	2
390	-	-	56000	1.7

Table 3.3: Cross-over values of the moduli for FLc and FMc

The relaxation times of the AE 250 polymer are shorter than those for PEEK, as seen in Fig. 3.14. The chains of FLc and FMc need less time than PEEK 450G to start moving. The ratio τ_w over τ_n gives an indication of the polydispersity I of the materials. Fig. 3.14 gives a representation of the width between τ_w and τ_n with temperature. FMc is more polydisperse than FLc since the ratio I is 76 for FMc and 22 pour FLc. This implies that the distribution of molecular weight, and hence the distribution of chain lengths, is higher for FMc. The polydispersity of PEEK 450G is around 900 and it is higher than both PAEK AE 250, as revealed by a larger gap between τ_w and τ_n in Fig. 3.14. A greater value of I indicates that small and long chains of polymer coexist. The manufacturing process, such

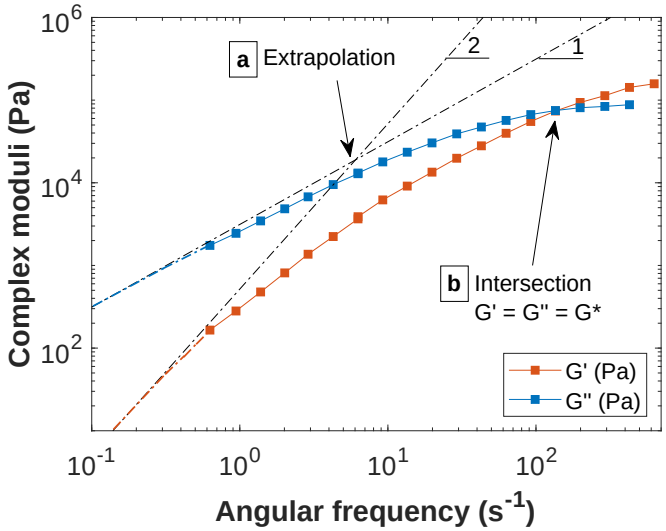

Figure 3.13: Complex moduli G' and G'' of FMc at 330 °C

as injection and compression molding, is therefore made more difficult since small chains will diffuse and degrade faster than longer chains. However, higher polydispersity can be interesting considering the assembly of two polymer parts since smaller chains will diffuse faster at the interface. Nevertheless, longer chains can entangle more easily and increase the elasticity of the material, which have a positive impact on Young's modulus.

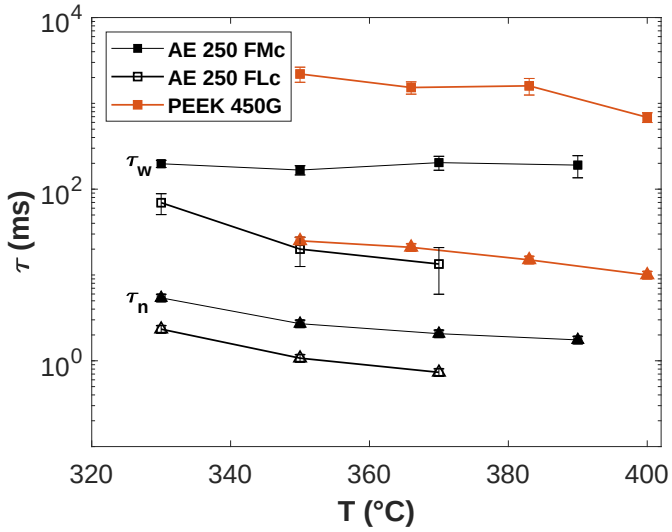

Figure 3.14: Relaxation times, τ_w (-□-) and τ_n (-△-), of FMc, FLc and PEEK 450G

3.4.3 Calculation of the molecular weight between entanglement

The plateau modulus G_N^0 is related to the density of entanglements [Larson and Larson, 1999], noted ν, by:

$$G_N^0 = \frac{4}{5}\nu k_B T \tag{3.11}$$

The molecular weight between entanglements is obtained from:

$$M_e = \frac{4}{5}\frac{\rho RT}{G_N^0} \tag{3.12}$$

Therefore, G_N^0 and ρ are needed to evaluate M_e. The plateau modulus G_N^0 is the value of $G'(\omega)$ at the frequency where the minimum of the loss tangent $tan\ \delta$ ($tan\ \delta = \frac{G''}{G'}$) is located. It is possible to measure the plateau modulus for amorphous polymers by dynamic oscillatory tests. It becomes more tricky for semi-crystalline polymers, because it is impossible to measure $G'(\omega)$ and $G''(\omega)$ at the plateau zone. A possibility to overcome this problem is the use of TTS. The frequency range of rheological measurements is comparatively small, due to the narrow temperature window between crystallization and degradation. Some attempts for predicting the value of G_N^0 from dynamic oscillatory measurements in the terminal region are proposed in the literature. G_N^0 is calculated from:

$$G_N^0 \approx \frac{\eta_0}{\tau_n} \tag{3.13}$$

When a polymer is heated, its volume changes, which modifies the density of the material. Its spatial evolution ΔL in one direction can be defined as:

$$\Delta L = L_0 \alpha \Delta T \tag{3.14}$$

where α is the coefficient of linear thermal expansion and L_0 is the initial length. ΔT is the variation of temperature. Considering that PAEK are isotropic polymers, its new volume can be defined as:

$$V = V_0(1 + \alpha\Delta T)^3 \tag{3.15}$$

The Taylor expansion approach states that in the case of $\epsilon << 1$:

$$(1+\epsilon)^n \approx 1 + n\epsilon \tag{3.16}$$

Using the Taylor expansion approach, the volume can be defined as follows:

$$V = V_0(1 + 3\alpha\Delta T) \tag{3.17}$$

Therefore, density ρ at 350 $°C$ is calculated from the following equation:

$$\rho_{350°C} = \frac{m}{V_0(1 + 3\alpha\Delta T)} \tag{3.18}$$

Density at room temperature is 1.28 $g.cm^{-3}$ in the case of AE 250 and 1.30 $g.cm^{-3}$ for PEEK 450G from supplier datasheets in Appendix A. α is 140 $ppm.K^{-1}$ for PEEK 450G. The same value is chosen for AE 250 as no other data is available in the literature. Therefore, densities at 350 $°C$ are 1.126 $g.cm^{-3}$ and 1.144 $g.m^{-3}$ for respectively AE 250 and PEEK 450G.

The molecular weight between entanglements is calculated with the previous data. M_e is about 2000 $g.mol^{-1}$ for PEEK 450G which is consistent with the values found by Herrmann-Schronherr [Herrmann-Schönherr et al., 1992] at 2100 $g.mol^{-1}$ and Roovers [Roovers et al., 1990] at 1300 $g.mol^{-1}$, the both from experiments at 350 $°C$. The values of M_e for FMc and FLc are respectively 7000 $g.mol^{-1}$ et 12000 $g.mol^{-1}$. The molecular weight between entanglements is unique for each polymer, reflecting the stiffness of the chemical structure. The higher M_e is, the stiffer the structure is. So PEEK has the more flexible chemical structure, followed by FLc and FMc, which are the most rigid chains.

3.4.4 Comparison to other PAEK

Finally, the zero-shear viscosity of AE 250 is compared to some commercial PEEK and PEKK in Fig. 3.15. It can be seen the divergence of activation energies and temperature ranges. The viscosity of PEEK 450G, which is the most widely used in industry, is higher than AE 250 and a lower viscosity implies easier manufacturing. It is due to the fact that the melting temperature of PEEK is about 40 degrees above Victrex AE 250 PAEK's one. PEKK 6002, PEKK 7003 and PEEK 151G show complex viscosity located between FMc and FLc considering the value of η_0. Similarly, PEKK 6002's slope is equivalent to those of FMc and FLc which suggests that the rheological behavior of Victrex AE 250 PAEK is close to PEKK 6002. As seen in Table 3.2, the activation energy of FMc and FLc are equivalent to the E_a of PEKK 6002 as noticed in Fig. 3.15. Activation energies of PEKKs 6003 and 7003 are higher due to the lower number of ether groups, which hinders the mobility of the polymeric chains.

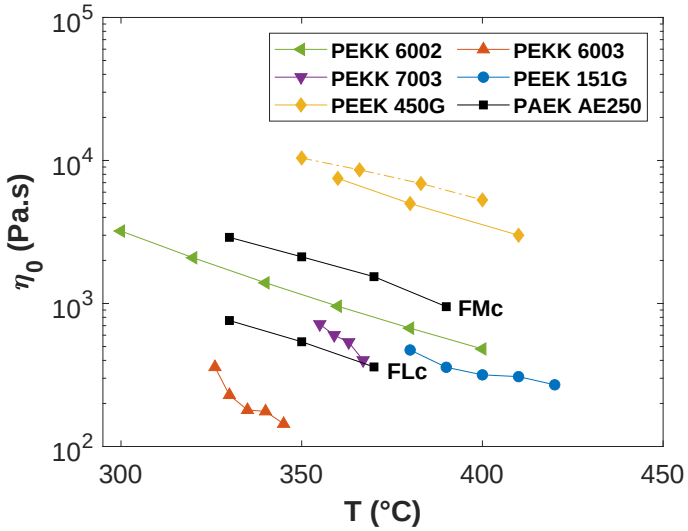

Figure 3.15: Zero-shear viscosity with temperature for PEKK 6002 [Choupin, 2017], PEKK 6003 [Coulson, 2018], PEKK 7003 [Coulson et al., 2018], PEEK 151G [Bessard, 2012], PEEK 450G [Shahriar et al., 2017, Nicodeau, 2005] and PAEK AE 250

3.5 Conclusion

This study gives a deeper knowledge of the crystallization and rheological properties of Victrex PAEK AE 250. This new polyaryletherketone has been recently launched with the promise of easier processing compared to other polyaryletherketones. The properties of PAEK AE 250 were investigated through the analysis of two shapes: films and flakes. DSC analysis was performed in order to quantify the thermal transitions and enthalpies. The films initially exhibit an amorphous structure compared to flakes that have a crystallinity between 19 % and 25 %. Therefore, cold crystallization will occur when the films are heated. As expected, the thermal transitions are delayed when the heating ramp or cooling ramp are faster. Also, the dependence of the crystallinity with the cooling ramp has been measured. From these results, it appears that the crystallization of AE 250 is slower than those of Victrex PEEK 450G. Similar to the latter, a second crystalline phase was observed at low cooling rate which increases the crystallinity up to 26 % at most. The crystallization must be thoroughly controlled during the forming process because the mechanical properties strongly depend on the crystallinity.

Then, dynamic rheological tests were carried out to evaluate the flowing properties above the melting temperature. The rheological behavior of both PAEK AE 250 films and

flakes looks similar to any melted polymer with a Newtonian plateau and a shear-thinning region, even if the data at low frequencies are not reached due to the evolution of the chemical structure with time. The shift of dynamic moduli fits the Time-Temperature Superposition, from which a_T coefficients show an Arrhenius-law dependency with an activation energy of 60 $kJ.mol^{-1}$. Then, two mean relaxation times were calculated: τ_w for the longest macromolecules in the terminal regime and τ_n for the shortest macromolecules at the cross-over point when $G' = G''$.

The relaxation times of AE 250 are between a few ms and 200 ms. They are lower than those found for PEEK 450G, meaning a faster mobility of macromolecules. Moreover, the relaxation times of the flakes are lower than those of films. The relaxation times of PEI have not been studied because they are shorter than those of PAEK [Rosa et al., 2016]. Indeed, the viscosity of PEI drastically drops right after T_g at 200 $°C$ as we will see in Chapter 5. The ratio of relaxation times gives an idea of the polydispersity. Both films and flakes demonstrate a sharper polydispersity than PEEK 450G. Then, an attempt to calculate the molecular weight between entanglements has been made to compare the chemical structure of these PAEK. Even if the uncertainty is high due to the lack of experimental data at low frequencies, we provide some information towards a better understanding of the properties of AE 250. As described by Victrex patent [Glynn et al., 2017], the PAEK chemical structure consists of chains of two repeat units: $-O-R1-O-R3$ and $-O-R2-O-R3$ with $R1$ selected from phenyl, terphenyl, napthyl or phenyletherphenyl moities, $R2$ is a biphenyl or terphenyl moities and $R3$ is a benzophenone or other similar benzenic compounds. We assume that the flakes are composed of more flexible moities compared to films.

Lastly, the complex viscosity of AE 250 flakes and films is compared with other commercial PAEK such as PEEK and PEKK from data available in the literature. The viscosity and its variation with temperature are similar to those for PEKK 6002. These results confirm that the properties of new Victrex AE 250 are high enough to compete with other commercially available PAEK among high performance thermoplastics. Moreover, a better control of the crystallization will be possible thanks to a slower kinetics compared to PEEK. A lower melting temperature and polydispersity will facilitate the processing conditions. Still, shorter relaxation times are decisive for welding, compression molding and additive manufacturing of polymers and composites.

When comparing the relaxation times, between 1 and 100 ms, to the characteristic time of the welding process, it looks that AE 250 is suitable to be welded by ultrasonic welding process. Indeed, the characteristic time is less than 1 second, giving the molecules enough time to diffuse across the interface between the two welded parts.

Chapter 4

Thermal analysis of ultrasonic welding

Contents

4.1 Introduction 94

4.2 Thermocouple insertion for welding specimens 94

4.2.1 Thermocouples preparation 94

4.2.2 Incorporation procedure 95

4.2.3 Characterization of specimens with integrated thermocouple 96

4.3 Applications to US welding 97

4.3.1 Post-synchronization of temperature results with welding output parameters 97

4.3.2 Temperature profiles during short impulsion time welding 98

4.4 Temperature profile measurements during welding 102

4.4.1 Analysis of a typical temperature curve 102

4.4.2 Influence of welding parameters 104

4.4.3 Influence of thermocouple on mechanical properties 108

4.5 Thermal diffusion modeling from the interface 109

4.5.1 Description of the finite element model 110

4.5.2 Model results 113

4.5.3 Influence of the number of PEI layers 116

4.6 Conclusion 119

4.1 Introduction

Monitoring the temperature field is crucial to relate process parameters to welds performance. As explained in Chapter 1, measuring the temperature during welding is challenging. No non-invasive technique does exist yet to assess the temperature profile at the interface during welding. Due to the closed contact between the two specimens, it is difficult to measure the temperature and impossible to control it. Moreover, the very short cycle times during US welding reduce the means available to measure the temperature. Any device placed between the two specimens would alter friction phenomena, thus, changing heat generation. In this work, microthermocouples are chosen to minimize their influence during welding. This chapter displays the thermal analysis conducted on CF/PEEK specimens using a PEI energy director. The first section presents the non-intrusive temperature measurement method developed. Then, temperature profiles are analyzed through the influence of welding parameters. Finally, the thermal diffusion through the sample thickness from the interface is investigated from a finite element analysis.

4.2 Thermocouple insertion for welding specimens

4.2.1 Thermocouple preparation

K-type thermocouple wires were purchased from Omega Engineering. They are called chromel (CHROMEGA™) and alumel (ALOMEGA™) wires. Diameter of both wires is 80 μm, and they have no insulation. Those both characteristics limit the invasiveness of the sensor and also minimize the response time. Indeed, the phenomena are very fast for ultrasonic welding. For this reason, the temperature is more difficult to measure than for other welding processes since the thermocouples must have response times adapted to the process. A chromel wire is manually arc welded to an alumel wire under an argon atmosphere. The two wires are held together at their ends by a metal clamp. The latter is the positive electric terminal of the device. They are brought close to a metal nozzle, negative electric terminal, where an electric arc is formed, linking the two wires, as seen in Fig. 4.1. Argon gas is sprayed around the nozzle to limit oxidation during the welding process. The diameter of each weld is measured and flattened with a metallic weight to not exceed the thickness of 80 μm.

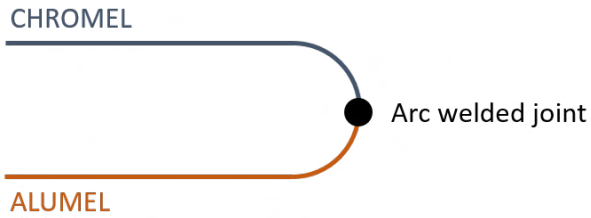

Figure 4.1: Layout of hand-made thermocouple from chromel and alumel wires

4.2.2 Incorporation procedure

As mentioned in Chapter 1, thermocouples have usually been placed at the welding interface prior to US welding [Tao et al., 2019, Koutras et al., 2019]. However, surface roughness is an essential factor as heat will nucleate most likely at the contact areas during friction. With this in mind, it is chosen in this study to integrate the thermocouples into the polymer layer to minimize their effect on the friction mechanism. They are integrated into the PEI layer prior to welding with the goal to measure the temperature evolution as close as possible to the welding interface while avoiding a protrusion effect at the interface. A dedicated integration procedure is defined taking advantage of PEI amorphous state. PEI undergoes a viscosity drop from T_g (220 $°C$) which allows the integration without melting of PEEK. As seen in Fig. 4.2, a 25 N metallic weight is applied on top of the thermocouple and specimen in an oven heated at 290 $°C$ for 40 min. These conditions are chosen based on many trials until a balance is found for the thermocouple between penetrating into the layer and preventing its flowing. A polyimide film is placed between the weight and PEI layer to ensure a repeatable roughness. This procedure is only applied to P2 plates.

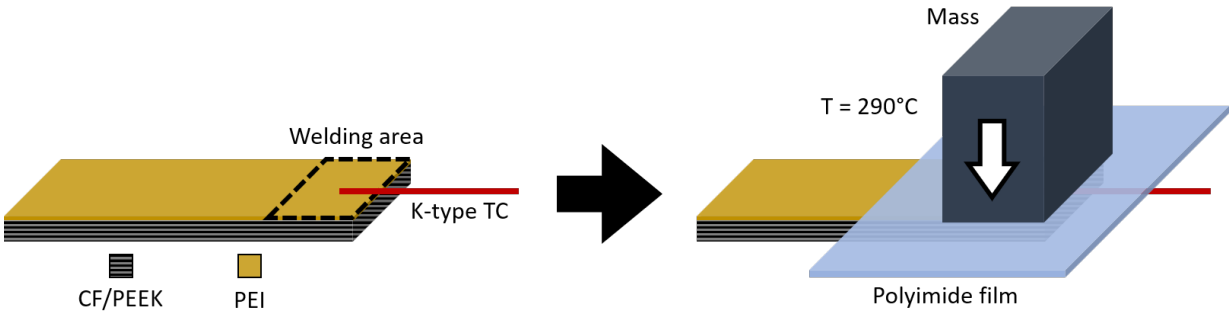

Figure 4.2: Thermocouple integration process inside the energy director

4.2.3 Characterization of specimens with integrated thermocouple

Optical micrographs of specimens with thermocouples are made to validate the implementing process, as seen in Fig. 4.3. The red square indicates the position of the thermocouple weld inside the specimen. From a general point of view, it can be seen in Fig. 4.3 (a) and (b) that some PEI is squeezed out of the sample edges. It is assumed that the quantity of flowing PEI is not sufficient to modify heat generation compared to welding in the same conditions without thermocouple. A successful implementation is presented in Fig. 4.3 (a) and (c), where the entire thermocouple flattened weld is pushed inside the layer. The wires also need to be fully embedded inside the PEI to avoid a modification of heat generation, especially closed to the thermocouple nozzle. Fig. 4.3 (b) and (d) is a non-successful implementation since a significant zone of the thermocouple is still visible on the surface. Only specimens with the thermocouple (TC) fully integrated into the polymer layer are used for further welding experiments.

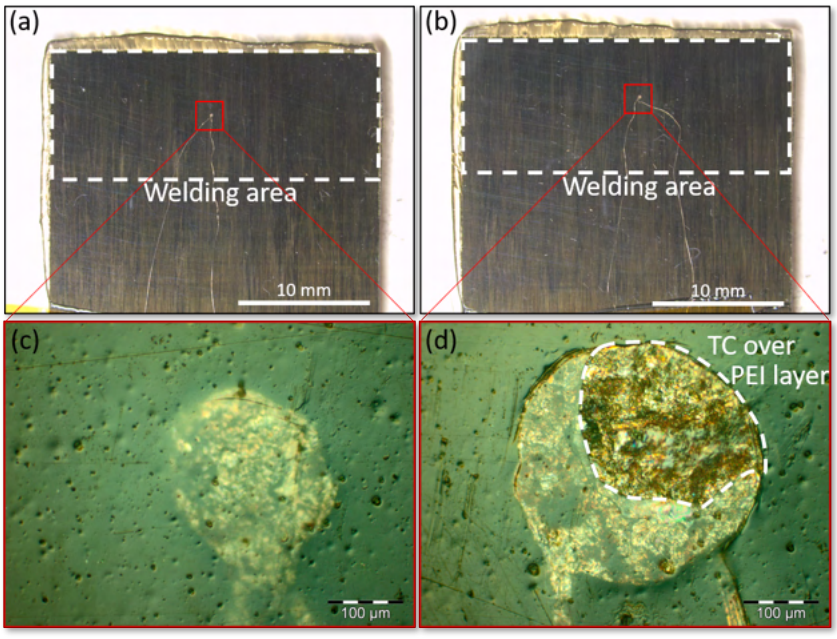

Figure 4.3: Micrographs of welding specimens after integration of thermocouples in the welding area with a magnification of x0.75 (a,b) and x20 (c,d)

4.3 Applications to US welding

4.3.1 Post-synchronization of temperature results with welding output parameters

The thermocouples are plugged into a processing unit supplied by Omega Engineering. It allows a maximal sampling frequency of 333 Hz, corresponding to a measured value every 3 ms which is sufficient for ultrasonic welding. The processing unit is also connected to the welder generator. Fig. 4.4 shows that data from both thermocouple and welder are processed by the processing unit, which transfers the information to a computer. The processing unit records the temperature from the thermocouple while it records the power (V) supplied by the welder generator. A typical output curve is presented in Fig. 4.5 (a). In Fig. 4.5 (b), sonotrode displacement and power are plotted as a function of time, which are the output data from the welder. Whereas the powers from the processing unit and the output data do not have the same unit, they exhibit similar behaviors. During the vibrations stage, the power is different from zero for both apparatus, whereas it is equal to zero for every other steps of the welding process, *i.e.* during the increase of welding load or during cooling. It means that the two power curves have the same duration. Therefore, the two power curves are superimposed to synchronize the temperature results with the welding output parameters.

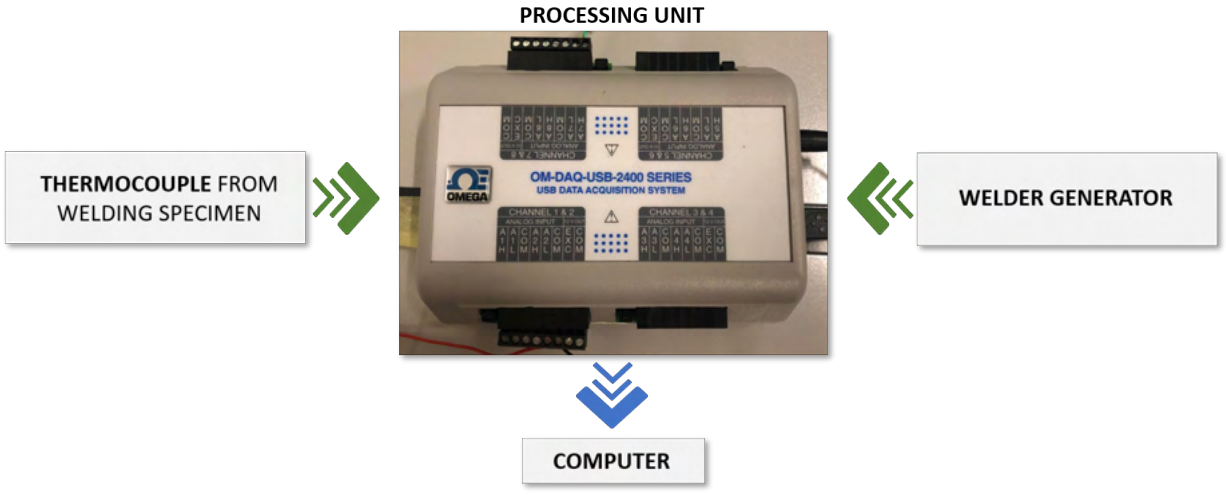

Figure 4.4: Layout of the profile temperature measurement set up

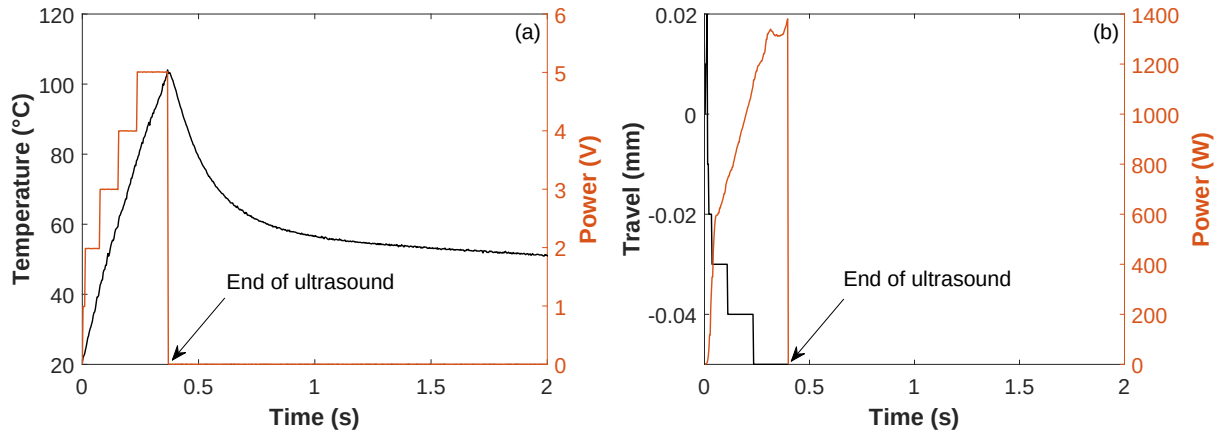

Figure 4.5: Synchronization of welding output data from the processing unit (a) and from ultrasonic welding device (b)

4.3.2 Temperature profiles during short impulsion time welding

In the following section, welding are made using the configuration shown in Fig. 4.6. The lower specimen is from P1 plate, *i.e.* CF/PEEK composite plates. To ensure a repeatability of the assembling tests, the thermocouples are always inserted in the upper specimens, which is made from P2 plates (CF/PEEK with a PEI energy director). The thickness of the energy director is 250 μm. Short impulsion times were applied for welding.

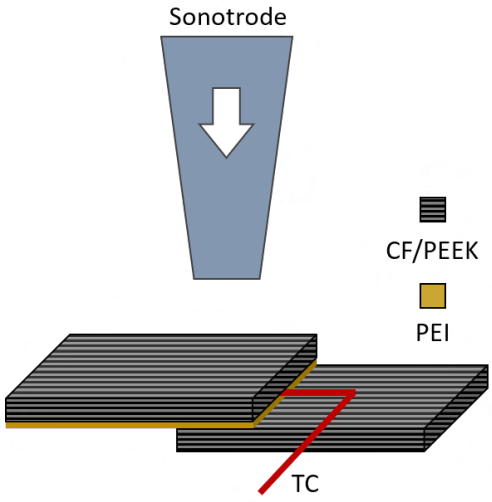

Figure 4.6: Welding configuration for short impulsion time welding experiments

The sampling rate and thermocouple response seem to be well adapted for this application: the curves are smooth, as it can be seen in Fig. 4.7, which displays the temperature within the energy director for short ultrasonic impulsion times. The impulsion time, or welding time, is the duration during which ultrasounds operate. Short impulsion times are applied successively to the same specimen since those times are not long enough to modify the specimens. Nevertheless, an increase of the impulsion duration is progressively done to adjust precisely the welding parameters. The impulsion time will be chosen to favor the polymer flowing while avoiding degradation due to over heating. The three curves in Fig. 4.7 (a) display the same trend, *i.e.* a high temperature rise until reaching a peak. The temperature drops rapidly as soon as the ultrasonic impulsion is stopped, indicated by the arrows in the figure. As expected, a longer impulsion time induces a higher maximal temperature, increasing from 40 $°C$ to 105 $°C$ when the impulsion rises from 200 ms to 400 ms. It is also important to note that the quasi linear slope in temperature rises of the three curves seem to be identical, indicating a repeatability in the temperature measurements which validate our experimental protocol. Fig. 4.7 (b) shows three curves for welds made with a 200 ms welding time and 32 μm amplitude. The curve at 100 N does not display any temperature rise, meaning that 100 N is too low. Indeed, the pressure is too low to obtain intimate surface contact to initiate friction. For a welding load of 300 N and 500 N, the same trend as Fig. 4.7 (a) is observed. Increasing the welding load increases the maximal temperature, and the temperature starts to decrease at the end of the vibration stage.

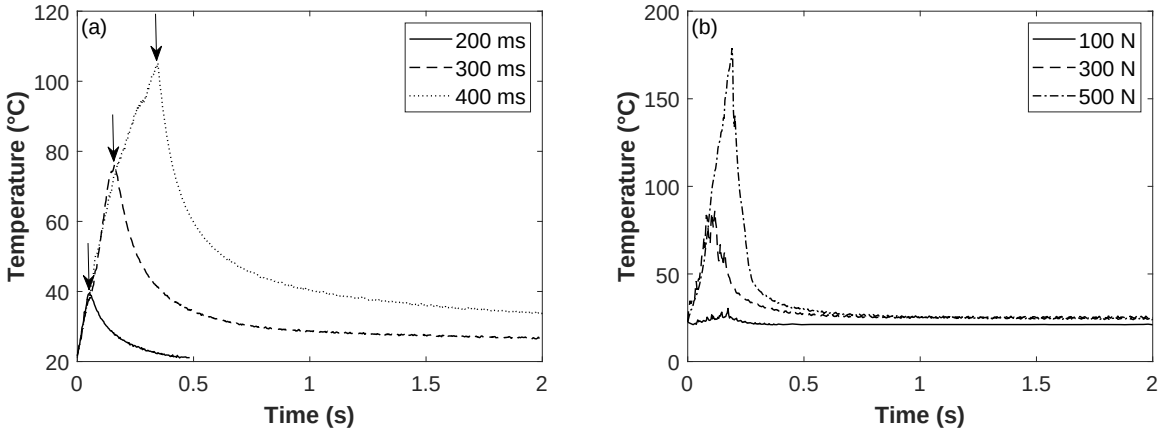

Figure 4.7: Temperature profiles at 200 N and increasing impulse times (a) and for 200 ms with increasing load (b) for a constant amplitude of 32 μm

Same measurements have revealed some rather unusual temperature results. Fig. 4.8 shows two examples. As before, each graph shows the results from the same specimen. In

both cases, the initial welding time increase causes the same trends as observed in Fig. 4.7 (a) and (b) until a threshold is reached where the values (slope and maximum temperature) change their behavior. In the graphs, the curves in orange are the ones after the threshold, *i.e.* for longer welding times. In Fig. 4.8 (a), the temperature behavior changes abruptly when the welding time is 500 ms. Before this threshold, the tests seem repeatable. The curve is difficult to analyze because it includes much noise from that starting point. In Fig. 4.8 (b), the trend is a little bit different. From the threshold, at 600 ms, the heating rate changes with the appearance of noise during the first half-second of measurement. The maximum temperature value is also lower for longer times (600 ms and 800 ms) than for shorter ones (200 ms and 400 ms).

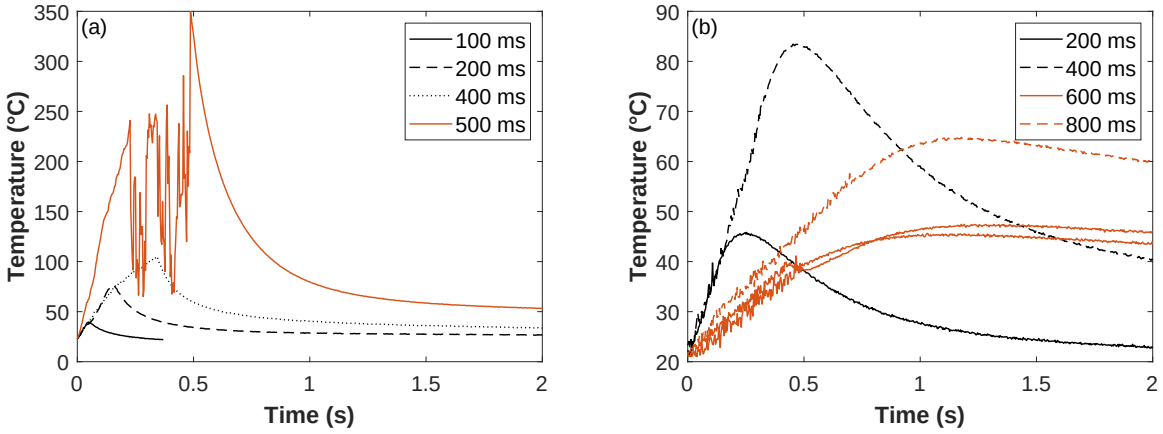

Figure 4.8: Influence of the thermocouple location on the temperature measurement for a welding load of 200 N and 32 μm amplitude (a) & a 200 N welding load and a 64 μm amplitude (b)

To understand this phenomenon, optical micrograph observations were made. It is possible to open such assemblies to take micrographs because impulsion times and welding are too low to create a strong bond between the specimens. Fig. 4.9 shows micrographs of the welding interface before and after heating ramps presented in Fig. 4.7 (a). Due to the unidirectional preg stacking used from the manufacturing of these samples, the fibers are easily squeezed outside the welding area, whereas the entire ED has not melted yet. Only the edges are impacted by the phenomena due to heat and friction. This could be due to prominent roughness at the specimen edges. The area around the TC does not seem to be physically affected, which is consistent with the maximal peak temperature value, around 100 $°C$. It is confirmed by Fig. 4.9 (c) and (d), which are high magnification of the TC before and after welding. Indeed, the TC remains inside the polymer layer, even after welding.

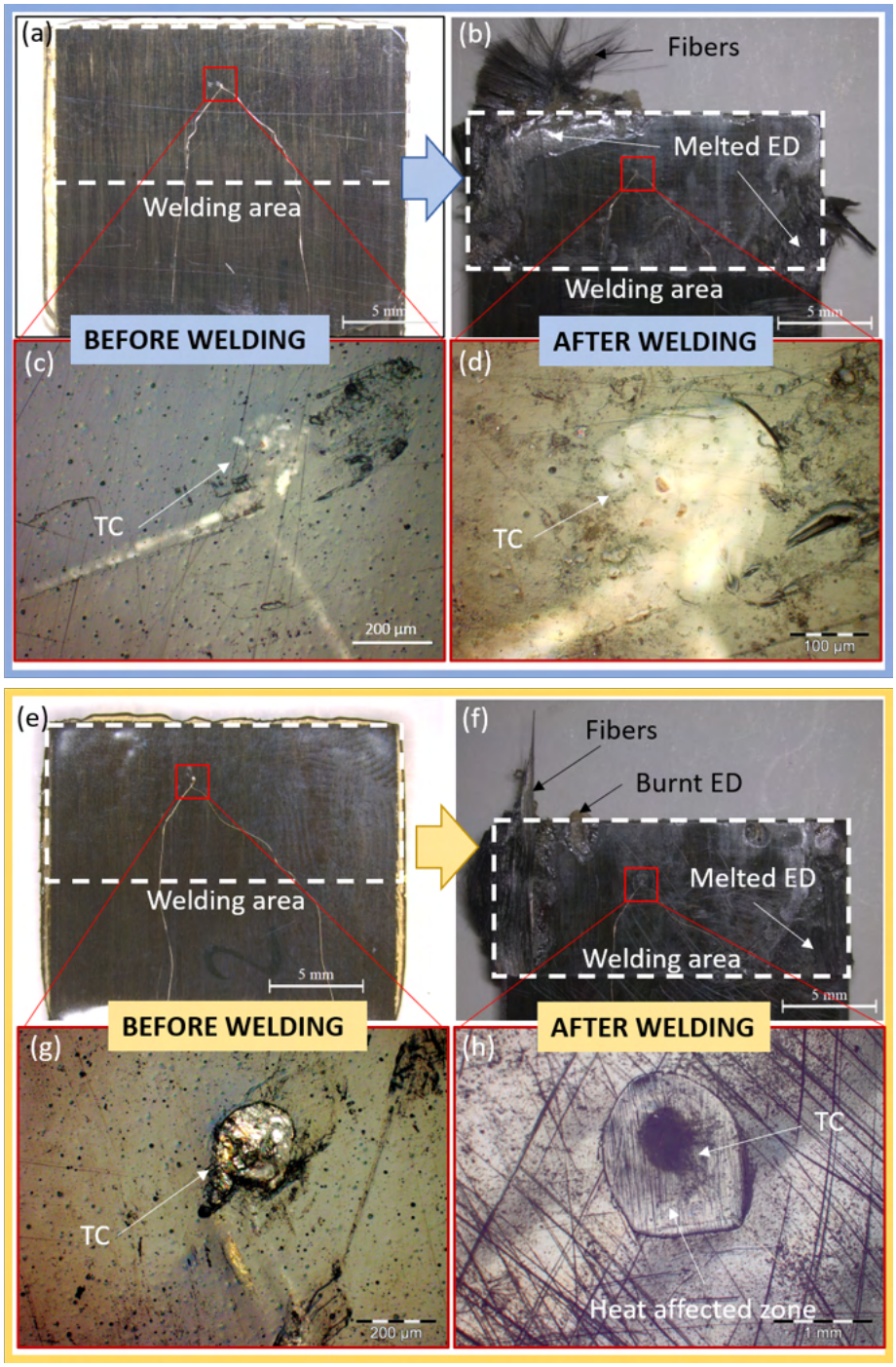

Figure 4.9: Micrographs of the welding interface before (a, c) and after (b, d) welding experiment of Fig. 4.7 (a) and before (e, g) and after (f, h) welding experiment of Fig. 4.8 (a)

Fig. 4.9 (e), (f), (g) and (h) are the micrographs before and after welding of the same specimen, corresponding to the temperature profiles in Fig. 4.8 (a). In this case, the TC has not been implemented correctly since part of it is still visible on the specimen surface (Fig. 4.9 (g)). In Fig. 4.9 (h), an heat-affected zone is observed around the TC after heating. At the thermocouple/polymer interface, a thermal resistance results in heat concentration, explaining why the polymer degradate at this location faster than elsewhere on the welding surface. It can also modify the real temperature value, as seen in Fig. 4.8 (a) where the curve at 500 ms does probably not correspond to friction phenomenon between PEI from specimen 1 and PEI from specimen 2 but rather between the metallic TC and the PEI. Moreover, as before, the entire ED has not melted, but some degradation of the specimens can be seen, especially in the upper left where fiber displacement and brown color related to a burnt matrix are visible, as seen in Fig. 4.9 (f). These micrographs also show that the ED thickness might be insufficient since the first layers of composite already seem to be thermally affected by the welding process while no strong joint is achieved. In the next section, the number of PEI layers is increased to overcome this issue.

4.4 Temperature profile measurements during welding

4.4.1 Analysis of a typical temperature curve

In this section, welding experiments are made using the configuration shown in Fig. 4.10. As previously mentionned, the specimen with TC is located in the upper specimen. The two specimens are from P2 plates, *i.e.* one integrated 250 μm PEI layer. A third 250 μm thick PEI layer is placed and taped between the two specimens to avoid moving during welding. A total thickness of 750 μm is thus used as energy director. In comparison to the previous welding configuration in Fig. 4.6, this configuration is easier to weld since only a PEI on PEI welding is required. In contrast, a PEEK on PEI welding was necessary in the previous configuration.

Fig. 4.11 illustrates a typical temperature-time curve during welding. The graph displays temperature and sonotrode displacement (or travel) as a function of time. The displacement of the sonotrode is differential, *i.e.* it is the difference between the initial position of the sonotrode and its position all along the welding experiment. The temperature results are combined with the travel data registered from the welding equipment in

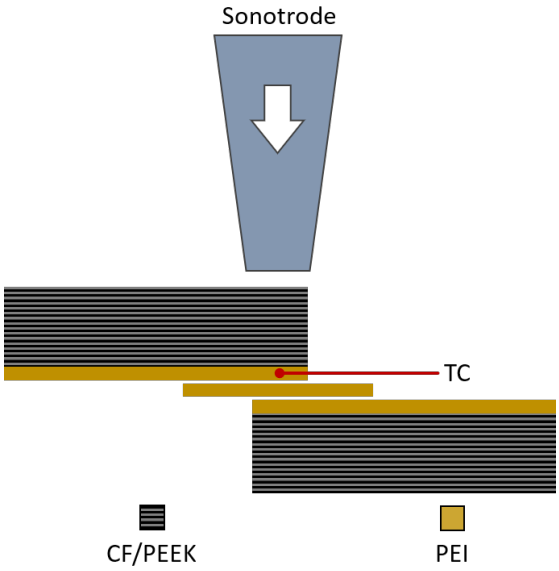

Figure 4.10: Welding configuration for temperature profile measurements

order to better understand the physical phenomena occurring during welding. Indeed, the sonotrode goes up or down to maintain a constant load during welding. Its value gives an indication of the polymer swelling or flowing. The welding conditions are the following: 32 μm of amplitude, 500 N welding load and 600 ms welding time. A 2500 ms holding time is chosen during cooling, and the holding load is the same as welding load.

Looking at the curves in Fig. 4.11, the first observation is that the phenomena are very fast since the time range is only 2 seconds. Several stages and breaking points are observed. First of all, a very fast heating ramp at around 1000 $K.s^{-1}$ takes place in stage 1, during which a slight travel increase is seen. This means the polymer is swelling when heating due to thermal expansion, and the sonotrode goes up to maintain a constant welding load. A clear slope break is then observed at point 2 associated with the starting of decrease in travel. This point is associated with the beginning of PEI flow that continues until a maximal temperature of 450 $°C$ is reached (point 3). This temperature value might seem high, but the phenomena are so fast that we can assume that PEI and PEEK do not have time to be entirely affected by such temperatures. Then, the polymer flows until reaching a maximal flow corresponding to a travel of around 250 μm (point 4). As the theoretical PEI thickness was 750 μm at the test beginning, it is assumed that only PEI has flowed and PEEK has not started to melt. Finally, a fast cooling at around 600 $K.s^{-1}$ occurs in stage 5. As PEI is an amorphous polymer, the cooling does not impact its physical structure. Besides, the cooling rate does not impact PEEK either, as it was assumed that

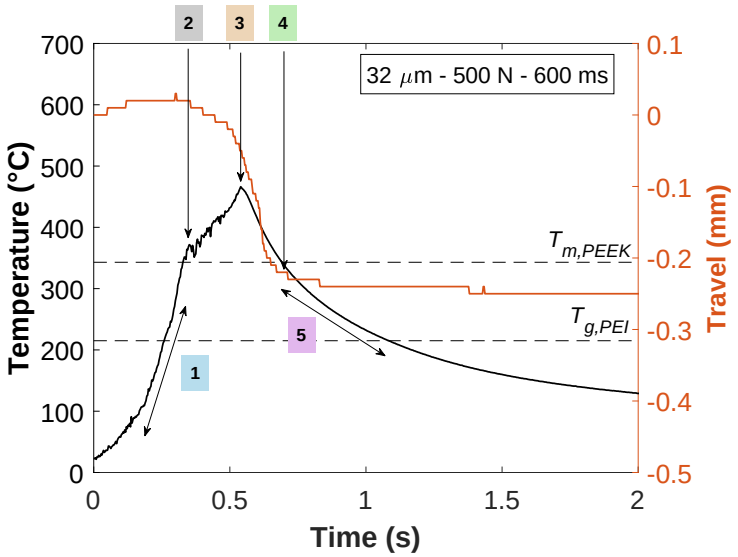

Figure 4.11: Temperature and travel curves for the following welding conditions: amplitude of 32 μm, 500 N welding load and 600 ms welding time showing different steps (1 to 5)

PEEK had not reached its melting temperature during welding. These temperature and travel curves are chosen as reference for the following section, and they are presented in bold in the next figures (Fig. 4.12, Fig. 4.13 and Fig. 4.14). Further analysis of these typical steps are presented in the following section.

4.4.2 Influence of welding parameters

To evaluate the influence of welding parameters on temperature profiles, several measurements were completed by changing only one parameter at a time. Fig. 4.12, Fig. 4.13 and Fig. 4.14 show the combined (temperature and travel) data to evaluate the influence of, respectively, welding time, amplitude and welding load.

Fig. 4.12 presents the sonotrode travel and temperature measurements for five different welding loads. First of all, the temperature curves do not show a similar behavior. For instance, the 500 N curve exhibits a sharp peak whereas the 300 N curve is rounded at its top. This difference may be attributed to the localization of hot-spots nucleation that can be more or less close to the thermocouple during the heating stage. The heating ramp is not linear for each welding load. They all display a change of slope that can be associated with the beginning of a physical change in the polymer structure, namely the beginning of softening or melting. The melting temperature T_m(PEEK) and glass transition temper-

ature T_g(PEI) are symbolized by horizontal lines in Fig. 4.12. According to this curves, this change seems to occur right after reaching PEEK melting temperature. However, the heating rates are very fast, around 1000 $K.s^{-1}$. As it has been shown in the literature, a fast heating rate shifts the melting temperature towards higher temperature. Upon very fast heating, the polymer reaches a metastable state called superheating. As demonstrated by Minakov et al. [Minakov et al., 2007] on linear PET, isotactic polypropylene (iPP) and isotactic polystyrene (iPS), the superheating magnitude $\Delta T = T_m - T_0$ with T_m the measured melting temperature and T_0 the melting temperature at equilibrium, depends on the melting process kinetics and increases with the heating rate. For instance, $\Delta T = 30\ K$ is measured with a heating ramp of 1000 $K.s^{-1}$ for PET. As refered in Chapter 3, the melting temperature of PEEK is $T_0 = 343\ °C$. To the best of our knowledge, no previous work reports the melting temperature shift to neither PEEK nor PEKK. Besides, the glass transition temperature of PEI is equal to 220 $°C$. To this end, considering the very fast heating, the beginning of slope change during the heating stage - right after the line representing the melting temperature of PEEK - could be associated with PEI glass transition. Moreover, the travel curves start decreasing at the same location where a change in the temperature slope occurs, confirming that softening of the energy director affects the temperature profiles. We assume that the melting temperature shift revealed by Minakov et al. would be similar to a glass transition shift for amorphous polymers. When the load increases from 300 N to 700 N, the temperature reaches a maximum close to 500 $°C$ for a few hundreds of milliseconds before decreasing. This peak is associated with the end of the ultrasonic vibrations.

The cooling behavior appears to be similar for all these testing conditions and the cooling rate is close to 600 $K.s^{-1}$ right after the end of vibrations. PEI is an amorphous polymer, which means that the cooling rate do not affect much its mechanical properties, in comparison with semi-crystalline ones for which a high cooling ramp inhibits the crystallization. The degree of crystallinity affects the mechanical properties as revealed by Martineau [Martineau et al., 2016]. E' is at 2.9 GPa for amorphous PEEK whereas it reaches 3.5 GPa for fully crystallized PEEK; the elongation rate is also affected.

As it can be seen in Fig. 4.12, the travel curves are quite different when the mechanical load rises from 300 N to 700 N. The 300 N curve shows that the polymer has started to heat but did not reach a full softened/melted state since its final displacement is around zero. The welding load was not high enough to create an intimate contact that could ensure an efficient friction and homogeneous heat generation at the interface, despite the value of temperature measured. The 500 N and 700 N welding load curves reach respectively 0.25 mm and 0.3 mm negative displacement of the sonotrode, meaning that PEI films

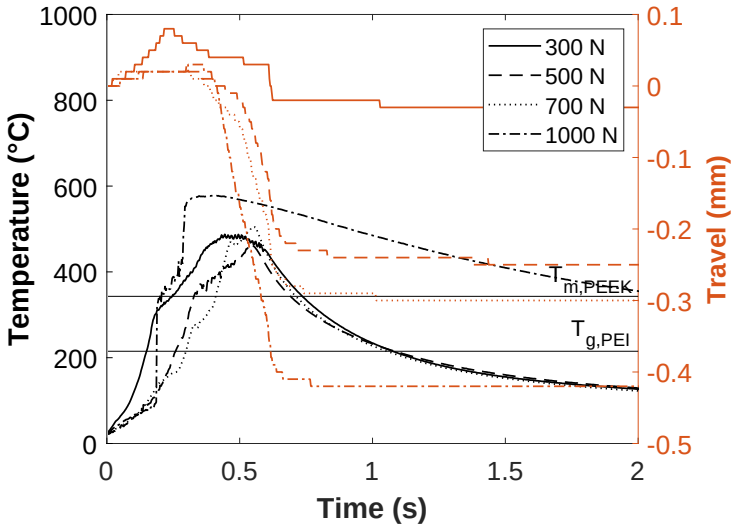

Figure 4.12: Temperature profiles and sonotrode travel during USW for a amplitude of 32 μm and a welding time of 600 ms for a 750 $\mu m-$thickness energy director

have started to squeeze, losing 0.25 mm and 0.3 mm of their initial thickness. On the other hand, the 1000 N test exhibits a different behavior with a maximal temperature close to 580 $°C$, and where the temperature stays above 400 $°C$ for a much longer time. In parallel, the travel reaches a final level of 0.4 mm, much higher than for the other welding conditions. In all welding load testing conditions, the final thickness of the interphase does not seem to have lost more than 300 μm from its initial thickness, which would confirm that the CF/PEEK plies have not been submitted to squeeze flow and therefore have not been enough thermally affected to reach the melting temperature.

Fig. 4.13 displays the amplitude influence on temperature profiles and travel. The temperature profiles appear to be equivalent in heating and cooling stages for every conditions and also equivalent to those in Fig. 4.12 (respectively 1000 $K.s^{-1}$ and 600 $K.s^{-1}$ at their maximal values). They all reach a maximum that varies from 460 $°C$ for the lowest amplitude to 560 $°C$ for the highest one. The travel curves feature a similar behavior while reaching different final values between 0.2 mm and 0.3 mm. The trend is not as expected since the highest travel is obtained for an amplitude of 48 μm followed by the one for 32 μm and finally the curve for 64 μm. This shows that reaching a higher maximal temperature does not necessarily mean that squeeze flow will be more important.

Other factors may affect welding, such as surface roughness or local heat nucleation points that may influence temperature profile and could be predominant in those results.

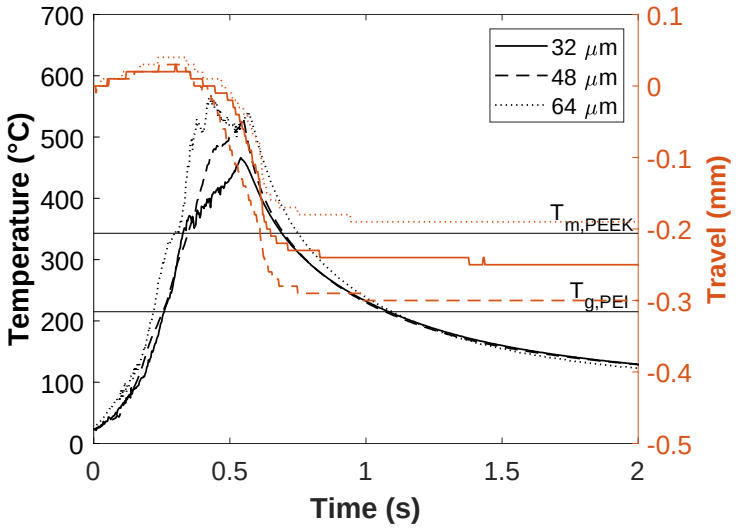

Figure 4.13: Effect of ultrasonic amplitude on temperature profiles and sonotrode travel (welding load: 500 N, welding time: 600 ms, energy director thickness: 750 μm)

Also, the PEI film has an initial thickness of 250 μm with a standard deviation of 40 μm. This variation is significative when comparing with the difference of 100 μm in the final travel values.

Finally, Fig. 4.14 shows the temperature profiles and travel for different welding times. As seen in Fig. 4.12, a change of heating ramp is noticed on those curves, related to the softening of PEI, except for the 400 ms curve where maximum measured temperature is below 300 $°C$. For this time, it can also be seen that the final travel is close to zero, confirming that PEI did not soften even if the T_g of PEI at equilibrium is 220 $°C$. This confirms our hypothesis on T_g(PEI) shift. The heating rates seem to be similar for all the welding times, as for the various welding loads and amplitudes investigated in Fig. 4.12 and Fig. 4.13. From 600 ms to 1000 ms, the curves reach a peak close to 500 $°C$. However, the 1000 ms curve seems to reach a temperature plateau for a few hundred of milliseconds before a temperature drop at the end of ultrasound impulsion. This would favor the motion of macromolecular chains which have more time to diffuse and entangle before the temperature goes down. The final travel increases with the increase of welding time, from 0.25 mm to 0.5 mm for respectively 600 ms and 1000 ms, confirming a larger squeeze flow for higher impulsion times. Finally, the curve at 1000 ms must have been affected by another phenomenon since the temperature curve drops from 450 $°C$ to 25 $°C$ in no time. From 1 second, we consider that the curve is not exploitable. An explanation could be the break of the thermocouple due to friction.

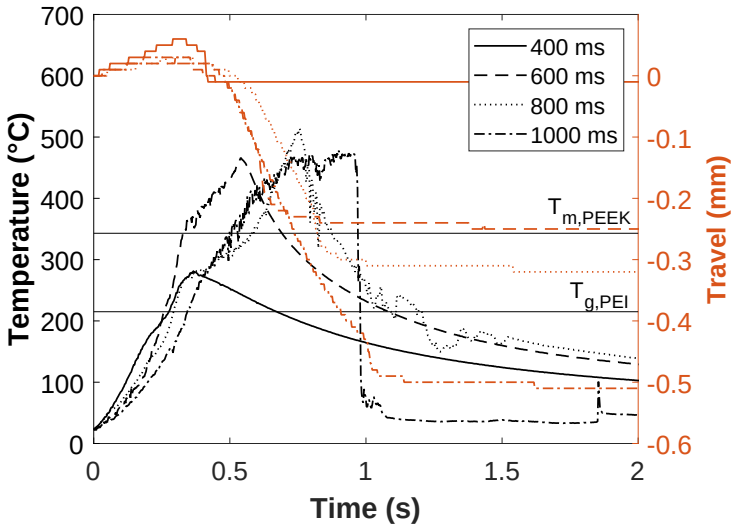

Figure 4.14: Influence of welding time on temperature profiles and sonotrode travel during USW (amplitude: 32 μm, welding load: 500 N, energy director thickness: 750 μm)

This section has shown that the welding load and the welding time strongly influence the temperature profiles. However, the curves for different values of amplitude show only a small influence of this parameter. The travel curves give information about the intensity of polymer squeezed out of the welding interface. Nonetheless, these graphs do not allow to know the temperature diffusion through the thickness of the specimens. To answer this issue, a finite element analysis is conducted in the section 4.5, and in particular to discuss the maximal temperature reached by the CF/PEEK layers during welding.

4.4.3 Influence of thermocouple on mechanical properties

To complete this section, single lap shear (SLS) experiments are conducted to evaluate the invasiveness of the thermocouple and its influence on the interfacial mechanical strength. A three PEI layers configuration is used for a welding load of 500 N, an amplitude of 32 μm and a welding time of 600 ms. For further information about the SLS layout, refer to Chapter 5, dedicated to the mechanical analysis of joints. The results are compared for the same welding configuration and parameters with and without thermocouple, and presented in Fig. 4.15. The lap shear strength (LSS) with thermocouple is slightly lower than the one without TC, 27 MPa compared to 32 MPa. However, considering the standard deviation measured for identical specimens and configuration, the difference in

LSS is small enough to state that the non-intrusive nature of the procedure is fulfilled.

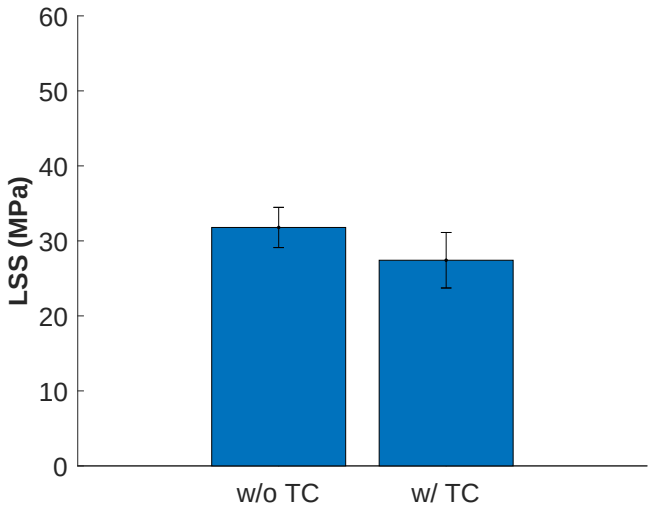

Figure 4.15: Lap shear strength with and without thermocouple (amplitude: 32 μm, welding load: 500 N, welding time: 600 ms and 750 $\mu m-$thickness energy director)

4.5 Thermal diffusion modeling from the interface

Temperature profiles in the previous section give information on what is happening at the welding interface. However, no information is available on heat diffusion throughout the specimens, especially in the first layers of composites. Overheating can lead to the deconsolidation of the layers and, in extreme cases, degradation of the polymer matrix. For each case, a decrease of mechanical properties and loss of structural integrity of the part can occur. Therefore, the knowledge of the through-thickness heat distribution is mandatory. To approximate it, a simple and robust finite element model for in-depth heat diffusion is developed in Abaqus software.
A non-stationary thermal model is developed, where the software uses the local heat equation:

$$div(\lambda \overrightarrow{\nabla} T) + \dot{q} = \rho C_p \frac{\partial T}{\partial t} \tag{4.1}$$

where λ is the thermal conductivity, T is the temperature, $\dot{q}$ is the source term, ρ is the density and C_p is the heat capacity. In this case, the heat source term $\dot{q}$ is considered to

be null because no volumetric internal energy is generated. So, the local heat equation can be written as follows:

$$div(\lambda \overrightarrow{\nabla} T) = \rho C_p \frac{\partial T}{\partial t} \tag{4.2}$$

The left-hand term $div(\lambda \overrightarrow{\nabla} T)$ corresponds to diffusion whereas the right-hand term $\rho C_p \frac{\partial T}{\partial t}$ corresponds to transient heat state.

4.5.1 Description of the finite element model

Framework & Hypothesis Transient thermal modeling is applied to the same welding configuration as the previous section, *i.e.* three layers of PEI, as seen in Fig. 4.16. The composite specimens are 2 mm thick, and each PEI layer is 0.250 mm thick. A narrow transverse slice corresponding to the stacking of the three materials is designed in two dimensions in Abaqus. Therefore, a $1D$ conduction model is performed, allowing the obtention of the through-thickness thermal fields. To create this model, following assumptions are used:

i) The interfaces between the ED and specimens are perfect (no thermal contact resistance),

ii) No interphase is considered. The materials can only be PEI or PEEK/CF but not a mix of both materials because the material properties vary with the concentration of each material and are not yet measured,

iii) Only through-thickness properties of materials are used. Despite the thermal anisotropy of the composite, only the through-thickness behaviour is considered,

iv) The sonotrode, steel plates or other tools and their thermal behaviour are not considered,

v) Only conduction is considered (neither convection nor radiation).

With these hypotheses, this $1D$ conduction model gives us an approximate thermal evolution at any point of the stack and the evolution of temperature gradients over time.

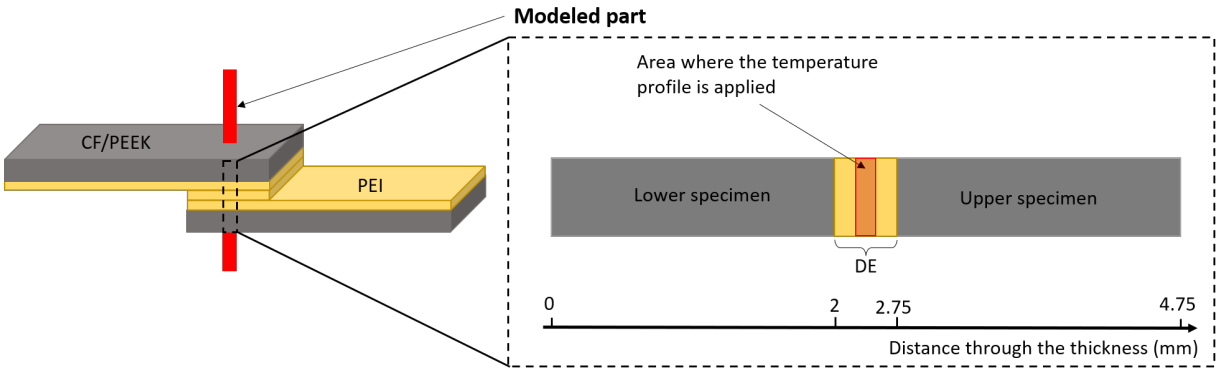

Figure 4.16: Through-thickness model of the welding configuration

Materials As the materials could evolve from a glassy state to a flow state or a molten state, temperature-dependent properties are used for PEEK in this model. These properties are presented in Table 4.1. Regarding PEI, the thermal properties used are presented in Table 4.2.

Temperature $(°C)$	Thermal conductivity $(W.m^{-1}.°C^{-1})$	Specific heat $(J.kg^{-1}.°C^{-1})$	Density $(kg.m^{-3})$
0	0.42	800	1601
50	0.52	930	1598
100	0.6	1040	1593
150	0.7	1260	1586
200	0.7	1300	1575
250	0.7	1400	1563
300	0.75	1550	1551
350	0.68	1650	1537
400	0.65	1700	1524

Table 4.1: Thermal properties of APC-2 [Ageorges et al., 1998]

Thermal conductivity $(W.m^{-1}.°C^{-1})$	Specific heat $(J.kg^{-1}.°C^{-1})$	Density $(kg.m^{-3})$
0.22	1248	1270

Table 4.2: Thermal parameters of PEI [Don et al., 1990]

Mesh elements Elements used for the model are four node linear heat transfer quadrilateral elements, called $DC2D4$ in Abaqus software. The mesh is composed of two elements

across the width of the studied area, as seen in Fig. 4.17. The three layers of PEI are meshed with 20 elements of 12.5 μm thick. The APC-2 layer is single bias meshed with an element size varying from 12.5 μm **to** 0.1 mm, and the mesh is increasingly finer near to the PEI layer.

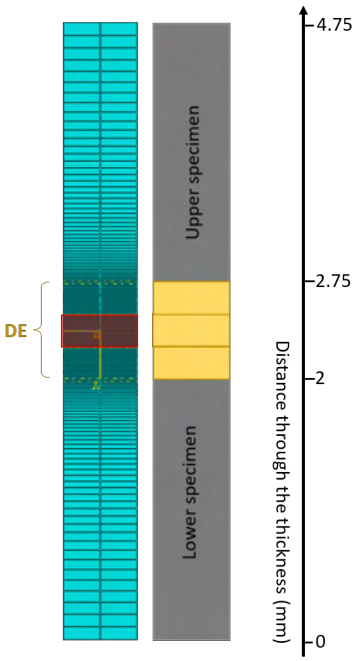

Figure 4.17: Mesh elements of the out-of-plane model

Initial condition As recorded experimentally, the initial temperature of the specimen is considered to be at 16 $°C$. Therefore, this initial temperature is applied to the whole model.

Thermal bondary conditions Adiabatic boundary conditions are used on the lateral sides and the upper and lower external surfaces of the specimens.

Thermal loading The recorded temperature profile, shown in Fig. 4.11, is applied to the PEI layer in red in Fig. 4.17. At $t = 0\ s$, the temperature corresponds to the initial temperature and his value is 16 $°C$. Then, temperature increases with a rate of 800 $°C.s^{-1}$ to reach its maximum value of 466 $°C$ at 0.573 s. This thermal profile is applied to the whole ED, *i.e.* the entire thickness of the intermediate PEI layer, because this layer is

not integrated to the specimens and subjected, on both faces, to the friction induced by the process. The vibration are likely to heat the entire thickness of this intermediate layer during friction phenomenon.

Steps & results Transient heat transfer analysis is used for this model and only the nodal temperature NT is computed as output data to understand the time and spatial evolution of the temperature field along the thickness of the assembly.
This model contains two steps corresponding to the heating phase and the cooling phase. The heating phase lasts 0.573 s as measured experimentally and the cooling phase lasts $t = 6\ s$.

4.5.2 Model results

Nodal temperatures are computed and their temporal evolution is compared, during the cooling phase, with the experimental thermogram recorded and plotted in Fig. 4.18. Two of the three curves correspond to different locations: $d = 2\ mm$ and $d = 2.25\ mm$, corresponding respectively to the interface between APC-2 and the integrated PEI layer and the interface between integrated and intermediate PEI layers.

Comparing the experimental value to the numerical thermogram at the interface between the integrated PEI layer and the free PEI layer ($d = 2.25\ mm$), location of the TC, a slight difference is highlighted. The model cools faster at the beginning exhibiting the lack of interface resistance that delays heat transfer. Then, the model cools slower and the experimental temperature becomes lower than the numerical one. It can be explained by either because input material data are from the litterature and do not fit with our material, or the model does not take into account some heat exchanges like convection or exchanges with the jaws (adiabatic upper and lower surfaces boundary conditions). Regarding the material, the composite substrate is made of unidirectionnal PEEK thermoplastic with carbon fiber. Thermal conductivity of carbon fiber is higher than the thermal conductivity of the PEEK and so, when the heat moves to APC-2 substrates, it is mostly evacuated by the fibers. Or, the through-thickness modelisation does not take into account transverse material properties and only propagate the heat through the thickness. Considering the end of the cooling phase, the difference between the two stabilized temperatures is around 20 $°C$, exhibiting that the model slightly overestimates the temperatures, that gives robustness of the model. Every simulated temperature could be considered a slightly overestimated.

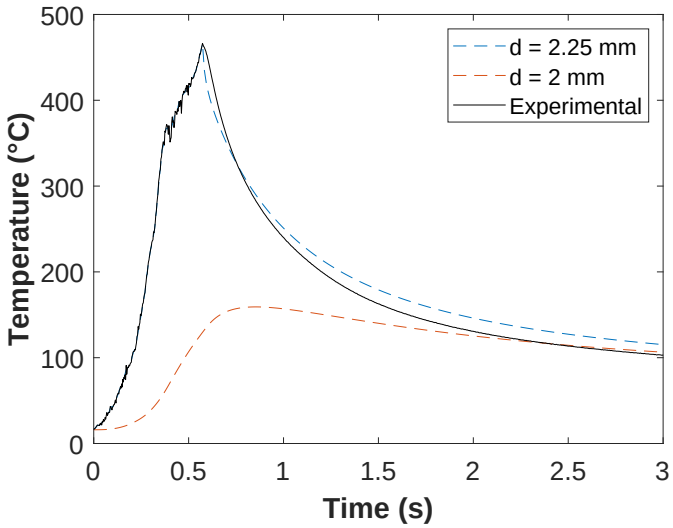

Figure 4.18: Experimental and numerical thermograms during welding process

Regarding the curve at the interface PEI/APC-2 ($d = 2\ mm$), the maximum reached temperature is 150 $°C$ and the time spent over the T_g(PEEK) is very short, and lasts around 0.520 s. The APC-2 substrate is very far from its melting point during welding in this configuration.

The spatial evolution of the temperature, right after the ultrasonic loading and during cooling phase, is plotted along the thickness in the Fig. 4.19. The x $axis$ corresponds to the through-thickness position with a reference value at the middle of the ED and y $axis$ is the temperature. Different welding times are plotted from $t = 0.573\ s$ (end of vibration step) to $t = 6.573\ s$ (end of the cooling phase). It can be noted that the profile is symmetric from the middle plane of the ED and, as expected, it is due to symmetry of the stacking sequence of the model (geometry, materials and section), the loading and boundary conditions. It can also be noted that the curves present breaking points at a distance of 2 mm (PEI/PEEK interface), 2.25 mm (PEI/PEI interface), 2.50 mm (PEI/PEI interface) and 2.75 mm (PEI/PEEK interface).

At $t = 0.573\ s$, as the thermal loading is applied to the entire thickness of this layer, the temperature of the ED is constant along its thickness reaching a value of 466 $°C$. The latter is above the glass transition temperature of PEI, measured at 220 $°C$, which implies that all the PEI is in the flowing state. Moving to the integrated PEI layer, $d \in [0.125\ mm\ ;\ 0.375\ mm]$, it appears that the temperature decreases from 466 $°C$ to reach 130 $°C$ at the interface with the composite layer. This thermal evolution higlights

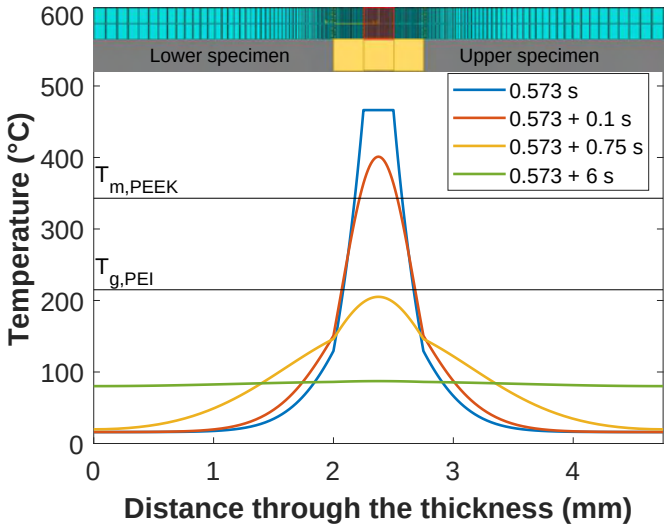

Figure 4.19: Temperature profiles through the assembly right after the end of the vibration step for different welding times

the fact that this layer, right after the ultrasonic loading, is partially in a flowing state (in a distance of 0.170 mm). The flowing material is located at the interface with the middle PEI layer and allows interdiffusion between those two PEI layers. Concerning composite parts, the maximum temperature reached during heating is 130 $°C$ that keeps it in a glassy state. The time $t = 0.573$ s is the starting point to the transfer of heat from the ED to the stack.

At $t = 0.673$ s, the heat flux has already started to be transferred from the middle PEI layer to the two integrated PEI layers. It can be noted that the two near ED breaking points are no longer visible due to the fact that the contact between middle and integrated PEI is considered to be perfect. The ED temperature decreases and its maximum temperature is around 400 $°C$ at the center of the ED. The heat moves from the center to the exterior, *i.e.* from the highest temperature to the lowest temperature. The temperature rapidly decreases as we move away from the interface. It is more difficult for heat to diffuse into the PEI because the thermal conductivity of PEI is lower than that of APC-2. It explains why the slope changes from PEI to APC-2. Focusing on the PEI layers, it appears that the temperature decreases from the ED to the interface with composite, with a temperature of 150 $°C$ at the interface compared to 130 $°C$ at $t = 0.573$ s. It proves that heat is moving from the ED to the exterior of the stack (upper and lower faces). The length of the PEI layer in a flowing state, above its T_g, is quite similar to the previous time, *i.e.* around 0.170 mm. Regarding the composite layer, its maximum temperature is 150 $°C$ at

the interface and only 26 μm are above its T_g giving mobility to the amorphous phase of the PEEK. However, at the interface between PEEK/CF and PEI, the PEEK is above T_g while PEI is in the glassy state: interdiffusion can not occur.

For the rest of the cooling process, it can be noted that the temperature at the center decreases while it increases at the end of the assembly reaching the quasi thermal equilibrium at 6.573 s.

In the studied configuration with 3 PEI layers, with a welding time of 573 ms, the temperature is above the glass transition temperature of PEI in almost the entire thickness of ED and in 170 μm in depth of the PEI layers at maximum. This indicates that interdiffusion is possible between the 3 PEI layers. Concerning APC-2, the maximum temperature reached is 150 $°C$. It can be assumed that PEEK matrix is not thermally affected during welding. This configuration gives the possibility to US weld without thermally affecting the composite parts, thus preventing part deconsolidation.

4.5.3 Influence of the number of PEI layers

The welding configuration seen in the previous section in Fig. 4.6 is modeled to predict the influence of the number of PEI layers. In that case, only one PEI layer is considered as the upper specimen is from a P2 plate, meaning that the PEI layer is already consolidated with the composite specimen. The lower specimen is only made of APC-2. Fig. 4.20 presents the mesh elements in this model. Besides, in that configuration, a temperature profile is applied where the ED comes into contact with the lower specimen. The same temperature profile as the previous model is used because of the difficulty to get viable experimental temperature profile in that configuration. All the other model conditions remain the same as in the previous section.

Fig. 4.21 shows the temperature profiles at different depths for this configuration. An asymmetric temperature distribution from the interface is visible. For $d < 2$ mm in Fig. 4.19, the heat is only dissipated in the lower CF/PEEK specimen. For $d > 2$ mm, the heat is first dissipated in the PEI layer and then in the upper CF/PEEK specimen. As mentioned before, the thermal conductivity of PEI is lower than APC-2, it is more difficult for heat to diffuse into the PEI. Therefore, the temperatures are lower in the PEI layer than in APC-2 for an equivalent distance from the interface. Moreover, the heat diffusion is very fast: after 3 seconds, the temperature reaches a quasi-homogeneous temperature at about 120 $°C$ in the whole studied geometry.

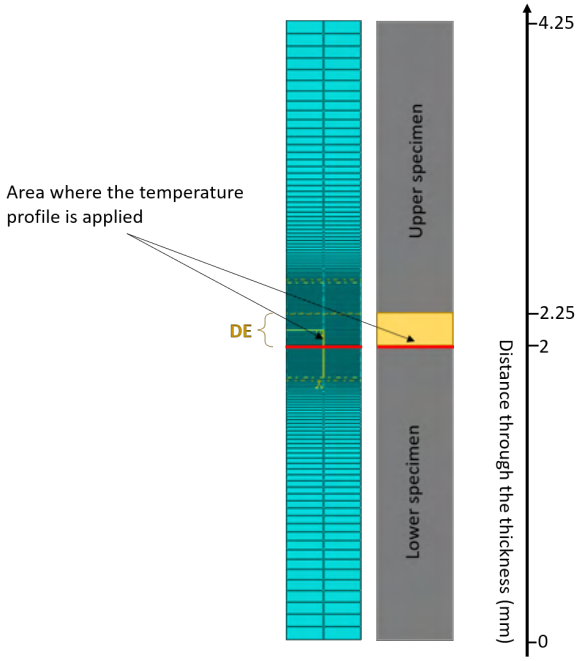

Figure 4.20: Mesh elements of the out-of-plane model with one PEI layer

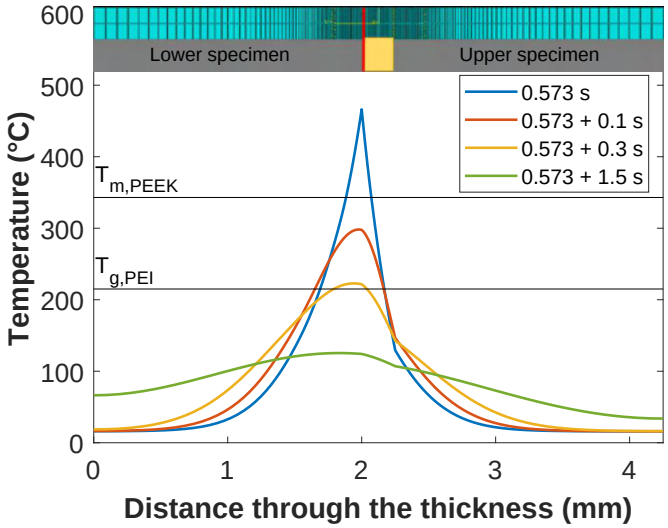

Figure 4.21: Temperature profiles through the assembly right after the end of the vibration step for different welding times for a one PEI layer configuration

Fig. 4.22 shows the evolution of temperature over time at different locations throughout the assembly. Predictably, the highest temperature is at the interface. The same trend seen earlier, that the temperature is lower in the PEI layer than in APC-2, is also observed here. For the same distance from the interface, the maximum temperature on the PEI layer ($d = 2.125\ mm$) is lower than the one located in APC-2 ($d = 1.875\ mm$) because of their respective thermal conductivity. At longer times, the temperatures tend to a plateau around 120 $°C$ which is the same as the plateau seen in Fig. 4.21. It is also found that the temperature exceeds the melting temperature of PEEK only in the first ply of the lower specimen and in the ED, considering that the thickness of a ply is 125 μm. With this welding configuration, which consists of a specimen with a PEI integrated layer over a CF/PEEK, PEEK and PEI must be assembled. For this, PEEK needs to melt to allow chain diffusion while avoiding degradation or deconsolidation in the material thickness. The modeling does not consider the flow of the PEI layer. In reality, the polymer is heated and then it partially flows at the interface. This results in the two APC-2 specimens being slightly closer, probably modifying the temperature.

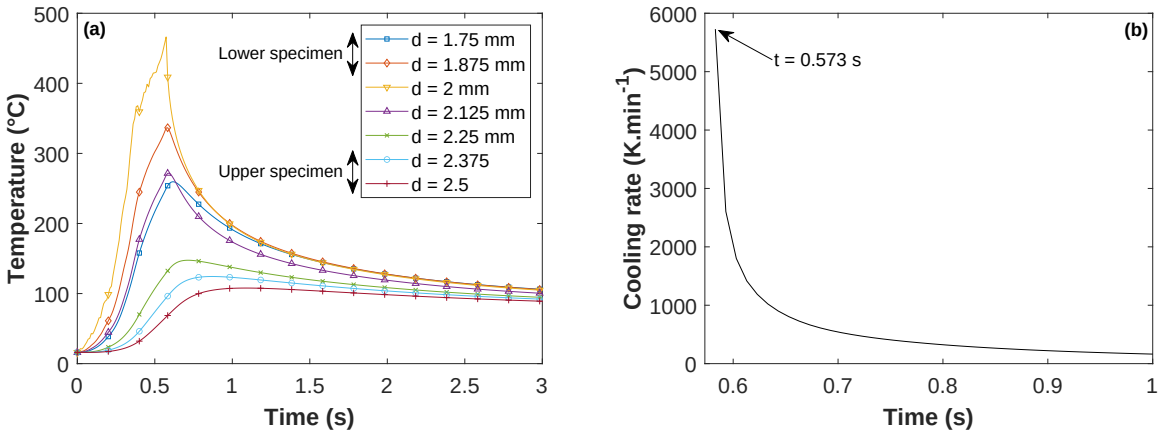

Figure 4.22: Temperature evolution at different location through the interface (a) and cooling rate evolution at the interface (b)

The cooling rates near the interface are evaluated from Fig. 4.22 (a). These cooling rates are determined from the end of the vibration phase. The PEI layer also influences the cooling since the cooling rates are different for the same depth in the two composite specimens. The cooling rates are lower on the polymer layer side because PEI is a less efficient heat conductor. The highest cooling rate is found at the interface (about 6000 $K.min^{-1}$, *i.e.*, 100 $K.s^{-1}$) and decreases as the distance from the interface increases, as seen in Fig. 4.22 (b). The cooling rates are very high and remain high after 0.1 s of cooling (from 100 $K.s^{-1}$ to 10 $K.s^{-1}$). These speeds are much higher than those used to perform DSC

tests (a few degrees per minute) and make the crystallinity evaluation difficult to predict. Nevertheless, the DSC results could be implemented in a model allowing the extrapolation to faster cooling speeds.

The one-layer welding configuration shows that the first layer of APC-2 reaches the melting temperature of PEEK. The crystallinity of the specimens can be altered and the composite ply can be deconsolidated. Squeeze flow of this first ply is also a possiblity and it has been experimentally observed. Those phenomena would contribute to lower the mechanical resistance of assemblies. However, in this configuration, it is necessary to reach the melting temperature of PEEK to obtain a PEEK/PEI welding. It requires more energy than the previous section, where only the glass transition temperature of PEI was necessary. Also, the model consisting of three PEI layers shows the PEEK is not thermally affected by the welding. So, a configuration with more PEI layers is considered as the best option for effective welding.

4.6 Conclusion

This chapter focuses on the temperature profiles during welding. A non-intrusive experimental procedure was developed to measure the temperature at the welding interface. K-type thermocouples were implemented into the PEI layer of the specimens. It was observed that the thermocouples must be inserted entirely inside the layer, otherwise they can alter the temperature measurement. The procedure does not significantly modify the polymer layer thickness.

A post-synchronization method was developed using power values during welding. Indeed, the power value can be measured by the processing unit and by the welder itself. The two power curves are identical as they are different from zero only when the vibration stage occurs. Therefore, the temperature profiles can be linked to output data from the welder, such as displacement of the sonotrode. Combining these data gives a deeper understanding of the physical phenomena happening during welding. The temperature profiles were first measured with short impulsion times on one specimen. It has been seen that heating rates are similar and very fast, around 1000 $K.s^{-1}$, demonstrating good repeatability.

Typical welding curves have shown that different stages and specific points can be identified: heating, flowing of PEI, final flowing and cooling. This study also focuses on the influence of welding parameters (welding load, amplitude and welding time) on the temperature profiles. As the interface is a closed contact during welding, measuring the

temperature at the interface is tricky. We were able to provide thermal profiles from micro thermocouples located close to the interface. The welding load has shown to have a strong influence on thermal history. The maximal temperature was achieved at 1000 N close to 580°C but for a short time, ensuring diffusion of PEI chains while avoiding the degradation of the PEEK matrix. The amplitude does not appear to have a strong influence since the curves look quite similar. The temperature profiles have shown, however, a strong dependency on welding time. At 1000 ms, the temperature curves seem to have reached a plateau that can favor the diffusion of polymer chains.

Finally, a finite element model was developed to evaluate the thermal diffusion from the interface to the edges of the specimens. In a three PEI layers welding configuration, PEEK is not thermally affected as the temperature does not exceed the melting temperature of PEEK in the first ply. On the contrary, in the case of a one PEI layer, the first ply goes above T_m(PEEK). Energy consumption would be more important in that case. It is easier to weld in a three layer configuration as only the T_g of PEI has to be reached to get macromolecular interdiffusion.

Chapter 5

Mechanical & morphological analyses of CF/PAEK welds

Contents

5.1 Introduction 122

5.2 Mechanical properties of CF/PEEK composite welds using a PEI energy director 122

5.2.1 Single lap shear test 122

5.2.2 Influence of welding parameters 123

5.2.3 Influence of the number of PEI layers 127

5.2.4 Influence of the ED nature 130

5.2.5 Analysis of the sonotrode final displacement 132

5.3 Characterization of the interphase & analysis of fracture mechanisms 134

5.3.1 Interfacial fracture mechanisms 134

5.3.2 Composition of PEI/PEEK interphase in the welded zone 137

5.3.3 Properties of PEI/PEEK blends 142

5.4 Ultrasonic welding of AE 250 composites 152

5.5 Conclusion 156

5.1 Introduction

This chapter focuses on the mechanical properties of welds of both PEEK and AE 250 composite specimens. Several parameters are investigated, such as welding parameters, the number of PEI layers, and the nature of the ED. Single lap shear tests are conducted to quantify the mechanical strength of assemblies. After mechanical testing, interfacial fracture analyses are conducted through SEM, Raman spectroscopy and optical microscopy. PEEK/PEI blends are analyzed through rheological, thermal and mechanical analyses to evaluate the properties at the welding interface. Moreover, the final sonotrode displacement for different sets of welding parameters is investigated to understand its influence on the mechanical strength. Finally, a comparison between CF/PEEK welds and CF/AE 250 welds is conducted.

5.2 Mechanical properties of CF/PEEK composite welds using a PEI energy director

5.2.1 Single lap shear test

Single lap shear (SLS) tests were conducted on an INSTRON 5800R testing machine, following the NF EN 2243-1 standard. Parallel shifted clamping jaws are used to avoid samples bending as much as possible in order to localize the fracture through the welded interface, as seen in Fig. 5.1. The experiments were conducted at a constant load rate of 2800 $N.min^{-1}$. The single lap shear strength (LSS) is deduced from equation (5.1). The contact area between the two specimens is 25 x 10 mm^2 and the specimen dimensions are 25 x 100 x 2 mm^2. The experiments are conducted for the same welding configuration as in the previous chapter (three PEI layers at the interface, *i.e.* 750 μm of PEI before welding). At least 5 SLS tests were performed for each set of welding parameters to estimate LSS results dispersion.

$$LSS\ (MPa) = \frac{Maximum\ load\ (N)}{Contact\ area\ (mm^2)} \tag{5.1}$$

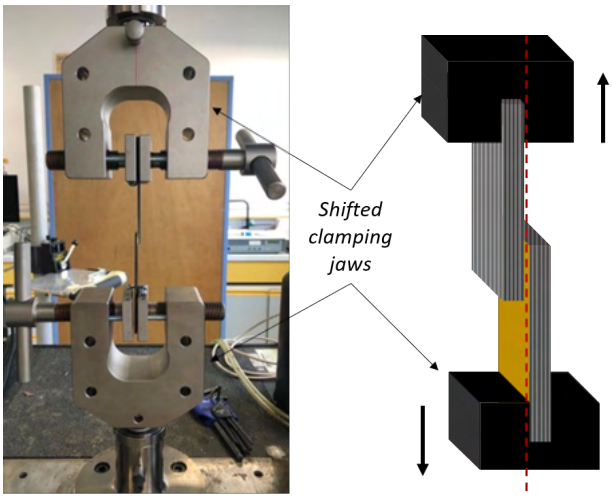

Figure 5.1: Single lap shear experiment layout

5.2.2 Influence of welding parameters

Single lap shear tests were carried out in order to evaluate the mechanical properties of the welds, and the results are shown in Fig. 5.2, 5.4 and 5.5. The error bars are a graphical representation of the standard deviation. Fig. 5.2 shows the LSS results for the different values of welding load investigated. The LSS tends to increase up to a maximal value of 49 MPa at 1000 N. After that, the LSS starts decreasing. Before 1000 N, it can be assumed that the intimate contact between the two specimens is not sufficient. As a consequence, the friction of the specimens is too low to induce local heating over the total contact area. Even if the temperature would reach the flowing temperature of the polymers, the contact area is too low to allow the macromolecular chain of PEI to diffuse and entangle at the interface.

The fracture surfaces after lap shear tests have been observed by optical microscopy to understand the crack propagation within the interphase. The interfacial fracture surface at 500 N reveals two different fracture mechanisms as can be seen in Fig. 5.3 (a). For all fractures, only one side of each specimen is presented. Firstly a failure occurs within the PEI layer as shown by the absence of fiber in the right of the picture. The other mode is a failure within the CF/PEEK layers, as fibers are observed on the left of the same picture. A deeper analysis of the fracture modes is presented in Section 5.3. At 1000 N and 1200 N, respectively Fig. 5.3 (b_1) and Fig. 5.3 (b_2), a failure within PEI also takes place but over a smaller surface than 500 N, explaining why the mechanical properties are lower at 500 N. Indeed, a failure located within the composite is better

because it shows that the PEI bond at the interface is stronger than the adhesion between CF/PEEK layers within the specimens. However, when increasing the welding load above 1000 N, the LSS decreases, but the one at 1200 N remains higher than the one at 500 N, as CF/PEEK failure is prevailing at 1200 N. Unmelted areas of PEI are also observed in Fig. 5.3 (b_3) at 1400 N, which would suggest that the vibration was not sufficient to melt the energy director homogeneously. It is also worth noting that at 1500 N, the specimens are not welded at all, meaning that the welding load was too high to allow any sonotrode vibration to occur. From this, we can conclude that welding over 1200 N hinders the sonotrode vibration.

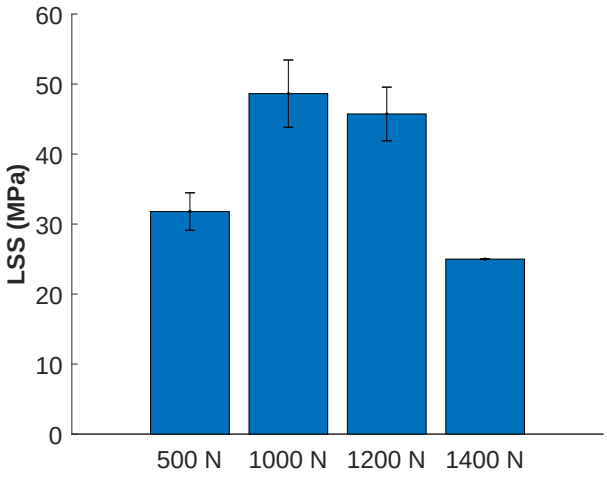

Figure 5.2: Lap shear strength for different values of welding load (amplitude: 32 μm and, welding time: 600 ms and 750 $\mu m-$thickness energy director)

Fig. 5.4 presents the LSS values for three amplitudes. An amplitude modification does not significantly influence the mechanical performance since the LSS values are quite similar. Besides, it was observed in Fig. 4.13 (Chapter 4) that the temperature and travel curves had a similar shape, further underlining the weak influence of amplitude on the mechanical properties of the welded interface. It is worth noticing that the LSS value at 48 μm appears to be slightly higher than the others. As seen in Fig. 4.13, it is also the same amplitude that demonstrated the highest travel during welding. This shows that a greater squeeze flow induces a higher LSS property, as explained by Smiley et al. [Smiley et al., 1991], who welded CF/PEEK substrates during an oven Thermabond™ process with a PEI film at the interface, similar to our US welding configuration. Moreover, the interfacial fractures in Fig. 5.3 (c_1) and Fig. 5.3 (c_2) also look similar, with a failure within the PEI layer on one side and a failure within the composite on the other.

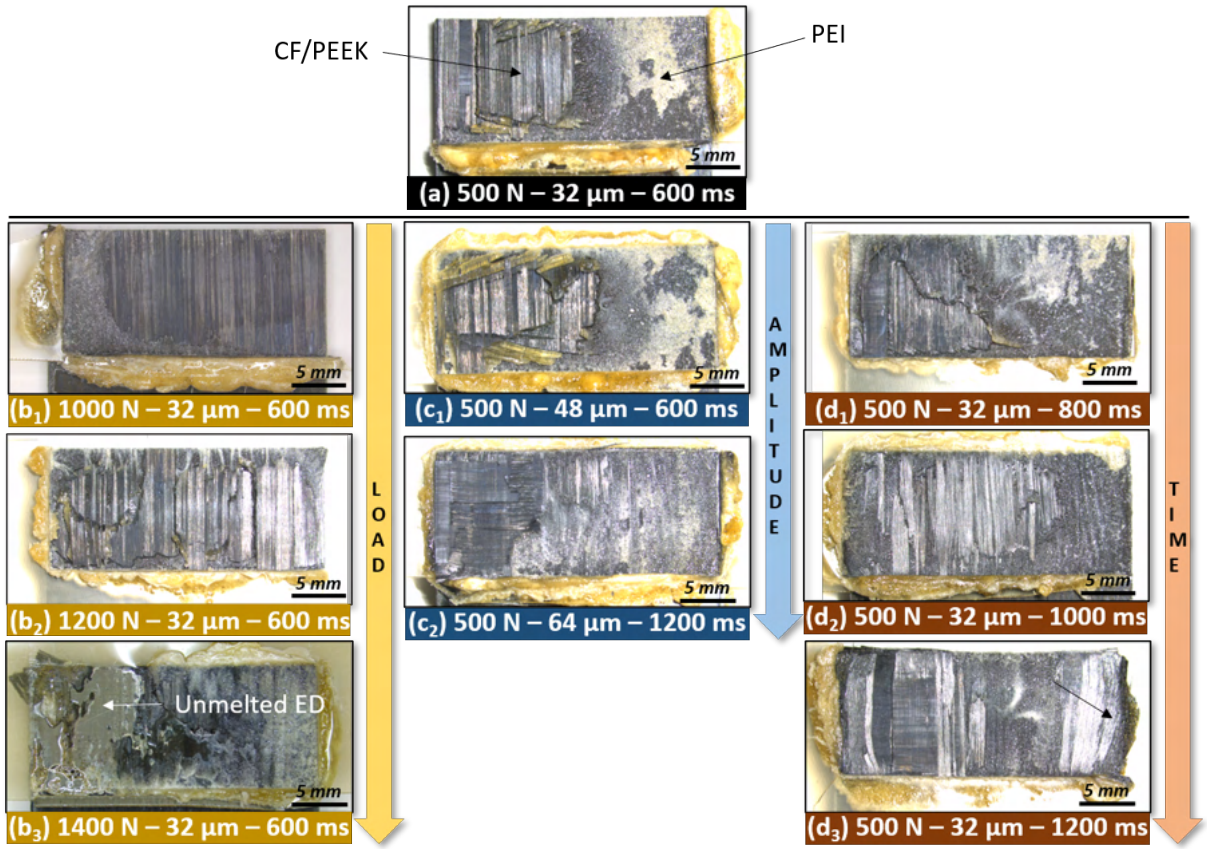

Figure 5.3: Interfacial fracture of welded specimens in several welding conditions

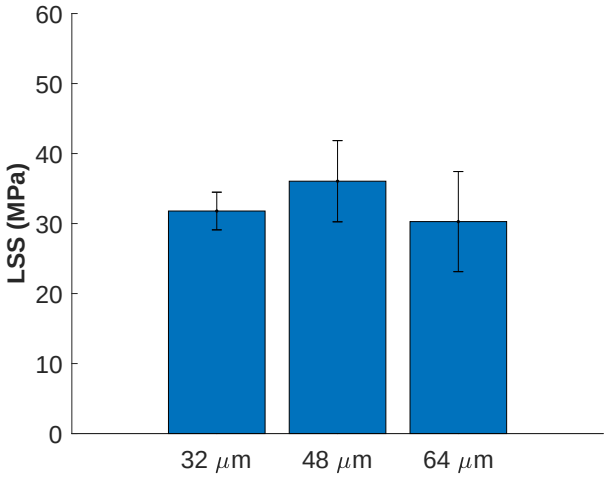

Figure 5.4: Lap shear strength for different values of amplitude (welding load: 500 N, welding time: 600 ms and 750 $\mu m-$thickness energy director)

The LSS values for several welding times are plotted in Fig. 5.5. LSS values tend to increase when increasing the welding time. Welding times under 1000 ms, Fig. 5.3 (a) and Fig. 5.3 (d_1), are presenting cohesive failures within the PEI layer for almost half of the welded surface, explaining their lower LSS. This confirms the hypothesis made in Fig. 4.12 that 1000 ms is a suitable welding condition. At 1000 ms, LSS values are slightly lower than the maximum found when investigating the influence of the welding load (*i.e.* 49 MPa). This could be explained by the interfacial surface of the weld. The fracture surfaces look similar with a majority occuring within the PEI interface. However, the fracture at 1000 ms seems to have a little bit more PEI fracture on the right side, as seen in Fig. 5.3 (d_2). At 1200 ms, a maximum LSS of 46 MPa is achieved, despite the fact that PEEK and carbon fibers have started to flow on one side (black arrow on the picture in Fig. 5.3 (d_3)). Another hypothesis might be that lap shear test is not an optimal option to evaluate the mechanical strength of welded joints as some mechanisms (*i.e.* flow of PEEK and carbon fibers) are not quantified with this technique. To conclude this section, the welding time has a strong influence on the mechanical properties as it increases the LSS. The limitation is when PEEK and carbon fibers start flowing at the edges of the welded area, decreasing mechanical strength linked to the alignment of the fibers. Thus, it can be assumed that a longer time (*i.e.* above 1200 ms) would not imply an LSS increase since the polymer matrix and carbon fibers would likely squeeze and flow even more, and LSS would drop.

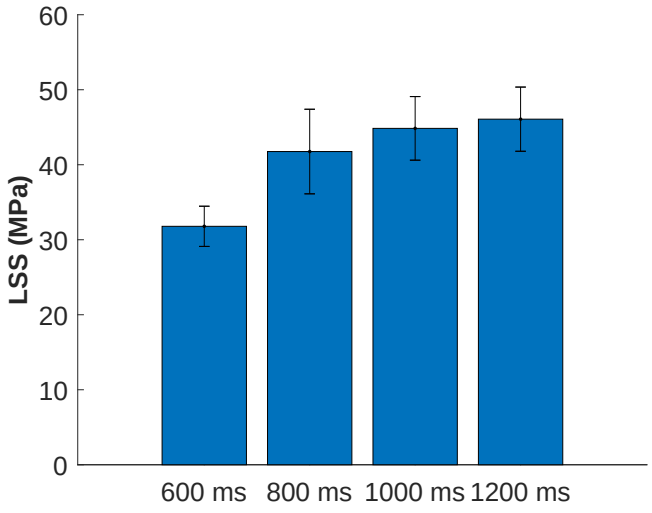

Figure 5.5: Lap shear strength for different values of welding time (amplitude: 32 μm, welding load: 500 N and 750 $\mu m-$thickness energy director)

For all welding loads except 1400 N, the values of LSS seem competitive with what can be found in the literature. Tsiangou et al. [Tsiangou et al., 2020] reached 43 MPa using similar materials (CF/PEEK and $250-\mu m-$thick PEI energy director). Villegas et al. [Villegas, 2014] found LSS values at 39 MPa for CF/PEI specimens with a PEI energy director and 35 MPa for CF/PPS specimens with a PPS energy director [Fernandez Villegas and Palardy, 2017]. Tao et al. [Tao et al., 2019] worked on US welding of CF/PEEK associated with a PEEK energy director and measured a LSS at 28 MPa. Regarding other bonding processes, it was found by Li et al. [Li et al., 2021] a 46 MPa value of LSS for CF/PEEK resistance welded joints and a 49 MPa value by Smiley et al. [Smiley et al., 1991] using Thermabond™ process on CF/PEEK specimens with a PEI interlayer. Those last results show that ultrasonic welding of CF/PEEK using a PEI energy director compete with industrially advanced bonding processes.

LSS is the most widely used mechanical test to characterize the interfacial resistance of welded assemblies: it is easy to implement and does not require any specimen preparation. Even if LSS is suitable for comparing welding conditions, it does not give information on the crack propagation resistance, unlike cleavage or double cantilever beam (DCB) tests for measuring the initiation and propagation values of Mode I fracture energy G_I. Moreover, the comparison of LSS values of US welding to other welding processes is not deeply evident since the whole thermomechanical history undergone during the process impacts the mesostructure of the welded specimens. Depending on the process, either the entire thickness or only the interface area is melted. Therefore, the final morphology or cristallinity of the materials can vary from one process to another due to the impact of the cooling rate.

5.2.3 Influence of the number of PEI layers

The number of PEI layers is investigated to determine the influence of ED thickness on the mechanical properties of welds. As amplitude does not seem to significantly impact the mechanical properties of joints, an amplitude of 32 μm is chosen for all further assemblies. As PEI is supplied as a 250 μm thick film, multiples of this value are used in this section. Fig. 5.6 presents the different configurations, from A to D. Configuration A is the one that has been previously used for the process parametric study. Configuration B uses two specimens from a P2 plate, *i.e.* one PEI layer implemented on each composite specimen before welding (see Chapter 2). Configuration C uses only one layer of PEI: configuration C1 is a free layer taped between the specimens, whereas C2 is one specimen made from a P2 plate and the other one made only of APC-2. Finally, configuration D does not use

any PEI layer at the interface.

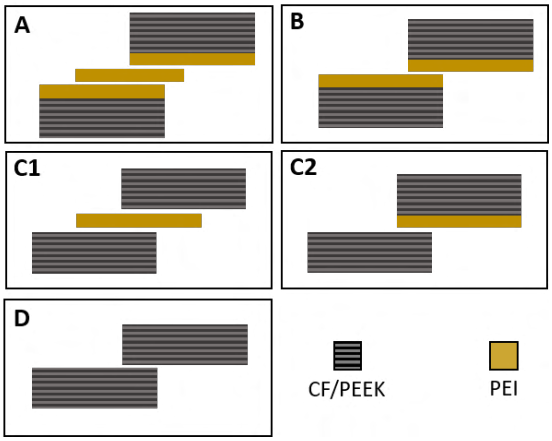

Figure 5.6: Welding configurations using different numbers of PEI layers

Three welding parameters sets have been used in this section. The first one is the reference parameter set (welding load of 500 N, amplitude of 32 μm and welding time of 600 ms). Then, the two conditions giving maximal LSS when investigating the influence of welding time and welding load: meaning 500 N – 32 μm – 1000 ms and 1000 N – 32 μm – 600 ms. The results are plotted in Fig. 5.7.

Overall, the LSS tends to decrease when decreasing the number of PEI layers for every welding parameter set, meaning that the number of PEI layers influences the mechanical properties. Configurations A and B display high LSS values for the optimal welding conditions obtained in the previous section (blue and red bars in the graph). The highest value is found at 50 MPa for the configuration A, a welding time of 600 ms and a welding load of 1000 N. Nonetheless, LSS values seem to be clustered either above 30 MPa or below 15 MPa. It highlights that using those welding parameters leads to either excellent bond or no adhesion occurs at all. Indeed, around or below 15 MPa, the adhesion is insufficient to provide a strong bond since the joint can be broken using one's own hands. Above 30 MPa, the evolution of LSS value tends to be linear. However, the slope is different for each parameter set. Indeed, the biggest slope is observed for high welding load (1000 N, in red in the graph), followed by high welding time (1000 ms, in blue in the graph) and average welding time and load (yellow in the graph). It means that the number of PEI layers impacts in different ways the evolution of LSS above 30 MPa, depending on the welding parameters. An hypothesis is that the polymer is not heated precisely the same way when welded with the different welding parameters. It has been seen in Chapter 4 that a welding time of 1000 N allows the polymer to stay above the T_g of PEI longer than

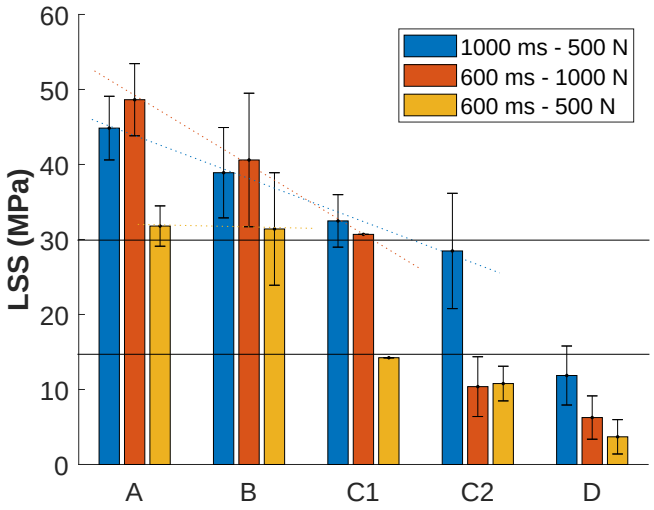

Figure 5.7: Lap shear strength for different numbers of PEI layers and for three welding parameter sets

for other welding conditions, allowing more time for the polymer to diffuse and entangle.

Also, the configurations leading to LSS above 30 MPa depends on the welding parameters. For example, only one welding parameter (high welding time) set leads to a high LSS value for configuration C2, whereas they are two for C1 and all of them for A and B. High welding time is more likely to lead to high mechanical strength without regard to the welding configuration. Fig. 5.8 illustrates that the configurations A, B, C1 and C2 all show interlaminar fractures, explaining the high LSS. C2 LSS is a bit lower, but it is explained by the presence of a small unmelted area in the welding zone. Configurations C1 and C2 have the same number of PEI layers. However, they exhibit different mechanical strengths. LSS is higher in the case of C1 whatever the welding parameter sets. The free PEI layer (C1) is thus more efficient than the integrated PEI layer (C2). The free movement of configuration C1 increases the friction phenomenon and the polymer is heated more efficiently than in configuration C2. However, for further industrial implementation, it is worth noting that it would be easier to weld specimens with an integrated layer, since it does not require a step like taping PEI between the specimens for configuration C1.

Also, some polymer degradation is seen by dark brown color of the matrix as well as fiber displacement at the edges for configuration C, explaining the lower LSS value compared to configurations A and B. The configuration D displays the lowest values of LSS since they all are below 15 MPa. The interfacial fracture in Fig. 5.8 shows that welding does

not impact almost half the welding area while fibers and PEEK have started to flow at the edges of the contact area. Since less polymer is present at the interface, the fibers are reached early in this configuration. The presence of the fibers hinder the diffusion of the PEEK matrix for consolidation of the interface. It shows that a polymer-based layer at the interface is mandatory to ensure a good joint.

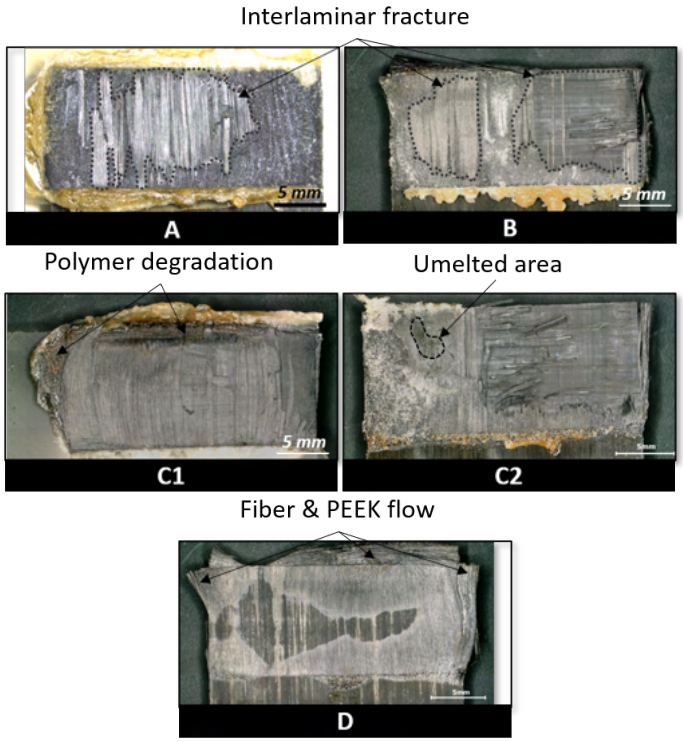

Figure 5.8: Interfacial fracture of welded specimens for all welding configurations (A, B, C1, C2 and D), for a welding time of 1000 ms and a welding load of 500 N

5.2.4 Influence of the ED nature

This section evaluates the mechanical strength using two energy directors: PEI or PEEK layers. The results for PEI come from section 5.2.1 and they are compared with PEEK ones. Only the welding time is changed for the comparison of PEI and PEEK because it was shown previously that increasing the welding time is more likely to lead to high-strength welds. The welding load is 500 N, and the amplitude is 32 μm. The welding configuration is B for both PEI and PEEK. PEEK specimens come from P3 plates, *i.e.* a PEEK film is added on top of the plate during manufacturing.

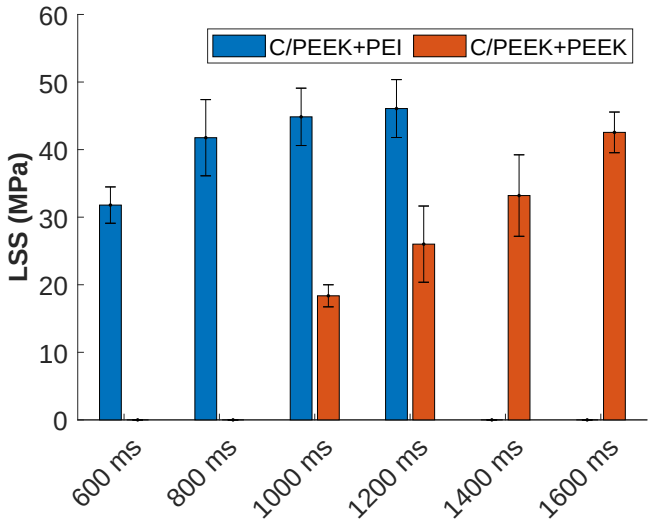

Figure 5.9: Lap shear strength for different welding times and for a PEI and a PEEK energy director (welding load: 500 N and amplitude: 32 μm)

LSS results are plotted in Fig. 5.9. As PEI energy director, LSS values using PEEK ED increase when increasing the welding time. The highest LSS value, 43 MPa, with PEEK is reached for 1600 ms, similar to the highest LSS with PEI. This result is in accordance with a LSS of 45 MPa found by Tsiangou et al. [Tsiangou et al., 2020] for CF/PEEK welds using a 250 μm thick PEEK energy director. The trends in the graph are similar, but the LSS values of PEEK are shifted towards longer welding times. As expected from the thermal transitions of both materials, the welds using a PEEK ED need more time to melt the interface and to allow sufficient diffusion of polymer chains at the interface. Fig. 5.10 demonstrates that for all welding times, unmelted zones are still found in the welding area. The mean relaxation time of PEEK 450G, which is related to the movement of long chains, was found at 1600 ms for a temperature of 400 $°C$ in Chapter 3. Also, temperature profiles in Chapter 4 showed that the maximal temperature is around $400 - 450$ $°C$ for welding of PEEK/CF with a PEI energy director. We assume that similar temperature ranges are reached when using PEEK energy director. Tsiangou et al. [Tsiangou et al., 2020] have found that temperature profiles are similar for CF/PEEK composite welded with both PEI and PEEK energy directors. Therefore, the mean relaxation time at 400 $°C$ is chosen to analyse these experiments and it is compared with the time during which the temperature remains above the melting temperature. Based on previous temperature profiles from Chapter 4, the increase in temperature is fast and exceeds the melting temperature of PEEK in around 300 ms. During cooling, the temperature remains above T_m for at

least 200 ms, suggesting that the welding time is similar than the time during which $T > T_m$. Therefore, when the welding time is 1600 ms, the chains remain above the melting temperature of PEEK for a time in the same order of magnitude as τ_w. The chains need at least around 1600 ms to move and diffuse through the welding interface, explaining why big unmelted areas are observed under 1600 ms. From 1.4 s, the fibers start to move at the edges and become the predominant mechanism at 1.6 s, even though the highest LSS is obtained for this welding parameter. Unlike PEI, more fibers seem to flow without impacting the mechanical strength. This phenomenon shows again that lap shear tests alone are not sufficient to quantify the mechanical strength of ultrasonically welded joints. Welding times longer than 1600 ms could lead to higher LSS values, closer to the ones with PEI. However, the damage in the welded area would be too important to be industrially acceptable. Overall, those results show that it is easier to weld with a PEI energy director than with a PEEK one.

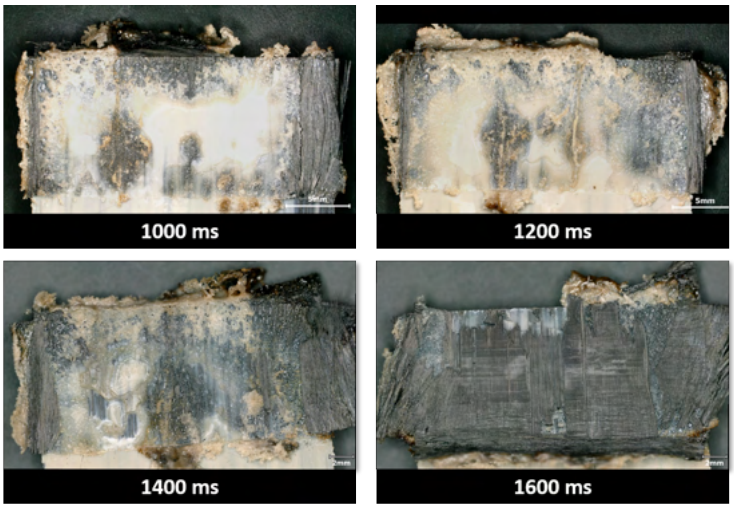

Figure 5.10: Interfacial fracture of welds for welding times of 1000 ms, 1200 ms, 1400 ms and 1600 ms and a PEEK energy director (welding load: 500 N, amplitude: 32 μm)

5.2.5 Analysis of the sonotrode final displacement

The sonotrode displacements from output data are analyzed. The welding parameters are not considered in this section. Only the LSS value and its associated final sonotrode displacements are considered because it removes the uncertainty linked to the LSS standard deviation for one welding parameter set. Fig. 5.11 (a) features the LSS value as a function

of the displacement of the sonotrode in configuration A for welds using a PEI energy director. The initial thickness of the energy director is around 750 μm.

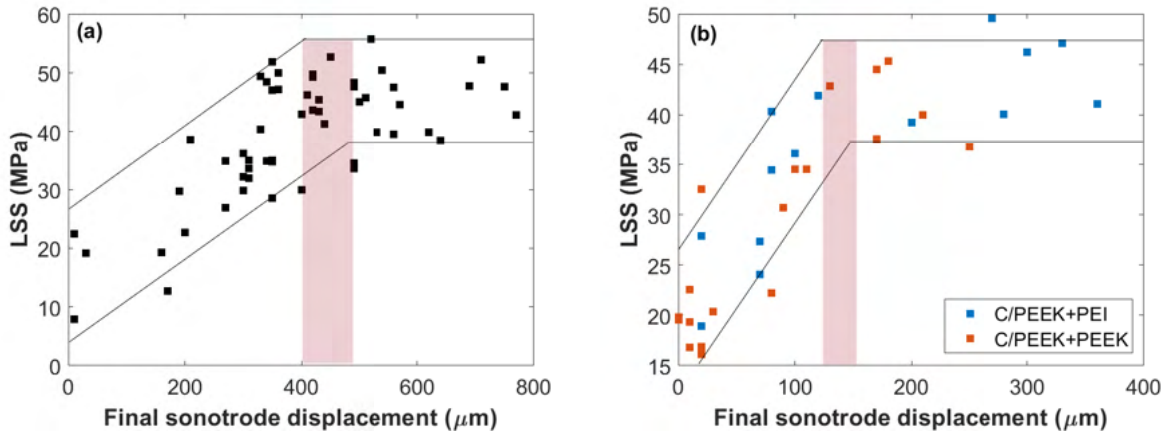

Figure 5.11: Final sonotrode displacements for CF/PEEK welds with PEI ED in configuration A (a) and for CF/PEEK welds with PEI and PEEK ED in configuration B

When plotting the LSS values with the final sonotrode displacement, it is clear that the LSS increases when the final sonotrode displacement increases. However, a plateau is reached for the highest value of LSS when the final sonotrode displacement is around $400 - 500$ μm. Since the sonotrode displacement matches the flow of PEI, it is assumed that the final thickness of the PEI is the difference between its initial thickness and the final sonotrode displacement. Therefore, when the ED has lost $400 - 500$ μm of its initial thickness, the LSS does not increase significantly. The final thickness of the PEI interface would be around $250 - 350$ μm. It is thus not useful to continue the welding test, as longer welding time lead to similar LSS.

Fig. 5.11 (b) shows the LSS values as a function of the final sonotrode displacement in configuration B with PEI and PEEK energy directors. The same trend is observed as Fig. 5.11 (a). LSS increases when the sonotrode is going down, up to a threshold reached around 150 μm for which the LSS remains stable for both ED. The threshold is obtained for lower final sonotrode displacement because the initial ED thickness is lower (500 μm for configuration B and 750 μm for configuration A). In that case, the final thickness would be around 350 μm, in the same range as configuration A. It seems that a final thickness of around 350 μm would lead to the highest LSS in the shortest time, no matter the material used as ED or its initial thickness. For all these tests, the welding was controlled using time, meaning that the ultrasound phase lasted for a defined duration. A displacement control of the process could be a way to ensure that this final thickness of 350 μm is

obtained. Indeed, it is possible to monitor the end of the ultrasound phase by choosing a final displacement [Fernandez Villegas and Palardy, 2017, Villegas, 2014, Palardy and Fernandez Villegas, 2017, Fernandez Villegas and Vizcaino Rubio, 2015]. The ultrasound phase will continue as long as the final displacement is not reached.

5.3 Characterization of the interphase & analysis of fracture mechanisms

5.3.1 Interfacial fracture mechanisms

Different fracture mechanisms were highlighted in section 5.2, *i.e.* a rupture within the PEI interphase and a rupture within the CF/PEEK layers. The hereby section aims to go deeper in analyzing the fracture mechanisms. Fig. 5.12 shows SEM images of PEI-localized fracture (5.12 (a)) and PEEK-localized fracture (5.12 (b)). PEI-localized fracture seems to be associated with brittle-type fracture whereas PEEK-localized fracture is a combination of brittle and ductile fractures. When considering brittle fracture in PEEK, cracks appear to initiate on one side at the fiber/matrix interface and to propagate transversaly until they reach another fiber. In other zones, a rugged surface stems from the stretching of the polymer matrix, representative of a ductile fracture.

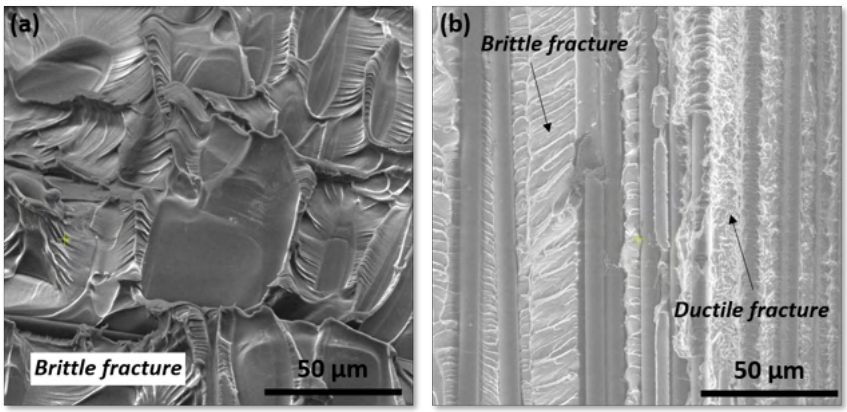

Figure 5.12: SEM micrographs of PEI-localized fracture (a) and PEEK-localized fracture (b)

Moreover, another type of fracture is observed in our specimens: fiber breakage. Fig. 5.13 (a) displays fracture within a CF/PEEK layer where fiber fracture is predominant.

Most of the fiber surfaces are smooth, indicating a poor fiber/matrix adhesion. It suggests that fracture within the composite specimen is cohesive, *i.e.* within a CF/PEEK layer as seen in Fig. 5.13 (b). In this scenario, the crack initiates close to the PEI-rich zone and propagates inside the first CF/PEEK ply. Fig. 5.14 shows the interfacial fracture of a weld that exhibits both cohesive and adhesive failure within APC-2 plies. The three images show the same weld but from different points of view. Fig. 5.14 (a) is an optical micrograph from the entire welding area after the lap shear test. Fig. 5.14 (b) and (c) are SEM images of the same location (white square in Fig. 5.14 (a)) from different point of views (orange and blue arrows). The full red arrows point out a fracture between two APC-2 plies (the first and second plies). Indeed, fiber imprints in the perpendicular direction of the first layer can be seen, meaning that the fracture happened between two plies. The red dotted arrows show fibers from the first ply. In that case, the fibers have been pulled out, confirming that a cohesive fracture within one ply occurs.

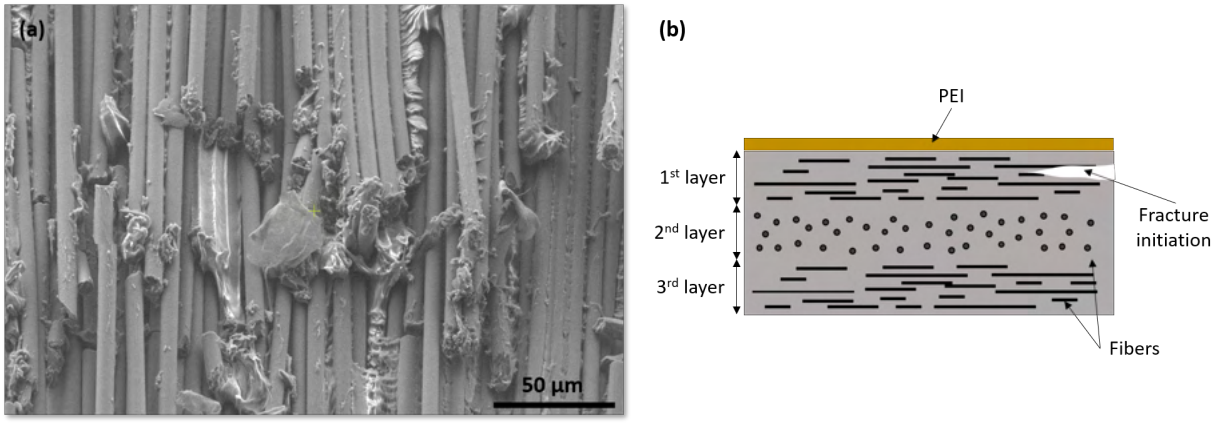

Figure 5.13: Cohesive failure within the CF/PEEK layer

For the welding conditions leading to LSS above 30 MPa, the welded surface is very rugged. An example is presented in Fig. 5.15. In this SEM image (Fig. 5.15 (a)), two layers of PEEK/CF are visible, separated by a PEI-rich interphase. It is obvious that the visible layers of CF/PEEK are not from the same composite specimen from the height difference of 250 microns mesured by optical microscopy (Fig. 5.15 (b)). The layer on the left belongs to the lower specimen whereas the layer on the right belongs to the upper specimen. An hypothesis is that cracks initiate in both welded PEEK/CF specimens. When propagating from one specimen to another, the cracks go through the PEI-rich interphase, giving rise to this rough surface. In the interfacial zone, PEEK and PEI are blended due to their miscibility. The concentration gradient of PEI comes from the manufacturing of welding specimens (see in Chapter 2). During manufacturing, the cycle time is long enough to

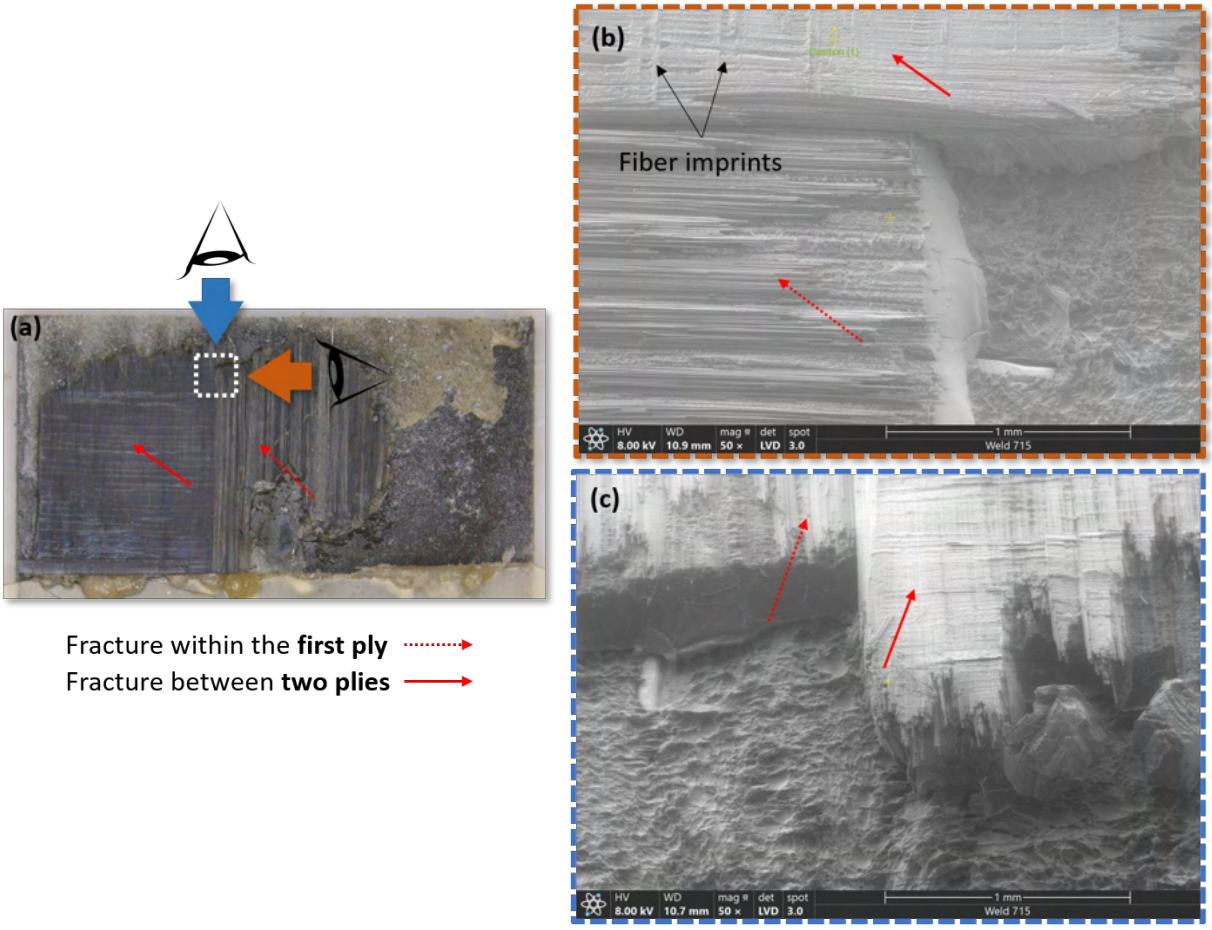

Figure 5.14: Interfacial cohesive failure APC-2 plies through SEM and optical micrographs

promote the diffusion of PEI and PEEK macromolecular chains. The next section aims to go further in analyzing the composition of such interphases. The thickness of this gradient and its influence on the mechanical properties and fracture mechanisms are not fully understood yet and need further investigation.

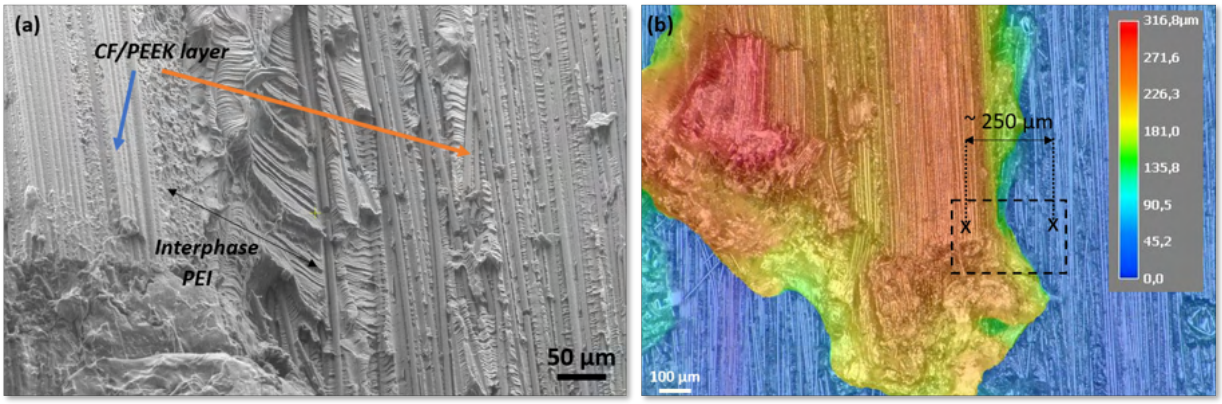

Figure 5.15: SEM (a) and optical (b) micrographs of interfacial fracture between two layers of CF/PEEK, color chart corresponds to a difference in height

5.3.2 Composition of PEI/PEEK interphase in the welded zone

Raman spectroscopy is a non-destructive method that allows the identification of molecule structures and compositions. This chemical analysis is based on the inelastic scattering of light, the Raman scattering. A monochromatic laser-type source is sent on the sample. A large part of the light is scattered elastically without any change in energy (the Rayleigh scattering). In contrast, a minimal amount of light is scattered inelastically with a change in energy compared to the incident radiation. This energy loss or gain is the energy difference between the vibrational levels of the molecule. This technique is complementary to molecular absorption spectroscopy. It gives qualitative and quantitative information about the sample's covalent groups, such as their environments, the orientation of molecular groups, their residual constraints, or the amorphous or crystalline phase ratio.

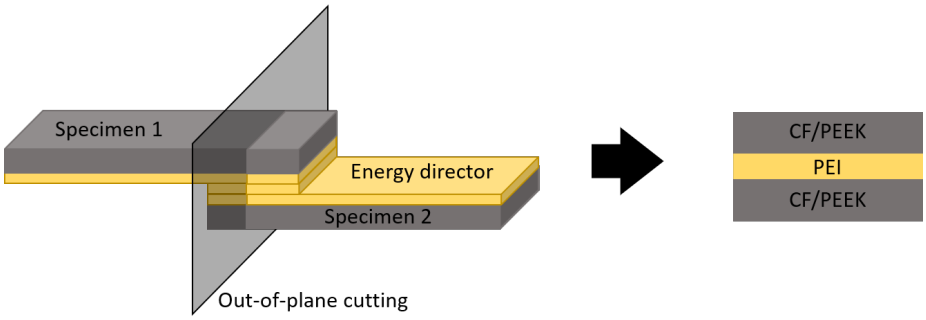

Figure 5.16: Out-of-plane cutting of welds for Raman spectroscopy

Raman spectroscopy was used to quantify the evolution of PEI concentration along the interphase. Raman samples are made from out-of-plane cutting of welds in configuration A (three PEI layers), as shown in Fig. 5.16. Raman maps are made at various locations along the interface of the same sample after welding using a Horiba Yvon Jobin Labram HR 800 RAMAN confocal microscope. The details concerning the experiments conditions are presented in Appendix B.

The spectra given in Fig. 5.17 show one distinct band at 1777 cm^{-1} (red area) attributable to the νC=O bond of PEI [Samyn and Schoukens, 2008, Devasahayam et al., 2006]. In addition, the area between $1550 - 1620\ cm^{-1}$, attributable to $\nu C{=}C_{cycle}$ (amorphous or crystallline phase) of PEI and PEEK (grey area in Fig. 5.17 and Fig. 5.18) is selected.

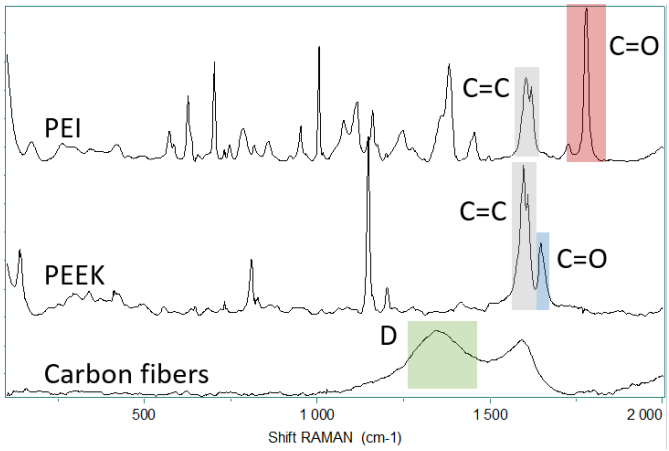

Figure 5.17: Raman spectra of PEEK, PEI and carbon fibers

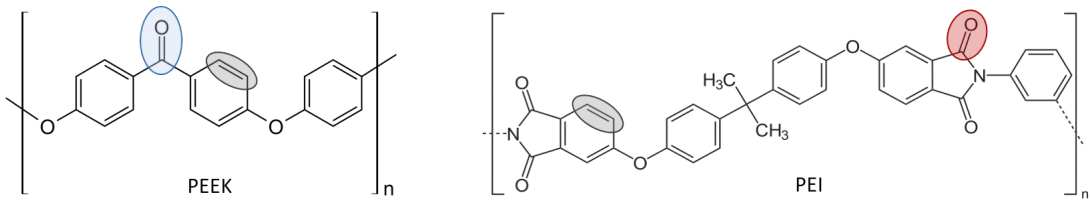

Figure 5.18: Chemical bonds (red, grey and blue) analyzed on Raman spectroscopy for PEEK and PEI

Fig. 5.19 (a) and (b) show mapping of the same interfacial zone after welding. The mapping area goes from the first ply of APC-2 from specimen 1 to the first ply of APC-2

from specimen 2, going through the entire PEI layer, as seen in Fig. 5.19. Fig. 5.19 (a) is done from the ratio of the band relative intensities of C=O (PEI) and C=C (PEEK + PEI). In the map, the edges of the first plies of APC-2 exhibit black color, which correspond to 100 % PEEK. When getting closer to the center, green color appears under $-100\ \mu m$ and above 100 μm, meaning that the ratio PEI/(PEI + PEEK) is higher than at the edges. Those section correspond to a blend of PEI/PEEK in the first plies of both specimens. This blend comes from the diffusion of PEI during specimens manufacturing. The thickness of the blend is around 25 μm. At the center of the map (from $-100\ \mu m$ to 75 μm), the highest ratio is obtained, around 1. It is clear that pure PEI is predominant in that zone.

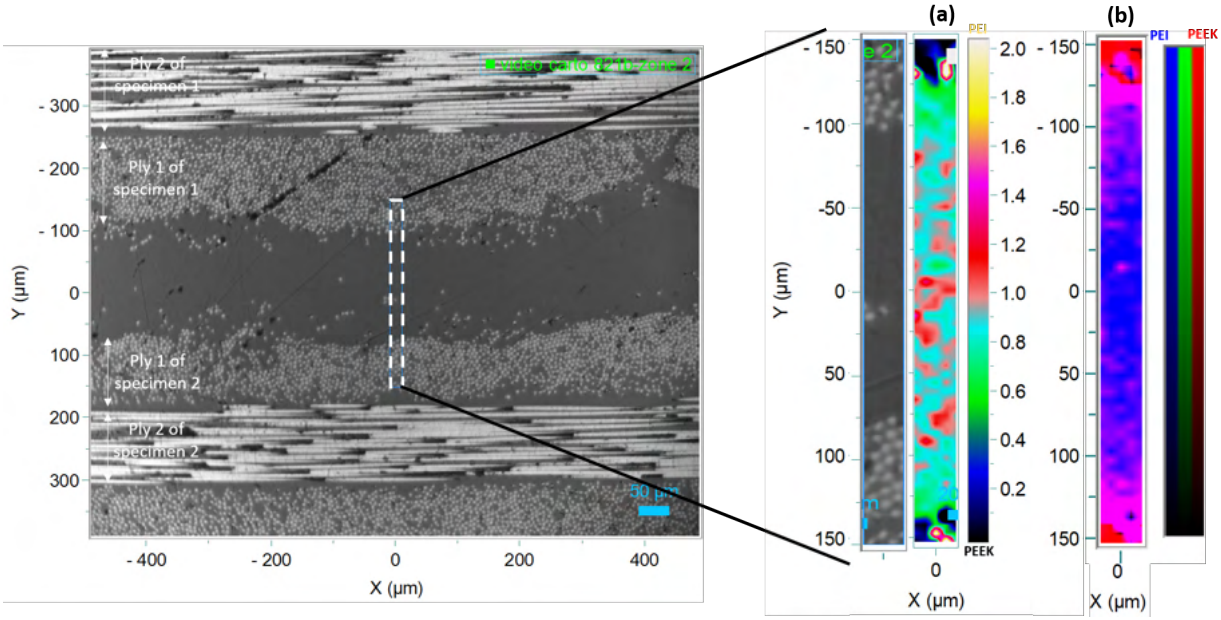

Figure 5.19: Mapping of the interphase zone after welding using the ratio of the band relative intensities of PEI and PEEK + PEI (a) and using a multicurve regression (b) from the first ply of specimen 1 to the first ply of specimen 2, going through the PEI interphase

Fig. 5.19 (b) uses a two components multi curve regression with the complete spectra of PEI and PEEK. Overall, the same observations can be made compared to the previous map. Indeed, the 100 % PEEK zone can be observed in red and the blend is visible in pink (mixed color: blue + red = pink). Only one shade of pink is visible because this technique does not allow information about the ratio of each component. In that case, the thickness of the blend seems to be higher than in the previous map because the treatments used are not the same, and they do not have the same measurement accuracy. A whole pink zone is visible with a length of around 25 μm on each side, corresponding to the first plies of APC-2. However, large zones of around 50 μm on each side (between $-100\ \mu m$ and

$-50\ \mu m$ and between 50 μm and 100 μm) present a blue and pink color mix. It probably means that the PEI/PEEK blend is present in that area to a lesser extent than in the first plies.

Finally, a large area between $-50\ \mu m$ and 50 μm is mainly PEI due to the strong blue color. It can be imagined that increasing or decreasing this $100 - \mu m-$length PEI-based area would not affect the mechanical strength of welds. The final displacement of this weld is 540 microns. Based on Fig. 5.11 (a), we are already in the plateau at high LSS. It confirms a longer welding time or further sonotrode displacement would not increase the mechanical strength. For welding, it would mean that a thinner ED of 100 μm would lead to similar mechanical properties, which agrees with the conclusion made from the final sonotrode displacement analysis in section 5.2.5. However, we have seen that increasing the number of PEI layer at the interface could increase the LSS value, and also that the way the energy director is put at the interface is important as seen by configuration C1 and C2 that have the same number of layers but exhibit different LSS. It suggests that further studies are still required to achieve optimal process configuration that could help decreasing the interface thickness.

In addition, a pink dot is visible in that area. It is associated with a fiber that has moved through the ED during welding specimens manufacturing. The fibers take along some part of the matrix when flowing. Due to the dot pink color, it is assumed that a PEI/PEEK blend surrounds fibers. This technique looks more precise than the previous one as fibers can be detected.

To better evaluate the diffusion of PEI inside APC-2, a mapping going deeper inside the composite plies is made from the PEI layer to the second APC-2 ply, in Fig. 5.20. Raman mapping of the distribution and location of species was achieved by integrating the area bands characteristic of each species present in the interphase. The green color is associated with carbon fibers (integration of the carbon D band). The red and blue colors respectively define PEI and PEEK thanks to the integration of the νC=O bands at 1777 cm^{-1} and 1650 cm^{-1} respectively. As before, a blend of PEI/PEEK is observed when the PEI meets the first ply of APC-2, marked by the pink color close to 50 μm. When going deeper inside the composite plies, small pink areas are observed between $-50\ \mu m$ and 25 μm, meaning PEI has flowed through almost the entire first APC-2 ply. Pink color is less intense in that area, which suggests that PEI flows to a lesser extent than in the area around 50 μm. During cooling, PEI is rejected into the amorphous phase of PEEK due to the crystallization of PEEK, leading to a modification of thermal properties of the blend [Ivanov and Jonas, 1998, Ramani and Alam, 2010]. Moreover, we demonstrate in

section 5.3.3 that the properties of the PEEK/PEI blends are different than those of each pure phase. Overall, Fig. 5.19 and Fig. 5.20 display a PEI/PEEK blend with a gradient concentration in the first ply of APC-2. The characterization of PEEK/PEI blends at various concentration is helpful to analyze the fracture mechanisms of welded assemblies. We assume a fracture within the first APC-2 ply, which can now be identified as a fracture within the PEI/PEEK blend.

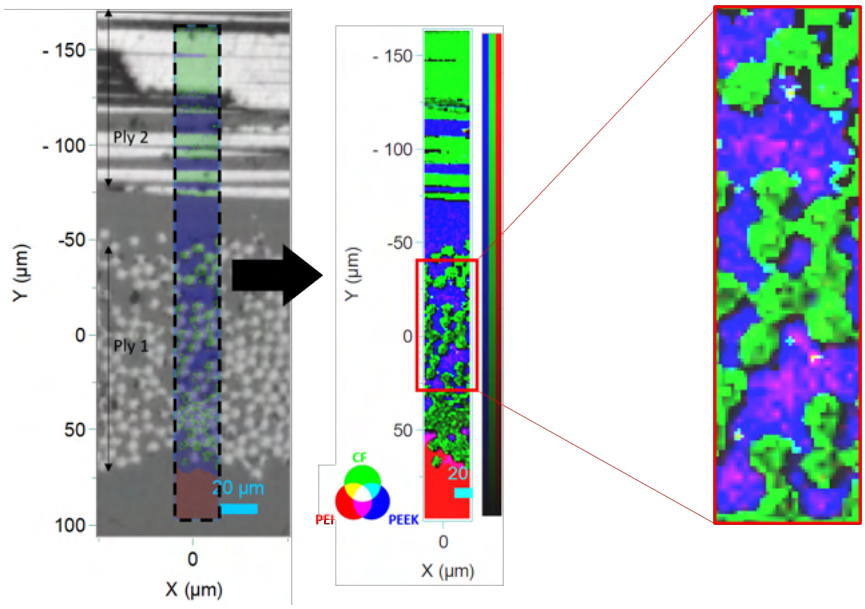

Figure 5.20: Raman mapping of species distribution in the interphase zone

Finally, a last mapping is made from the PEI layer to the first APC-2 ply, in Fig. 5.21. The map is made from a multi-curve regression with the complete spectra of PEI, PEEK and carbon fibers. Green areas associated with carbon fibers are observed deep in the PEI layer in blue, at around 20 μm. A thin red zone is also seen around the green dots, associated with PEEK. It confirms fiber displacement upon polymer flow during the manufacturing of welding specimens. It also implies that a small volume of polymer matrix is taking along. It has been seen before that this polymer flow is a PEI/PEEK blend. Based on this map, we suggest that the blend is probably made of a majority of PEEK since the color is red.

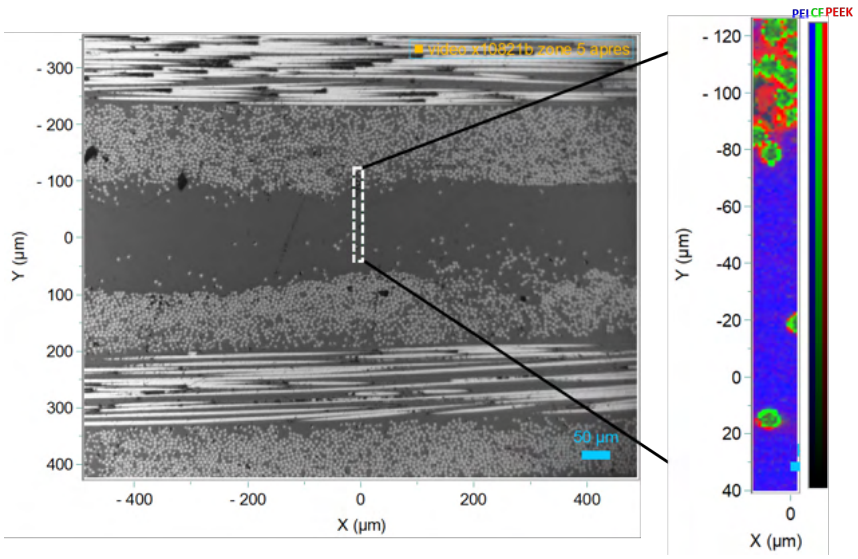

Figure 5.21: Mapping of interphase zone after welding using a multicurve regression from the PEI layer to the first ply of the upper specimen

5.3.3 Properties of PEI/PEEK blends

As seen in the previous section with Raman spectroscopy, a gradient concentration of PEI is present at the interphase. To evaluate the effect of this gradient on the assembly mechanical strength, rheological, crytallinity and mechanical analyses are performed on PEI/PEEK blends. The aim is to anticipate the properties of the interphase, and to understand the crack propagation mechanisms. Also, we aim to check whether the presence of PEI in the interphase weakens the assembly in comparison with a PEEK/PEEK weld. Five blends have been prepared with the following volume ratio: 10/90, 30/70, 50/50, 70/30 and 90/10. The details concerning the blend preparation and characterizations are presented in Appendix C.

5.3.3.1 Miscibility of PEI/PEEK blends

The evaluation of the miscibility or non-miscibility between two polymers can be done using the glass transition temperature [Wetton and Corish, 1988]. Fig. 5.22 lays out the glass transition temperature for different PEEK ratio in PEI/PEEK blends evaluated by DSC experiments. Two points are plotted for each concentration, representing the results of two experiments. Further information about the experiments are detailed in Appendix C.

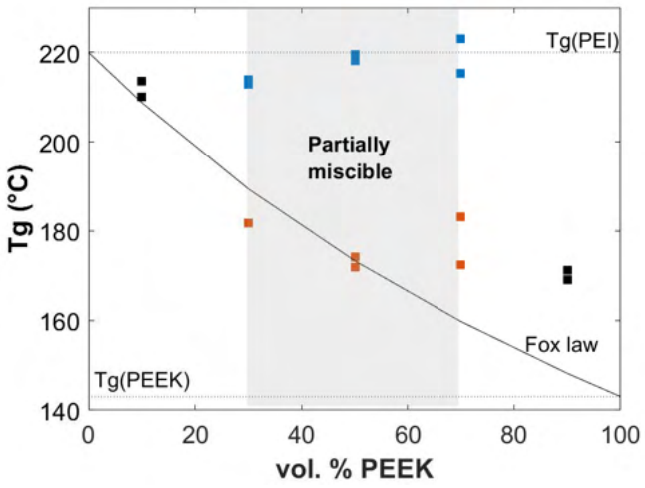

Figure 5.22: Glass transition temperature for different ratio of PEEK in PEI/PEEK blends. Blue and red dots define different amorphous phases in the same blend

Three sections can be identified in the graph. The first one is for vol. % PEEK lower than 30 % where only one T_g is observed close to 220 $°C$, meaning that the blend is miscible and made of a majority of PEI. The decrease in T_g indicates that PEEK chains, whose T_g is 150 $°C$, are miscible with the PEI phase. Between 30 % and 70 % of PEEK, two T_g are clearly visible. Two partially miscible phases are present in the blend, one illustrated by the blue dots and the other one illustrated by the red dots. The red dots range between 172 $°C$ and 183 $°C$, and demonstrate an amorphous phase made of both PEEK and PEI in similar proportions. The T_g of PEEK is shifted towards higher temperature due to the presence of PEI. During cooling, the PEI is rejected into the amorphous phase of PEEK when PEEK chains crystallize [Hsiao et al., 1998]. In that case, only the shortest chains of PEI have mixed with PEEK. The blue dots are close to 220 $°C$, which means a PEI-rich phase. The longest chains have not been able to blend, creating a second amorphous phase of pure PEI. The blue dots can be associated with that second amorphous phase. Finally, a last section above 70 % of PEEK is observed where the blend is fully miscible and its T_g is around 170 $°C$. This phase is a PEEK-rich phase.

Moreover, the Fox law for polymer blends states that the glass transition temperature of blend of polymers A and B follows the following equation [Fox, 1956]:

$$\frac{1}{Tg} = \frac{\omega_A}{Tg_A} + \frac{\omega_B}{Tg_B} \tag{5.2}$$

where ω_A and ω_B are the weight ratio of each component. We see that those blends do not follow the Fox equation. The latter is valid for fully miscible amorphous polymers. This result is not in accordance with Crevecoeur et al. who found that PEI/PEEK blends follow the Fox equation for every weight ratio [Crevecoeur and Groeninckx, 1991]. This difference could stem from the polymer grades they choose: the shorter the macromolecules, the more miscible the blend. Moreover, the preparation protocol affect the miscibility. They elaborated the blends by injection molding which results in fully amorphous state. Overall, PEEK/PEI miscibility depends on the composition of the blend. The miscibility is present only for high weight ratio of PEI or PEEK.

The miscibility of polymer blends can also be determined by DMA using the loss factor, $tan(\delta)$, as shown in Fig. 5.23 (a). Fig. 5.23 (b) represents the same curves but shifted along the y axis for a better visualization. The peak at 220 $°C$ associated with the glass transition, T_α, of PEI is really intense, especially for high PEI weight ratio. Another peak is visible at around 175 $°C$ when the weight ratio of PEEK is above 30 %, associated with the glass transition of PEEK. The two peaks are both present for PEEK weight ratio of 30 %, 50 % and 70 %, confirming the immiscibility of PEI and PEEK only for those weight ratio. For 90 % of PEEK or 90 % of PEI, only one T_α is observed, when the two polymers are miscible.

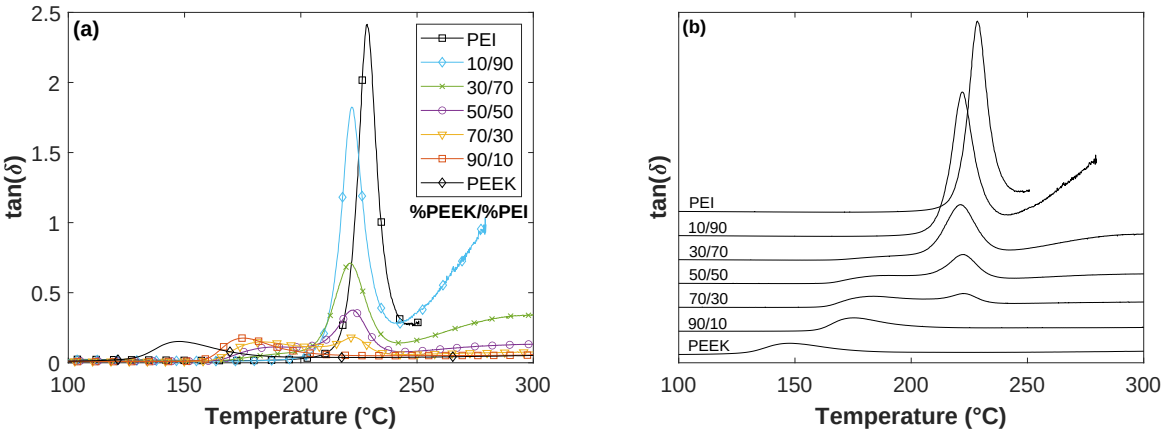

Figure 5.23: Loss factor from DMA for different ratio of PEEK in PEI/PEEK blend (a) and shifted curves for a better visualization (b)

5.3.3.2 Crystallization kinetics of PEEK in PEI/PEEK blends

The cooling thermograms obtained for different ratio of PEI/PEEK blends are presented in Fig. 5.24. The crystallization peak of PEEK is shifted towards lower temperatures when the weight ratio of PEI increases. The presence of PEI limits the mobility of long macromolecular chains of PEEK. As explained by Jenkins [Jenkins, 2001], the viscosity of the blend is increased by the presence of PEI in this temperature range. It is more difficult for the chains to gain mobility, which delays the crystallization of PEEK. Therefore, the longest chains of PEEK have more difficulty to crystallize, explaining why the crystallization peak appears at lower temperatures. Besides, PEEK is known to have really fast crystallization rate. Adding PEI could be a good way of controlling the crystallinity of PEEK. Below 50 % of PEEK, no crystallization is observed in thoses curves because there is too much PEI for PEEK to crystallize. Moreover, the glass transition temperature is shifted towards higher temperatures when the volume ratio of PEI increases. Indeed, during the crystallization of PEEK, PEI is rejected into the amorphous phase of the blend. As PEI ratio increases, the composition of this amorphous phase is changed [Crevecoeur and Groeninckx, 1991]. PEI is known for its high rigidity that results in high glass transition temperature: more energy is required to allow mobility of chains. The increasing amount of PEI chains into the amorphous phase implies higher T_g because the amorphous phase becomes more rigid. In our case, T_g goes from 155 $°C$ (90 % of PEEK) to 208 $°C$ (10 % of PEEK).

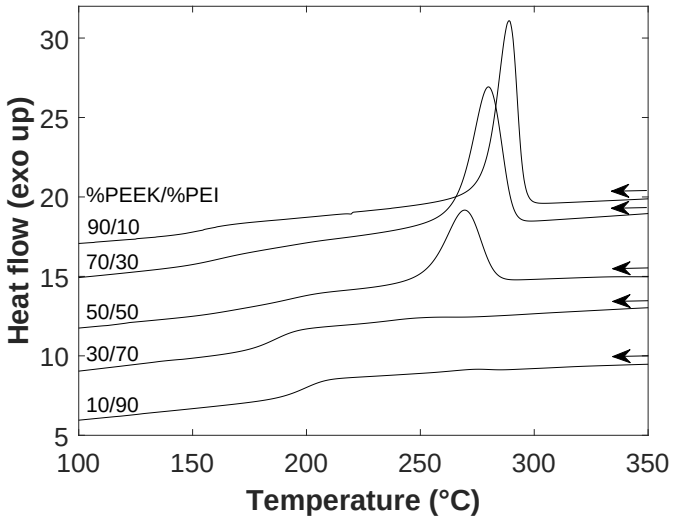

Figure 5.24: DSC thermogram of PEI/PEEK blends for cooling rate of 20 $°K.min^{-1}$

Fig. 5.25 shows crystallinity of PEEK, quantified using the following equation:

$$\chi_c = \frac{\Delta H_m}{\omega_{PEEK} \Delta H_\infty} \tag{5.3}$$

with ω_{PEEK} the weight fraction of PEEK, ΔH_∞ the theoretical melting enthalpy of the 100 % crystalline PEEK, 130 $J.g^{-1}$, and ΔH_m the melting enthalpy of each blend. In this equation, the enthalpy is corrected by the real ratio of PEEK in the blend. The crystallinity increases when increasing the volume ratio of PEI. It goes from 32 % for pure PEEK to 55 % (30 % of PEEK). The value of pure PEEK was taken from Chapter 3, when studying the influence of the cooling rate on PEEK and AE 250 crystallinities. PEI acts as a lubricant for PEEK, reducing the intermolecular friction coefficient. The chains can slide more easily on each other and gain mobility, increasing the crystallinity. This phenomenon has already been observed by Crevecoeur et al. [Crevecoeur and Groeninckx, 1991]. In their study, the crystallinity goes from 43 % (25 % of PEEK) to 37 % (pure PEEK), for PEEK/PEI blends.

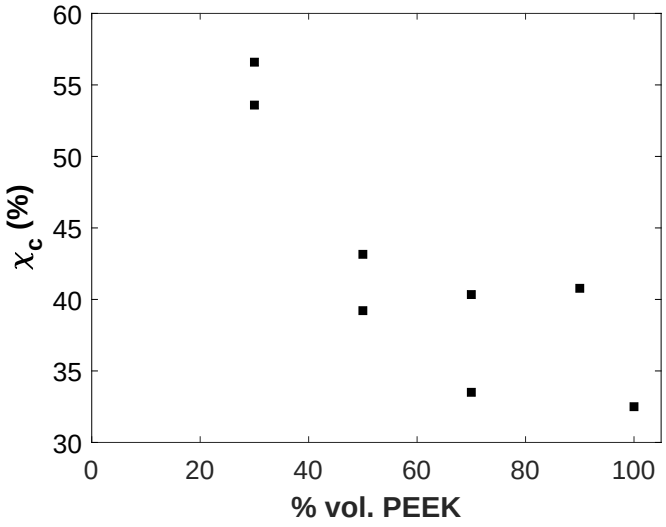

Figure 5.25: Normalized crystallinity of PEEK in PEI/PEEK blends

5.3.3.3 Mechanical properties of PEI/PEEK blends

The thermomechanical properties were evaluated by DMA. The storage and loss moduli, respectively E' and E'', are presented in Fig. 5.26 (a) and (b). The storage modulus E' corresponds to the elastic contribution of the material's response whereas the loss modulus

E'' is its viscous conterpart. The storage modulus of the 90/10 (PEEK/PEI) ratio exhibits a typical semi-crystalline polymer behavior, identical to pure PEEK, with a glassy plateau for low temperatures. When reaching the glass transition temperature, T_α, a transition region is observed. The blend loses its stiffness due to the motion of chains. This gain in motion stems from the disappearance of weak interactions such as hydrogen and Van der Walls bonds from the glass transition region. Finally, a rubbery region is seen. The length of the latter is linked to the molecular weight between entanglement M_e. In this last region, E' continuously decreases until all losing its entire mechanical strength. When lowering the ratio of PEEK, the behavior of the storage modulus changes. E' in the glassy plateau decreases when decreasing the weight ratio of PEEK, meaning that PEI decreases the stiffness of the blend, from 200 $°C$. For 70 % and 50 % of PEEK, two glass transition temperatures are visible by two changes in slope after the rubbery plateau, confirming that these blends are immiscible. For 30 and 10 % of PEEK, amorphous-like curves are visible. E' severly decreases from T_g(PEI), when increasing the temperature. The drop in modulus is so intense that the values are not measurable in torsion mode. A plate/plate configuration should be used to complete the curve. This behavior is typical of amorphous polymers. In the intended temperature range of applications, meaning below 150 $°C$, the presence of PEI slightly decreases the material stiffness, the latter remains next to 1 GPa.

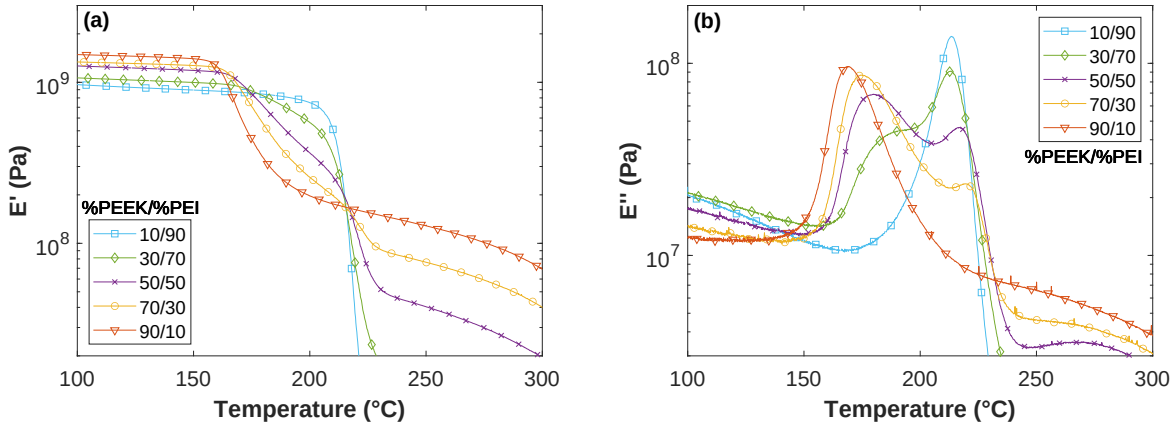

Figure 5.26: Storage (a) and loss (b) moduli of PEEK/PEI blends

The loss modulus E'' reflects the viscous character of the material. It represents the flow of chains one on top of the other, without modification of their chemical structure. Due to molecular friction, heat is dissipated; this energy is lost by the material. The loss modulus E'' is equal to 10 MPa, before the glass transition in Fig. 5.26 (b). In this glassy state, E' is greater than E''; this indicates a "solid-like" behavior of the viscoelastic material, which

is preserved throughout the temperature range studied. Below T_g, the thermal energy is insufficient to cause rotational and translational motions of chain segments. At T_g, micro-Brownian motion of molecular segments begins where short range diffusion can take place. On the contrary, above 300 $°C$ (not shown), E'' becomes dominant, the material then exhibits a "liquid"-like behavior. The peak maximum of E'' corresponds to the beginning of significant segmental motion of the polymer chains. Thus, the mechanical energy is dissipated as heat by the internal friction caused by chain motion, which characterize the damping phenomenon. Pure PEEK and PEI exhibit only one peak: the value of E'' increases sharply and then decreases in Fig. 5.26 (b). This peak indicates the maximum amount of heat dissipated per deformation unit. At the molecular level, this maximum value of the loss modulus indicates that intermolecular bonds are broken, macromolecules have more mobility to flow by rubbing against each other. The damping factor ($tan\ \delta$ curve) follows a shape identical to that of E'', with a maximum at the time of the glass transition. The peak maximum is at 150 $°C$ for PEEK and 220 $°C$ for PEI. The peak of PEEK is also broader than those of PEI, showing more resistance to motion at the onset of T_g for PEI, which strongly suggest a tighter structure that led to shorter rotational freedom. Molecular chain sliding and internal friction, which are responsible for the viscous behavior of polymers, occur predominantly in the amorphous domains. For semi-crystalline polymers, the crystalline zones act as physical crosslinking, resulting in decrease of the loss modulus.

For the 90/10 PEEK/PEI blend, only one peak is recorded with a maximum at 165 $°C$. This maximum is shifted towards higher temperatures when increasing the PEI ratio because of the miscibility of some PEI chains within the PEEK amorphous phase. For the 70/30 blend, the higher T_g(PEI) is reduced to a shoulder. This is due to the presence of soluble PEEK in the PEI phase, reducing and broadening the T_g of that phase. Then, the amplitude of the PEI peak increases with the PEI content. Being the sum of both contributions, the 50/50 blend corresponds to the highest viscous behavior. This viscous response from E'' curves is a strong indicator that the molecular structure of PEEK/PEI blend will dissipate more heat when mechanical stress is applied.

Lastly, three-point-bending tests were carried out to evaluate the resistance to crack propagation according to the PEEK/PEI ratio. Details about the experiment are presented in Appendix C.

The load-displacement curves are plotted in Fig. 5.27. For all blend ratios, the load-displacement curves display typical linear trend corresponding to the loading of specimen up to the maximum load before crack propagation. The initial stiffness (*i.e.* the slope

of the curves) decreases with PEI concentration increase, with the lowest level for 10/90 PEEK/PEI blend. A lower stiffness is usually associated with a less rigid behavior: the material tends to more deformation under identical mechanical load. In our case, the lowest initial stiffness is obtained for 10/90, 30/70 and 50/50 PEEK/PEI blends. Based on DSC results in Fig. 5.22, 10/90 blend is identified as miscible from only one glass transition. Moreover, we have demonstrated that PEEK does not crystallize in 10/90, explaining its more ductile behavior. 30/70 and 50/50 are partially miscible with two glass transitions. For those blends, the co-existence of PEEK/PEI amorphous phase and a large amount of PEI-rich phase probably weaken the behavior of the whole specimens. In some images like the one in Fig. 5.28, a ductile behavior of PEEK is observed.

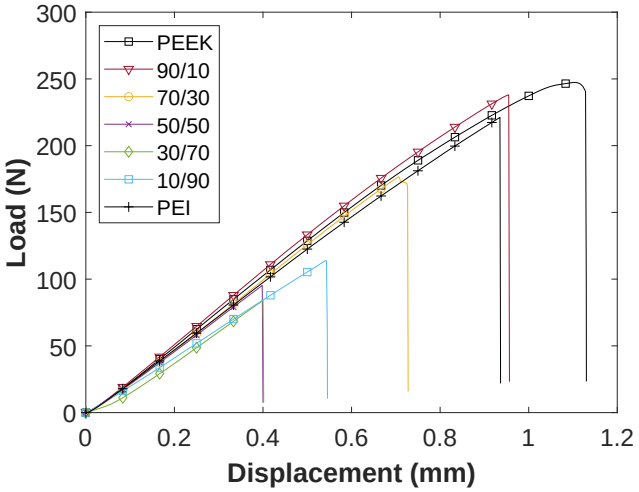

Figure 5.27: Load-displacement curves of pure PEEK, pure PEI and different blend ratios

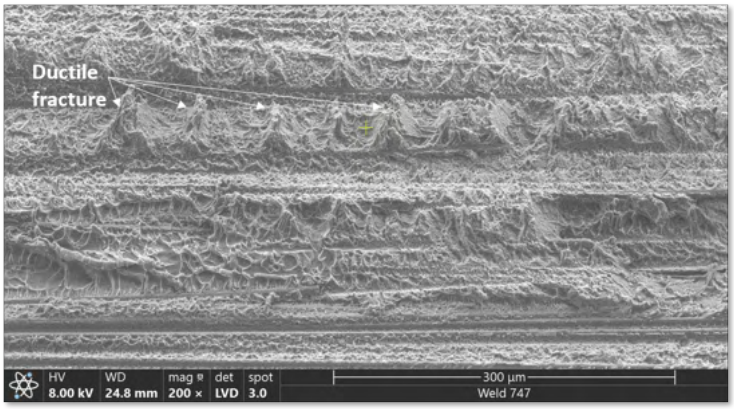

Figure 5.28: SEM micrograph of a PEEK-based fracture

A high maximum load is related with a strong resistance to crack propagation. For immiscible blends and composites, for which cracks propagate through interface opening, it usually suggests that the polymer/polymer or fiber/matrix interfacial adhesion is strong. The maximum loads of blends are lower than those of pure PEEK and pure PEI. For pure PEEK, it means that the cristallites are strongly anchored within the PEEK amorphous phase. When increasing the PEI ratio, the material evolves towards a complex morphology. Indeed, according to Fig. 5.22. the blends are composed of three phases:

- PEEK crystalline zones,
- A PEEK/PEI fully miscible amorphous phase in which the composition could be as much PEEK as PEI,
- A PEI-rich amorphous phase.

Each of this zone is chemically compatible with another, meaning that there is no phase separation nor interfaces in our blends. In contrast, we consider that the morphology of blends consists in the three zones described above, linked together by interphases with a continuous concentration decrease. This hypothesis agrees with the high maximum loads obtained. Crack propagation in fully immiscible blends would be very fast because of low interfacial adhesion of phases and it would lead to low maximum loads.

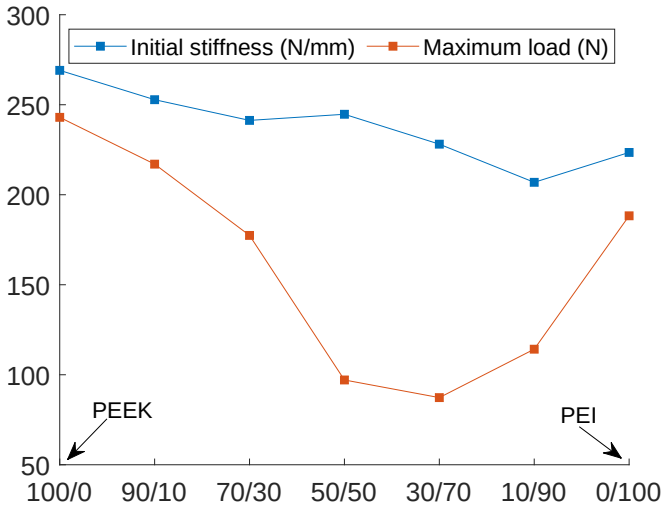

Figure 5.29: Initial stiffness and maximum load of pure PEEK, pure PEI and different blend ratios

Initial stiffness and maximum loads are plotted versus PEEK/PEI ratio in Fig. 5.29. For highest PEEK ratios, their variation is linear with concentration, meaning that adding PEI does not modify the global behavior despite a slight decrease. When adding more PEI, from 50/50, the PEI quantity is too high to be diluted into the PEEK amorphous phase, explaining the presence of a pure PEI phase. The latter drastically changes the behavior of the blends: the peak load is much lower for 50/50, 30/70 and 10/90 blends than pure PEEK and pure PEI. This could be due to the lower toughness of PEI or lower entanglement rate within the blends.

From these results, the critical stress intensity factor K_{IC}, or fracture toughness, is calculated for all blends using the following equation:

$$K_Q = \left(\frac{P_Q}{BW^{1/2}}\right) f(x) \tag{5.4}$$

where P_Q is the maximum load, B the specimen thickness, W the width specimen and, for $0 < x < 1$:

$$f(x) = 6x^{1/2}\frac{[1.99 - x(1-x)(2.15 - 3.93x + 2.7x^2)]}{(1+2x)(1-x)^{3/2}} \tag{5.5}$$

PEEK/PEI blends *% vol. PEEK/% vol. PEI*	Stress intensity factor K_Q $(MPa.m^{1/2})$
100/0	8.1
90/10	7.3
70/30	3.9
50/50	3.2
30/70	2.9
10/90	3.8
0/100	4.0

Table 5.1: K_Q of pure PEEK, pure PEI and different blend ratios

Finally, $x = a/W$ where a is the crack length. The specimen dimensions do not follow the requirement of the standard ASTM B5045-14 because of the small amount of each blend. The assumption is made that K_Q is equal to K_{IC} due to the brittle nature of the material deduced by the load-displacement curves. Table 5.1 displays that K_Q of pure PEEK is 8.1 $MPa.m^{1/2}$ and 4 $MPa.m^{1/2}$ for pure PEI. As a comparison, values of 6.3 $MPa.m^{1/2}$ [Gensler et al., 1996] and 6.5 $MPa.m^{1/2}$ [Motz and Schultz, 1990, Friedrich et al., 1986] were found for PEEK and 3.5 $MPa.m^{1/2}$ [Kim and Ye, 2004, Gensler et al., 1996] for PEI in the literature. K_{IC} depicts the resistance of a material to crack extansion

under linear-elastic conditions when no plastic deformation occurs at the crack tip. A low K_{IC} means that the material is brittle and the crack propagation is fast, *i.e.* nothing deviates the fast propagation of the crack tip. Indeed, for a similar crack length between PEI and PEEK, the required energy to initiate fast propagation of the crack will be lower in the case of PEI. Regarding blends, crack propagation is the easiest for 50/50 and 30/70 blends, which in adequation with Fig. 5.29.

Even if such blends are not exactly in line with the diffusion zone in our welds, we consider that they help to understand their fracture mode. We have demonstrated that PEEK/PEI blend is more likely to crack propagation than pure PEEK and pure PEI. When going back to the fracture surfaces described in section 5.2.1. after SLS tests, we have explained why the fracture occurs in the blending zone.

5.4 Ultrasonic welding of AE 250 composites

Finally, ultrasonic welding of the new composite preg from Victrex, AE 250, has been conducted. Based on our previous results, the welding configuration is B, and the amplitude is 32 μm for all welds in this section. A parametric welding investigation has been conducted, and the LSS results are presented in Fig. 5.30. A welding load of 800 N leads to the highest LSS values regardless the welding time. At 600 ms, the difference of LSS between all welding loads (500 N, 800 N and 1000 N) is only 5 MPa. The difference is 8 MPa at 1000 ms and 5 MPa at 1200 ms. The welding load does not strongly influence the mechanical properties of AE 250 joints. The intimate contact between the specimens is probably already sufficient at 500 N. However, the welding time has a stronger influence on the mechanical properties. For example, for a welding load of 800 N, LSS vary from 17 MPa to 34 MPa when increasing the welding time from 600 ms to 1200 ms.

When looking at the fracture surfaces, almost half of the energy director in the welding area has not melted for a welding time of 600 ms, as seen in Fig. 5.31. The mean relaxation time of AE 250 was found to be a few hundred milliseconds at 390 $°C$. As a reminder, we previously assumed that the welding time is similar to the time for which the specimens stay above the melting temperature of PEEK. We make the same assumption for AE 250 because in the temperature profiles, the time during which the temperature is above 300 $°C$ (melting temperature of AE 250) is almost the same as the time above the melting temperature of PEEK. Thus, 600 ms is insufficient for the polymer chains to diffuse, while it is sufficient for a welding time of 1000 ms.

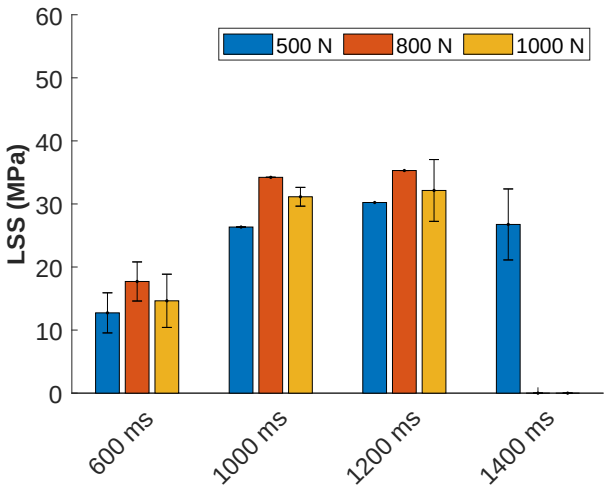

Figure 5.30: LSS for different welding parameters of AE 250 welds (amplitude: 32 μm)

At 1000 ms and 1200 ms, fiber displacement and matrix degradation become predominant, as seen in Fig. 5.31. As explained for APC-2 welds, lap shear tests alone do not seem ideal for characterizing US welds since high strength welds over 30 MPa are obtained whereas degradation of the matrix is observed. The quantification of the degradation is tricky, even more in our case where it is localized within the welds. We assume that the degradation level does not affect much the mechanical strength of the welds.

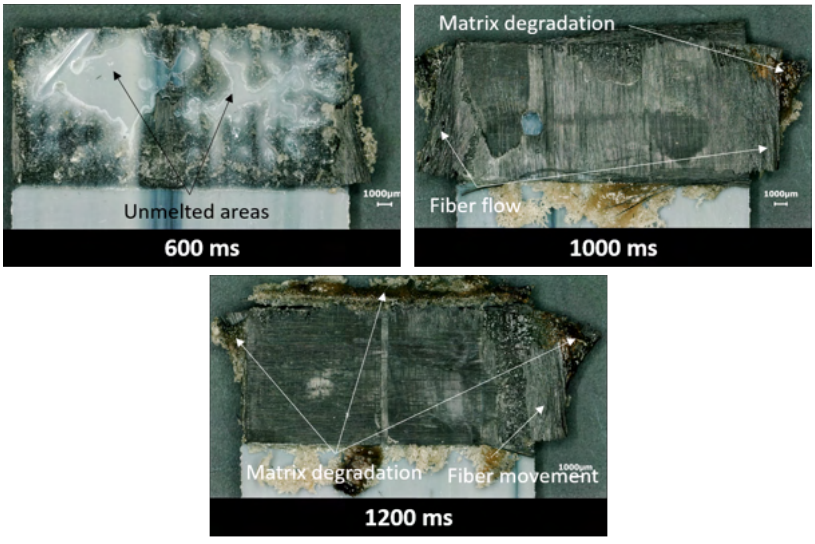

Figure 5.31: Interfacial fracture of AE 250 welds for a different welding times (welding load: 500 N, amplitude: 32 μm)

Finally, at 1400 ms, only one welding load is tested because its LSS value is lower than at 1200 ms, so it is assumed that LSS would also be lower for 800 N and 1000 N following the same trend. The optimal welding parameter set is found for a welding load of 800 N and a welding time of 1200 ms.

The hereby results about AE 250 are compared with CF/PEEK + PEI welds and CF/PEEK + PEEK welds for similar welding conditions, as seen in Fig. 5.32. LSS values of CF/PEEK + PEI welds and CF/PEEK + PEEK welds have already been presented in Fig. 5.9. Overall, the mechanical strength of AE 250 welds follow the same trend as CF/PEEK welds. LSS increases when increasing the welding time until reaching a plateau. The plateau of AE 250 is lower than PEEK composite with both ED, around 35 MPa for AE 250 and 45 MPa for PEEK. The mechanical strength of AE 250 composites is lower than PEEK composites for all welding parameters. Moreover, the plateau is obtained around 30 MPa for AE 250 for a welding time of 1200 ms and a welding load of 500 N. For the same welding conditions, LSS of CF/PEEK + PEEK is in the same range (26 MPa). For both PEI or PEEK energy directors, welding of CF/PEEK leads to higher LSS than AE 250. In the three cases, the maximal LSS were found when interfacial fracture occurs inside the composite plies, so it can be assumed that using a PEI energy director for AE 250 composite specimens would not increase the LSS values.

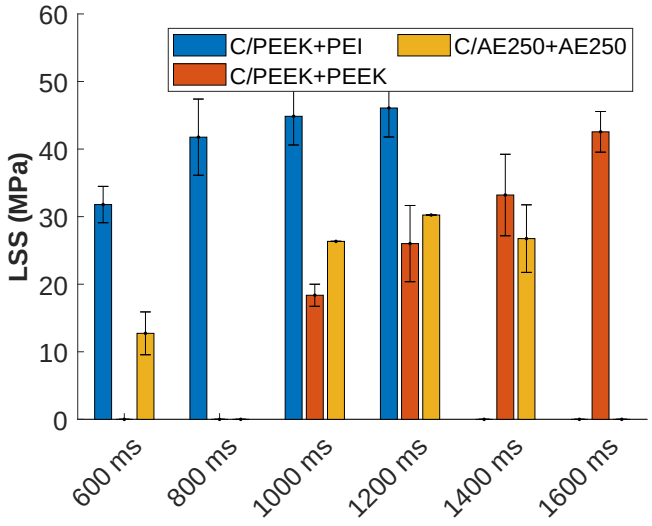

Figure 5.32: Lap shear strength in configuration B for different welding time of PEEK and AE 250 composite specimens (amplitude: 32 μm, welding load: 500 N)

Most of the previous studies about ultrasonic welding show that controlling the final sonotrode displacement is a way to obtain reliable and reproducible composite welds

[Fernandez Villegas and Palardy, 2017, Villegas, 2014, Palardy and Fernandez Villegas, 2017, Fernandez Villegas and Vizcaino Rubio, 2015]. However, such studies do not deal with PEEK composites, and always with an energy director of the same composition as the composite matrix. We wonder whether the LSS value is linked to the final sonotrode displacement. For that, LSS values are plotted as a function of the final sonotrode displacement in Fig. 5.33. A similar trend as PEEK composite welds is observed. LSS increases when the final sonotrode displacement is increasing until reaching a plateau. This plateau value is around $125 - 150\ \mu m$. The LSS value does not increase after the final sonotrode displacement reaches $125 - 150\ \mu m$. This threshold value is similar to the ones of PEEK composite specimens with PEI and PEEK energy director in configuration B. The optimal final sonotrode displacement does not seem to be dependant on the material since it is the same for AE 250, PEI and PEEK energy directors. It has been shown that the optimal parameters differ from one material to another. However, a displacement control could be used to control the process, regardless of the material. The optimal thickness is found to be around $350\ \mu m$. It is worth noting that this value should be consider just as an order of magnitude due to the uncertainty of the energy director thickness.

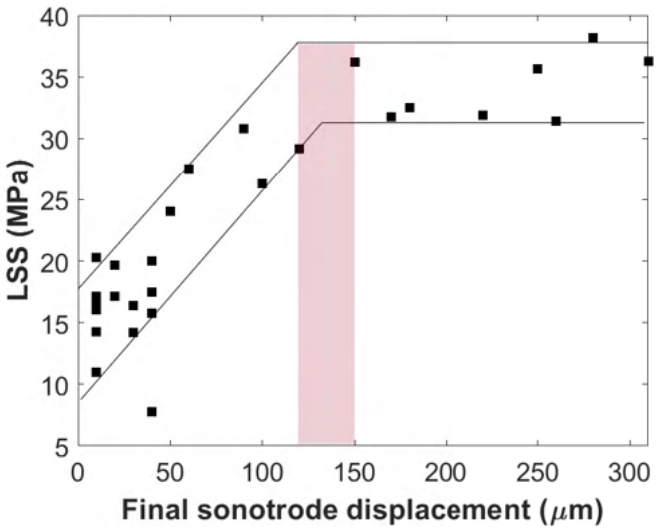

Figure 5.33: Final sonotrode displacements for AE 250 specimens in configuration B

5.5 Conclusion

This chapter aims to understand the effect of each process parameter on the mechanical strength of welds. We evaluated the mechanical properties of CF/PEEK specimens using PEI and PEEK energy directors. The influence of the welding parameters has shown that welding load, but mostly the welding time, greatly influences the mechanical properties. The thickness of the energy director has been investigated through the number of PEI layers. It has been highlighted that a three-layer configuration leads to the highest LSS. The optimal parameters have been identified, 1000 ms and 500 N for a PEI energy director and 1600 ms and 500 N for a PEEK energy director, leading to high LSS values around 50 MPa, which compete with LSS found in the literature for the same process.

The welds have been characterized through interfacial fracture analysis, Raman spectroscopy and output data from the welder. SEM micrographs have pointed out that several failure mechanisms take place. A PEI-based fracture in the energy director seems to be mostly a brittle fracture, while a PEEK-based fracture is a competition between brittle and ductile fracture. Cracks going from one specimen to the next one is observed. It has been demonstrated that the fracture goes from the first ply of the upper specimen to the first ply of the second specimen, going through the entire layer of PEI.

The fracture within the composite is explained by two mechanisms. It can either be a fracture between two plies or within the first ply. Raman spectroscopy has demonstrated that a PEI gradient concentration exists in the first ply of the composite specimen. The PEI has diffused within the composite during the manufacturing of welding specimens. This blend probably weakens the mechanical strength of the ply, and the fracture is most likely to happen in this location. As seen by the analysis of PEEK/PEI blends with different weight ratios, the presence of PEI decreases the mechanical strength of blend. It also impacts thermal transitions, crystallinity and microstructure of the material.

In a last part, AE 250 composite have been welded in configuration B, meaning with two energy director layers. The optimal welding parameters are identified as 800 N and 1200 ms, leading to a maximal LSS of 35 MPa. The mechanical strength of AE 250 specimens is lower than those of PEEK composite specimens.

Finally, the final sonotrode displacement has pointed out that it is unnecessary to flow the entire polymer layer to reach high mechanical strength. Optimal displacements have been defined, they lead to optimum final energy director thickness. This thickness is close to 350 μm & not dependent on the material or the initial ED thickness.

Conclusion & perspectives

Conclusion

This thesis work contributes to extend the knowledge on ultrasonic welding of PAEK composites. In a context of continuously increasing production rates and cost savings, the necessity of developing a reliable assembling process has never been more important. Recent research works have identified ultrasonic welding as a promising technology to assemble thermoplastic composites. Therefore, the different chapters allow a deeper understanding of the ultrasonic welding process, from macroscopic to molecular scale.

Chapter 1 is an introduction to ultrasonic welding of thermoplastic composites, aiming to highlight the strengths and weaknesses of the process, based on existing literature. With this state of the art in mind, CF/PAEK composites were chosen to be the main materials of this study due to their increasing value in the aerospace industry. **Chapter 2** offers a detailed description of the manufacturing process for welding specimens. The energy director was integrated into the specimens prior welding. Different types of specimens were produced using vacuum bag process:

- CF/PEEK composites with either a 250 μm PEEK or PEI film as top layer,
- CF/PEEK composites,
- CF/AE 250 composite with a 250 μm AE 250 film as top layer.

Moreover, the ultrasonic welding device used in this study is also presented. Welding time, welding load and vibration amplitude are the three parameters chosen for parametric studies in Chapters 4 and 5. The output parameters from the device are used to identify the physical phenomena occurring during welding, such as PEI softening or PEEK melting.

During the welding process, the materials must be in their molten state to insure interdiffusion of macromolecules. Therefore, a thorough analysis of the rheological behaviors of molten PEEK 450G and AE 250, and of their crystallization on cooling is exposed in **Chapter 3**. Besides their difference in melting temperature, the crystallinity of AE 250 is lower than PEEK, whether for flakes or films. PEEK is well known for its fast crystallization. AE 250 crystallization is slower than those of PEEK, allowing a better control of the

crystallization during welding. Then, dynamic rheological tests offer a deeper vision of AE 250 behavior. Both films and flakes exhibit similar behavior as any molten polymer with a Newtonian plateau and shear-thinning region. Master curves of the complex viscosity show an Arrhenius law dependency with activation energy close to 60 $kJ.mol^{-1}$. Those results were used to quantify relaxation times, which are the diffusion times needed for the macromolecules to interpenetrate and to entangle. AE 250 relaxation times were lower than PEEK 450G, 200 ms over 2 s, allowing easier molecular diffusion. Finally, AE 250 complex viscosity was compared with other PAEK from data available in the literature. The behavior of AE 250 was found similar to PEKK 6002.

A temperature measurement method was developed in **Chapter 4** to assess the temperature cycle as close as possible to the interface. Thermocouples were integrated inside the energy director. A post-synchronization was necessary to match the temperature curves with output parameters of the welder. Indeed, the displacement of the sonotrode was added to temperature profiles to better understand physical changes during welding. Using those curves, different steps and specific points were found from heating and squeeze flow of PEI. Considering welding parameters, temperature profiles change significantly when modifying the welding time or welding load. However, the modification of welding amplitude did not change the temperature profiles. Finally, a simple finite element modelling was made to evaluate the thermal diffusion through the specimen thickness. In a three PEI layers welding configuration, PEEK was found not to be thermally affected by welding. Only PEI at the interface would reach high temperature, above 400 $°C$. In the case of one PEI layer, however, the first ply of the lowest specimen would be above the melting temperature of PEEK. It is necessary in a one-layer configuration to reach the melting temperature of PEEK since the welding interface is PEEK/PEI. However, in a three layers configuration, the welding interface is PEI/PEI. Therefore, welding with a one-layer configuration is more difficult since higher temperatures have to be reached.

In **Chapter 5**, a similar parametric study than in Chapter 4 was conducted but this time, regarding the mechanical strength of CF/PEEK welds. Through SLS tests, we notice that welding time is the most impacting welding parameter, followed by the welding load. Vibration amplitude does not display a significant influence on mechanical results. Moreover, a three PEI layers configuration reaches the highest LSS values compared to a lesser number of PEI interfacial layers. The highest LSS are close to 50 MPa and those values are among the highest reported in the literature. Fracture surfaces showed different fracture mechanisms. Indeed, a fracture within the PEI interphase is mostly a brittle fracture. When fractures are located within PEEK, the behavior is either brittle or ductile. Cracks going from one specimen to the other one were observed, especially for

welds resulting in high LSS. Two types of morphology were seen for this type of fracture: a fracture at the interface between the first two plies or a fracture within the first ply. Also, a PEI concentration gradient was found at the interface due to the prior integration of PEI layer inside the welding specimens. Raman spectroscopy and PEEK/PEI blends analysis were used to further understand the fracture mechanism. The thickness of this gradient is around 100 μm, and PEEK/PEI blends analysis showed that the presence of PEI would decrease the mechanical toughness. For this reason, it is assumed that the fracture within the first ply was probably within the PEEK/PEI blend.

Moreover, using a PEEK energy director results in high LSS values, similar to those with a PEI energy director. However, longer welding time are needed to reach them, resulting in higher energy consumption. Same experiments on AE 250 show that the maximum LSS of such welds would be reached at a similar welding time than for weld using a PEI energy director. However, the maximum LSS was lower for AE 250 than for PEEK using either a PEEK or a PEI energy director. Finally, the final sonotrode displacement displays interesting results on how to monitor the process. Indeed, a final thickness close to 350 μm was found to be optimal, no matter the material used.

From those results, this PhD work main contribution is a deeper understanding of the ultrasonic welding process applied to carbon fiber/PAEK composites. More specifically, this work has brought significant improvements regarding:

i) The rheological behavior of Victrex PAEK AE 250 during mechanical sollicitations and its competitiveness with other commercial PAEK polymers,

ii) The temperature measurement during US welding by developping a non-intrusive measurement method at the welding interface,

iii) The influence of welding parameters from a thermal and mechanical point of view,

iv) The weldability window for PEEK and AE 250 composites leading to high strength welds, around 50 MPa,

v) The comparison of different energy director polymer films, that can lead to similar high mechanical strength,

vi) In the case of bi-material welding, the measurement of the gradient concentration at the welding interphase.

Perspectives

These results have opened new possibilities listed hereafter. Short-term perspectives are introduced, including the thickness of the energy director, thermal management during welding and surface preparation. Finally, this paragraph ends with long-term perspectives.

Thickness of the energy director:

- An important part lies with the thickness of the energy director. Using an integrated energy director is easy to manufacture since it does not require any additional step to the process. In the case of bi-material welding, the number of PEI layers significantly influences the mechanical resistance. However, all films were 250 μm thick. A future study could consider different thicknesses of PEI for an identical welding configuration. Indeed, the final sonotrode displacement proves that the highest LSS is reached well before the squeeze flow of the entire PEI layer. An optimized thickness could reduce assembling costs and prevent unnecessary polymer at the interface, weakening the resistance of welds. Moreover, a deeper study on the PEI gradient concentration is necessary to fully understand this optimal thickness and the fracture mechanism. The gradient thickness could be studied by Fourier transform infrared spectroscopy (FTIR), atomic force microscopy (AFM) or X-ray diffraction (XRD). More knowledge about the PEI gradient thickness could be used to decrease the energy director thickness. For example, in the case of a three PEI-layer-energy director, the thickness of the two integrated PEI films on each specimen could be reduced to allow just the right amount of macromolecular chains to diffuse and create a bond with the intermediate layer.

- Another essential issue is how the energy director is placed at the interface. Indeed, the study on the number of PEI layers showed that the highest LSS was found for the highest number of layers. However, to reduce costs and improve mechanical strength, the use of non-integrated films at the interface could be another option that would allow higher LSS. Indeed, non-integrated films configuration reached higher LSS than integrated films. The use of two non-integrated polymer films with different thicknesses is worth studying.

- An optimized thickness has not yet been found that could be generalized to all polymers. However, similar trends regarding the final thickness were found for CF/PEEK welds using PEEK and PEI energy directors and CF/AE 250 welds. This study could be broadened to other materials within the PAEK family and other high-performance

polymers. We assume that comparable thicknesses could be found for other polymers in the same welding configuration (*i.e* the same thickness and/or the number of films). In this case, a displacement-controlled process would allow to reach directly the final thickness. A parametric study to define optimum welding parameters would not be necessary anymore.

Thermal management during welding:

- Regarding the temperature profile at the welding interface, the methods developed in this thesis are only applied for PEI. Implementing thermocouples inside PEEK or AE 250 layers to evaluate their temperature profiles could be fruitful. For semi-crystalline polymers, knowing the cooling rate is essential as it defines the crystallinity and, therefore, the mechanical strength of the interfacial zone.

- The influence of welding load has been shown in this work. The pressure is known to promote intimate contact that is responsible for intermolecular diffusion and entanglement. It is possible to make multiple steps on an electrical welder during the vibration phase, steps in which the load profile, vibration amplitude, and welding time can be modified. Chapter 4 displays that the temperature keeps increasing until the end of the vibration phase. The pressure modification during this phase could modify/slow this increase in temperature. It would be therefore easier to control and to reach the suitable temperature, allowing optimum chain diffusion and entanglement.

- The numerical modelling of the thermal diffusion could be improved. For example, our model does not consider the movement of the upper specimen during welding. When the energy director squeeze flows at the interface, the upper and lower specimens are put closer, increasing the temperature. Moreover, the gradient concentration is not taken into account. Future work could deal with measuring the thermal properties of different materials that could be implemented in the model. Besides, the latter can be used to determine the optimal thickness of the energy director. In the case of a three PEI layers configuration, the optimum thickness would be the minimum thickness for which the temperature of the first ply does not exceed the melting temperature of PEEK.

Surface preparation

- Finally, it has been shown that heat generation is not homogeneous over the entire welding area. Unmelted areas were observed while polymer degradation and fiber movement was visible. A modification of the surface roughness with a surface treatment could improve the quality of the weld. A patterned surface on the whole area to be welded could be an option to uniformaly distribute friction and heat. The welding time could be reduced as the entire surface would melt/flow earlier.

Long term approach of the process

- This entire work is based on static ultrasonic welding, meaning only specific geometries can be welded. For more complex ones, the process would need to be adapted. Continuous US welding would be the ultimate goal, but several issues make his development difficult at the moment. First of all, good quality welds require sufficient pressure during cooling, which is more difficult to apply with a moving device. Thermal management also has to be considered, especially how to homogeneously heat the welding area. Heat diffusion would not be the same at the beginning and end of a large parts compared to the middle area since the environment is not the same. The question would be how to reach a steady-state for heat diffusion in the entire welding area. Heat diffusion is also related with welding speed. A moving welder implies to define a proper speed to insure constant weld quality. Finally, we could wonder how static US welding conditions can be transposed to continuous US welding. Even though some authors have studied this problem [Senders, 2016, Jongbloed et al., 2018], a relevant solution has not yet been found.

- Lauak Group has decided to focus on US spot welding as a step towards continuous welding, bringing yet new challenges to overcome. First, the sealing of the welded parts would have to be ensured, meaning the distance between two spots would have to be defined. The influence of a new spot on the previous one would have to be understood, especially regarding how the vibration impacts a cooled weld. The dimensions of the heat-affected zone around spots would have to be quantified. Indeed, the process would have to ensure that no chemical degradation occurs around spots, especially if a heating ramp is repeated several times. Finally, we can wonder how static welding parameters could be applied to those spot welds, as squeeze flow of the material is not tolerated in US spot welding.

Appendix A

Material datasheets

Material datasheets discussed in this manuscript thesis are presented in the following order:

- APC-2 prepreg datasheet from Solvay (pages 164 - 170)
- HexTow AS4 carbon fibers datasheet from Hexcel (pages 171 - 172)
- AE 250 prepreg datasheet from Victrex (pages 173 - 174)
- PEEK 450G datasheet from Victrex (pages 175 - 176)

TECHNICAL DATA SHEET

APC-2

PEEK THERMOPLASTIC POLYMER PREPREG

APC-2 UNIDIRECTIONAL TAPE

Solvay's APC -2 composites have a thermoplastic matrix of poly(ether-ether-ketone) commonly referred to as PEEK. The polymer is semi-crystalline with a glass transition temperature of 289°F (143°C). The composites possess excellent environmental resistance, toughness, and fire resistant properties.

APC-2 prepreg can be stored at ambient conditions and has an indefinite shelf life. APC-2 composites retain good mechanical properties at cryogenic temperatures. The excellent composite properties result from the PEEK matrix's full wetting and tailored fiber matrix interface achieved in the impregnation process.

Laminates and parts can be fabricated from APC-2 using a wide range of processes including autoclave consolidation, rapid stamping techniques, and automated lay down including in-situ.

Typical applications for Solvay's APC-2 include aircraft and space structure, and other structural engineering components.

Features and Benefits

- Semi-crystalline, thermoplastic matrix
- Fully impregnated, unidirectional prepreg
- Large database
- Very high toughness and damage tolerance
- Dry Tg at 289°F (143°C) with less than 0.2 weight percent moisture uptake at equilibrium.
- Excellent environmental resistance
- Good resistance to creep and fatigue
- Outstanding fire resistance
- Very good wear resistance
- Processed using wide range of fabrication techniques at 725°F to 752°F (385°C to 400°C)
- Indefinite shelf life at ambient condition

RESIN CHARACTERISTICS

Table 1 | Nominal Neat Resin Properties of APC-2

Property	Result
DMA Tg, °F (°C)	289 (143)
Density, pcf (g/cc)	82.4 (1.32)
Dielectric constant at 1 MHz	4.60
Loss Tangent at 1 MHz	<0.001

Table 2 | Typical Polymer Properties of APC-2 (PEEK) Resin

Property	Test Condition	Result
Tensile Strength ksi (MPa)	75°F (24°C) 250°F (121°C) 250°F (121°C)/ wet	14.5 (100) 8.5 (59) 8.5 (59)
Tensile Modulus Msi (GPa)	75°F (24°C) 250°F (121°C) 250°F (121°C)/ wet	0.52 (3.6) 0.49 (3.4) 0.49 (3.4)
Tensile Failure Strain %	75°F (24°C) 250°F (121°C) 250°F (121°C)/ wet	50 70 70
Flexural Strength ksi (MPa)	75°F (24°C) 250°F (121°C) 250°F (121°C)/ wet	24.7 (170)* 14.5 (100)* 14.5 (100)*
Flexural Modulus Msi (GPa)	75°F (24°C) 250°F (121°C) 250°F (121°C)/ wet	0.59 (4.1) 0.58 (4.0) 0.58 (4.0)

* Yield value at >5% strain
**Wet = Water immersion for 14 days at 160°F (71°C).

PREPREG CHARACTERISTIC

Table 3 | Product Availability and Nominal Physical Properties of APC-2 (PEEK)

Property			
Form	12 inch (30.5 cm) Unidirectional Tape		
Fiber	AS4 12K	IM7 12K	S2 Glass
Resin Content , wt. %	34	32	29
Areal Weight, psf (gsm)	0.030 (145)	0.030 (145)	0.040 (195)
CPT, in (mm)	0.0055 (0.140)	0.0052 (0.132)	0.0054 (0.137)

PROPERTIES

Table 4 | Mechanical Properties: High Strength (>500 ksi/ 3450 MPa) Standard Modulus (33 Msi/ 228 GPa) Carbon Fiber Reinforced Unidirectional Tape

Property	Test Condition	Result
0° Tensile Strength ksi (MPa)	-67°F (-55°C) 75°F (24°C) 180°F (82°C) 180°F (82°C)/ wet 250°F (121°C) 250°F (121°C)/ wet	300 (2070) 300 (2070) 295 (2030) 295 (2030) 290 (2000) 290 (2000)
0° Tensile Modulus Msi (GPa)	-67°F (-55°C) 75°F (24°C) 180°F (82°C) 180°F (82°C)/ wet 250°F (121°C) 250°F (121°C)/ wet	20 (138) 20 (138) 20 (138) 20 (138) 20 (138) 20 (138)
0° Tensile Failure Strain	-67°F (-55°C)	1.45

TECHNICAL DATA SHEET

APC-2

PEEK THERMOPLASTIC POLYMER PREPREG

%	75°F (24°C) 250°F (121°C)	1.45 1.35
0°Tensile Poisson's Ratio	67°F (-55°C) 75°F (24°C)	0.30 0.30
0° Compression Strength ksi (MPa)	-67°F (-55°C) 75°F (24°C) 180°F (82°C) 180°F (82°C)/ wet 250°F (121°C) 250°F (121°C)/ wet	220 (1520) 197 (1360) 180 (1240) 180 (1240) 170 (1170) 170 (1170)
0° Compression Modulus Msi (GPa)	-67°F (-55°C) 75°F (24°C) 180°F (82°C) 180°F (82°C)/ wet 250°F (121°C) 250°F (121°C)/ wet	19 (131) 18 (124) 18 (124) 18 (124) 18 (124) 18 (124)
0° Flexural Strength ksi (MPa)	75°F (24°C) 180°F (82°C) 180°F (82°C)/ wet 250°F (121°C) 250°F (121°C)/ wet	290 (2000) 270 (1860) 270 (1860) 257 (1770) 257(1770)
0° Flexural Modulus Msi (GPa)	75°F (24°C) 180°F (82°C) 180°F (82°C)/ wet 250°F (121°C) 250°F (121°C)/ wet	18 (124) 18 (124) 18 (124) 18 (124) 18 (124)
90° Tensile Strength ksi (MPa)	-67°F (-55°C) 75°F (24°C) 180°F (82°C)/ wet	14 (97) 13 (90) 12 (83)
0° Tensile Modulus Msi (GPa)	-67°F (-55°C) 75°F (24°C) 180°F (82°C)/ wet	1.52 (10.5) 1.48 (10.2) 1.39 (9.6)
0° Tensile Failure Strain %	-67°F (-55°C) 75°F (24°C) 180°F (82°C)/ wet	0.94 0.88 0.86
In-plane Shear Strength ksi (MPa)	-67°F (-55°C) 75°F (24°C) 180°F (82°C) 180°F (82°C)/ wet 250°F (121°C)	30 (207) 27 (186) 23 (159) 24 (165) 21 (145)
In-plane Shear Modulus Msi (GPa)	-67°F (-55°C) 75°F (24°C) 180°F (82°C)/ wet	0.92 (6.3) 0.82 (5.7) 0.74 (5.1)
Open Hole Tensile Strength ksi (MPa)	75°F (24°C)	56 (386)
Open Hole Compression Strength ksi (MPa)	75°F (24°C) 180°F (82°C) 180°F (82°C)/ wet 250°F (121°C) 250°F (121°C)	47 (324) 42 (290) 41 (283) 38 (262) 37 (255)

*Property values listed are typical for laminates with 60% fiber volume.

**Wet = Water immersion for 14 days at 160°F (71°C).

Table 5 | Toughness Properties: High Strength (>500 ksi/ 3450 MPa) Standard Modulus (33 Msi/ 228 GPa) Carbon Fiber Reinforced Unidirectional Tape

Property	Test Condition	Result
Compression After Impact Strength after 1500 in-lb/in (6.67 J/mm) impact ksi (MPa)	75°F (24°C)	49 (338)
Interlaminar Fracture Toughness Mode I G_{IC} in-lb/in^2 (kJ/m^2)	-67°F (-55°C) 75°F (24°C)	8.6 (1.5) 9.7 (1.7)
Interlaminar Fracture Toughness Mode II G_{IIC} in-lb/in^2 (kJ/m^2)	-67°F (-55°C) 75°F (24°C)	10.3 (1.8) 11.4 (2.0)

*Property values listed are typical for laminates with 60% fiber volume.

Table 6 | Mechanical Properties: High Strength (>750 ksi/ 5170 MPa) Intermediate Modulus (40 Msi/ 276 GPa) Carbon Fiber Reinforced Unidirectional Tape

Property	Test Condition	Result
0° Tensile Strength ksi (MPa)	-67°F (-55°C) 75°F (24°C) 250°F (121°C)	410 (2830) 420 (2900) 400 (2760)
0° Tensile Modulus Msi (GPa)	-67°F (-55°C) 75°F (24°C) 250°F (121°C)	25 (172) 25 (172) 25 (172)
0° Tensile Failure Strain %	-67°F (-55°C) 75°F (24°C) 250°F (121°C)	1.5 1.5 1.4
0°Tensile Poisson's Ratio	-67°F (-55°C) 75°F (24°C) 250°F (121°C)	0.26 0.27 0.30
0° Compression Strength ksi (MPa)	-67°F (-55°C) 75°F (24°C) 250°F (121°C) 250°F (121°C)/ wet	220 (1520) 190 (1310) 170 (1170) 170 (1170)
0° Compression Modulus Msi (GPa)	-67°F (-55°C) 75°F (24°C) 250°F (121°C) 250°F (121°C)/ wet	22 (152) 22 (152) 21 (145) 21 (145)
0° Flexural Strength ksi (MPa)	-67°F (-55°C) 75°F (24°C) 250°F (121°C) 250°F (121°C)/ wet	350 (2410) 315 (2170) 260 (1790) 260 (1790)
0° Flexural Modulus Msi (GPa)	-67°F (-55°C) 75°F (24°C) 250°F (121°C) 250°F (121°C)/ wet	23 (159) 23 (159) 22 (152) 22 (152)
90° Tensile Strength ksi (MPa)	-67°F (-55°C) 75°F (24°C) 250°F (121°C)	9.2 (63) 8.7 (60) 7.0 (48)

TECHNICAL DATA SHEET

APC-2

PEEK THERMOPLASTIC POLYMER PREPREG

90° Tensile Modulus Msi (GPa)	-67°F (-55°C) 75°F (24°C) 250°F (121°C)	1.6 (11.0) 1.5 (10.0) 1.2 (8.3)
90° Flexural Strength ksi (MPa)	-67°F (-55°C) 75°F (24°C) 250°F (121°C) 250°F (121°C)/ wet	16 (110) 15 (103) 13 (90) 13 (90)
90° Flexural Modulus Msi (GPa)	-67°F (-55°C) 75°F (24°C) 250°F (121°C) 250°F (121°C)/ wet	1.4 (9.7) 1.4 (9.7) 1.1 (7.6) 1.1 (7.6)
In-plane Shear Strength ksi (MPa)	-67°F (-55°C) 75°F (24°C) 250°F (121°C) 250°F (121°C)/ wet	28 (193) 26 (179) 20 (138) 19 (131)
In-plane Shear Modulus Msi (GPa)	-67°F (-55°C) 75°F (24°C) 250°F (121°C) 250°F (121°C)/ wet	0.86 (5.9) 0.80 (5.5) 0.52 (3.6) 0.40 (2.8)
Open Hole Tensile Strength ksi (MPa)	-67°F (-55°C) 75°F (24°C) 250°F (121°C) 250°F (121°C)/ wet	74 (510) 69 (476) 66 (455) 63 (434)
Open Hole Compressive Strength ksi (MPa)	-67°F (-55°C) 75°F (24°C) 250°F (121°C) 250°F (121°C)/ wet	50 (345) 47 (324) 38 (262) 36 (248)

*Property values listed are typical for laminate with 60% fiber volume.

**Wet = Water immersion for 14 days at 160°F (71°C).

Table 7 | Toughness Properties: High Strength (>750 ksi/ 5170 MPa) Intermediate Modulus (40 Msi/ 276 GPa class) Carbon Fiber Reinforced Unidirectional Tape

Property	Test Condition	Result
Compression after impact Strength after 1500 in-lb/in (6.67 J/mm) impact ksi (MPa)	75°F (24°C)	53 (365)
Interlaminar Fracture Toughness Mode I G_{IC} in-lb/in^2 (kJ/m^2)	-67°F (-55°C) 75°F (24°C)	9.2 (1.6) 13.0 (2.3)
Interlaminar Fracture Toughness Mode II G_{IIC} in-lb/in^2 (kJ/m^2)	-67°F (-55°C) 75°F (24°C)	12.0 (2.1) 11.0 (1.9)

*Property values listed are typical for laminates with 60% fiber volume.

Table 8 | Mechanical Properties: S-2 glass fiber reinforced unidirectional tape, APC-2/ S-2 glass

Property	Test Condition	Result
0° Tensile Strength ksi (MPa)	75°F (24°C) 250°F (121°C) 250°F (121°C)/ wet	170 (1170) 165 (1140) 150 (1030)
0° Tensile Modulus Msi (GPa)	75°F (24°C) 250°F (121°C) 250°F (121°C)/ wet	8.0 (55) 8.0 (55) 8.0 (55)
0° Compression Strength ksi (MPa)	75°F (24°C) 250°F (121°C)	160 (1100) 150 (1030)
0° Compression Modulus Msi (GPa)	75°F (24°C)	8.0 (55)
0° Flexural Strength ksi (MPa)	75°F (24°C)	225 (1550)
0° Flexural Modulus Msi (GPa)	75°F (24°C)	8.0 (55)

*Property values listed are typical for laminate with 60% fiber volume.

**Wet = Water immersion for 14 days at 160°F (71°C).

PROCESSING

Typical Autoclave Consolidation Cycle

- Apply minimum 24 in (610 mm) of Hg vacuum to the bagged assembly and maintain throughout the entire cure cycle.
- Heat from RT, 75°F (24°C), to 735°F ± 15°F (391°C ± 8°C) at any available rate based on part temperature.
- Apply 100 psi ± 5 psi (689 kPa ± 34 kPa) autoclave pressure when the temperature reaches 735°F (391°C).
- Hold at 735°F (391°C) for 20 +10/-0 minutes.
- Cool down at a rate of 20°F (11°C)/minute.
- Maintain pressure until temperature is below 140°F (60°C).

* Time at temperature is based on lagging thermocouple

** Press consolidation cycle may vary depending on equipment parameters

TECHNICAL DATA SHEET

APC-2

PEEK THERMOPLASTIC POLYMER PREPREG

Lay-Up/ Bagging

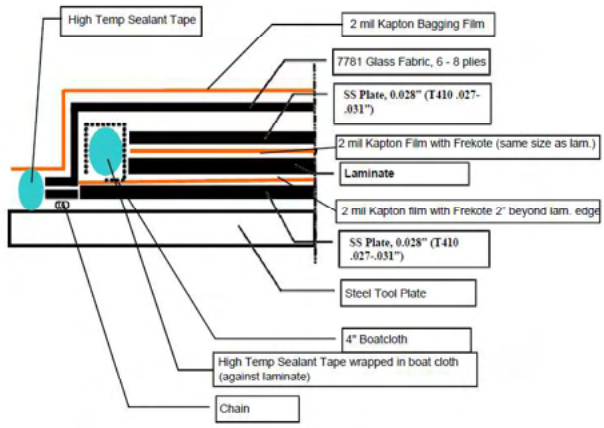

Figure 1 | Recommended Vacuum Bag Scheme

PRODUCT HANDLING

Solvay recommends the wearing of clean, impervious gloves when working with prepreg materials in order to reduce skin contact and to avoid contamination of the product. See the Safety Data Sheet for more information.

SHIPPING

APC-2 is typically shipped as rolls in containers at ambient temperature. Standard roll form is 12 inches wide (30.5 cm) and approximately 600 linear feet (183 meter). It is not necessary to seal the material in bags.

DISPOSAL OF SCRAP MATERIAL

Discarded APC-2 is not a hazardous waste under RCRA, 40 CFR261. Disposal of material should be in accordance with local, state, and federal regulations, which may vary by location. Questions concerning the disposal should be directed to the Solvay Safety, Health, and Environmental Affairs Department in Winona, Minnesota at (507) 454-3611 for evaluation on a case-by-case basis.

HEALTH & SAFETY

Please refer to the product SDS for safe handling, personal protective equipment recommendations and disposal considerations.

Solvay
Composite Materials HQ
4500 McGinnis Ferry Rd
Alpharetta, GA 30005-3914 USA

SOLVAY
asking more from chemistry®

HexTow® AS4
Carbon Fiber

HEXCEL®

Product Data Sheet

HexTow® AS4 carbon fiber is a continuous, high strength, high strain, PAN based fiber available in 3,000 (3K), 6,000 (6K) and 12,000 (12K) filament count tows. This fiber has been surface treated and can be sized to improve its interlaminar shear properties, handling characteristics, and structural properties, and is suggested for use in weaving, prepregging, filament winding, braiding, and pultrusion.

AS4-GP 3k (1%), AS4-GP 12k (0.9%), and AS4 12k carbon fibers have been qualified to NMS 818 Carbon Fiber Specification (NCAMP). This allows customers to call out an industry standard, aerospace grade carbon fiber without the need to write and maintain their own specification.

Typical Fiber Properties	U.S. Units	SI Units
Tensile Strength		
3K	685 ksi	4723 MPa
6K	650 ksi	4482 MPa
12K	645 ksi	4447 MPa
Tensile Modulus (Chord 6000-1000)	33.5 Msi	231 GPa
Ultimate Elongation at Failure		
3K	1.8%	1.8%
6K	1.7%	1.7%
12K	1.7%	1.7%
Density	0.0647 lb/in^3	1.79 g/cm^3
Weight/Length		
3K	11.8 x 10^{-6} lb/in	0.210 g/m
6K	23.9 x 10^{-6} lb/in	0.427 g/m
12K	48.0 x 10^{-6} lb/in	0.858 g/m
Approximate Yield		
3K	7,086 ft/lb	4.75 m/g
6K	3,485 ft/lb	2.34 m/g
12K	1,734 ft/lb	1.17 m/g
Tow Cross-Sectional Area		
3K	1.82 x 10^{-4} in^2	0.12 mm^2
6K	3.70 x 10^{-4} in^2	0.24 mm^2
12K	7.43 x 10^{-4} in^2	0.48 mm^2
Filament Diameter	0.280 mil	7.1 microns
Carbon Content	94.0%	94.0%
Twist	Never Twisted	Never Twisted

Typical HexPly 8552 Composite Properties (at Room Temperature)	U.S. Units	SI Units	Test Method
0° Tensile Strength	310 ksi	2137 MPa	ASTM D3039
0° Tensile Modulus	19.6 Msi	135 GPa	
0° Tensile Strain	1.6%	1.6%	
0° Flexural Strength	274 ksi	1889 MPa	ASTM D790
0° Flexural Modulus	18.4 Msi	127 GPa	
0° Short Beam Shear Strength	18.5 ksi	128 MPa	ASTM D2344
0° Compressive Strength	222 ksi	1530 MPa	ASTM Mod. D695
0° Compressive Modulus	18.6 Msi	128 GPa	
0° Open Hole Tensile Strength	63.5 ksi	438 MPa	ASTM D5766
90° Tensile Strength	9.3 ksi	64 MPa	ASTM D3039
Fiber Volume	60%	60%	

HexTow® AS4 carbon fiber

HEXCEL

Product Data Sheet

Yarn/Tow Characteristics	U.S. Units	SI Units
Specific Heat	0.28 Btu/lb-°F	0.27 cal/g-°C
Electrical Resistivity	5.6 x 10^{-5} ohm-ft	1.7 x 10^{-3} ohm-cm
Coefficient of Thermal Expansion	-0.35 ppm/°F	-0.63 ppm/°C
Thermal Conductivity	3.95 Btu/hr-ft-°F	6.83 W/m-°K

Carbon Fiber Certification
This carbon fiber is manufactured to Hexcel aerospace grade specification HS-CP-5000. A copy of this specification is available upon request. A Certification of Analysis will be provided with each shipment.

Available Sizing
Sizing compatible with various resin systems, based on application are available to improve handling characteristics and structural properties. Please see additional information on available Sizes on our website or contact our technical team for additional information.

Packaging
Standard packaging of HexTow® AS4 is as follows:

Filament Count	Size	Nominal Weight		Nominal Length	
		(lb)	(kg)	(ft)	(m)
3K	G	5.0	2.3	35,430	10,800
	GP	6.0	2.7	42,520	12,960
6K	G	3.0	1.4	10,450	3,190
	GP	6.0	2.7	20,910	6,375
12K	GP	8.0	3.6	13,880	4,230
	Unsized	10.0	4.5	17,340	5,290

Other package sizes may be available on request. The fiber is wound on a 3-inch ID by 11-inch long cardboard tube and overwrapped with plastic film.

Safety Information
Obtain, read, and understand the Safety Data Sheet (SDS) before use of this product.

For more information
Hexcel is a leading worldwide supplier of composite materials to aerospace and industrial markets. Our comprehensive range includes:

- HexTow® carbon fibers
- HexForce® reinforcements
- HiMax™ multiaxial reinforcements
- HexPly® prepregs
- HexMC®-i molding compounds
- HexFlow® RTM resins
- HexBond™ adhesives
- HexTool® tooling materials
- HexWeb® honeycombs
- Acousti-Cap® sound attenuating honeycomb
- Engineered core
- Engineered products
- Polyspeed® laminates & pultruded profiles
- HexAM® additive manufacturing

For US quotes, orders and product information call toll-free 1-866-556-2662. For other worldwide sales office telephone numbers and a full address list, please go to:

http://www.hexcel.com/contact

CTA 311 JA20

victrex

AE250 UDT PROCESSING

6th November 2018

victrex

PROCESS CYCLES

Process cycle heat-up and cooldown rates are limited by the processing equipment and not the material.

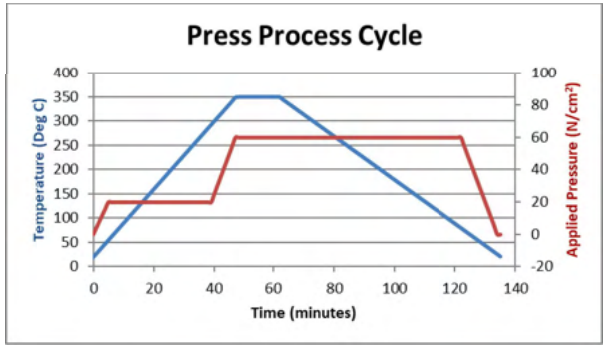

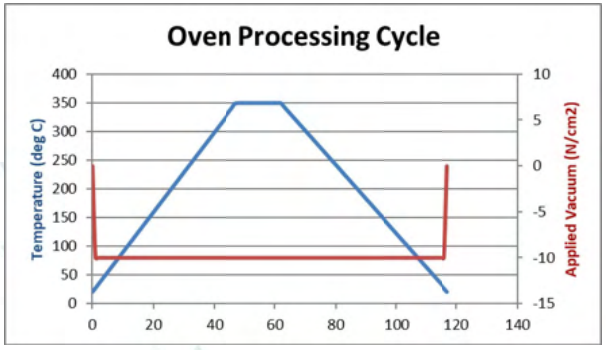

Press	Hydraulic
Platen	Heating Electrical
Cooling	Water/Air mix
Heat up rate	7°C/minute
Hold temperature	350 °C
Hold time at temp.	15 minutes
Hold pressure	Two step: ramp 2 Bar then 6 Bar at max. temp.
Cool down rate	-4.5 °C/minute

Oven	Electrical
Heat up rate	7°C/minute
Hold temperature	350 °C
Hold time at temp.	15 minutes
Hold pressure	-1 Bar (Vacuum)
Cool down rate	-6 °C/minute

Note:
These process cycles are applied to our 134gsm (AS4), 143gsm (AS4) and 192 gsm (AS7) tapes at 50mm width. We use these cycles to make test panels for mechanical testing.

Fibre content 58 Vol. %
Polymer content 34 wt. %
Prepreg thickness range 0.14-0.19 mm CPT 0.13-0.18

Laminate thickness range 1mm to 4.5mm.

VICTREX™ PEEK 450G™

victrex

Product Description

High-performance thermoplastic material, unreinforced **P**oly**E**ther**E**ther**K**etone (PEEK), semi-crystalline, granules for injection moulding and extrusion, standard flow, FDA food contact compliant, colour natural/beige.

Typical Application Areas

Applications for higher strength and stiffness as well as high ductility. Chemically resistant to aggressive environments, suitable for sterilisation for medical and food contact applications.

MATERIAL PROPERTIES				
	CONDITIONS	TEST METHOD	UNITS	TYPICAL VALUE
Mechanical Data				
Tensile Strength	Yield, 23°C	ISO 527	MPa	98
Tensile Elongation	Break, 23°C	ISO 527	%	45
Tensile Modulus	23°C	ISO 527	GPa	4.0
Flexural Strength	At 3.5% strain, 23°C	ISO 178	MPa	125
	At yield, 23°C			165
	125°C			85
	175°C			19
	275°C			12.5
Flexural Modulus	23°C	ISO 178	GPa	3.8
Compressive Strength	23°C	ISO 604	MPa	125
	120°C			70
Charpy Impact Strength	Notched, 23°C	ISO 179/1eA	kJ m^{-2}	7.0
	Unnotched, 23°C	ISO 179/1U		n/b
Izod Impact Strength	Notched, 23°C	ISO 180/A	kJ m^{-2}	8.0
	Unnotched, 23°C	ISO 180/U		n/b
Thermal Data				
Melting Point		ISO 11357	°C	343
Glass Transition (Tg)	Onset	ISO 11357	°C	143
	Midpoint			150
Coefficient of Thermal Expansion	Along flow below Tg	ISO 11359	ppm K^{-1}	45
	Average below Tg			55
	Along flow above Tg			120
	Average above Tg			140
Heat Deflection Temperature	As moulded, 1.8 MPa	ISO 75-f	°C	152
Thermal Conductivity	Along flow, 23°C	ISO 22007-4	W m^{-1} K^{-1}	0.32
	Average, 23°C			0.29
Relative Thermal Index	Electrical	UL 746B	°C	260
	Mechanical w/o impact			240
	Mechanical w/impact			180
Flow				
Melt Viscosity	400°C	ISO 11443	Pa.s	350
Miscellaneous				
Density	Crystalline	ISO 1183	g cm^{-3}	1.30
Shore D hardness	23°C	ISO 868		84.5
Water Absorption by immersion	Saturation, 23°C	ISO 62-1	%	0.45
	Saturation, 100°C			0.55

VICTREX™ PEEK 450G™

Electrical Properties				
Dielectric Strength	2mm thickness	IEC 60243-1	kV mm^{-1}	23
	50 µm thickness			200
Comparative Tracking Index		IEC 60112	V	150
Loss Tangent	23°C, 1 MHz	IEC 60250	n/a	0.004
Dielectric Constant	23°C, 1 kHz	IEC 60250	n/a	3.1
	23°C, 50 kHz			3.0
	200°C, 50 kHz			4.5
Volume Resistivity	23°C	IEC 60093	Ω cm	10^{16}
	125°C			10^{15}
	275°C			10^{9}
Fire Smoke Toxicity				
Glow Wire Test	2mm thickness	IEC 60695-2-12	°C	960
Limiting Oxygen Index	0.4 mm thickness	ISO 4589	% O_2	24
	3.2 mm thickness			35
Toxicity Index	CO content	NES 713	n/a	0.074
	CO_2 content			0.15
	Total gases			0.22

Typical Processing	
Drying Temperature / Time	150°C / 3h or 120°C / 5h (residual moisture <0.02%)
Temperature settings	355 / 360 / 365 / 370 / 375°C (Nozzle)
Hopper Temperature	Not greater than 100°C
Mould Temperature	170°C - 200°C
Runner	Die / nozzle >3mm, manifold >3.5mm
Gate	>1 mm or 0.5 x part thickness

Mould Shrinkage + spiral flow					
Spiral Flow	375°C nozzle, 190°C tool	1mm thick section	Victrex	mm	110
Mould Shrinkage	375°C nozzle, 190°C tool	Along flow	ISO 294-4	%	1.0
		Across flow			1.3

Important notes:

1. Processing conditions quoted in our datasheets are typical of those used in our processing laboratories
   - *Data for mould shrinkage should be used for material comparison. Actual mould shrinkage values are highly dependent on part geometry, mould configuration, and processing conditions.*
   - *Mould shrinkage differs for along flow and across flow directions. "Along flow" direction is taken as the direction the molten material is travelling when it exits the gate and enters the mould.*
   - *Mould shrinkage is expressed as a percent change in dimension of a specimen in relation to mould dimensions.*
2. Data are generated in accordance with prevailing national, international and internal standards, and should be used for material comparison. Actual property values are highly dependent on part geometry, mould configuration and processing conditions. Properties may also differ for along flow and across flow directions.

Detailed data available on our website www.victrex.com or upon request.

World Headquarters
Victrex plc
Hillhouse International
Thornton Cleveleys, Lancashire
FY5 4QD, United Kingdom
TEL +44 (0)1253 897700
FAX +44 (0)1253 897701
MAIL victrexplc@victrex.com

Appendix B

Raman spectroscopy

CF/PEEK composite welds are analyzed with Raman spectroscopy. The experiments have been carried out by Olivier Marsan at CIRIMAT, INP-ENSIACET, University of Toulouse, Toulouse. The experimental configuration is detailed in the following.

The samples were exposed to continuous laser radiation provided by a He/Neon laser at 633 nm with a power of 8 mW. Attenuation filters have been used to avoid any degradation of the materials, reducing the laser power by two. The sample was placed under a BX 41 Olympus microscope and focused under a x100 objective with a numerical aperture of 0.90 which gave the system a lateral resolution of 0.72 μm ($1.22x\lambda$/ON) and an axial resolution of 2.61 μm ($4x\lambda$/O.N2). The maps were produced using a motorized XYZ table with an accuracy of 0.1 μm and a measurement step of 1 μm. The use of an autofocus whose amplitude range was optimized with the roughness of the area studied made it possible to adjust the focusing of the laser. A silicon standard made it possible to calibrate the equipment in frequency using the line of order 1 of silicon at 520.7 cm^{-1} with an accuracy of $\pm$ 1 cm^{-1}. The spectra were acquired using a 600 rpm grating with a spectral resolution of 1 cm^{-1} and collected with a quantum well detector cooled to -60 $^{\circ}C$ by the double Peltier effect (CCD Synapse). Each spectrum of the maps was acquired with a time of 10 seconds and 2 accumulations. Data processing was performed using Labspec 6 software.

Appendix C

Characterization of PEEK/PEI blends

Blends preparation

The polymer blends are elaborated by melt mixing with the internal mixer Rheomix 600 from ThermoFischer equipped with rollers rotors. PEI ULTEM 1000 from Sabic is selected in pellets, this grade is supposed to be the same as the PEI films used as energy director. To be as close as possible from the APC-2 matrix, we choose PEEK 450G from Victrex in pellets. Indeed, even though the composition of APC-2 matrix is not clearly elucidated, some works report similar properties to PEEK 450G and PEEK 150G [Nicodeau, 2005]. The polymer pellets are dried at 150 $°C$ during 24 h to remove any moisture before processing. They are weighted to reach the following volume ratio: 10/90, 30/70, 50/50, 70/30 and 90/10. The chamber is filled at 70 %, meaning 48 cm^3 and so, about 60 g for each blend. Weights of PEI and PEEK for each blend is presented in Table C.1. The chamber temperature is regulated at 360 $°C$. The procedure is as following: the roller rotation is started at 10 $tr.min^{-1}$, then half of the pellets are introduced inside the chamber. The rotating speed is increased at 40 $tr.min^{-1}$ corresponding to a mean shearing rate of 40 s^{-1}. After 2 min, the rest of the pellets is introduced inside the chamber while the rotors still rotate. The rotation is stopped after 10 minutes to prevent polymer degradation. Based on the experience of blends and composite preparation in the laboratory, these conditions are suitable to attain homogeneous blends.

Each blend is then manually grounded and molded into 2 mm thick plates with the hydraulic compression press LAB 800P from Pinette Emidecau Industries. A steel mould with a 149 mm x 76 mm x 2 mm cavity has been used. Granules of blends were kept in the cavity between two steel foils and placed between the plates of the hot press, which was preheated at 200 $°C$. Next, the temperature was increased at 10 $°C.min^{-1}$ up to 360 $°C$. A pressure of 50 kN was applied for 5 min at 360 $°C$. Then, still under pressure,

vol. % PEEK *(%)*	vol. % PEI *(%)*	m(PEEK) *(g)*	m(PEI) *(g)*	Total weight *(g)*
10	90	6.28	55.21	61.49
30	70	18.84	42.94	61.78
50	50	31.40	30.67	62.07
70	30	43.95	18.40	62.35
90	10	56.51	6.13	62.64

Table C.1: Proportion of PEI and PEEK for each volume ratio

the moulded samples were cooled down until 200 $°C$ at the speed of 4 $°C.min^{-1}$ under pressure. Finally, the plates were separated from steel foils and left at room temperature to slowly cool down to favor crystallization. Then, the plates are kept at 150 $°C$ to prevent water absorption. The appropriated sample geometries are cut into these plates.

Thermal analysis of blends

For DSC analysis, all blends undergone the same temperature cycle: a first increase in temperature from 25 $°C$ to 380 $°C$ at 20 $K.min^{-1}$, a decrease from 380 $°C$ to 25 $°C$ at 20 $K.min^{-1}$. The experiments were made under nitrogen atmosphere and with a sample of around 10 mg. Dynamical mechanical analysis (DMA) were perfored with an ARES LN2 rheometer from Rheometrics to evaluate the thermomechanical properties in 45 mm x 10 mm x 2 mm rectangular samples. The tests were carried out in torsion mode at a frequency of 1 Hz within the viscoelastic linear domain at a heating rate of 3 $K.min^{-1}$ from 25 $°C$ to 350 $°C$ under nitrogen atmosphere. All DSC and rheometry experiments were performed at least twice for the same experimental conditions.

Mechanical analysis of blends

Three-point-bending tests have been carried out, using notched specimens submitted to quasi-static loading conditions. The test conditions are inspired from a recent work on PMMA [Braun et al., 2021]. Due to the small amount of each type of blend (about 60 g is produced in one batch of internal mixer), the specimen size cannot fit the standard ASTM B5045-14. The specimen dimensions were 33.4 mm in width (L), 7.6 mm in high (W) and a thickness of 1.9 mm (B), the distance between supports (S) was 30.4 mm, as seen in Fig.

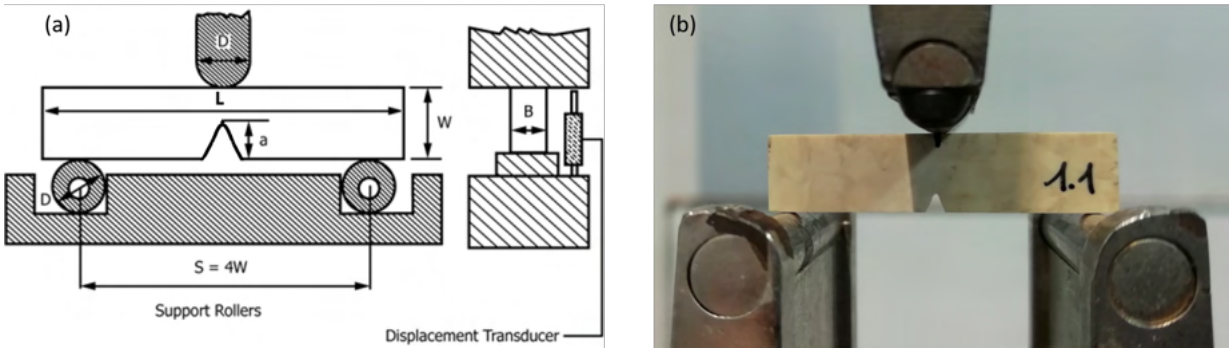

Figure C.1: Three-bending test schematic representation from ASTM B5045-14 (a) and actual set up (b)

PEEK/PEI blends *% vol. PEEK/% vol. PEI*	Initial stiffness *($N.mm^{-1}$)*	Maximum load *(N)*
100/0	269.1	243.0
90/10	252.8	217.0
70/30	241.3	117.4
50/50	244.7	97.1
30/70	228.1	87.3
10/90	206.9	114.2
0/100	223.5	118.3

Table C.2: Initial stiffness and maximum load of pure PEEK, pure PEI and different blend ratios

C.1. The specimens were cut from plates, and notched using a V shaped mechanical notch maker, creating a 0.25 mm notch-tip radius with an angle of 45°. The notch is located in the middle of the specimen length. Three-point-bending tests have been carried out using notched specimens submitted to quasi-static loading conditions. The chosen displacement rate is 1 $mm.min^{-1}$ and the load cell is 500 N. Three specimens were tested for each blend. Load-displacement curves are plotted in Fig. C.2. Initial stiffness and maximum load are displayed in Table C.2

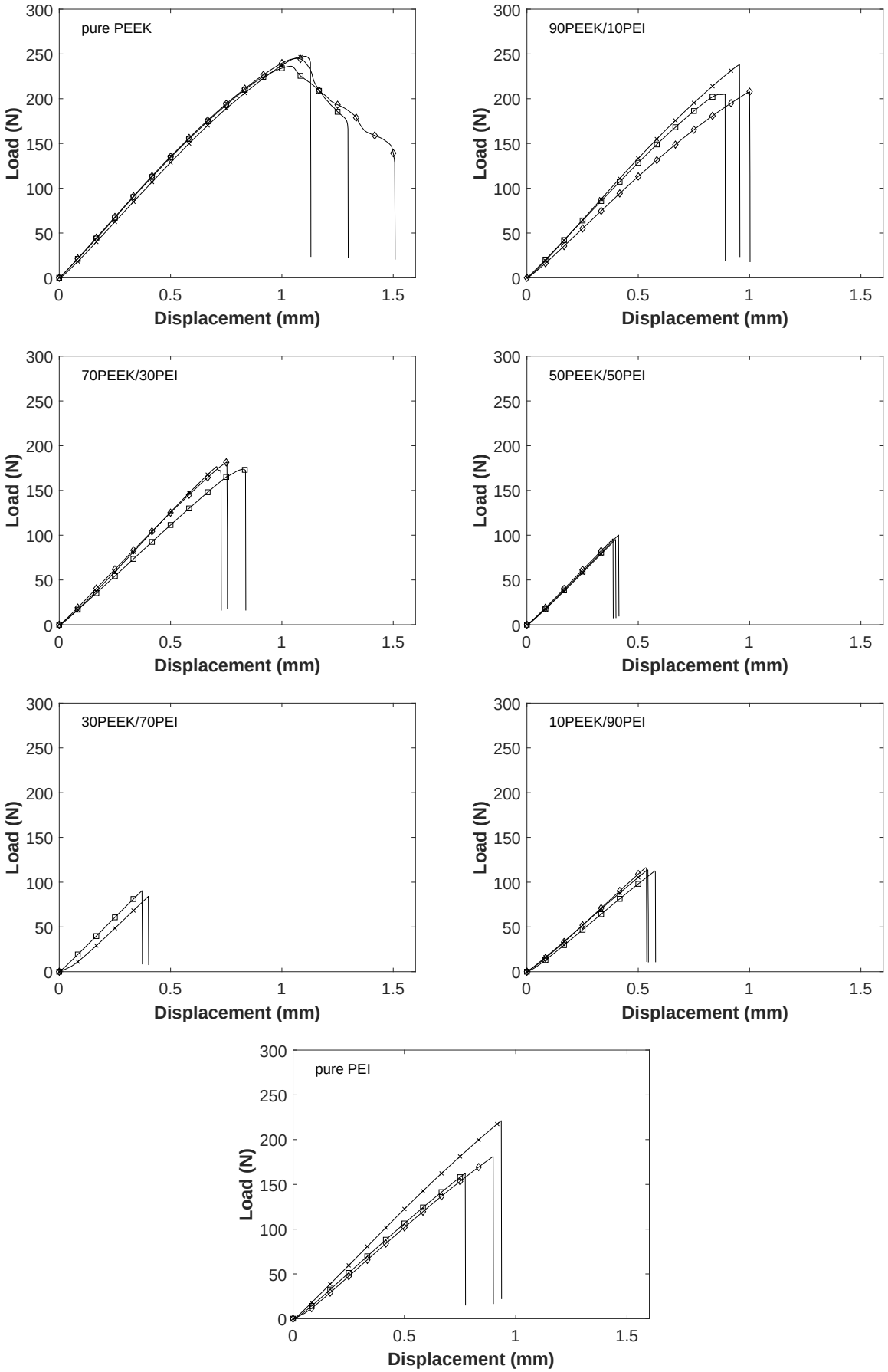

Figure C.2: Load-displacement curves of pure PEEK, pure PEI and different blend ratios

Bibliography

[Ageorges et al., 1998] Ageorges, C., Ye, L., Mai, Y.-W., and Hou, M. (1998). Characteristics of resistance welding of lap shear coupons. Part I: Heat transfer. Composites Part A: Applied Science and Manufacturing, 29(8):899–909.

[Attwood et al., 1981] Attwood, T. E., Dawson, P. C., Freeman, J. L., Hoy, L. R. J., Rose, J. B., and Staniland, P. A. (1981). Synthesis and properties of polyaryletherketones. Polymer, 22(8):1096–1103.

[Audoit et al., 2018] Audoit, J., Rivière, L., Dandurand, J., Lonjon, A., Dantras, E., and Lacabanne, C. (2018). Thermal, mechanical and dielectric behaviour of poly(aryl ether ketone) with low melting temperature. Journal of Thermal Analysis and Calorimetry, 135:2147–2157.

[Avenet, 2018] Avenet, J. (2018). Assemblage par fusion de composites à matrice thermoplastique : caractérisation expérimentale et modélisation de la cinétique d'auto-adhésion hors équilibre. PhD thesis, in French, Nantes.

[Awaja, 2016] Awaja, F. (2016). Autohesion of polymers. Polymer, 97:387–407.

[Bangarusampath et al., 2009] Bangarusampath, D. S., Ruckdäschel, H., Altstädt, V., Sandler, J. K. W., Garray, D., and Shaffer, M. S. P. (2009). Rheology and properties of melt-processed poly(ether ether ketone)/multi-wall carbon nanotube composites. Polymer, 50(24):5803–5811.

[Bas, 1994] Bas, C. (1994). Microstructure et propriétés thermomécaniques du poly(aryl éther éther cetone) (peek) amorphe et semi-cristallin. PhD thesis, in French, Chambéry.

[Bas et al., 1994] Bas, C., Battesti, P., and Albérola, N. D. (1994). Crystallization and melting behaviors of poly(aryletheretherketone) (PEEK) on origin of double melting peaks. Journal of Applied Polymer Science, 53(13):1745–1757.

[Benatar and Cheng, 1989] Benatar, A. and Cheng, Z. (1989). Ultrasonic welding of thermoplastics in the far-field. Polymer Engineering & Science, 29(23):1699–1704.

[Benatar and Gutowski, 1989] Benatar, A. and Gutowski, T. G. (1989). Ultrasonic welding of PEEK graphite APC-2 composites. Polymer Engineering & Science, 29(23):1705–1721.

[Bernhart and Erb, 2018] Bernhart, G. and Erb, G. (2018). Investigation of continuous induction welding of C/PAEK laminates. ECCM18: 18th European Conference on Composite Materials.

[Berry and Fox, 1968] Berry, G. C. and Fox, T. (1968). The viscosity of polymers and their concentrated solutions. In Fortschritte der Hochpolymeren-Forschung, volume 5 of Advances in Polymer Science, pages 261–357.

[Bessard, 2012] Bessard, E. (2012). Matériaux composites structuraux à base PEEK élaborés par thermo-compression dynamique : relation procédé-propriétés. PhD thesis, in French, Toulouse 3.

[Bhudolia et al., 2020] Bhudolia, S. K., Gohel, G., Leong, K. F., and Islam, A. (2020). Advances in Ultrasonic Welding of Thermoplastic Composites: A Review. Materials, 13(6):1284.

[Blackman et al., 1994] Blackman, B. R. K., Kinloch, A. J., and Watts, J. F. (1994). The plasma treatment of thermoplastic fibre composites for adhesive bonding. Composites, 25(5):332–341.

[Bonmatin et al., 2021] Bonmatin, M., Chabert, F., Bernhart, G., and Djilali, T. (2021). Rheological and crystallization behaviors of low processing temperature poly(aryl ether ketone). Journal of Applied Polymer Science, 138(47):51402.

[Bouvet, 2019] Bouvet, C. (2019). Mécanique de la rupture des composites : délaminage et fissuration. In French.

[Braun et al., 2021] Braun, M., Aranda-Ruiz, J., and Fernández-Sáez, J. (2021). Mixed Mode Crack Propagation in Polymers Using a Discrete Lattice Method. Polymers, 13(8):1290.

[Brown and Bangs, 1986] Brown, B. and Bangs, E. (1986). The Measurement and Monitoring of Resistance Spot Welds Using Infrared Thermography. In Thermosense VIII: Thermal Infrared Sensing for Diagnostics and Control, volume 0581, pages 57–71. SPIE.

[Cebe et al., 1987] Cebe, P., Chung, S. Y., and Hong, S.-D. (1987). Effect of thermal history on mechanical properties of polyetheretherketone below the glass transition temperature. Journal of Applied Polymer Science, 33(2):487–503.

[Chatain, 2001] Chatain, M. (2001). Matériaux composites : présentation générale. In French.

[Chatillon, 2006] Chatillon, J. (2006). Limites d'exposition aux infrasons et aux ultrasons. Étude bibliographique. In French.

[Chen et al., 2016] Chen, H., Ginzburg, V. V., Yang, J., Yang, Y., Liu, W., Huang, Y., Du, L., and Chen, B. (2016). Thermal conductivity of polymer-based composites: Fundamentals and applications. Progress in Polymer Science, 59:41–85.

[Choupin, 2017] Choupin, T. (2017). Mechanical performances of PEKK thermoplastic composites linked to their processing parameters. PhD thesis, Ecole nationale supérieure d'arts et métiers - ENSAM.

[Choupin et al., 2019] Choupin, T., Debertrand, L., Fayolle, B., Régnier, G., Paris, C., Cinquin, J., and Brulé, B. (2019). Influence of thermal history on the mechanical properties of poly(ether ketone ketone) copolymers. Polymer Crystallization, 2(6):e10086.

[Chuah et al., 2000] Chuah, Y. K., Chien, L.-H., Chang, B. C., and Liu, S.-J. (2000). Effects of the shape of the energy director on far-field ultrasonic welding of thermoplastics. Polymer Engineering & Science, 40(1):157–167.

[Cognard, 2003] Cognard, P. (2003). Assemblage des composites - Les points forts du collage. In French.

[Costa et al., 2012] Costa, A. P. d., Botelho, E. C., Costa, M. L., Narita, N. E., Tarpani, J. R., Costa, A. P. d., Botelho, E. C., Costa, M. L., Narita, N. E., and Tarpani, J. R. (2012). A Review of Welding Technologies for Thermoplastic Composites in Aerospace Applications. Journal of Aerospace Technology and Management, 4(3):255–265.

[Coulson, 2018] Coulson, M. (2018). Conductivité, diffusivité, émissivité thermiques de composites poly (EtherKetoneKetone) - charges carbonées : fibres continues et particules. PhD thesis, in French, Université Paul Sabatier - Toulouse III.

[Coulson et al., 2018] Coulson, M., Cortés, L. Q., Dantras, E., Lonjon, A., and Lacabanne, C. (2018). Dynamic rheological behavior of poly(ether ketone ketone) from solid state to melt state. Journal of Applied Polymer Science, 135(27):46456.

[Cox and Merz, 1958] Cox, W. P. and Merz, E. H. (1958). Correlation of dynamic and steady flow viscosities. Journal of Polymer Science, 28(118):619–622.

[Crevecoeur and Groeninckx, 1991] Crevecoeur, G. and Groeninckx, G. (1991). Binary blends of poly(ether ether ketone) and poly(ether imide): miscibility, crystallization behavior and semicrystalline morphology. Macromolecules, 24(5):1190–1195.

[Day et al., 1990a] Day, M., Cooney, J. D., and Wiles, D. M. (1990a). The thermal degradation of poly(aryl—ether—ether—ketone) (PEEK) as monitored by pyrolysis—GC/MS and TG/MS. Journal of Analytical and Applied Pyrolysis, 18(2):163–173.

[Day et al., 1990b] Day, M., Sally, D., and Wiles, D. M. (1990b). Thermal degradation of poly(aryl-ether-ether-ketone): Experimental evaluation of crosslinking reactions. Journal of Applied Polymer Science, 40(9-10):1615–1625.

[Day et al., 1988] Day, M., Suprunchuk, T., Cooney, J. D., and Wiles, D. M. (1988). Thermal degradation of poly(aryl-ether–ether-ketone) (PEEK): A differential scanning calorimetry study. Journal of Applied Polymer Science, 36(5):1097–1106.

[de Gennes, 1971] de Gennes, P. G. (1971). Reptation of a Polymer Chain in the Presence of Fixed Obstacles. J. Chem. Phys., 55(2):572–579.

[de Gennes, 1979] de Gennes, P. G. (1979). Brownian motions of flexible polymer chains. Nature, 282(5737):367–370.

[Devasahayam et al., 2006] Devasahayam, S., Hill, D. J. T., and Connell, J. W. (2006). FT-Raman studies of a range of polyimides subjected to high-energy radiations at room and elevated temperatures. Journal of Applied Polymer Science, 101(3):1575–1582.

[Dominguez, 2013] Dominguez, S. (2013). Relation structure/propriétés de polymères et mélanges thermoplastiques thermostables - Applications Aéronautiques Hautes Températures. PhD thesis, in French, Pau.

[Don et al., 1990] Don, R., Bastien, L., Jakobsen, T., and Gillespie, J. W. (1990). Fusion bonding of thermoplastic composites by resistance heating. SAMPE Journal, 26:59–66.

[Doumeng et al., 2022] Doumeng, M., Berthet, F., Delbé, K., Marsan, O., Denape, J., and Chabert, F. (2022). Effect of size, concentration, and nature of fillers on crystallinity, thermal, and mechanical properties of polyetheretherketone composites. Journal of Applied Polymer Science, 139(5):51574.

[Doumeng et al., 2021] Doumeng, M., Makhlouf, L., Berthet, F., Marsan, O., Delbé, K., Denape, J., and Chabert, F. (2021). A comparative study of the crystallinity of polyetheretherketone by using density, DSC, XRD, and Raman spectroscopy techniques. Polymer Testing, 93:106878.

[Dubé et al., 2007] Dubé, M., Hubert, P., Yousefpour, A., and Denault, J. (2007). Resistance welding of thermoplastic composites skin/stringer joints. Composites Part A: Applied Science and Manufacturing, 38(12):2541–2552.

[Fernandez Villegas and Palardy, 2016] Fernandez Villegas, I. and Palardy, G. (2016). Ultrasonic welding of thermoplastic composite coupons for mechanical characterization of welded joints through single lap shear testing. Journal of Visualized Experiments, 108.

[Fernandez Villegas and Palardy, 2017] Fernandez Villegas, I. and Palardy, G. (2017). Ultrasonic welding of CF/PPS composites with integrated triangular energy directors: melting, flow and weld strength development. Composite Interfaces, 24(5).

[Fernandez Villegas and Vizcaino Rubio, 2015] Fernandez Villegas, I. and Vizcaino Rubio, P. (2015). On avoiding thermal degradation during welding of high-performance thermoplastic composites to thermoset composites. Composites Part A: Applied Science and Manufacturing, 77:172–180.

[Fox, 1956] Fox, T. G. (1956). Influence of Diluent and of Copolymer Composition on the Glass Temperature of a Polymer System. Bulletin of the American Physical Society, 1:123.

[Friedrich et al., 1995] Friedrich, K., Lu, Z., and Hager, A. M. (1995). Recent advances in polymer composites' tribology. Wear, 190(2):139–144.

[Friedrich et al., 1986] Friedrich, K., Walter, R., Voss, H., and Karger-Kocsis, J. (1986). Effect of short fibre reinforcement on the fatigue crack propagation and fracture of PEEK-matrix composites. Composites, 17(3):205–216.

[Gao et al., 2018] Gao, Y.-H., Zhi, Q., Lu, L., Liu, Z.-X., and Wang, P.-C. (2018). Ultrasonic Welding of Carbon Fiber Reinforced Nylon 66 Composite Without Energy Director. Journal of Manufacturing Science and Engineering, 140(5).

[Garcia-Leiner et al., 2017] Garcia-Leiner, M., Reitman, M. T. F., El-Hibri, M. J., and Roeder, R. K. (2017). Structure-property relationships in commercial polyetheretherketone resins. Polymer Engineering & Science, 57(9):955–964.

[Gensler et al., 1996] Gensler, R., Béguelin, P., Plummer, C. J. G., Kausch, H. H., and Münstedt, H. (1996). Tensile behaviour and fracture toughness of poly(ether ether ketone)/poly(ether imide) blends. Polymer Bulletin, 37(1):111–118.

[Glynn et al., 2017] Glynn, H., Richard, L. A., Nigel, P. S., and John, L. (2017). Polymeric materials. Patent GB2543362A.

[Goto et al., 2019] Goto, K., Imai, K., Arai, M., and Ishikawa, T. (2019). Shear and tensile joint strengths of carbon fiber-reinforced thermoplastics using ultrasonic welding. Composites Part A: Applied Science and Manufacturing, 116:126–137.

[Herrmann-Schönherr et al., 1992] Herrmann-Schönherr, O., Schneller, A., Seifert, A. M., Soliman, M., and Wendorff, J. H. (1992). Chain dimensions, entanglement molecular weights and molecular weight distributions of poly(aryl ethers). A combined rheological and MNDO analysis. Die Makromolekulare Chemie, 193(8):1955–1974.

[Ho et al., 1994] Ho, R.-M., Cheng, S. Z. D., Hsiao, B. S., and Gardner, K. H. (1994). Crystal Morphology and Phase Identifications in Poly(aryl ether ketone)s and Their Copolymers. 1. Polymorphism in PEKK. Macromolecules, 27(8):2136–2140.

[Howie et al., 1993] Howie, I., Gillespie, J., and Smiley, A. (1993). Resistance Welding of Graphite-Polyarylsulfone/Polysulfone Dual-Polymer Composites. Journal of Thermoplastic Composite Materials, 6(3):205–225.

[Hsiao et al., 1998] Hsiao, B. S., Verma, R. K., and Sauer, B. B. (1998). Crystallization study of poly(ether ether ketone)/poly(ether imide) blends by real-time small-angle x-ray scattering. Journal of Macromolecular Science, Part B, 37(3):365–374.

[Ivanov and Jonas, 1998] Ivanov, D. A. and Jonas, A. M. (1998). Vitrification/devitrification phenomena during isothermal and nonisothermal crystallization of poly(aryl–ether–ether–ketone) (PEEK) and PEEK/poly(ether–imide) blends. Journal of Polymer Science Part B: Polymer Physics, 36(5):919–930.

[Jenkins, 2001] Jenkins, M. J. (2001). Crystallisation in miscible blends of PEEK and PEI. Polymer, 42(5):1981–1986.

[Jiang et al., 2019] Jiang, Z., Liu, P., Sue, H.-J., and Bremner, T. (2019). Effect of annealing on the viscoelastic behavior of poly(ether-ether-ketone). Polymer, 160:231–237.

[Jongbloed et al., 2018] Jongbloed, B. C. P., Teuwen, J. J. E., Palardy, G., and Fernandez Villegas, I. (2018). Improving weld uniformity in continuous ultrasonic welding of thermoplastic composites. ECCM18: 18th European Conference on Composite Materials.

[Kemmish and Hay, 1985] Kemmish, D. J. and Hay, J. N. (1985). The effect of physical ageing on the properties of amorphous PEEK. Polymer, 26(6):905–912.

[Kim and Ye, 2004] Kim, K.-Y. and Ye, L. (2004). Effects of thickness and environmental temperature on fracture behaviour of polyetherimide (PEI). Journal of Materials Science, 39(4):1267–1276.

[Ko and Woo, 1996] Ko, T. Y. and Woo, E. M. (1996). Changes and distribution of lamellae in the spherulites of poly(ether ether ketone) upon stepwise crystallization. Polymer, 37(7):1167–1175.

[Koutras et al., 2019] Koutras, N., Amirdine, J., Boyard, N., Fernandez Villegas, I., and Benedictus, R. (2019). Characterisation of crystallinity at the interface of ultrasonically welded carbon fibre PPS joints. Composites Part A: Applied Science and Manufacturing, 125:105574.

[Lamethe, 2004] Lamethe, J.-F. (2004). Etude de l'adhésion de composites thermoplastiques semi-cristallins; application à la mise en oeuvre par soudure. PhD thesis, in French, Université Pierre et Marie Curie - Paris VI.

[Lamèthe et al., 2005] Lamèthe, J.-F., Beauchêne, P., and Léger, L. (2005). Polymer dynamics applied to PEEK matrix composite welding. Aerospace Science and Technology, 9(3):233–240.

[Larson and Larson, 1999] Larson, R. G. and Larson, R. G. (1999). The Structure and Rheology of Complex Fluids. OUP USA.

[Lee et al., 2011] Lee, S., Nam, J., Hwang, W., Kim, J., and Lee, B. (2011). A study on integrity assessment of the resistance spot weld by Infrared Thermography. Procedia Engineering, 10:1748–1753.

[Levy, 2010] Levy, A. (2010). Modeling and simulation of vibrating flow. Application to the ultrasonic welding of thermoplastic matrix composites. PhD thesis, in French, Ecole Centrale de Nantes (ECN).

[Levy et al., 2014] Levy, A., Le Corre, S., and Fernandez Villegas, I. (2014). Modeling of the heating phenomena in ultrasonic welding of thermoplastic composites with flat energy directors. Journal of Materials Processing Technology, 214(7):1361–1371.

[Li et al., 2021] Li, X., Zhang, T., Li, S., Liu, H., Zhao, Y., and Wang, K. (2021). The effect of cooling rate on resistance-welded CF/PEEK joints. Journal of Materials Research and Technology, 12:53–62.

[Liu et al., 2001] Liu, S.-J., Chang, I.-T., and Hung, S.-W. (2001). Factors affecting the joint strength of ultrasonically welded polypropylene composites. Polymer Composites, 22(1):132–141.

[Lu et al., 1996] Lu, S. X., Cebe, P., and Capel, M. (1996). Thermal stability and thermal expansion studies of PEEK and related polyimides. Polymer, 37(14):2999–3009.

[Ma et al., 1992] Ma, C.-C. M., Lee, C.-L., and Tai, N.-H. (1992). Chemical resistance of carbon fiber-reinforced poly(ether ether ketone) and poly(phenylene sulfide) composites. Polymer Composites, 13(6):435–440.

[Martineau, 2018] Martineau, L. (2018). Mise en forme de composites carbone/PEEK dans le domaine caoutchoutique. PhD thesis, in French, Ecole des Mines d'Albi-Carmaux.

[Martineau et al., 2016] Martineau, L., Chabert, F., Bernhart, G., and Djilali, T. (2016). Mechanical behavior of amorphous PEEK in the rubbery state. In ECCM17 - 17th European Conference on Composite Materials.

[Martineau et al., 2019] Martineau, L., Chabert, F., Boniface, B., and Bernhart, G. (2019). Effect of interfacial crystalline growth on autohesion of PEEK. International Journal of Adhesion and Adhesives, 89:82–87.

[Minakov et al., 2007] Minakov, A. A., Wurm, A., and Schick, C. (2007). Superheating in linear polymers studied by ultrafast nanocalorimetry. Eur. Phys. J. E, 23(1):43.

[Mitschang et al., 2002] Mitschang, P., Rudolf, R., and Neitzel, M. (2002). Continuous Induction Welding Process, Modelling and Realisation. Journal of Thermoplastic Composite Materials, 15(2):127–153.

[Monich et al., 2016] Monich, P. R., Henriques, B., Novaes de Oliveira, A. P., Souza, J. C. M., and Fredel, M. C. (2016). Mechanical and biological behavior of biomedical PEEK matrix composites: A focused review. Materials Letters, 185:593–597.

[Motz and Schultz, 1990] Motz, H. and Schultz, J. (1990). Mechanical Failure in PEEK and Its Short-Fiber Composites. Journal of Thermoplastic Composite Materials, 3(2):110–130.

[Mylläri et al., 2015] Mylläri, V., Ruoko, T.-P., Vuorinen, J., and Lemmetyinen, H. (2015). Characterization of thermally aged polyetheretherketone fibres – mechanical, thermal, rheological and chemical property changes. Polymer Degradation and Stability, 120:419–426.

[Nicodeau, 2005] Nicodeau, C. (2005). Continuous welding modeling of thermoplastic matrix composites. PhD thesis, in French, Arts et Métiers ParisTech.

[Novacek et al., 2017] Novacek, V., Vackova, T., Spatenka, P., and Jenikova, Z. (2017). Application of low temperature plasma treatment for thermoplastic composites. In International Conference on Optimization of Electrical and Electronic Equipment

(OPTIM) Intl Aegean Conference on Electrical Machines and Power Electronics (ACEMP).

[Palardy and Fernandez Villegas, 2017] Palardy, G. and Fernandez Villegas, I. (2017). On the effect of flat energy directors thickness on heat generation during ultrasonic welding of thermoplastic composites. Composite Interfaces (Print), 24(2).

[Palardy and Villegas, 2015] Palardy, G. and Villegas, I. (2015). Ultrasonic welding of thermoplastic composites with flat energy directors: Influence of the thickness of the energy director on the welding process. ICCM 20: 20th International Conference on Composite Materials, Copenhagen, Denmark, 19-24 July 2015.

[Pétrier et al., 2008] Pétrier, C., Gondrexon, N., and Boldo, P. (2008). Ultrasons et sonochimie. In French.

[Ramani and Alam, 2010] Ramani, R. and Alam, S. (2010). Composition optimization of PEEK/PEI blend using model-free kinetics analysis. Thermochimica Acta, 511(1):179–188.

[Rashli et al., 2013] Rashli, R., Bakar, E. A., Kamaruddin, S., and Othman, A. R. (2013). A Review of Ultrasonic Welding of Thermoplastic Composites. Caspian Journal of Applied Sciences Research, 2(3):1–16.

[Roopa et al., 2008] Roopa, R. M., Prakasan, K., and Rudramoorthy, R. (2008). Studies on High Density Polyethylene in the Far-field Region in Ultrasonic Welding of Plastics. Polymer-Plastics Technology and Engineering, 47(8):762–770.

[Roovers et al., 1990] Roovers, J., Toporowski, P., and Ethier, R. (1990). Viscoelastic Properties of Melts of 'RADEL R' Polysulfone Fractions. High Performance Polymers, 2(3):165–179.

[Rosa et al., 2016] Rosa, M., Grassia, L., D'Amore, A., Carotenuto, C., and Minale, M. (2016). Rheology and mechanics of polyether(ether)ketone – Polyetherimide blends for composites in aeronautics. AIP Conference Proceedings, 1736(1):020177.

[Samyn and Schoukens, 2008] Samyn, P. and Schoukens, G. (2008). Tribochemical reactions on polyimide sliding surfaces evaluated with Raman spectroscopy and atomic force microscopy. Surface and Interface Analysis, 40(3-4):853–857.

[Senders, 2016] Senders, F. J. M. (2016). Continuous Ultrasonic Welding of Thermoplastic Composites. Master of Science Thesis. Delft University of Technology.

[Seo et al., 2020] Seo, J., Parisi, D., Gohn, A. M., Han, A., Song, L., Liu, Y., Schaake, R. P., Rhoades, A. M., and Colby, R. H. (2020). Flow-Induced Crystallization of Poly(ether ether ketone): Universal Aspects of Specific Work Revealed by Corroborative Rheology and X-ray Scattering Studies. Macromolecules, 53(22):10040–10050.

[Shabaev et al., 2018] Shabaev, A. S., Zhansitov, A. A., Kurdanova, Z. I., Kuchmenova, L. K., and Khashirova, S. Y. (2018). Investigation of thermal and thermo-oxidative degradation of poly(ether ether ketone) by gas chromatography. Chinese Journal of Chromatography, 36(4):395.

[Shahriar et al., 2017] Shahriar, B. B., France, C., Valerie, N., Arthur, C., and Christian, G. (2017). Toward improvement of the properties of parts manufactured by FFF (fused filament fabrication) through understanding the influence of temperature and rheological behaviour on the coalescence phenomenon. AIP Conference Proceedings, 1896(1):040008.

[Smiley et al., 1991] Smiley, A. J., Chao, M., and Gillespie, J. W. (1991). Influence and control of bondline thickness in fusion bonded joints of thermoplastic composites. Composites Manufacturing, 2(3):223–232.

[Speka et al., 2008] Speka, M., Matteï, S., Pilloz, M., and Ilie, M. (2008). The infrared thermography control of the laser welding of amorphous polymers. NDT & E International, 41(3):178–183.

[Takahashi, 1954] Takahashi, S. (1954). Cole-Cole's circular arc rule on dynamic properties of viscoelastic materials. Journal of Colloid Science, 9(4):313–320.

[Tao et al., 2019] Tao, W., Su, X., Wang, H., Zhang, Z., Li, H., and Chen, J. (2019). Influence mechanism of welding time and energy director to the thermoplastic composite joints by ultrasonic welding. Journal of Manufacturing Processes, 37:196–202.

[Taylor et al., 1989] Taylor, N. S., Jones, S. B., and Weld, M. (1989). The feasibility of welding thermoplastic composite materials. Construction and Building Materials, 3(4):213–219.

[Tsiangou et al., 2020] Tsiangou, E., Teixeira de Freitas, S., Villegas, I. F., and Benedictus, R. (2020). Ultrasonic welding of epoxy- to polyetheretherketone- based composites: Investigation on the material of the energy director and the thickness of the coupling layer. Journal of Composite Materials, 54(22):3081–3098.

[Van Beurden, 2015] Van Beurden, M. Q. C. (2015). Development & assessment of equipment and procedure for continuous ultrasonic welding of thermoplastic composites. Master of Science Thesis. Delft University of Technology.

[Velisaris and Seferis, 1986] Velisaris, C. N. and Seferis, J. C. (1986). Crystallization kinetics of polyetheretherketone (peek) matrices. Polymer Engineering & Science, 26(22):1574–1581.

[Villar et al., 2018] Villar, M., Garnier, C., Chabert, F., Nassiet, V., Samélor, D., Diez, J. C., Sotelo, A., and Madre, M. A. (2018). In-situ infrared thermography measurements to master transmission laser welding process parameters of PEKK. Optics and Lasers in Engineering, 106:94–104.

[Villegas, 2014] Villegas, I. F. (2014). Strength development versus process data in ultrasonic welding of thermoplastic composites with flat energy directors and its application to the definition of optimum processing parameters. Composites Part A: Applied Science and Manufacturing, 65:27–37.

[Villegas, 2015] Villegas, I. F. (2015). In situ monitoring of ultrasonic welding of thermoplastic composites through power and displacement data. Journal of Thermoplastic Composite Materials, 28(1):66–85.

[Villegas and Bersee, 2010] Villegas, I. F. and Bersee, H. E. N. (2010). Ultrasonic welding of advanced thermoplastic composites: An investigation on energy-directing surfaces. Advances in Polymer Technology, 29(2):112–121.

[Villegas et al., 2015] Villegas, I. F., Grande, B. V., Bersee, H. E. N., and Benedictus, R. (2015). A comparative evaluation between flat and traditional energy directors for ultrasonic welding of CF/PPS thermoplastic composites. Composite Interfaces, 22(8):717–729.

[Villegas et al., 2013] Villegas, I. F., Moser, L., Yousefpour, A., Mitschang, P., and Bersee, H. E. (2013). Process and performance evaluation of ultrasonic, induction and resistance welding of advanced thermoplastic composites. Journal of Thermoplastic Composite Materials, 26(8):1007–1024.

[Vinodhini et al., 2021] Vinodhini, J., Sudheendra, K., Balachandran, M., and Bhowmik, S. (2021). Influence of argon plasma treatment on carbon fibre reinforced high performance thermoplastic composite. High Performance Polymers, 33(3):285–294.

[Wang et al., 1993] Wang, F., Roovers, J., and Toporowski, P. M. (1993). Synthesis and molecular characterization of narrow molecular weight distribution fractions of methyl-substituted poly(aryl ether ether ketone). Macromolecules, 26(15):3826–3832.

[Wang et al., 2017a] Wang, K., Li, Y., Banu, M., Li, J., Guo, W., and Khan, H. (2017a). Effect of interfacial preheating on welded joints during ultrasonic composite welding. Journal of Materials Processing Technology, 246:116–122.

[Wang et al., 2017b] Wang, K., Shriver, D., Li, Y., Banu, M., Hu, S. J., Xiao, G., Arinez, J., and Fan, H.-T. (2017b). Characterization of weld attributes in ultrasonic welding of short carbon fiber reinforced thermoplastic composites. Journal of Manufacturing Processes, 29:124–132.

[Wetton and Corish, 1988] Wetton, R. E. and Corish, P. J. (1988). DMTA studies of polymer blends and compatibility. Polymer Testing, 8(5):303–312.

[White et al., 2013] White, K. L., Jin, L., Ferrer, N., Wong, M., Bremner, T., and Sue, H.-J. (2013). Rheological and thermal behaviors of commercial poly(aryletherketone)s. Polymer Engineering & Science, 53(3):651–661.

[Wise, 1999] Wise, R. J. (1999). Thermal Welding of Polymers. Woodhead Publishing.

[Wool et al., 1989] Wool, R. P., Yuan, B.-L., and McGarel, O. J. (1989). Welding of polymer interfaces. Polymer Engineering & Science, 29(19):1340–1367.

[Xu et al., 2020] Xu, J., Huang, X., Davim, J. P., Ji, M., and Chen, M. (2020). On the machining behavior of carbon fiber reinforced polyimide and PEEK thermoplastic composites. Polymer Composites, 41(9):3649–3663.

[Yousefpour et al., 2004] Yousefpour, A., Hojjati, M., and Immarigeon, J.-P. (2004). Fusion Bonding/Welding of Thermoplastic Composites. Journal of Thermoplastic Composite Materials, 17(4):303–341.

[Zhi et al.,] Zhi, Q., Tan, X.-R., and Liu, Z.-X. Effects of Preheat Treatment on the Ultrasonic Welding of Carbon Fiber Reinforced Polyamide 66 Composite. Welding Journal.

[Zitoune et al., 2013] Zitoune, R., El Mansori, M., and Krishnaraj, V. (2013). Tribo-functional design of double cone drill implications in tool wear during drilling of copper mesh/CFRP/woven ply. Wear, 302(1):1560–1567.

Résumé — Les dernières avancées sur l'application des pièces composites à matrice PAEK ont mis en avant des problématiques d'assemblages. Le soudage par ultrasons représente un enjeu prometteur pour l'utilisation à grande échelle de telles pièces. En effet, il s'agit d'un procédé très rapide et facile d'utilisation. Au cours de l'élaboration des éprouvettes de soudage, un film polymère a été intégré à la surface des composites à matrice PEEK et AE 250. Ce film est appelé directeur d'énergie et est nécessaire pour optimiser l'assemblage. Différents directeurs d'énergie ont été utilisés pour le soudage, tels que le PEEK, le PEI et l'AE 250. Des analyses rhéologiques et de cristallisation ont été réalisées pour caractériser le comportement de la nouvelle matrice Victrex PAEK AE 250. Dans le cas du soudage bi-matériau, une analyse rhéologique de mélanges PEEK/PEI a été réalisée, donnant des informations sur le comportement thermo-mécanique pendant le soudage. En complément, une procédure non-intrusive d'intégration de thermocouples a donné lieu à des mesures de profils de températures à l'interface pour différentes conditions de soudage. Ces données ont permis de développer un modèle par élément finis pour étudier la diffusion thermique dans l'épaisseur des éprouvettes. Enfin des essais mécaniques de cisaillement simple recouvrement ont permis d'évaluer l'influence de différentes conditions de soudage sur la qualité de la soudure. L'analyse des faciès de rupture a permis une compréhension plus approfondie des phénomènes physiques se déroulant pendant le soudage. Enfin, une étude paramétrique du soudage de composites à matrice AE 250 a été réalisée et comparée avec les résultats obtenus pour du soudage de composites à matrice PEEK.

Mots clés : Soudage par ultrasons, PAEK, composite, thermoplastique, aéronautique.

Abstract — The latest advancements in PAEK matrix composite parts have brought to light assembly issues. Ultrasonic welding represents a promising issue for the large-scale use of such parts. Indeed, the process is fast and easy to use. During their development, a polymer film was integrated on the surface of PEEK and AE 250 matrix composites. This film is called an energy director and is necessary for optimizing the assembly. Different energy directors have been used for welding, such as PEEK, PEI and AE 250. Crystallization and rheological analysis have been carried out to characterize the behavior of the new Victrex PAEK AE 250 matrix. In the case of bi-material welding, rheological analysis of PEEK/PEI mixtures has been conducted, giving information about the thermomechanical behaviors during welding. Moreover, a non-intrusive procedure of thermocouple integration allowed measurements of temperature profiles at the interface for different welding conditions. These data were used to develop a finite element model that gives information about the thermal diffusion in the specimen thickness. Finally, single lap shear tests were used to evaluate the influence of different welding conditions on the quality of the weld. The analysis of fracture surfaces allowed a deeper understanding of the physical phenomena occurring during welding. Finally, a parametric study of AE 250 composites welding was compared with the results obtained for PEEK composites joints.

Keywords: Ultrasonic welding, PAEK, composite, thermoplastic, aerospace.